

Growth and characterisation of earth-abundant semiconductor nanostructures for solar energy harvesting

Présentée le 16 décembre 2020

à la Faculté des sciences et techniques de l'ingénieur
Laboratoire des matériaux semiconducteurs
Programme doctoral en science et génie des matériaux

pour l'obtention du grade de Docteur ès Sciences

par

Simon Robert ESCOBAR STEINVALL

Acceptée sur proposition du jury

Dr Y. Leterrier, président du jury
Prof. A. Fontcuberta i Morral, Dr R. Zamani, directeurs de thèse
Prof. P. C. McIntyre, rapporteur
Prof. E. Alarcon-Llado, rapporteuse
Dr A. Hessler-Wyser, rapporteuse

Acknowledgements

The work presented in this thesis would not have been possible without the support of many individuals, both inside and outside the lab, be it friends, family, supervisors, colleagues, or collaborators, and my time during the PhD has been significantly enriched by their presence. I am incredibly grateful for everyone involved, and I want to thank them for helping me reach this stage. This short section will hardly give enough credit to many of the people involved, but here we go.

First and foremost I would like to thank Anna Fontcuberta i Morral for giving me this opportunity and supporting me throughout this journey. In addition to Anna's vast breadth of experience helping guide her students' scientific endeavours; she is very compassionate, kind and passionate about the well-being of her students. For me this was particularly noticeable with the slow start of the project and the (at the time) seemingly impossible task of getting the new molecular beam epitaxy system up and running (may it rest in pieces). Her attitude and mentoring has made this project possible, and has helped foster an amazingly supportive and pleasant atmosphere that is LMSC. This has helped me grow to the person and scientist I am today, and for this I thank you Anna.

While having joined later on in my PhD, I must also thank my co-supervisor Reza R. Zamani for his guidance in electron microscopy (I started that sentence with a "while" on purpose Reza). Reza is an expert electron microscopist, and has helped me delve deeper into my scientific endeavours and better understanding the materials we are working with through his expertise. I also thank him for invaluable insight and discussions regarding academia in Sweden.

I would also like to extend my gratitude to Yves Leterrier, Paul C. McIntyre, Esther Alarcón Lladó, and Aïcha Hessler-Wyser for their participation in my defence and taking the time to go through the thesis. I look forward to our discussion about it and your invaluable feedback that it will undoubtedly result in.

Next I would like to thank Jean-Baptiste Leran. Together we spent countless hours together working on getting the molecular beam epitaxy system working, and I have no doubt that if it had not been for Jean-Baptiste it would never have reached an operational status. I would also like to thank my colleagues working on earth-abundant semiconductors (+magnetic MBE): Elias Z. Stuts, Rajrupa Paul, Mahdi Zamani and Anna Kúkol'ová. Your input in this work has been invaluable, and it has been a pleasure to have you as colleagues both during and outside of work. I would also like to thank the undergraduate students who have contributed to my work here at EPFL: Virginie de Mestral, Calixte Bénier, Alexandre Looten, Leonardo Pires, and Gregoire de Jerphanion.

While my work was part of a budding project mainly carried out in our own lab, I would like to thank the collaborators who have helped us so far. I would like to thank Masoomah Ghasemi and Nelson Y. Dzade for their help in modelling zinc phosphide related aspects, and Fredrik S. Hage and Quentin M. Ramasse for allowing me to come and do some experiments using their incredible electron microscopy facilities. I would also like to acknowledge Milo Y. Swinkels and Ilaria Zardo for a fruitful collaboration to explore the optical properties of our nanostructures. Finally, I also want to thank the staff at CIME and CMi who have made a lot of this work possible, in particular Thomas LaGrange, Zdenek Benez, Duncan T. L. Alexander, and Marco Cantoni.

I want to thank all members from LMSC, past and present, for making my time here such a pleasure. I would like to thank the "old guard" who were here when I first arrived (Gözde, Heidi, Francesca, Marco, Eleonora, Pranit, Jelena, Dmitry, Pablo, Andres, Luca, Andreana and Martin). You all helped me settle in and enjoy it here in Lausanne and in LMSC. Gözde and Andreana made sure that no one missed (or could refuse) an opportunity for drinks. Heidi was my first call when learning to work the Talos, and showed how to be organised in a working environment (an ideal I am yet to reach, by a long shot). Dmitry and Pablo were the experts on nanowire photovoltaics (and Counter-Strike), and I learnt a lot from them. Marco for trying to explain to me why it is an atrocity to eat risotto with a spoon, among other

Italian food related knowledge. Luca for teaching about and how to use various setups for optical spectroscopy. Martin is an amazing person to have had as a colleague, who at the same time is one of the most practical people when it comes to making and programming new setups, and a brilliant and kind man through and through. He always made time when someone needed his help, almost to a fault, and your help we would not have been able to achieve nearly as much when it came to selective area epitaxy. The gatherings at your place (and of course Irene and Kiwi's as well) were always a pleasure. Maybe not the time I brought surströmming, but that one is on me.

I am also very grateful for the scientific and social intercourse with the current members of LMSC. In addition to the earth-abundant sub-group, the people who I have worked alongside throughout are Lea, Wonjong, Nico (the CL god), Nick, Andrea, Lucas, Akshay, Mintae and Didem. Work wise I want to thank Nico for all the help with everything CL related, as well as organising several excellent excursions around Switzerland (and bringing along Tosca). I would like to thank Lea for an interesting collaboration on figuring out the formation of zigzag nanowires, and for increasing my knowledge of cursing in Italian when you wrote up your master thesis. I am also indebted to Nick, Didem and Wonjong for their support when starting with selective area epitaxy as well as for their drive to arrange and participate in social activities. It was a pleasure showing you around Colombia Nick, next we will have to do Texas. The environment around the lab would not be the same without Akshay, Mintae, Andrea, and Lucas. For once I might admit that you are not the worst Andrea, but don't get used to it. While my overlap in LMSC with the newest members, Santhanu, Valerio and Mirjana, has been relatively short, we are very thankful for our discussions on fellowship applications among various topics.

In my time in Lausanne I have also had the pleasure to get to know many people outside of LMSC who have made this time more memorable. I would like to thank the people from LMGN: Sho, Maria Carmen, Korbinian, and Ping. In particular Sho for the unofficial language exchange helping me retain my Japanese; there is never a dull moment with you around. Then there are the people down the hall in PBL: Eva, Alice, Hale (and Jose), Giacomo, and Filippo. Procrastination breaks were much improved by strolling over and complaining about experiments not working, and it was always fun to go for a drink at Sat at the end of a long day. I have also had some great times here with a long list of people who I have met through EPFL, French courses, Sat, EDMX, and THEOS, and I could go on.

Finally I want to thank my family, without whom none of this would be possible. I am forever thankful for the love and support from my wife, Meg, who makes every day much more enjoyable. I would also not be the person I am today without the support of my parents, Lina and Robert, and my brother, Martin. They have helped me realise my dreams and encourage me to go and do whatever I want.

Lausanne, 28th September 2020

Abstract

Zinc phosphide (Zn_3P_2) is a compound semiconductor based on earth-abundant elements with functional properties ideal for solar cell applications. Cheap, abundant, and renewable energy sources are increasingly imperative due to the imminent threat posed by climate change. So far, zinc phosphide has not been exploited due to limitations in the fabrication of a high-quality material as a consequence of challenges in growth, controllable doping, and heterostructure formation. The maximum conversion efficiency ($\sim 6\%$) was obtained 40 years ago. One route with potential to circumvent or minimise the impact of the limiting factors is the growth of zinc phosphide in the form of nanostructures. By growing the material into nanoscale objects one opens up new elastic strain relaxation mechanisms, minimise the interface area, and loosen the lattice-matching constraints for high-quality epitaxial growth. This thesis focuses on the growth and characterisation with electron microscopy of (i) zinc phosphide nanowires grown through a vapour-liquid-solid approach, and (ii) nanopyramids and thin films grown through selective area epitaxy and lateral epitaxial overgrowth.

The first part of this thesis will introduce the reader to the motivation behind the research with regards to renewable energy and a review of zinc phosphide (Chapter 1), the growth of nanostructures (Chapter 2) with focus on molecular beam epitaxy and nanowires, and then the use of electron microscopy for characterisation of these structures (Chapter 3).

The second part of this thesis will focus on the scientific results from the investigations into the growth of zinc phosphide nanostructures. First, the epitaxial growth of zinc phosphide nanowires using an indium-catalysed vapour-liquid-solid approach was investigated (Chapter 4). The growth parameters and mechanism were explored, as well as their impact on the functional properties of the material. Four different nanowire morphologies were achieved, and a followup study focused on the structure and formation of the zigzag ones (Chapter 5). The structure of the zigzag nanowires was found to be analogous to the twin superlattices found in e.g. III-V nanowires, with one exception. Instead of the standard twin, the zinc phosphide nanowires were found to contain a heterotwin based on a \sim monolayer thick inclusion of indium at the mirror plane. It was shown that they did not influence the optoelectronic properties. A more general model for the superlattice formation was also developed, taking into account the non-polar nature of zinc phosphide. The last study explored zinc phosphide growth by selective area epitaxy (Chapter 6). The growth was limited to nanoscale holes using a nanopatterned oxide mask, where it proceeds through a vapour-solid mechanism. Zinc phosphide then forms nanopyramids enclosed by (101) facets, its most energetically stable configuration. If allowed to grow for long enough, the pyramids would coalesce into a thin film, via so-called lateral epitaxial overgrowth. This approach constitutes a step forward in the quest of high-quality, reproducible, and tunable growth of zinc phosphide, and offers a new pathway for its use as an earth-abundant photovoltaic material.

Finally, the work is summarised at the end alongside an outlook of future research building on the findings presented in this thesis (Chapter 7). The supplementary information to the different chapters can be found in appendices at the end of the thesis.

Keywords

Zinc phosphide, earth-abundant, photovoltaics, compound semiconductor, growth, molecular beam epitaxy, nanowires, vapour-liquid-solid, heterotwins, superlattices, nanopyramids, selective area epitaxy, lateral epitaxial overgrowth, characterisation, electron microscopy

Résumé

Le phosphure de zinc (Zn_3P_2) est un semi-conducteur à base d'éléments abondants dans la croûte terrestre et possédant des propriétés fonctionnelles idéales pour des applications dans le photovoltaïque. Des sources d'énergie bon marché, abondantes et renouvelables sont de plus en plus nécessaires en raison de la menace imminente posée par la crise climatique. Jusqu'à présent, le phosphure de zinc n'a pas beaucoup été exploité, en raison de limitations rendant difficile la fabrication d'un matériau de haute qualité. Ces défis sont le contrôle de la croissance et du dopage ainsi que la formation d'hétérostructures. La cellule solaire à base de phosphure de zinc avec le record d'efficacité énergétique ($\sim 6\%$) a été obtenue il y a 40 ans. La croissance du phosphure de zinc sous forme de nanostructures est une voie susceptible de contourner ou de minimiser l'impact des facteurs limitants. En faisant croître le matériau en structures d'échelle nanométrique, on obtient accès à de nouveaux mécanismes de relaxation de la déformation élastique, minimise la zone d'interface et assouplit les contraintes de correspondance des réseaux cristallins pour une croissance épitaxiale de haute qualité. Cette thèse traite de la croissance et la caractérisation par microscopie électronique de (i) nanofils de phosphure de zinc crûs par une approche vapeur-liquide-solide, et (ii) de nanopyramides et de couches minces obtenues par croissance sélective épitaxiale et surcroissance latérale épitaxiale.

La première partie de cette thèse présentera au lecteur la motivation derrière la recherche en discutant d'énergie renouvelable et en présentant un examen de la littérature sur le phosphure de zinc (Chapitre 1), la croissance des nanostructures (Chapitre 2) en mettant l'accent sur l'épitaxie par jets moléculaires et les nanofils, et la caractérisation de ces structures par microscopie électronique (Chapitre 3).

La deuxième partie de cette thèse portera sur les résultats scientifiques des recherches sur la croissance des nanostructures de phosphure de zinc. Tout d'abord, la croissance épitaxiale de nanofils de phosphure de zinc par une approche vapeur-liquide-solide catalysée par de l'indium a été étudiée (Chapitre 4). Les paramètres et mécanismes de croissance ont été explorés, ainsi que leur impact sur les propriétés fonctionnelles du matériau. Quatre morphologies de nanofils différentes ont été réalisées, suivies par une étude approfondie de la structure et la formation des nanofils zigzag (Chapitre 5). La structure des nanofils en zigzag s'est avérée être analogue aux super-réseaux maclés observés par exemple dans des nanofils III-V, à une exception près. Au lieu de contenir des macles standards, les nanofils de phosphure de zinc contiennent des hétéro-macles formées par une inclusion d'indium dans la monocouche atomique au plan miroir qui n'a pas d'impact sur les propriétés optoélectroniques. Un modèle plus général de la formation du super-réseau a également été développé, en tenant compte de la nature apolaire du phosphure de zinc. La dernière étude a exploré la croissance du phosphure de zinc par croissance sélective épitaxiale (Chapitre 6). La croissance a été limitée à des trous nanométriques en utilisant un masque d'oxyde, où elle se déroule par un mécanisme vapeur-solide. Le phosphure de zinc forme alors des nanopyramides entourées de facettes (101), la configuration la plus stable sur le plan énergétique. En les laissant croître suffisamment longtemps, les pyramides finissent par fusionner en un film mince par surcroissance latérale épitaxiale. Cette approche constitue un pas en avant vers la croissance de phosphure de zinc reproductible, ajustable et de haute qualité et offre une nouvelle voie pour son utilisation comme matériau photovoltaïque abondant dans la croûte terrestre.

Finalement, les travaux sont résumés avec une perspective de recherche future s'appuyant sur les résultats présentés dans cette thèse (Chapitre 7). Les informations complémentaires aux différents chapitres se trouvent dans les annexes à la fin de la thèse.

Mots-clés

Phosphure de zinc, abondant dans la croûte terrestre, photovoltaïque, semi-conducteur composé, croissance, épitaxie par jets moléculaires, nanofils, vapeur-liquide-solide, hétéro-macle, super-réseau, nano-pyramides, croissance sélective épitaxiale, surcroissance latérale épitaxiale, caractérisation, microscopie électronique

Contents

Acknowledgements	v
Abstract.....	vii
Keywords.....	vii
Résumé	viii
Mots-clés.....	viii
Contents	ix
List of Figures.....	xi
List of Tables.....	xvi
Chapter 1 Introduction – Motivation and Literature Review.....	1
1.1 Renewable Energy	1
1.2 Solar Cells	2
1.3 Emerging Material Systems for Photovoltaics	3
1.4 Zinc Phosphide.....	6
1.4.1 Overview	6
1.4.2 Compositional and Structural Properties	7
1.4.3 Optoelectronic Properties.....	8
1.4.4 Electrical Properties	9
1.5 Outlook.....	11
Chapter 2 Introduction – Nanomaterials: Growth and Properties.....	13
2.1 Growth.....	13
2.2 Molecular Beam Epitaxy	15
2.2.1 Operating Principles and Requirements.....	16
2.2.2 Competing Techniques.....	18
2.3 Nanowires.....	20
2.3.1 Properties.....	20
2.3.2 Nanowire Growth.....	21
2.4 Summary and Outlook.....	26
Chapter 3 Introduction – Characterisation.....	27
3.1 Electron Microscopy	27
3.2 Electron-Matter Interactions.....	28
3.3 Sample Requirements and Preparation.....	29
3.4 Electron Microscope Components	30
3.5 Aberrations and their Correction in Electron Microscopes	33
3.6 Imaging Modes	35

3.7	Analytical Electron Microscopy	37
3.8	Summary.....	40
Chapter 4	Vapour-Liquid-Solid Growth of Zinc Phosphide	41
4.1	Multiple Morphologies and Functionality of Nanowires made from Earth-Abundant Zinc Phosphide.....	42
4.1.1	Abstract.....	42
4.1.2	Introduction	42
4.1.3	Results and Discussion	43
4.1.4	Conclusion.....	49
4.1.5	Methodology.....	49
4.1.6	Supplementary Information.....	50
4.1.7	Acknowledgements.....	50
Chapter 5	Heterotwin Superlattice Nanowires	51
5.1	Heterotwin Zn ₃ P ₂ Superlattice Nanowires: the Role of Indium Insertion in the Superlattice Formation Mechanism and their Optical Properties	52
5.1.1	Abstract.....	52
5.1.2	Introduction	52
5.1.3	Experimental	53
5.1.4	Results and Discussion	54
5.1.5	Conclusion.....	57
5.1.6	Supplementary Information.....	57
5.1.7	Acknowledgements.....	57
Chapter 6	Selective Area Epitaxy of Zinc Phosphide	59
6.1	Towards Defect-Free Thin Films of the Earth-Abundant Absorber Zinc Phosphide by Nanopatterning	59
6.1.1	Abstract.....	60
6.1.2	Introduction	60
6.1.3	Results and Discussion	61
6.1.4	Conclusion.....	65
6.1.5	Supporting Information.....	65
6.1.6	Acknowledgements.....	65
Chapter 7	Summary and Outlook	66
	References.....	68
	Appendix A – Supplementary Information for “Multiple Morphologies and Functionality of Earth-Abundant Zinc Phosphide Nanowires”.....	92
	Appendix B – Supplementary Information to “Heterotwin Zn₃P₂ Superlattice Nanowires: the Role of Indium Insertion in the Superlattice Formation Mechanism and their Optical Properties”.....	98
	Appendix C – Supporting Information to “Towards Defect-Free Thin Films of the Earth-Abundant Absorber Zinc Phosphide by Nanopatterning”.....	101
	Curriculum Vitae – Simon Escobar Steinvall	104

List of Figures

Figure 1.1. (a) Band diagram of the charge separation mechanism of a p-n junction including the steps 1. photon absorption 2. electron excitation and 3. charge separation. (b) Charge separation through charge selective contacts.	2
Figure 1.2 Examples of the working principles of (a) plasmonic light trapping in solar cells (reproduced from [27] with permission from Springer Nature), (b) photon up-conversion in rare-earth nanoparticles, and (c) photonic crystal light trapping in solar cells (reproduced from [30] with permission from American Institute of Physics Publishing).	3
Figure 1.3 Example cross section designs of solar cells based on absorber layers made from (a) CIGS ³³ , (b) kesterites ³⁴ , (c) oxides ³⁵ , (d) organic ³⁶ , (e) DSSC ³⁷ , and (f) hybrid lead-halide perovskites ³⁸	4
Figure 1.4 (a) Zinc-phosphorus binary phase diagram simulated through the CALPHAD method by Ghasemi <i>et al.</i> ⁶⁷ (b) Visualisation of the zinc phosphide unit cell (COD ID: 1010287 from Crystallography Open Database) and (c) a diagram of how the standard unit cell (red) compares to the pseudo-cubic unit cell (black). 7	
Figure 1.5 Barrier height of evaporated contacts on zinc phosphide as measured by N. Convers Wyeth and A. Catalano in [72], reproduced with permission from American Institute of Physics Publishing.	10
Figure 2.1 Illustrations of (a) top-down manufacturing of nanowires and (b) bottom-up growth of nanowires.	13
Figure 2.2 Illustrations of (a) steric stabilisation and (b) charge stabilisation of chemically derived nanoparticles.	14
Figure 2.3 Illustrations of (a) pseudomorphic growth, (b) misfit dislocation at an interface and (c) van der Waal's epitaxy.	15
Figure 2.4 Illustrations of (a) layer-by-layer growth, (b) island growth, and (c) mixed growth.	15
Figure 2.5 (a) picture of the Veeco GENxplor MBE system highlighting the main components/sections (phosphorus cell and recovery system not visible). (b) illustration of the growth chamber.	16
Figure 2.6 Schematics of different cell types commonly used in MBE, depicting (a) Knudsen/effusion cells, (b) cracker cells, (c) sublimation cells, (d) electron-beam cells, and (e) gaseous cells.	17
Figure 2.7 (a) Illustration of the observed RHEED patterns for different growth configurations and (b) of the signal oscillation as a function of surface step density.	18
Figure 2.8 Diagrams of setups for (a) MOVPE, (b) PLD, (c) sputtering, and (d) evaporation.	18
Figure 2.9 Visualisation of (a) substrate heterojunctions, (b) axial heterojunctions, and (c) radial heterostructures. The black material is the substrate, green is material X, and blue is material Y.	21
Figure 2.10 Illustration of the VLS process, highlighting the contact angle and triple phase line of the droplet with the nanowire.	22
Figure 2.11 Illustration of (a) growth ready substrate, (b) surface processes during growth, and (c) grown sample.	24
Figure 2.12 (a) Diagram of the Wulff diagram which is symmetric around the Wulff point (0) in free space. (b) shows the inclusion of a substrate in the Winterbottom construct and how it alters the thermodynamic crystal shape.	25

Figure 2.13 Illustration of LEO, showing cross sections of (a) the initial substrate, (b) the early stages of growth, and (c) the coalescence of the structures into a film.....	26
Figure 3.1 Iterative and interdependent feedback loop which is the basis of current material science development.....	27
Figure 3.2 (a) Illustration of the electron-matter interactions in a TEM configuration and (b) the interaction volume in a SEM configuration.	28
Figure 3.3 Diagrams of the major components of the columns of (a) a SEM, (b) a conventional TEM, and (c) a STEM. Note that in a dedicated STEM setup the gun will be at the base, and the configuration will be flipped.	30
Figure 3.4 Comparison of the in-lens and standard secondary electron detector configuration.	32
Figure 3.5 Illustrations of (a) chromatic aberrations, (b) spherical aberrations, (c) comatic aberrations, and (d) astigmatism.....	34
Figure 3.6 Illustration of the relative secondary electron emission on a flat surface (left) and tilted surface (right) due to the proximity to the surface of a larger fraction of the interaction volume being within the escape depth.	35
Figure 3.7 (a) BF-TEM image of two zinc phosphide nanopillars in cross section and (b) the corresponding DF-TEM image. (c) is a HR-TEM image of the interface between zinc phosphide and the substrate, indium phosphide.	36
Figure 3.8 Illustration of a 2D slice of the Ewald's sphere, with 0 representing the non-diffracted beam, K_0 the non-diffracted wavevector and K_D the diffracted wavevector. Each dot represents a plane in reciprocal space.	38
Figure 3.9 (a) Illustration of the characteristic x-ray generation process and (b) HAADF-STEM and EDX maps showing the tip of an indium-catalysed vertical nanowire with the solidified droplet balancing on top.	39
Figure 4.1(a)-(d) are SEM images of vertical, straight-tilted, zigzag and crawling nanowires with scale bars of 500 nm. The first image is at 20°, whilst the others are normal to the substrate. (e) shows the growth condition and manipulator temperature combination which resulted in what morphologies and (f) is an illustration of the proposed growth mechanism.....	43
Figure 4.2 (a)-(c) are SEM images of nanowire ensembles obtained after 0 s (a), 5 s (b), and 10 s (c) argon ion beam exposure respectively. We observe an increase in nucleation density of 16x and 82x with respect to (a). All scale bars are 10 μ m.	44
Figure 4.3 (a) HAADF STEM image of the top of a vertical nanowire. (b)-(d) corresponding elemental map of indium, zinc and phosphorus. All scale bars are 50 nm. (e) shows the ternary phase diagram of the Zn-In-P system calculated using the CALPHAD method at 250 °C. (f) shows the deviation from stoichiometry of vertical nanowires grown at different V/II ratios. The straight lines indicate the ideal stoichiometry. The vertical and zigzag nanowires were grown at 250 °C, whilst the straight-tilted ones were grown at 235 °C.....	45
Figure 4.4 (a)-(d) HRTEM images of a zigzag nanowire grown at a V/II ratio of 1.30 at different magnification highlighting the superlattice formation along the growth axis and the superimposed SAED pattern along the [100] zone axis indicating a [101] growth direction. (a) is rotated 90° with respect to the other images. (e) shows a AC-HAADF STEM image inside a vertical nanowire, grown at a V/II ratio of 1.00, nanowire with an overlay of the zinc and phosphorus atoms as matched with the crystal structure as seen down the [100] axis (zinc is green and phosphorus red) alongside with an inset of the simulated structure. (f)-(i) are HRTEM and SAED images of a straight-tilted nanowire grown at a V/II ratio of 1.00 as seen along the [100] zone axis, indicating a growth direction of [101], note, e is rotated 120° in relation to the other images. (j) is an AC-HAADF STEM image of the surface of a vertical nanowire. (k)-(m) TEM images and the SAED pattern of a vertical nanowire along the [100] direction, indicating a growth direction along [001]. (n) is the corresponding STEM EDX line scan going from the bulk (0 nm) to the surface and vacuum (20 nm). Scale bars in a, f, k, and l are 200 nm. In b, g and h the scale bars are 10 nm, in c it is 5 nm, and finally in e and j they are 1 nm.	47

Figure 4.5 (a) is a SEM image of the zigzag nanowire analysed, and (b) shows a colour specific emission map of the zigzag nanowire, where green indicates the Zn_3P_2 emission whilst yellow is the background, InP, emission. (c) is a SEM image of a vertical nanowire grown at a V/II ratio of 1.15. (d) is an intensity map of the emission, showing higher intensity at the base of the nanowire. (e) is the spectra observed at different parts of the zigzag nanowire and also indicates the peak colouring in (b). (f) shows the spectra taken from the different parts of the vertical nanowire in (c), and (g) shows normalised emission spectra from vertical nanowires grown at different V/II ratios. All scale bars are 500 nm.....48

Figure 5.1 a) Secondary electron SEM image of a superlattice nanowire. b) Aberration corrected BF-STEM image taken along a [111] zone axis in the region around the zigzag interface with an inset illustrating the viewing direction. c) Aberration corrected HAADF-STEM image taken along a [101] zone axis in the region around the zigzag interface. The top inset illustrates the viewing direction and the bottom inset displays a “close up” on the interface. d) HAADF-STEM image ([111] zone axis) of the region where the EELS maps were acquired (green). e-g) Core-loss EELS maps of Zn (blue - e), In (orange - f), and the combination (g), showing the localised presence of In in the region around the stacking fault.....54

Figure 5.2 a) Secondary electron SEM image of a zigzag Zn_3P_2 nanowire b) schematic of the development of the cross-section of the nanowire as a function of the nanowire's growth axis, c) Results of the computation of the system (droplet and nanowires top facet) normalised surface energy (normalisation explained in the text) as a function of the variation of the geometry of the NW's top facet for three different referential droplet volume: small (red), medium (blue) and large (green); d) 3D sketch of the large droplet morphology upon the zigzag period.....56

Figure 5.3 (a) High-resolution panchromatic CL intensity map of a zigzag nanowire with the white arrow indicating the linescan of the extracted spectra in (b), of which the second and fourth from the top were extracted from regions on top of the heterotwin.....57

Figure 6.1 (a) SEM images of a flux series, varying the phosphorus to zinc (V/II) ratio at a constant zinc flux of 6.04×10^{-7} Torr from 0.18 to 0.72 for 60 min growth time at 290 °C manipulator temperature (30 nm nominal hole size, 200 nm pitch, 100 nm scale bars). (b) SEM images of a temperature series, varying the manipulator temperature between 280-300 °C at a V/II ratio of 0.5 for a growth time of 60 minutes (150 nm nominal hole size, 800 nm pitch, 500 nm scale bars). (c) SEM images of a time series of a pyramid spanning from 5 minutes to 240 minutes acquired at a V/II ratio of 0.61 (0.69 for the 240 minutes sample) and a manipulator temperature of 290 °C (note: last one taken at lower magnification to fit the full pyramid, 150 nm nominal hole size, 800 nm pitch, 100 nm scale bars). (d) AFM images of pyramids at different growth times and lattice structure models showing the different planes. (e) SEM image of initial stages of coalescence as seen with pyramids with 400 nm pitch and 75 nm nominal hole size (scale bar 500 nm). (f) SEM image of fully overgrown pyramid array with 200 nm pitch and 30 nm nominal hole size, still exhibiting a textured surface (scale bar 500 nm).....61

Figure 6.2 (a-c) Low-magnification HR-TEM images along the zinc phosphide [100] zone axis of pyramids grown in 30, 60, and 90 nm nominal holes for 1 hour at a V/II ratio of 0.5 and temperature of 290 °C (100 nm scale bars). (d) A representative SAED pattern showing diffraction from indium phosphide along the [110] zone axis superimposed on the relaxed zinc phosphide pattern along the [100] and [111] zone axes. (e) HR-TEM image of part of a pyramid highlighting areas where the FFT is acquired (100 nm scale bar). (f) FFT patterns from different parts of the pyramid, where 1-3 show a [100] zone axis and 4 shows a [111] zone axis. (g-h) Aberration corrected HAADF-STEM images of the core (g) along a [100] zone axis showing the systematic absences of zinc and the shell (h) along a [111] zone axis where the absences are not observed (2 nm scale bars). (i) Low-magnification HR-TEM image of a 30 nm nominal hole pyramid cut at 45° with respect to (a-c), resulting in a [110] zone axis with respect to zinc phosphide, highlighting the core-shell structure of the pyramids (100 nm scale bar). (j) Aberration corrected HAADF STEM image of the zinc phosphide and indium phosphide interface, showing pseudomorphic growth (2 nm scale bar). (k) Plot of the composition dependence on the nominal hole size as measured by STEM-EDX with the horizontal lines indicating the ideal stoichiometry. (l) Low-magnification HR-TEM image of the cross-section of a coalesced film grown from 30 nm nominal holes and 200 nm pitch with identical conditions as (a-c) but with a 6 hour growth time (100 nm scale bar).....62

Figure 6.3 (a) Atomic model of the core-shell configuration when observed along the [100]/[111] zone axes and (b) along the [110]/[001] zone axes. Blue represents zinc and orange phosphorus.....	63
Figure 6.4 (a) PL spectrum acquired from an array with 600 nm pitch and 150 nm nominal hole size, showing the indium phosphide, zinc phosphide, and defect emission. (b) c-AFM I-V curves of zinc phosphide grown on intrinsic, n-type, and p-type indium phosphide.....	64
Supplementary Figure A.S 1. SEM of nanowires at different magnifications. (a) and (b) are of vertical nanowires observed at 20° tilt (V/II ratio = 1.15 and 1.30, respectively). (c) shows a straight-tilted and vertical nanowire in close proximity (V/II ratio = 1.00) (d) is a top view image of zigzag nanowires (V/II ratio = 1.45). a, b and d have 10 µm scalebars, c has a 1 µm scale bar.	92
Supplementary Figure A.S 2. SEM of thin film overgrowing the catalyst particles. 10 µm scalebar....	93
Supplementary Figure A.S 3. SEM images of the initial catalyst particles at room temperature at different magnifications. The particles were generated using a 5 minutes zinc predeposition at 200 °C at a flux of 3.4×10^{-7} Torr. The average size was 365 nm with a standard deviation of 8 nm, and a density of one particle per 323 µm ² . Scale bars are 10 µm and 200 nm respectively.	93
Supplementary Figure A.S 4. Vertical section between Zn and InP, showing the transition at 156.3 °C from the liquid phase to the room temperature phases.	94
Supplementary Figure A.S 5. HAADF-STEM image of a vertical nanowire grown at a V/II ratio of 1.45 used for full wire EDX analysis. The composition of Area 1 (top) is 60.34% Zn and 39.66% P. The composition of Area 2 (bottom) is 60.71% Zn and 39.29% P. The scale bar is 250 nm.....	94
Supplementary Figure A.S 6 SEM of VS grown Zn ₃ P ₂ nanowires. (a) and (b) are top view images, whilst (c) is acquired at 20° tilt. Scale bars are 500 nm.	95
Supplementary Figure A.S 7. (a) shows the SAED pattern along the [111] zone axis. (b) is a low magnification image of the whole nanowire. (c) and (d) are HRTEM images of the nanowire in regions close to the droplet and towards the centre of the nanowire, respectively. Note that no stacking faults are observed along this zone axis. Scale bar in b is 1 µm, scale bars in c and d are 10 nm.....	95
Supplementary Figure A.S 8. (a) is a low magnification AC-HAADF STEM image of the surface of a vertical nanowire. (b) shows the FFT, and the red circles show the areas where we applied a mask to do an inverse FFT (c). (c) highlights the areas with a different crystal structure based on the applied mask. (d) shows a low magnification AC-HAADF STEM image of the bulk of the nanowire. The red line indicates where the line profile, presented below, was taken to compare with models to match the pattern and composition. Scale bar in c is 10 nm, in a and d they are 5 nm.	96
Supplementary Figure A.S 9. (a) Simulated STEM image of the zinc rich Zn ₃ P ₂ along the [100] zone axis. The edges shows the expected pattern for stoichiometric Zn ₃ P ₂ whilst the centre shows Zn ₂ P, where all vacant sites are filled with Zn atoms, assuming no change in crystal symmetry. The pattern observed in Figure 4I and Supplementary Figure S5d corresponds to a very Zn rich material, close to the highlighted region, as supported by the line intensity profiles of the measured (b) and modelled (c) intensities.	97
Supplementary Figure B.S 1. Illustration of the parameters used to model the droplet behaviour....	98
Supplementary Figure B.S 2. (a) EEL spectrum showing the In peak and (b) EEL spectrum showing the Zn peak used for mapping.....	98
Supplementary Figure B.S 3. a) TEM image of zigzag Zn ₃ P ₂ nanowire grown by MBE and b) plot of the development of an approximation of the nanowire's width as a function of the nanowire's growth axis: the dots represent the measurements taken on the sample shown in a) with fitting function reported in Equation 5.1.	99
Supplementary Figure B.S 4. CASINO Simulation of energy deposited in the sample for different edge configuration. Coloured surfaces show the decrease in energy density deposited in the sample, normalised to	

the maximum. Annotations show the fraction of backscattered electrons (η) and the total amount of energy (in keV) deposited in the sample per electron, for each edge configuration. It is observed that outwards facing apices (left) show enhanced backscattering compared to inwards facing apices (right) or facets (middle). Simulations were performed using a collimated electron beam of 10 nm diameter at 3 kV and a density of 4.55 g cm^{-3} for Zn_3P_2 . Due to the limited possibilities of simulating complex geometries in CASINO 3, we model the sample with truncated pyramids. This approximation reproduces well local edge configuration, but would not be valid in experiment conditions where a significant part of the beam energy is transmitted through the sample, e.g. at high beam energies. 100

Supplementary Figure C.S 0-1. Surface energies for the different planes considered and an illustration of the structures used for the DFT calculations. 102

Supplementary Figure C.S 0-2. SEM images of a V/II series grown at a manipulator temperature of 300 °C, showing how the ideal growth conditions shift from a V/II ratio of 0.5-0.63 to 0.27-0.39 (500 nm scale bars). 102

Supplementary Figure C.S 0-3. (a) HAADF image of pyramid grown in a 30 nm nominal hole along [100]. (b-e) EDX maps of P, Si, In, Zn of the pyramid. (f) Line-scan of the interface between the base and the pyramid showing a diffuse boundary between In and Zn in the area as indicated by the arrow in (a). (g) HAADF image of a pyramid grown in a 30 nm nominal hole along [110]. (h-k) EDX maps of P, Si, In, Zn of the pyramid. (l) Line-scan showing a homogeneous composition along the pyramid along the area indicated by the arrow in (g). (50 nm scale bars.) 103

Supplementary Figure C.S 0-4. (a) AC-HAADF-STEM of a pyramid grown from a 30 nm nominal hole. (b) Strain map acquired through GPA in the in-plane (xx) direction, perpendicular to the surface normal. (c) Line-scan along the arrow in (b) showing the strain relaxation of the zinc phosphide (right) in relationship to the indium phosphide (0) as it grows out from the hole. 103

List of Tables

Table 1.1 List of energy levels of acceptor-like defects and how they were measured. The energies below 0.8 eV are with respect to the valence band, while the ones above correspond to the defect level to conduction band transition.	8
Table 1.2 List of material combinations used for zinc phosphide based photovoltaics, highlighting the performance and fabrication method achieved by record devices.	11
Table 3.1 Summary of different types of electron guns and their properties. Values based on Egerton, Physical Principles of Electron Microscopy. ³⁴²	31

Chapter 1 Introduction – Motivation and Literature Review

1.1 Renewable Energy

The energy consumption in today's society is constantly increasing, and historically we have relied on expendable fossil fuels to cover our energy needs. The technologies related to the extraction, processing, and conversion are all very mature and used on a global scale. Whilst this has allowed us to easily achieve a very comfortable standard of living in the West, the detrimental effects of fossil fuels on the environment have long been known, and can manifest on smaller and larger scales. One example of a small-scale effect is the Great Smog of London, which lasted five days and killed an estimated 12,000 people.¹ Climate change due to a change in the atmospheric composition is impacting humanity on a global scale. The direct impact of climate change is difficult to quantify, but a long-term analysis predicts an increase in the average global temperature, which in turn affects the local ecosystems.^{2–4} The impact is seldom beneficial, and is affecting the habitability of various regions of the world. This has also been linked to an increase in extreme weather conditions, such as hurricane severity and numbers in the Atlantic, and forest fires in Australia.^{5–7} Climate change was first predicted back in the 19th century, with the first detailed model being presented by Svante Arrhenius in 1896.^{2,3} However, the topic of climate change has been a controversial issue, initially due to uncertainties in early models of this complex phenomenon, but with more supporting evidence amassing, the misinformation pushed by people with a vested interest in fossil fuels increased.^{3,8} Another drawback is the finite nature of the fossil fuel reserves, which cannot be replenished. To help mitigate and eventually counteract our detrimental effect on the planet there is currently a drive for renewable energy sources.

Renewable energy sources rely on plentiful natural phenomena which are widely accessible, such as water flow, wind, sun, and geothermal energy. There are some geographical limitations to the availability, but countries such as Norway utilise its rivers to cover a majority of its electricity production through hydropower.⁹ These sources are all promising, however, the one source with the greatest potential is solar energy due to its widespread availability and essentially unlimited supply.^{10,11} There are four main ways to harvest the solar energy, namely photovoltaics, direct heating, water splitting, and hydrocarbon production. Photovoltaic devices convert the incoming light straight to electricity, which will be covered in more detail below. The direct heating approach uses the incoming light to heat water and buildings without any intermediate steps. The last two approaches, water splitting and hydrocarbon production, rely on photocatalytic effects, utilising the incoming light and a catalyst to facilitate chemical reactions.^{12–14} The products of both cases, hydrogen and hydrocarbons, can be stored as fuels for later conversion to energy, and the hydrocarbons have the potential to be used for other applications as well. All of these approaches show promise, and a combination of various renewable energy harvesting techniques will likely be used to effectively cover our future energy needs.

In 2017, the yearly global power consumption was 23 696 TWh according to the International Energy Agency (IEA), whilst the amount of energy the Earth receives through sunlight is approximately 460 EWh per year (assuming 1000 W/m² reaching ground level for an area of the Earth's cross section), which is four orders of magnitude higher.^{11,15} Whilst this fact paints a pretty picture, there are still challenges with harnessing it. First, some of the areas with highest levels of insolation, such as the Sahara Desert and the Australian inlands, are scarcely populated and the generated electricity would have to be transported to areas where it would be used. Then there are areas such as oceans, making up roughly 71% of the surface, which are not particularly suitable either. Furthermore, the power generation and consumption rates throughout the day do not always match, with the peak power generation being at noon, while the peak consumption being in the evening, in addition to the consumption during the night when there is no generation. This creates a need for large-scale and high efficiency energy storage. Research into this is pursued in the form of batteries, hydrogen evolution or hydrocarbon generation.^{12,14} Finally, the implementation of solar energy has been limited by the cost, set by production and installation alongside limited efficiency of industrial-scale modules.¹¹ However, with the increasing demand for renewable energy and intense research efforts, the price is now down below 1 Euro cent per kWh, making them industrially viable.^{16,17}

The photovoltaic modules used today for large-scale applications are mainly based on silicon. The material availability alongside the knowledge of how to process silicon from the electronics industry has helped propel this material to its current leading position. Unfortunately, silicon's indirect bandgap forces the use of thicker absorber layers, increasing associated costs of the overall device.¹¹

Current research into photovoltaics to improve the applicability is split into two main paths: investigating new device structures/implementation for light management and new materials. A brief overview of new devices will be given next, with a more detailed explanation of nanowire for photovoltaics in the next chapter, whilst the materials perspective will be covered later in this chapter.

1.2 Solar Cells

Solar cells rely on the photovoltaic effect, which allows for the direct conversion of light to electricity. To generate useful power a couple of requirements have to be met, namely that (i) the charge carriers can be separated to create a photocurrent and (ii) there being a potential difference between the holes and electrons exiting the device, allowing for them to perform work.^{11,18} The materials ideal for this application are semiconductors, which have an electronic structure with a bandgap in the order of a few eV, compatible with the incoming solar spectrum.^{11,18} Furthermore, semiconductor devices can be designed to provide mechanisms, such as internal electric fields or charge selective contacts, to separate the charges. When a valence band electron in a semiconductor absorbs a photon with an energy greater than that of the bandgap, it is promoted to the conduction band and a positively charged hole is left in its place, as illustrated in Figure 1.1a. The oppositely charged particles can then be separated and forced to do work before recombining to the low-energy state. In Figure 1.1a the charges are separated by the internal electric field generated by the p-n homojunction. The internal electric field can also be generated by joining two dissimilar semiconductors, forming a heterojunction, allowing efficient charge separation. Figure 1.1b on the other hand illustrates the use of charge selective contacts, which is another common approach to separate the charges. Finding the best material combinations for these processes is a highly active area of research.

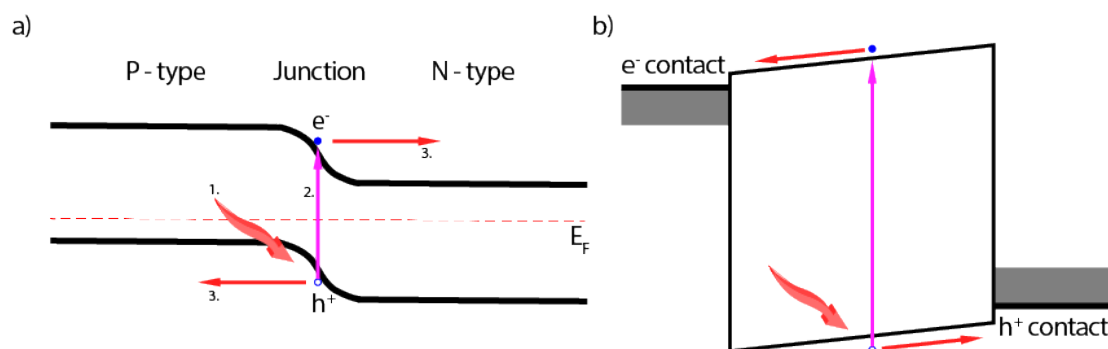


Figure 1.1. (a) Band diagram of the charge separation mechanism of a p-n junction including the steps 1. photon absorption 2. electron excitation and 3. charge separation. (b) Charge separation through charge selective contacts.

The performance of photovoltaic devices is characterised by their conversion efficiency, which can be defined as the electrical power output over the incident light power as a percentage.¹¹ The maximum theoretical efficiency is defined by the Shockley-Queisser limit.^{11,19} This model takes into account losses due to photons with an energy below the bandgap, which thus cannot be absorbed, and the energy loss due to the thermal relaxation of electrons which have been excited above the bandgap. Current estimates of the optimum value of the bandgap for a single junction solar cell based on this model is 1.34 eV, resulting in a maximum conversion efficiency of roughly 33.7%.¹¹ This efficiency has not been achieved in real devices, which can be attributed to defects resulting in leakage currents, charge recombination, series resistance, among other limiting factors.¹¹ So far, the highest efficiencies achieved in single layer photovoltaics (without concentrators), is 29.1% in gallium arsenide-based devices and 26.7% in silicon-based devices.^{20–22} Combining materials with different bandgap into one device, a so-called tandem cell, allows one to reach even higher efficiencies.^{11,23} Tandem cells can be made by either stacking several non-interacting and separately contacted devices (multi-terminal), or by having several lattice and current matched layers integrated monolithically (two-terminal).^{11,23} While the theoretical efficiencies in this case can reach up to 72% for an infinite number of layers, the highest achieved efficiency in a tandem cell is 47.1%.^{11,24} Unfortunately, the fabrication becomes increasingly complex with each additional layer and the associated costs have limited their application.

The presence of defects in devices is often detrimental to their performance, and there are multiple origins of defects in semiconductors. These defects include vacancies, interstitials, dislocations, grain boundaries, precipitates, and so forth.^{11,18,25} One of the ways they can affect the performance is by acting as scattering centres for the electrons, reducing their mobility and in turn lowering the

probability of a separated charge being successfully extracted. They can also act as non-radiative recombination centres, which reduce the lifetime of the separated charges and again hinder their successful extraction. Whilst these defects occur anywhere in the device to a certain extent, the regions with the highest prevalence tends to be the interfaces between different layers. Misfit dislocations due to lattice mismatch and incoherent boundaries have hindered the successful application of more than one material system combination. Nonetheless, there are ways to get around this, or at least mitigate its influence, as will be discussed in more detail in the next chapter.

In addition to improving the materials and finding better combinations, multiple approaches are currently being investigated to improve light management in devices. A more detailed review at the current state of this field was recently published by Garnett *et al.*²⁶ The most prominent approach is the texturing of the front surface of the photovoltaic and antireflective coatings, which can bring down the light lost due to reflection from ~35% down to 2%.¹¹ Furthermore, light management can be used to increase the optical pathlength in a layer, allowing for higher absorption in thinner layers, which reduces losses, or allowing it to access different parts of the solar spectrum. Currently, there are multiple approaches proposed to improve the light management in photovoltaics, some of them being plasmonics, photon down/upconversion, and light trapping with photonic crystals, as illustrated in Figure 1.2. Plasmonic nanoparticles, as shown in Figure 1.2a, have been used to trap parts of the incoming light in the regions best suited to absorb it, and for resonant energy transfer into the absorber material.²⁷ Photon conversion relies on rare-earth or organic nanoparticles capable of either splitting a high-energy photon into two (down), reducing the energy wasted through thermal relaxation, or by combining multiple sub-bandgap photons into one with the capability to excite over the bandgap (up).^{28,29} The upconversion is illustrated in Figure 1.2b, where two low-energy photons (red) are combined to form a high-energy photon (blue).²⁸ Photonic crystals, on the other hand, can be used to suppress bandgap emission by trapping photons of the emission wavelength inside the device.^{30,31} Whilst they all show promise in increasing device performances, they are still in the research stage. Another area of intense research in the photovoltaic community is new materials systems suitable for photovoltaics, which will be covered next.

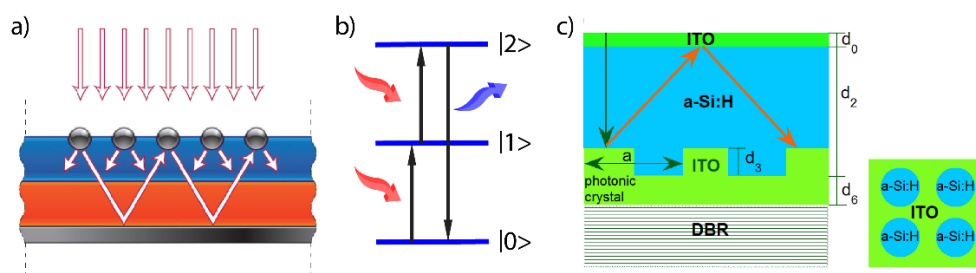


Figure 1.2 Examples of the working principles of (a) plasmonic light trapping in solar cells (reproduced from [27] with permission from Springer Nature), (b) photon up-conversion in rare-earth nanoparticles, and (c) photonic crystal light trapping in solar cells (reproduced from [30] with permission from American Institute of Physics Publishing).

1.3 Emerging Material Systems for Photovoltaics

This section will briefly highlight and compare the different material systems actively investigated for their potential in photovoltaic applications. The materials can loosely be split into two categories: mature and emerging materials. The first one includes silicon and III-V materials such as gallium arsenide and indium phosphide. Whilst there is still research into how to further optimise these materials, efficiencies comparable to their respective Shockley-Queisser limit and long device lifetimes have been achieved. Hence we have lately seen a great increase in the deployment of silicon photovoltaics for terrestrial applications, whilst III-V based systems, often tandem ones, have been used for space applications due to their superior efficiency to weight ratio. The limitations related to these technologies is the poor optical absorption of silicon due to its indirect bandgap, increasing the associated processing cost of sufficiently thick and efficient layers, and the reliance on scarce elements in III-V systems, resulting in high material costs.¹⁷

The emerging technologies are heavily researched as they show promise for low-cost and large scale application, however, may struggle with either achieving high conversion efficiencies or sufficiently long lifetimes to become industrially viable. The main material systems in this category are “thin-film materials”, kesterites, oxides, organics, and hybrids. This list is by no means exhaustive, and there is a plethora of materials currently explored, such as zinc phosphide, and new systems are emerging with the help of studies

such as the Materials Project based on computational screening.³² For brevity, we will limit ourselves to giving a brief overview of the ones listed above. Example device cross-sections of the previously listed above are shown in Figure 1.3, and more detailed descriptions will be provided next.

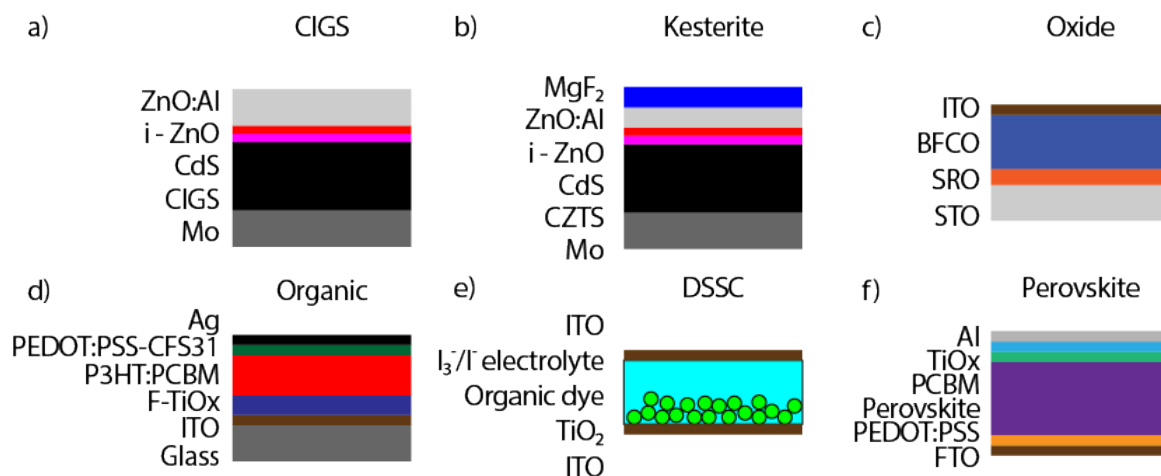


Figure 1.3 Example cross section designs of solar cells based on absorber layers made from (a) CIGS³³, (b) kesterites³⁴, (c) oxides³⁵, (d) organic³⁶, (e) DSSC³⁷, and (f) hybrid lead-halide perovskites³⁸.

The main thin-film materials, namely copper indium gallium selenide (CIGS) and cadmium telluride, have both achieved lab scale efficiencies above 20% and decent lifetimes (10-15 years), which would make them the most mature of the emerging materials (and one could argue that they already are mature). Unfortunately, they still suffer from the use of scarce materials, or in the case of cadmium telluride, suffers from fears due to the toxicity of cadmium.^{22,39,40} There is already commercial production of these cells, however, it is less than 2% of the total market, and they are having difficulties competing with silicon with their comparably lower efficiency, or poor publicity due to toxicity.⁴⁰ The cross section of a CIGS-based device is shown in Figure 1.3a. The thickness is in the order of a few micrometres, which is a fraction of that of a standard silicon cell.³³

Kesterites are one of the most heavily researched earth-abundant photovoltaic material systems and derive their name from the mineral on which their crystal structure is based.⁴¹ Kesterites used in photovoltaics are generally based on copper zinc tin selenide (CZTS – Cu₂ZnSnSe₄).⁴¹ All the constituent elements are earth-abundant, and the product is a stable inorganic material with a bandgap of 1.4-1.5 eV, ideal for photovoltaic applications. To date, the highest verified efficiency of these cells is 12.6%, achieved by IBM in 2014.³⁴ A cross-section of the record device is shown in Figure 1.3b, where the black CZTS layer is the kesterite absorber.³⁴ Similar to CIGS, the thickness of the full device is in the order of a few micrometres. Whilst promising for earth-abundant thin film applications, kesterites are limited by various factors including deep defects, composition inhomogeneities, cation disorder, among other factors.⁴¹ There is plenty of research into solving these issues by groups around the world, hoping to enable them for large-scale commercial application.

The last of the fully inorganic systems covered in this section are the oxide-based photovoltaics. Whilst most systems tend to utilise at least one oxide component, in the form of indium tin oxide (ITO – In₂O₃:Sn) as the transparent top contact, there is also research done into completely oxide-based photovoltaics.^{35,42–44} These systems are attractive due to their inherent stability towards oxidation, however, this is still an issue for copper oxide based modules. The ideal stoichiometry for copper oxide-based photovoltaics is cupric oxide (CuO), which has a direct bandgap of 1.4 eV (and indirect at 1.2 eV), however, it readily changes oxidation state, forming cuprous oxide (Cu₂O), shifting the bandgap to the less ideal region of 2.1 eV. Furthermore, the existence of two phases that usually occurs at this stage creates a multitude of non-radiative recombination paths, effectively killing any devices. Solar cells based on only cuprous oxide have been more stable and successful, reaching conversion efficiencies of 8.10%.⁴³ While the maximum conversion efficiency is capped at ~20%, the abundance and low cost makes this an interesting material system. Photoferroelectrics on the other hand have started to garner interest due to the anomalous photovoltaic effect because of their polar non-centrosymmetric structure.^{35,45} The anomalous photovoltaic effect facilitates the charge separation through its spontaneous internal electric field, which can be up to four orders of magnitude higher than that generated in a standard semiconductor device.⁴⁵ The anomalous photovoltaic effect in photoferroelectrics results in large open-circuit voltages, and potentially allowing for high-efficiency devices.⁴⁵ However, the carrier diffusion length is limited in these materials (<100 nm), reducing the short circuit current. The maximum conversion efficiency achieved so far is 8.1% in Bi₂FeCrO₆ (BFCO).^{35,44} The structure of the highest efficiency BFCO photovoltaic device is illustrated in Figure

1.3c, where all the layers are oxide based (strontium titanate (STO – SrTiO_3), strontium ruthenate (SRO – SrRuO_3), and ITO). The thickness of the active layer is in the order of ~ 100 nm to allow for the efficient charge extraction, resulting in very thin devices.

Organic photovoltaics have attracted a lot of attention because of the high availability of carbon, and their potential to be solution processed, resulting in low production costs.⁴⁶ The vast number of organic semiconducting compounds allow for a wide range of material combinations. However, organic semiconductors produce Frenkel excitons under illumination, as compared to the Mott-Wannier excitons in inorganic semiconductors, which are characterised by their high binding energy ($E_{\text{Frenkel}} \sim 0.5 - 1.0 \text{ eV} > E_{\text{Mott-Wannier}} \sim 0.1 \text{ eV}$). As such, they cannot be separated as easily. The excitons thus have to diffuse to an interface to fully dissociate with the help of charge-selective layers or Schottky barriers. These layers are referred to as the electron-transport layer or hole-transport layer depending on their charge selectivity. The example device shown in Figure 1.3d used P3HT:PCBM as the absorber layer, fluorinated titania as the electron-transport layer, and PEDOT:PSS-CFS31 as the hole-transport layer.³⁶ The vision behind organic photovoltaics has been to achieve low-cost solar cells in a spray can, or printable photovoltaics.⁴⁶ However, the limitations of organic photovoltaics are the difficulty to achieve efficient charge separation without using expensive hole-transport layers, and the stability of some of the layers limiting its lifetime.⁴⁶ Commercial utilisation of organic photovoltaics is attractive as working devices, albeit low conversion efficiencies, can be readily achieved at a low production cost, and is commonly found in small and portable devices such as calculators. Organic light emitting diodes (OLEDs) have also shown great promise, and in the last decade has been applied on industrial scales in flat-screen TVs and mobile phones.

The last category discussed, the hybrid cells, utilise a combination of inorganic and organic components, and are made up of two main systems: dye-sensitised solar cells (DSSC) and lead-halide hybrid perovskite solar cells. A cross section of a DSSC is shown in Figure 1.3e.³⁷ DSSCs rely on an organic dye (black layer coating the spheres) to efficiently absorb the incoming light, coated onto a porous inorganic layer (green spheres, initially made from titania) and then encapsulated by an ionic liquid (blue, initially an I_3^-/I^- electrolyte).^{37,47} The dye is optimised to absorb the light, however, as it is only a monolayer thick, several passes are required to capture all the light.^{37,47} Multiple passes are achieved by utilising a porous support structure. The charges can be separated without the movement of the exciton due to its monolayer thickness, and the electron goes into the titania while the hole is transported by the liquid electrolyte. By using dyes which only capture part of the solar spectrum it is possible to make coloured solar panels using DSSCs, which was used at the SwissTech Convention Center where they covered one side of the building with an ornate solar panel display to honour Michael Grätzel who invented the DSSCs at EPFL in the early 1990's. At their invention, they were heavily researched due to their low production cost and high initial conversion efficiency. Similar to organic photovoltaics, the processing of DSSCs can be done at very low costs and using high-throughput methods.⁴⁷ Unfortunately, due to the thermodynamics involved and the voltage drop at the required charge transfer steps, the efficiency is capped at $\sim 12\%$, and the lifetimes of commercially produced cells are also limited.^{22,47}

One technology with similarities to DSSC technology, and often considered to be a continuation of DSSCs, is the hybrid lead-halide perovskite solar cells.⁴⁸ Perovskite is a crystal structure based on the ABX_3 stoichiometry, where A and B are in two cubic sublattices displaced by $(\frac{1}{2}, \frac{1}{2}, \frac{1}{2})$, and the X species in an octahedral geometry around the B species. The standard hybrid lead-halide perovskite has three main components: methylammonium (A), lead (B), and halides (X).⁴⁸ Hybrid perovskite cells for solar cells were first reported in 2009, with an efficiency of 3.5%, and was essentially a DSSC but with a hybrid lead-halide perovskite as the dye.⁴⁹ Since then the structure has changed significantly, with modern versions looking more like the version in Figure 1.3f, exhibiting a geometry more similar to traditional thin-film photovoltaics. Through intense research, hybrid lead-halide perovskite-based solar cells have now reached record efficiencies above 25%.^{22,38,48,50} Furthermore, the relatively high bandgap of the hybrid perovskite (1.8-2.3 eV depending on exact composition), makes it an excellent tandem cell companion to silicon photovoltaics, and these modules have currently reached maximum conversion efficiencies of 29.1%.^{50,51} Consequently, hybrid perovskites have garnered great interest from researchers all around the world, and are by far the most researched photovoltaic materials today. However, despite their impressive efficiency, there are still a few limitations. First, the lead content is a concern, due to its inherent toxicity, and as it can separate from the compound easily.⁴⁸ Researchers have tried to exchange it for tin, however, this resulted in a decrease in efficiency, and the product sometimes forms precipitates due to the multiple oxidation states of tin.⁵² The thermodynamics stability of the system is also a point of active research. For example, they have been shown to segregate into two less optimal phases upon illumination, which is undesirable for long-term photovoltaic applications.^{53,54} Solutions are being actively searched for with the prospect of making hybrid perovskites an option for cheap and efficient photovoltaics for industrial scale applications.

To summarise, research into the next commercially viable material system for photovoltaics is well underway in all corners of the world. Multiple promising systems have been identified, with the capacity to reach high conversion efficiencies or low production costs, or a combination of the two, which would have a significant positive impact on the renewable energy generation which is imperative to sustain our climate.

1.4 Zinc Phosphide

1.4.1 Overview

One material system which was only briefly mentioned above was zinc phosphide (Zn_3P_2), which will now be described in more detail as it is the focus of this thesis. Zinc phosphide is an earth-abundant semiconductor, and in the stoichiometry mentioned above, studies have found a direct bandgap of 1.5 eV, long carrier diffusion lengths (5–10 μm), and high absorption in the optical range ($>10^4 \text{ cm}^{-1}$), making it ideal for photovoltaic devices.^{55–62} Both zinc and phosphorus are mined on industrial scales, and their extraction is well known, which would simplify any industrial-scale application of the material.^{63,64} However, zinc mining is the largest source of cadmium, a heavy metal, and if not handled properly, phosphorus poses a danger due to its neurotoxicity and flammability.^{63,65} Furthermore, the only industrial scale application of zinc phosphide is its use as a rodent toxin.⁶⁶ While posing a challenge, proper encapsulation during production can readily be achieved, and as a direct bandgap semiconductor the material needed can be minimised, making it a viable platform for large-scale photovoltaic applications.

As can be seen from the zinc-phosphorus phase diagram in Figure 1.4, there is a second stable stoichiometry, zinc diphosphide (ZnP_2), which has a bandgap of 1.8 eV.⁶⁷ Whilst less ideal for single-junction photovoltaics, this stoichiometry could potentially be useful for tandem cells with silicon or for water-splitting applications. However, this stoichiometry has not been actively investigated in this project, and will only be mentioned in passing.

The earliest characterisation of zinc phosphide was reported in 1935, investigating the synthesis by sublimation and its crystal structure through x-ray diffraction experiments.⁶⁸ To the best of my knowledge, no research was published concerning its semiconducting properties until late 1953, when Lagrenaudie brought attention to it.⁶⁹ The first significant study of zinc phosphide as a potential photovoltaic material was carried out at the University of Delaware on a government contract in the late 1970's, where they reported on the synthesis through mass transport, doping, contacting, electrical properties, and optical properties of bulk crystals.^{56,61,70–72} Using magnesium as a dopant/Schottky contact (later proved to generate a heterojunction forming ternary phase) a maximum conversion efficiency of 5.96% was achieved.⁶² The challenges with the material, whilst described in more detail below, can be summarised to three main factors. First, zinc phosphide lacks a lattice matched growth substrate. Growth on lattice mismatched substrates results in detrimental defects at the interface or strain build up, which in turn inhibits high-performance devices. Moreover, its high thermal expansion coefficient compared to other semiconductors further complicates defect-free growth of zinc phosphide.^{73,74} High temperature synthesis techniques which were initially investigated resulted in the build-up of internal strains and defect formation.^{73,74} Finally, control of the intrinsic doping, mainly p-type through phosphorus interstitials, and stable extrinsic doping required for efficient charge separation and extraction has been challenging.^{71,75–78} Heterojunction alternatives have also shown limited success, most likely due to the mismatch. The highest achieved conversion efficiency for a heterojunction device published to date used ITO as a partner material, achieving 2.1% conversion efficiency.⁷⁹

Whilst it was never a mainstream material with a multitude of research into it, the initial research at the University of Delaware did spark some research interest by other groups. The main investigations into zinc phosphide during the following decades were carried out at two institutes, namely Wroclaw University of Technology, by Pawlikowski and Misiewicz, and Polytechnic University of Japan by Suda. Researchers at Wroclaw University focused on the optical characterisation of the material^{57,59,78,80–84}, whilst the group in Japan investigated different growth methods.^{79,85–99} One of the main outcomes from the research in Japan is that they managed to achieve n-type zinc phosphide by growing at low phosphorus fluxes using molecular beam epitaxy (MBE).⁸⁹ However, devices with improved conversion efficiencies were never demonstrated. In the 2000's the first nanostructures from zinc phosphide were reported at the National Institute for Materials Science (NIMS) in Tsukuba, Japan, by the group of Golberg.¹⁰⁰ They grew zinc phosphide in the form of nanowires, nanotrumpets and nanoribbons using chemical vapour deposition.^{100–103} The next reported devices based on zinc phosphide were produced at the California Institute of Technology in the Atwater group, where they were investigating the synthesis, doping, and heterojunctions based on sublimation grown ingots and thin films grown by MBE.^{55,75,75,104–110} They produced thin film devices reaching a maximum efficiency of 4.50%, which is the current record for this configuration based on zinc phosphide.⁷⁵

Zinc phosphide colloids have also been of interest for the use in quantum dot-based photovoltaics.¹¹¹ The only device in this field was reported in 2014 by the Buriak group at the University of Alberta.^{112–114} Colloid synthesis allows for a low-cost, low-temperature, and high-throughput synthesis method, however, the reported devices exhibited a short-circuit current density of 0 A cm^{-2} .¹¹² Nonetheless, there are groups continuing this research, such as the Corrigan group at the University of Western Ontario¹¹⁵ and the Cossairt group at the University of Washington.^{116–118}

Currently, I am aware of three other groups investigating zinc phosphide for photovoltaic applications. Besides our group, the other experimental lab is the Nose group at Kyoto University.^{76,119–122} They work on the doping and heterostructure growth based on ingot solidification and vapour-transport. The investigations at Kyoto University have shown how magnesium in high concentrations does not act as a dopant, but forms a ternary alloy with zinc phosphide, and they have done interesting research investigating possible dopants, such as indium, in bulk structures.^{76,119} Nonetheless, the materials grown using physical deposition methods show greater promise. Finally, the one group investigating zinc phosphide through computational means is based in Cardiff, the Dzade group, where they conduct density functional theory (DFT) modelling to elucidate the surface behaviour of zinc phosphide.^{123,124} They are investigating the stability of different surfaces to oxidation, and possible passivation routes through DFT. Whilst there are many hurdles left to overcome before commercial production becomes viable, the material is still of great interest and warrants continued research.

1.4.2 Compositional and Structural Properties

Figure 1.4a depicts the zinc-phosphorus binary phase diagram, and as can be seen there are two stable stoichiometries, namely zinc phosphide (Zn_3P_2) and zinc diphosphide (ZnP_2).^{67,68} The crystal structure of room temperature zinc phosphide, as illustrated in Figure 1.4b, has a tetragonal unit cell with the $\text{P4}_2/\text{nmc}$ crystal symmetry (space group). The lattice parameters are $a=b=8.097\text{Å}$ and $c=11.45\text{Å}$.⁶⁸ This structure is referred to as $\alpha\text{-Zn}_3\text{P}_2$, which is essentially a pseudo-fluoritic crystal structure with 25% of the cubic sublattice empty in an ordered fashion. N.B. The ordered vacant sites should not be confused with vacancies, as there is not supposed to be any atoms in these positions in the stoichiometric compound. The high availability of vacant sites has been investigated as a potential asset in battery electrode applications, where lithium or sodium would go into the vacant sites.^{125–127} To the best of my knowledge, no significant breakthrough has yet been published. These sites have also been of interest when it comes to the doping of the material, as will be explained in more detail below. There is a high-temperature phase of zinc phosphide ($\beta\text{-Zn}_3\text{P}_2$), which has a cubic crystal structure ($a=5.82\text{Å}$), however, it is only stable above $\sim 880^\circ\text{C}$.⁶⁷ Similarly, zinc diphosphide also has a low and high temperature phase, which are $\alpha\text{-ZnP}_2$ (tetragonal) and $\beta\text{-ZnP}_2$ (monoclinic) respectively.⁶⁷ There are also a few metastable high-pressure phases, of which a comprehensive list can be found in Ghasemi *et al.*⁶⁷ The focus of this thesis is on $\alpha\text{-Zn}_3\text{P}_2$, which hereon forward will be referred to simply as zinc phosphide. The structural properties of zinc phosphide have led to challenges in its synthesis in the form of lattice mismatch, self-interstitial formation, and thermal expansion coefficient, which will be covered next.

One consequence of zinc phosphide's large lattice parameter is that it complicates epitaxial growth. Most commercially available substrates for epitaxial growth have lattice parameters in the range of $5.4\text{--}6.0\text{Å}$, making them incompatible, and would in theory result in incoherent or heavily defective growth. However, the large lattice parameters observed in α -zinc phosphide is related to the ordering of the vacant sites. It is possible to construct a pseudo-cubic unit cell for the material, which is shown in Figure 1.4c. This pseudo-cubic cell has a lattice parameter of 5.72Å , which shows that it can be grown pseudomorphically on commercial substrates, such as gallium arsenide.^{87,106,107} Furthermore, the face-centred cubic (FCC) sublattice of the phosphorus has been shown to match well with that of indium phosphide, which also has a $\sim 2.3\%$ lattice mismatch with the pseudo-cubic cell ($a_{\text{InP}} = 5.87\text{Å}$).^{128–130} Whilst the III-V substrates do not benefit from the earth-abundant advantages of zinc phosphide, they provide an excellent platform for initial studies to better understand the growth of the material.

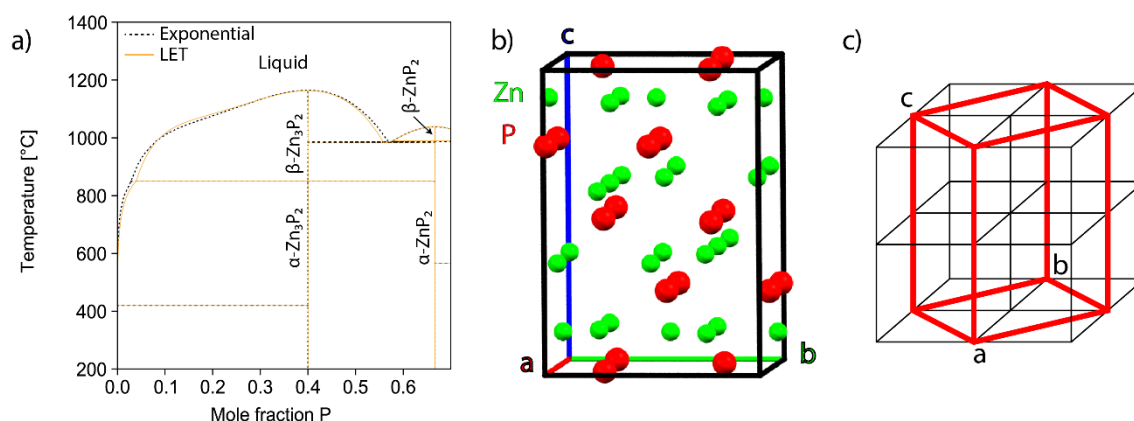


Figure 1.4 (a) Zinc-phosphorus binary phase diagram simulated through the CALPHAD method by Ghasemi *et al.*⁶⁷ (b) Visualisation of the zinc phosphide unit cell (COD ID: 1010287 from Crystallography Open Database) and (c) a diagram of how the standard unit cell (red) compares to the pseudo-cubic unit cell (black).

The empty sites in the lattice create a low-energy pathway for interstitial formation. Whilst some attempt to exploit this for storage purposes, it can also result in the formation of self-interstitials if the synthesis occurs in phosphorus- or zinc-rich conditions. These extra atoms may incorporate in the lattice, resulting in off-stoichiometry composition, which in turn has been shown to affect the electrical properties of the material, and will likely impact other functional properties as well.⁷¹

The last notable factor which has complicated the application of zinc phosphide is its high coefficient of thermal expansion compared to other semiconductors.^{73,74} For example, it is approximately an order of magnitude higher than that of indium phosphide, silicon, and gallium arsenide. Therefore, there will be high levels of residual strain in the zinc phosphide if the growth transpires at elevated temperatures, which can lead to cracking and/or defect formation. The material with the best matching thermal expansion coefficient is steel, which has been demonstrated as a possible substrate for growth, however, the electrical and epitaxial compatibility is far from ideal.⁷³ A more practical solution is to synthesise the material at lower temperatures, for which MBE has been shown to be a promising technique.^{89,106,107}

1.4.3 Optoelectronic Properties

The first studies of the semiconductor properties of zinc phosphide were published in 1953 and 1955 by Lagrenaudie, and an optical bandgap of 1.1 eV was reported.^{69,131} Later studies have shown a larger bandgap value. An indirect transition at a slightly lower energy than the direct transition has also been reported. The experimental techniques used to quantify the bandgap include optical absorption, photoluminescence spectroscopy (PL), and reflectivity among others.^{55,56,58,60,78,80,82,132} The results are consistent with a direct transition in the range between 1.3-1.8 eV, and the indirect in the range 1.3-1.4 eV. More recent studies, based on PL, narrowed it down to 1.38 eV for the indirect bandgap and 1.50 eV for the direct one, the latter one agreeing well with values calculated through DFT.^{55,123,124}

However, unless the material is of very high quality, the recombination observed in PL is due to defect-related pair-transitions.⁸⁶ Although counterintuitive when compared to other materials, the defect transitions dominate the optical response when lowering the temperature, whilst bandgap transitions are more pronounced at room temperature.^{55,86} The defect-related transitions were investigated using a range of optical techniques, and the defect type and density were shown to be a function of growth technique and post-treatments. The different defect levels in the material have also been investigated using photovoltaic spectroscopy and deep level transient spectroscopy, among other techniques. A summary of the reported defect energy levels in zinc phosphide is presented in Table 1.1. The listed defects are all acceptor-like defects, as no donor-like defects have been reported to the best of my knowledge. While some defect levels are consistently observed, there are significant differences between studies using different synthesis methods. Although they cannot all be attributed with high accuracy, the main defect formation has been attributed to the formation of phosphorus self-interstitials sitting in the vacant sites in the zinc sublattice.

Table 1.1 List of energy levels of acceptor-like defects and how they were measured. The energies below 0.8 eV are with respect to the valence band, while the ones above correspond to the defect level to conduction band transition.

Technique	Energy (eV)								Ref
$\sigma(T)$, optical absorption	0.05	0.17	0.28	0.36	0.55	0.66	0.85		133
Photovoltaic spectroscopy		0.19	0.29						78
Optical Absorption		0.17	0.26	0.36	0.55	0.65	0.87	1.28	134
$\sigma(T)$					0.51				135
Cathodoluminescence spectroscopy	0.034								136
Optical absorption and $\sigma(T)$		0.18			0.40				137
$\sigma(T)$ and Hall effect	0.02, 0.034	0.15	0.25		0.47				138
$\sigma(T)$	0.045	0.14				0.6			139
$\sigma(T)$	0.0034		0.27						140
DLTS		0.20		0.36	0.48	0.73			86
DLTS		0.13*,0.20		0.36	0.49				88
$\sigma(T)$ and Hall effect					0.59				71

* Defect level observed only after significant hydrogen annealing.

Studies going back to the 1980's have shown that different post-treatments, such as polishing and chemical passivation, may improve the optoelectronic properties of the material. These treatments influence the defect density of materials, reducing their influence on the optoelectronic properties. For example, a study by Muñoz *et al.* showed that by polishing bulk crystals they observed a substantial increase in photoconductivity, indicating that by producing a smoother surface they reduced the number of recombination sites, resulting in higher performance devices.¹⁴¹ Chemical passivation has been achieved using a bromine-methanol etching and atomic hydrogen.^{79,88} Both of these techniques show promise in improving the performance of the material.

Zinc phosphide has shown optical properties promising for photovoltaic applications. For example, it has a relatively high optical absorption in the visible range ($>10^4 \text{ cm}^{-1}$), measured at the University of Delaware. The excellent absorption was similarly demonstrated for zinc phosphide nanowires, which showed absorption levels an order of magnitude higher than gallium arsenide nanowires investigated in the same study.¹⁴² Studies of zinc phosphide determined a refractive index of ~ 3.3 .^{55,56} The record devices fabricated at the University of Delaware minimised the reflective losses due to the high refractive index through a silicon dioxide antireflective coating as it has an intermediate refractive index (1.5), which results in a significant improvement in the device performance.⁶² A top contact of ITO would have the same antireflective properties whilst acting as a transparent contact, which brings reflective losses down significantly. The combination of optoelectronic properties described above makes zinc phosphide a promising earth-abundant absorber material for photovoltaic applications.

1.4.4 Electrical Properties

Lagrenaudie described the inherent p-type conductivity of zinc phosphide in his early publications, where he also reported a room temperature mobility of $10 \text{ cm}^2\text{V}^{-1}\text{s}^{-1}$, and resistance of $10^3 \Omega$ in a 1 mm crystal.^{69,131} More recent estimates however have achieved values up to $1000 \text{ cm}^2\text{V}^{-1}\text{s}^{-1}$, which in turn allows for minority carrier diffusion lengths in the order of 7-10 μm .⁵⁵ Whilst this makes charge extraction out of thin films feasible, the difficulty in controlling the intrinsic doping has complicated the fabrication of high-quality devices. The work carried out at the University of Delaware attributed the p-type behaviour to phosphorus interstitials.⁷¹ The phosphorus interstitials act as shallow acceptors, with a low energy of formation, and would readily form when there is an excess of phosphorus in the material.^{71,77} The phosphorus-rich zinc phosphide was also observed through other growth methods, such as metalloorganic vapour phase epitaxy (MOVPE) and close space vapour transport (CSVT).^{73,87,143} The only reported method for achieving n-type zinc phosphide is MBE by the relative increase of the zinc partial pressures.⁸⁹

Various studies have addressed the extrinsic doping of zinc phosphide. The main elements investigated are magnesium, indium, silver, and cadmium.^{62,75,76,79,81,109,122,144–146} Magnesium was initially thought to only act as an n-type dopant and was used in the highest efficiency device to date.⁶² However, recent studies from the Nose group in Kyoto showed that magnesium actually forms a ternary alloy with zinc phosphide, providing an n-type heterojunction.^{76,122} The formation of the ternary occurs mainly through inter-diffusion, and thus magnesium could still act as a dopant if introduced at low enough concentrations homogeneously throughout. Indium has also been proposed as an n-type dopant by the Nose group, however, the achievable carrier concentration (10^{10} – 10^{13} cm^{-3}) is too low for device applications.¹¹⁹ Both silver and cadmium, on the other hand, were shown to act as p-type dopants.^{79,81,146} Whilst p-type doping itself has not been difficult to achieve in zinc phosphide, these elements would provide a more controlled approach to doping.

Another important area for the fabrication of devices is the contacts. There are two main types of metal-semiconductor contacts, namely ohmic and Schottky contacts.¹⁸ Ohmic contacts are generally preferred in solar cells as they form when there is no energy barrier for charge transfer, and the contact resistance should be minimal.^{11,18} Schottky contacts occur when there is an energy barrier for charge transfer.¹⁸ These have been used to generate charge selective contacts and through the contacts introduce the asymmetry needed to separate charges in solar cells.^{11,18} The barrier heights of different metals with zinc phosphide were reported by the Delaware group, and are presented in Figure 1.5.⁷² They identified zinc, silver, copper, gold and nickel as potential ohmic contact metals, as seen by their placement on top of the horizontal axis in the graph. Magnesium, beryllium, indium, manganese, aluminium, chromium and iron formed Schottky contacts, and the respective heights can be seen in Figure 1.5. More recent studies also showed that titanium-gold and gold-platinum contacts can work as potential ohmic contacts.^{128,147}

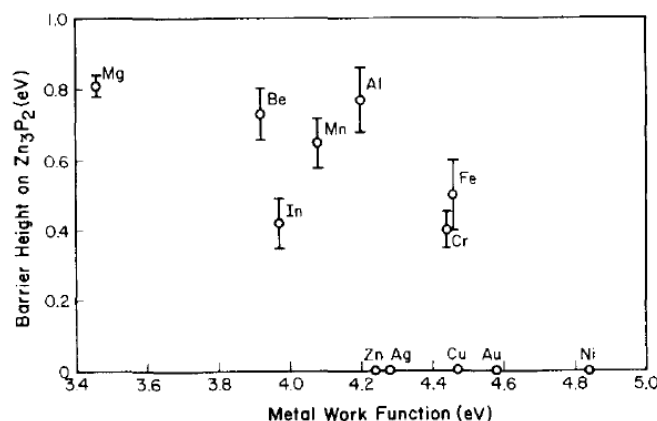


Figure 1.5 Barrier height of evaporated contacts on zinc phosphide as measured by N. Convers Wyeth and A. Catalano in [72], reproduced with permission from American Institute of Physics Publishing.

The most common photovoltaic devices utilise p- and n-doped homojunctions of the same material.¹¹ This has not been achieved yet with zinc phosphide due to the complexity and lack of controlled doping. Instead, the explored routes have mainly been heterostructures with other materials and Schottky devices. In this section I will briefly review the different semiconductor heterostructures which have been explored, and how they compare between themselves and against Schottky-based devices.

When fabricating heterostructures there are two main factors which decide the suitability, namely the band alignment and lattice mismatch of the interface. When two dissimilar materials are put in contact, the bands will align such that the Fermi level is constant throughout.¹⁸ This causes the movement of charge carriers across the junction, and results in the internal electric field necessary for the charge separation inside a photovoltaic device.^{11,18} Depending on the bandgap, the electron affinity, the doping level, and how the bands have moved in relation to each other to align themselves there are a few different types of heterojunctions. The ideal one for photovoltaics is the type II staggered junction, which allows for charge separation and is the case illustrated in Figure 1.1a.^{11,18} Other cases include staddling gap (type I), where both charges are swept in to the same side of the junction which has a much smaller bandgap, and broken gap (type III), where the gaps do not overlap and direct charge transfer between the n-type conduction band and p-type valence band is possible.^{11,18} Furthermore, discontinuities can be formed in the band during the alignment, which can act as traps and hinder efficient charge transport across the junction, which is undesired in photovoltaics. The second aspect mentioned is the lattice mismatch. Coherent interfaces with no or a small mismatch allow for lossless charge transfer, however, this is not the case if the mismatch is large enough to yield an incoherent interface, misfit dislocations or other defects at the interface.^{11,18} The defects may create interface states in the middle of the bandgap, which provide a recombination pathway for the charge carriers, and greatly reduce the efficiency of the devices.

While defective interfaces complicate the material selection, a few systems have been explored as heterojunction partners, namely zinc selenide (ZnSe)^{95,106,148,149}, zinc sulphide (ZnS)^{103,105,150}, zinc oxide (ZnO)^{151–153}, ITO⁷⁹, magnesium-zinc-phosphide (Mg(Mg,Zn_{1-x})₂P₂)^{76,109,122}, and cadmium sulphide (CdS)¹⁵⁴. A list of the best devices based on these heterojunctions is presented in Table 1.2. The ones which have garnered the most interest are zinc selenide, ITO, and magnesium-zinc-phosphide. Zinc selenide has a cubic zincblende crystal structure with a lattice parameter similar to the pseudocubic one of zinc phosphide (5.68 Å and 5.72 Å respectively), and a bandgap of 2.82 eV, with a modelled type II alignment.¹⁰⁴ This combination was investigated initially at the University of Delaware, but subsequently was also investigated by Suda in Japan, and then in the Atwater group at the California Institute of Technology.^{95,104,148} However, the maximum efficiency of these devices have only reached 0.81%, with the limiting factor being the high resistivity and low charge extraction efficiency resulting in a low short-circuit current. ITO based heterojunctions, on the other hand, have reached higher values, up to 2.1% efficiency in a study by Suda *et al.*, and is attractive as the ITO will simultaneously act as a transparent top contact and anti-reflective coating.⁷⁹ However, the lattice match is not ideal, and the resulting interface may limit the potential efficiency. The last, and so far the most impactful, combination is based on magnesium. Initial studies at the University of Delaware used magnesium to create devices based on the Schottky contact it produces with the zinc phosphide, reaching a maximum efficiency of 5.96%.⁶² However, based on their observations of annealed samples, they also claimed that the magnesium would diffuse into the material and act as an n-type dopant, and they also reported on an interface layer of magnesium phosphide (Mg₃P₂), which would aid the charge separation.¹⁴⁴ Whilst magnesium is still believed to act as a dopant, the nature of the interface was investigated using higher resolution techniques at Kyoto University, and they proposed that a ternary phase of the composition Mg(Mg_xZn_{1-x})₂P₂ was formed instead of the doping/alloy as previously reported.^{76,122} This alloy exhibits a good epitaxial relationship

with zinc phosphide, and the junction provides the internal electric field for charge separation. However, the Fermi-level of the ternary phase does not lie close to the conduction band, resulting in a severely limited potential open-circuit voltage (0.58 V as compared to the theoretical maximum of 1.2 V).^{76,122} Hence they concluded that magnesium-based heterostructures or Schottky devices experience severe limitations for practical applications, but its potential as a dopant may still be the key to homojunction devices if an improved doping route can be developed.

Table 1.2 List of material combinations used for zinc phosphide based photovoltaics, highlighting the performance and fabrication method achieved by record devices.

Partner Material	Efficiency (%)	V _{oc} (mV)	J _{sc} (mA cm ⁻²)	Fill Factor	Growth*
Mg	5.96	492	14.93	0.71	PVT ⁶²
ITO	2.1	280	18.4	0.4	PVT ⁷⁹
ZnO	1.97	260	11	0.59	PVT ¹⁵²
CdS	1.6	300	11.1	0.35	Evaporation ¹⁵⁴
ZnSe	0.81	810	1.55	0.5	CSS ^{148**}
ZnS	0.01	780	0.05	0.35	MBE ¹⁰⁵

* Growth method abbreviations: physical vapour transport (PVT), close-space sublimation (CSS), and molecular beam epitaxy (MBE).

**Under AM1.0

1.5 Outlook

Photovoltaics show great potential as one of the main sustainable energy technologies, and zinc phosphide is one of the material systems which could facilitate this happening. Challenges related to zinc phosphide's lattice parameter, thermal expansion coefficient, and doping need to be addressed to achieve its potential. There is still plenty left to explore regarding zinc phosphide. The areas of highest priority are defect-free growth, controlled doping, passivation and heterojunction combinations. The work in this thesis will focus on the first part, and in the following chapters I will present some background pertaining to the growth and characterisation of semiconductor nanostructures.

Chapter 2 Introduction – Nanomaterials: Growth and Properties

2.1 Growth

The origin of nanotechnology and nanoscience is often attributed to the 1959 talk by Richard Feynman, titled "There's Plenty of Room at the Bottom".¹⁵⁵ However, the field did not take off until the late 1990's, when advances in characterisation technologies allowed us to elucidate all phenomena and material properties down at the nano and atomic scales (some of which will be covered in Chapter 3). The main advantages of nanomaterials can roughly be broken down into two main categories: enabling new functionalities not observed in bulk, or circumventing the factors limiting the application of bulk materials. This has generated interest for applications of nanomaterials in medicine^{156–160}, electronics^{161–163}, lighting^{164,165}, energy production and storage^{126,166–169}, catalysis, and so forth. An example of the first case is transition metal dichalcogenides, such as molybdenum disulphide (MoS_2). As a bulk material it exhibits an indirect bandgap of 1.23 eV. If it is exfoliated into monolayers however, it changes to a direct bandgap of 1.8 eV.¹⁷⁰ The second case can be exemplified by the enhanced permeability and retention (EPR) effect of nanoparticles in cancerous cells.^{158,159} The EPR effect essentially acts to concentrate any injected nanoparticles in cancerous cells. Thus, if they are functionalised with chemotherapy drugs, EPR can be used to concentrate the delivery to the tumours and reduce the potential side effects on healthy tissue.^{158,159} The reduction of the side effects allows for the re-exploration of drugs which when applied on their own had too severe side effects. In short, nanomaterials are a vibrant research topic with many potential applications spanning a wide variety of areas, and a large part of it is focusing on different ways to synthesise the materials and its effect on the properties of the end product.

The techniques to create nanomaterials can be broadly split into two categories: top-down and bottom-up, as illustrated in Figure 2.1.^{171–174} In the top-down approach, Figure 2.1a, one starts with a bulk material and breaks it down, through mechanical or chemical means, until the structural dimensions reach the nanoscale. Top-down methods are currently the dominating type in industry, as the large-scale reproducibility and throughput are well established. The most generic example is the use of lithography and etching techniques in the fabrication of computer chips by companies such as Intel. The bottom-up approach, Figure 2.1b, relies on the synthesis of materials through atomic or molecular precursors that self-assemble into the desired nanomaterial through a combination of thermodynamic and kinetic effects. This allows for the creation of complex heterostructures, shapes and functionalities not achievable through top-down manufacturing.^{171,173} Nonetheless, they both offer their advantages for different applications, and hybrid approaches are also of great interest to try and combine the best of both paradigms.^{175,176} One such approach is selective area epitaxy, as will be discussed later in this chapter.

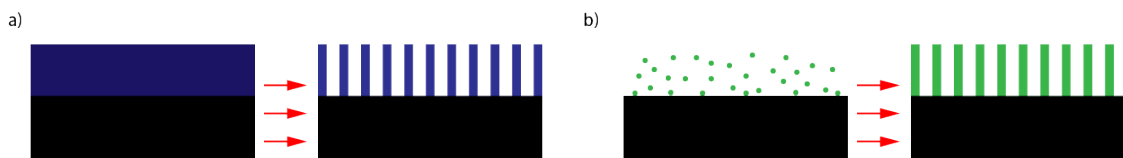


Figure 2.1 Illustrations of (a) top-down manufacturing of nanowires and (b) bottom-up growth of nanowires.

One of the main types of techniques used for nanomaterial creation are the so-called physical deposition techniques. As the name suggests, these techniques employ physical phenomena to generate the nanomaterials, some examples being evaporation, sputtering, and spark discharge.^{177–179} Many of these techniques, such as the first two, were initially developed for the growth of thin films and are very versatile. The evaporation route to form nanoparticles utilises an intermediate thin film, which is subsequently annealed to form the nanoparticles.¹⁷⁷ Sputtering, on the other hand, can be combined with a size-selective magnetic filter to deposit nanoparticles of controlled size.¹⁷⁹ The last technique, spark discharge, relies on the ablation by the rapid discharge of a sufficiently high amount of energy to disintegrate the material close to the surface and generate nanoparticles.¹⁷⁸ A final route to mention, which has

been extensively used for semiconductor nanoparticles, is the strain induced Stranski-Krastanov (SK) growth of nanoparticles, covered in more detail below.¹⁷⁷ The advantages of these approaches are the achievable purity and cleanliness of the surface in comparison to chemically derived nanoparticles. If combined with lithographic approaches, one can also achieve site-controlled synthesis, which is more challenging for chemically derived nanoparticles.

Chemical synthesis relies on precursors reacting to form the desired material, in combination of a surfactant that stabilises the resulting product in the form of nanoparticles.^{180,181} Using metal nanoparticles as an example, the stabilisation can occur through either steric or charge stabilisation, as illustrated in Figure 2.2.^{180,181} The steric case utilises organic ligands which physically separate nanoparticles to avoid agglomeration, whilst the charge-based ones exploit Coulomb interactions. It is possible to finely tune the size of the nanoparticles by controlling the relative concentration of the surfactant and precursors. Furthermore, the affinity of a surfactant can differ between crystal facets of the nanoparticles, and can thus be used to stabilise differently shaped nanoparticles.^{180,181} This is particularly desirable in catalyst nanoparticles, where some crystal surfaces show enhanced catalytic activity and product selectivity compared to others, as observed in the generation of different hydrocarbons from the electrocatalytic carbon dioxide (CO_2) reduction reaction using copper nanoparticle catalysts.¹⁸² The advantage of chemically derived nanoparticles is the ease of fabrication, facilitating highly controlled, cheap, and high-throughput fabrication of well-defined nanoparticles, which can subsequently be transferred through for example drop casting. The main disadvantage of this technique is that the ligands themselves may affect the functionality of the particles, and removal or modification before application may be necessary. Similar to the top-down/bottom-up classification, there are methods such as electrochemical deposition and molecular beam epitaxy (MBE) that can be a combination of physical and chemical synthesis routes, of which the latter will be covered in more detail in the next section.

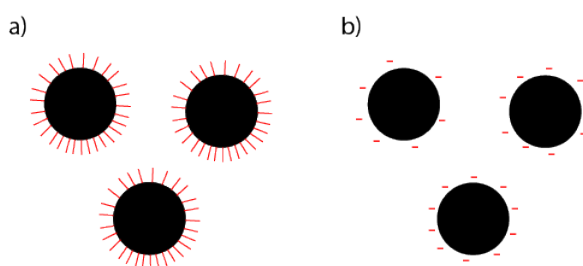


Figure 2.2 Illustrations of (a) steric stabilisation and (b) charge stabilisation of chemically derived nanoparticles.

One last aspect to note is the epitaxial relationship when growing one material on another. Epitaxy concerns the crystalline relationship between the growth substrate and the new material, the epilayer. This affects the nature of the interface, which in turn influences the structural and functional properties of the epilayer. For ideal epitaxial growth, the growing material adopts the crystal structure of the substrate. This is generally the case if the grown material has a crystal structure and lattice constant similar to that of the substrate, of which there are two possible scenarios. The first scenario is homoepitaxy, when the epilayer exhibits a similar chemistry to the substrate but a slight lattice misfit (e.g. doped silicon on silicon).¹⁸³ Another scenario is heteroepitaxy, in which the main difference is the chemistry of the different layers rather than the lattice parameter (e.g. indium gallium arsenide on indium phosphide).¹⁸³ If the grown material has a different crystal structure, but there is one combination of facets which have a similar lattice structure and spacing, so called pseudomorphic growth can be achieved, which is illustrated in Figure 2.3a. In this scenario, the crystal structure shifts between the layers but a high-quality interface is formed.

If the mismatch between the substrate and grown material is too large ($\sim 4\%$), the mismatch will not be able to be accommodated through elastic relaxation mechanisms.^{177,183} Instead it will have to be accommodated plastically through e.g. misfit dislocations, as illustrated in Figure 2.3b. These dislocations occur at regular intervals, depending on the lattice parameters, and are essentially extra or missing planes of atoms depending on whether the new layer is in compressive or tensile strain, respectively. These defects usually stay at the interface, but in for example gallium nitride they are known to migrate to form low-energy threading dislocations.^{184,185} The dislocations are undesirable as they tend to be detrimental to optoelectronic properties, which was one of the challenges when developing blue gallium nitride-based light-emitting diodes (LEDs).^{184,185} New areas of research are investigating epitaxy on weakly interacting surfaces to decouple the influence of the substrate on the grown material, such as the case in Figure 2.3c. The surfaces used, e.g. graphene and mica, do not form covalent bonds with the grown material, but only interact through van der Waals' interactions, hence the technique is commonly referred to as van der Waals' epitaxy.¹⁸⁶

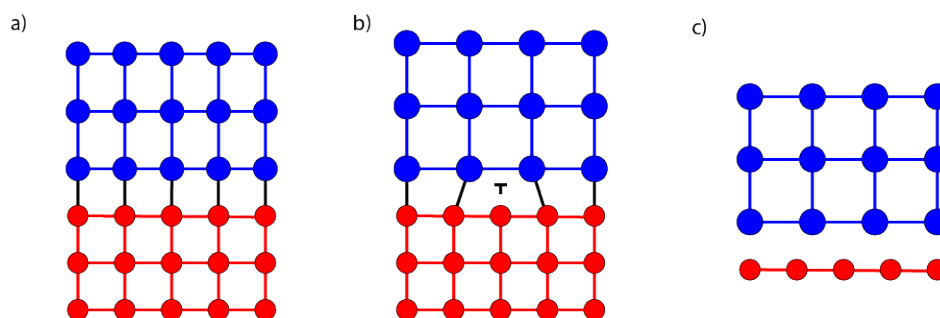


Figure 2.3 Illustrations of (a) pseudomorphic growth, (b) misfit dislocation at an interface and (c) van der Waal's epitaxy.

The level of mismatch also influences the epitaxial growth mechanism in combination with interface energies. With reference to thin films there are three main growth mechanisms, namely layer-by-layer (Frank-van der Merwe, Figure 2.4a)^{187–190}, island (Volmer-Weber, Figure 2.4b)¹⁹¹, and mixed (Stranski-Krastanov – SK, Figure 2.4c)^{192, 177, 183}. The first mechanism, layer-by-layer, is in a sense the simplest. It occurs when the growing layer has a high chemical affinity for growing on the underlying substrate, usually with a closely matching crystal structure. This results in a monocrystalline thin film, which is often desired due to their low level of defects and therefore ideal functional properties. If, on the other hand, the material prefers to grow on itself rather than on the substrate, it will start to grow as islands instead of a film as shown in Figure 2.4b. The islands are not necessarily well aligned, and when they coalesce, they form grain boundaries, anti-phase boundaries or other types of defects. The last growth mode, SK growth, occurs when there is an affinity, however, the mismatch is too large to accommodate the strain elastically after more than a few monolayers of the new material is grown. Consequently, the growth mode transitions to an island forming mechanism to accommodate the strain, as illustrated in Figure 2.4c. SK growth has been extensively researched as a method to generate quantum-dots in mismatched systems, such as indium arsenide quantum-dots on gallium arsenide. SK quantum-dots are interesting for their optoelectronic and electrical properties, suitable in e.g. single-photon emission applications.^{193, 194}



Figure 2.4 Illustrations of (a) layer-by-layer growth, (b) island growth, and (c) mixed growth.

Finally, a factor which is of vital importance to epitaxy is the temperature at which the process occurs, as it will determine the affinity, kinetics, and mobility of the incoming species. For example, if the temperature is too low, the incoming atoms will not have enough thermal energy to diffuse to low-energy locations. They will instead stay (stick) where they land. Layer-by-layer growth cannot occur under these conditions, and island growth based on multiple nuclei tends to dominate. Furthermore, if molecular (e.g. metalorganic) precursors are used, there might not be enough energy to break them down to initiate the reaction, and no growth can occur. On the other hand, if the temperature is too high, there are issues with re-evaporation of the species before they can contribute to the growth. The temperature ranges for these processes are material dependent, and vary between systems. With an overview of the growth of nanomaterials I will now shift to the techniques used in the growth of semiconductor nanostructures, with focus on MBE, the main technique used in this thesis.

2.2 Molecular Beam Epitaxy

MBE is an ultra-high vacuum (UHV) method to deposit materials and grow compound semiconductors, known for its high levels of material purity, high degree of control of all parameters, and compatibility with *in situ* characterisation tools. The pioneering work on MBE was carried out in the 1960's and early 1970's. The work which led to the expanded interest in MBE in its current form originated from Bell Labs (currently Nokia Bell Labs), carried out by Alfred Y. Cho and John Arthur.^{195–199} Cho and Arthur demonstrated the usefulness of MBE through the growth of high-quality III-V semiconductor structures with previously unachievable precision. The precise level of control it allows for has made it one of the foremost techniques currently used to investigate the fundamentals of semiconductor growth and to grow crystals of the highest possible quality. In this section, I will describe the operating principles and requirements, as well as contrast it against other techniques and highlight areas where MBE is of interest.

2.2.1 Operating Principles and Requirements

MBE is achieved by depositing or reacting one or multiple incoming particle fluxes, either elemental or molecular, on a substrate in UHV. The main parameters one can control are the precursor sources, precursor fluxes, and substrate temperature. In this section we will look at how it is achieved, and the potential implications. A picture of the system used in my work, a Veeco GENxplor manual MBE system, and an illustration of the growth chamber is presented in Figure 2.5. The relevance of the components will be discussed further down this section.

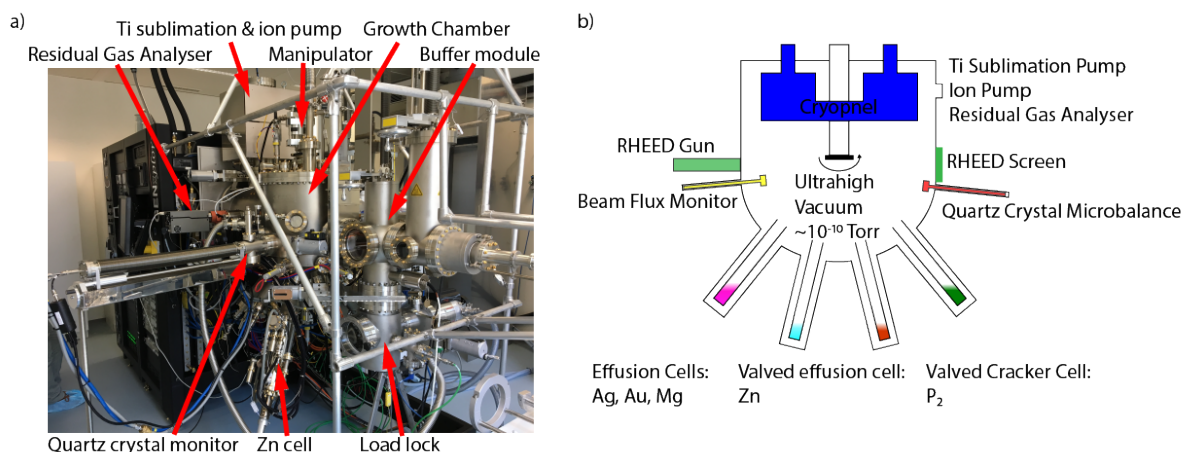


Figure 2.5 (a) picture of the Veeco GENxplor MBE system highlighting the main components/sections (phosphorus cell and recovery system not visible). (b) illustration of the growth chamber.

To achieve the desired UHV and cleanliness level, the growth chamber in an MBE system is constantly kept pumped down, and substrates are introduced through a multi-stage system, each with its own set of vacuum pumps. In our system this included ion pumps, titanium sublimation pumps, cryopanel, cryopumps, turbomolecular, and scroll pumps. The only section in our system which was regularly vented to atmospheric pressure (using argon gas) was the load-lock. The load-lock was degassed after every loading using quartz lamps at 150 °C for at least two hours to remove any humidity or other potential pollutants introduced into the system when it was open, so that they were not outgassed in later stages. Subsequently, the substrates were stored in the buffer module, where they were also degassed for a second time at higher temperatures, ranging from 300-600 °C depending on the material. Finally, the substrates were introduced into the growth module, which in our case had an operational background pressure in the order of 1.5×10^{-10} Torr, and placed on a substrate manipulator which can rotate to improve deposition homogeneity. Before the growth occurs, there is usually a surface preparation step *in situ*, which is materials dependent. In some cases, the materials were pre-treated before insertion, and less stringent steps are necessary. The temperature of the substrate was adjusted through a back heating radiative graphite heater ($T = 20$ -1200 °C), and the temperature was measured through three methods: a thermocouple at the manipulator, a pyrometer (only applicable at $T > 500$ °C), and an infrared (IR) camera. The setup allowed for temperature control down to ± 0.1 °C. The combination of multiple *in situ* cleaning steps and temperature control facilitates the extreme control of the growth surface characteristic of MBE.

The material fluxes for growth come from cells, in our case they were placed at the bottom of the growth chamber facing the substrate at an angle of $\sim 45^\circ$ (this can vary between different system configurations). The cells are filled using ultra-pure raw materials to minimise potential contamination during growth. There are a few different source configurations depending on the material in question, summarised in Figure 2.6. The most common types of solid-state cells are the Knudsen/effusion cells (Figure 2.6a), cracker cells (Figure 2.6b), sublimation cells (Figure 2.6c), and electron-beam (e-beam) evaporation cells (Figure 2.6d).¹⁹⁶ In a Knudsen cell, the material is placed in a crucible which is heated until the vapour pressure reaches the desired levels for growth. This type of cells is generally used for materials which produce atomic precursors on evaporation. Molecular precursors, however, may need to be broken down (cracked) before they reach the substrate to effectively contribute to the growth, and thus utilise so-called cracker cells. One example of such a cell are the arsenic cells used in III-V MBE, which have an additional heated section to the cell. By controlling the temperature of the cracker one can then generate As_4 (low temperature) or As_2 molecular beams, with the desired one depending on the growth application. Sublimation cells rely on the heating of the material until it spontaneously evaporates by driving high-current pulses through a filament such that the Joule heating causes the material to sublime. The final type of cell, e-beam evaporation cells, use an electron beam which is steered onto the source material and locally heat a small region until it starts to evaporate. This sort of cells is advantageous when the material has a low vapour pressure, as the local temperature can reach the high values

necessary to achieve the desired fluxes without affecting the integrity of nearby components. Furthermore, for some cells, such as cracker and Knudsen cells, it is possible to have a valve at the end of the cell that allows for control of the flux without adjusting the temperature. The precise control of the flux by these valves is greater than that achieved simply by controlling the temperature. Moreover, it is relatively instantaneous as the changing of the flux does not include a ramping and stabilisation of the temperature. While the valve significantly improves the control over the flux, it does make the cell itself bulkier and makes maintenance, such as refilling of material, much more cumbersome. However, the increased control is often worth the effort for the main growth components.

MBE can also utilise gaseous sources, as shown in Figure 2.6e. Gaseous-MBEs are commonly used in the growth of oxides and nitrides. The growth is achieved by injecting e.g. ozone, oxygen, nitrogen, or ammonia through a gas outlet placed next to the substrate. Ammonia can be cracked simply by the temperature of the growth substrate, while the other components may require the use of a plasma source (e.g. electron cyclotron resonant plasma source) to crack them. Gaseous-MBEs generally require higher levels of pumping to maintain UHV conditions. Furthermore, the oxide environment complicates the use of some materials, such as molybdenum in substrate holders, which are commonly used in conventional MBE. These components have to be replaced by oxidation compatible/resistant versions manufactured from, for example, stainless steel.¹⁹⁸

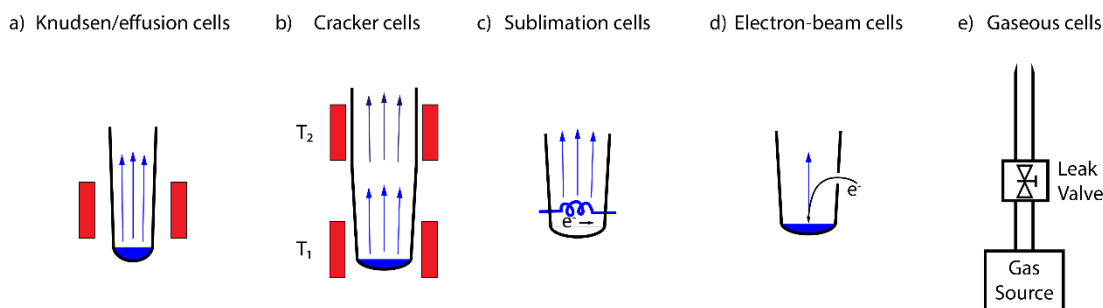


Figure 2.6 Schematics of different cell types commonly used in MBE, depicting (a) Knudsen/effusion cells, (b) cracker cells, (c) sublimation cells, (d) electron-beam cells, and (e) gaseous cells.

Having described how the fluxes are generated, the next vital components are the ones used to calibrate them. The most common tools for calibration purposes are beam flux monitors (BFMs), quartz crystal monitors/microbalances (QCMs), and reflective high-energy electron diffraction (RHEED). The first method, BFM, uses a hot cathode gauge on an extendable arm which can be placed in front of the flux. The ionisation rate, and thus the current, through the gauge can be used to estimate the quantity of incident atoms, giving a measure of the flux. The disadvantage of this technique is that it cannot be used *in situ*, as it blocks the beam, and it does not take into account the varying sticking coefficients or ionisation rates of different incoming fluxes. Its advantages on the other hand is that it is easy to implement and calibrate, and it works for all materials. The second method, QCM, utilises a quartz crystal which oscillates under an applied bias. The frequency of oscillation is a function of the mass of the crystal. Hence, by depositing on the QCM one can measure the change in frequency, and by taking into account the deposited material density, it can be converted into a deposition rate. In techniques such as evaporation and sputtering, the QCM can be placed next to the sample and measure the rate *in situ*. In MBE, however, it has to be introduced into the flux beam to measure the deposition rate and thus has to be used *ex-situ*. Furthermore, the QCM is usually kept at a low temperature to maximise the sticking, which will then not match that of normal growth conditions and it will be less accurate for materials which readily desorb at elevated temperatures. The final technique, RHEED, is by far the most complex of the techniques but can provide the most information. RHEED relies on an electron beam incident on the substrate surface at a gracing angle ($<5^\circ$), which are then diffracted by the surface layer. First, by looking at the diffraction one can deduce the crystal structure of the material and the growth mode, as shown in Figure 2.7a. For example, if lines are observed it indicates a 2D layer-by-layer growth, as the compression of one dimension in real space results in the elongation of the dots into lines in reciprocal space. However, a dot pattern indicates diffraction from a 3D surface, and island growth will be the dominating growth mode. Randomly ordered polycrystalline growth results in ring patterns. Furthermore, during layer-by-layer growth the diffracted intensity will be a function of the step density on the surface, as illustrated in Figure 2.7b. When a layer is complete there will be a maximum of the diffracted intensity, however, when a new monolayer is nucleated steps will be created on the surface. The steps act as scattering centres, and thus lower the diffracted intensity. The step density, and thus the scattering, will be at a maximum when the monolayer is half formed, in turn causing a minimum in the diffracted intensity. As the layer starts to complete the diffracted intensity will start to recover, resulting in an oscillation in the RHEED signal. This oscillation can be used to measure the layer-by-layer growth rate *in situ*, and has proven useful for calibrations and the growth of superlattice structures with monolayer precision. The disadvantages with RHEED are that it is not always straightforward to align, and it requires UHV conditions for the electron mean

free path to be high enough to reach the screen, making it suitable for a limited number of growth techniques only. Finally, to accurately observe the intensity oscillations the sample has to remain stationary. The lack of rotation creates an inhomogeneous thickness distribution over the substrate. These three techniques all have their advantages and disadvantages, however, in this project we found BFM calibrations to be the most reliable for our intended applications.

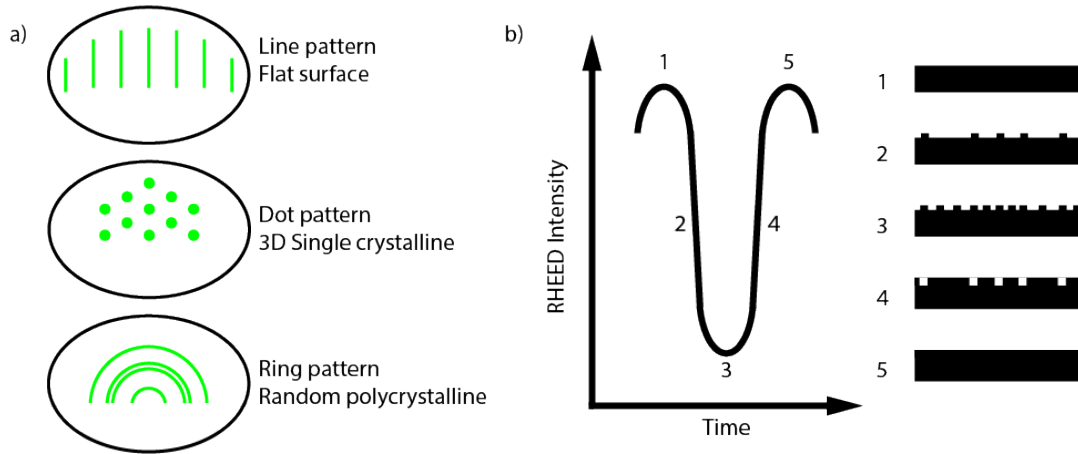


Figure 2.7 (a) Illustration of the observed RHEED patterns for different growth configurations and (b) of the signal oscillation as a function of surface step density.

2.2.2 Competing Techniques

MBE has successfully been applied in a range of cases, such as semiconductor superlattices²⁰⁰, high T_c superconductors^{201,202}, and topological insulators²⁰³. Its precise control of all parameters and purity has produced some of the highest quality materials and heterostructures to date, allowing for studies of the fundamental science of material growth, making it ideal for research purposes. However, MBE has a very low throughput of samples due to all the stringent requirements. It is thus less suitable for industrial scale applications. Some of the other growth techniques competing with MBE in the growth of compound semiconductors are metalorganic vapour phase epitaxy (MOVPE), pulsed laser deposition (PLD), sputtering, and evaporation. Simplistic diagrams of the setups needed for these techniques are shown in Figure 2.8. In this section I will briefly outline the different techniques and how they compare to MBE.

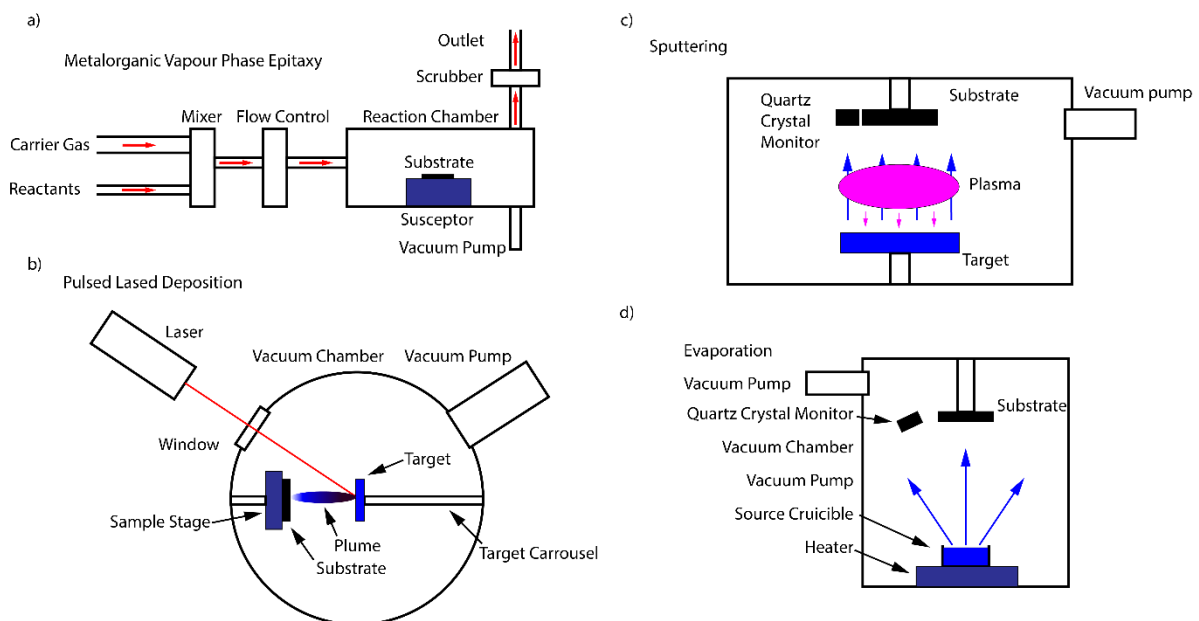


Figure 2.8 Diagrams of setups for (a) MOVPE, (b) PLD, (c) sputtering, and (d) evaporation.

MOVPE (sometimes referred to as metalorganic chemical vapour deposition – MOCVD) relies on gaseous precursors, metalorganics, being transported by a carrier gas at controlled concentrations to the substrate, under controlled temperature, where they decompose and react to form the desired material.²⁰⁴ The setup is shown in Figure 2.8a. This technique usually operates under rough vacuum conditions (>10 Torr), making the vacuum requirements less stringent than MBE. Furthermore, while still allowing for great levels of control, the growth rate and sample throughput achievable in MOVPE are much greater than those of MBE. MOVPE is thus the preferred method for industrial scale applications. Drawbacks of MOVPE include it not being as compatible with *in situ* characterisation as MBE. While for example *in situ* scanning tunnelling microscopy has been demonstrated in MOVPE, it can be greatly complicated by the atmosphere.²⁰⁵ For example, RHEED is not MOVPE compatible. The precursors used in MOVPE of e.g. III-V semiconductors, such as arsine and phosphine, also have to be handled and stored with great care due to their potentially dangerous nature. The gas outlet after growth has to be equipped with a scrubber in order to neutralise any unused precursors, and assure the safety of the expunged gas. Finally, there are concerns that the organic components of the precursor gasses may influence the growth negatively, and in worst case scenarios act as contaminants, reducing the quality of the final product.²⁰⁴ If the precursor is not a metalorganic the technique is simply referred to as chemical vapour deposition (CVD).

PLD utilises laser ablation of a target and the subsequent transportation of the ablated material to a growth substrate.^{206,207} The chamber itself, shown in Figure 2.8b, can generally be kept at UHV conditions, making it compatible with *in situ* characterisation techniques. It is commonly used jointly with RHEED. The ablation process makes this technique ideal for congruent deposition of compound targets and has been widely applied in the deposition of oxides.²⁰⁷ The laser beam and ablated plume can also be used to ionise a gas, such as oxygen/ozone or nitrogen, generating a reactive atmosphere for deposition. These two factors have made PLD the main competitor to MBE in the highly controlled growth of complex oxides. However, drawbacks of PLD include limitations on the potential target, as high reflectance materials will not readily ablate. Moreover, homogeneous deposition is limited by the plume area, and is thus not suitable for large scale applications. Finally, as the ablation plume can contain larger particles breaking off from the surface, a common issue in PLD is particle inclusion causing inhomogeneities in the deposited films. Rastered PLD has been proposed to circumvent the area limitation issue, and techniques such as off-axis deposition have been demonstrated to reduce particle inclusion, but PLD is still mainly used for research applications.²⁰⁸

Sputtering is a technique widely used in industry for the deposition of coatings or metal contacts. A target of the desired material is sputtered by bombarding it with argon ions, generated by a plasma just above the target and then accelerated using an electric field, as shown in Figure 2.8c. The sputtered atoms then travel to a substrate where they form a film. This technique allows for high deposition rate and high throughput, and the diffuse transport of the deposited material facilitates high step coverage over uneven surfaces. Multiple materials can be deposited (co-sputtered) using either a compound target, or by using multiple separate plasmas and targets simultaneously. Standard sputtering setups require the targets to be conductive, as otherwise they will accumulate charge at the surface from the incoming ions, and eventually start to repel them. This is solved by using radio frequency (RF) sputtering. RF sputtering switches the polarity of the target and substrate at set intervals, using the electrons from the plasma to neutralise the target surface and allow for continued deposition. Disadvantages of sputtering compared to MBE are that the degree of control over growth rate, composition or crystal structure are much reduced. Although it may be a fringe application, the growth of monolayer thin superlattices for example cannot be achieved through sputtering. Furthermore, the gas used for the plasma generation can also be implanted in the material, acting as defects.

The final technique mentioned is evaporation, as shown in Figure 2.8d. It has many similarities to MBE, as the Knudsen cells are essentially directed evaporators. However, the main difference is the beamlike nature of MBE, and the increased control by using for example valved cells, allowing for the creation of more complex structures. While evaporation has shown itself as a possible high-throughput technique for the production of compound semiconductors such as cadmium telluride, it is mainly used to deposit high-quality metal contacts and films in industry today. If compared to sputtered contacts, evaporated contacts tend to be of higher quality, however, the step coverage of evaporated films are not as good on rough surfaces.

To summarise, there are various techniques which are currently used in the growth of compound semiconductors other than MBE. The advantage of MBE is its high degree of control over all the parameters controlling growth and its cleanliness through UHV conditions and ultra-pure precursors, making it ideal for fundamental studies of the growth of compound semiconductors. However, other techniques, such as MOVPE and sputtering, allow for higher throughput of samples, and are thus more desirable for industrial scale production.

2.3 Nanowires

One morphology which has received significant attention in the scientific community is the nanowire. Nanowires are 1D filament crystals, and they have garnered interest because of their mechanical, optical and electrical properties, which have shown promise for applications such as sensing, photovoltaic, lasing, solid-state lighting, energy storage, and quantum computing.^{164–166,168,169,172–175,177,185,209–216} There are various books and review papers which cover nanowires in general or specific aspects in great detail.^{171,172,174,177,211–213,215,217,218} This section will briefly cover their origin, advantages, and potential application in photovoltaic technologies, while the following sections will focus on their growth.

Nanowires can track their origin to a study by Wagner and Ellis published in 1964, where they discovered that gold particles could act as a catalyst for one dimensional growth of silicon “microwhiskers”.²¹⁹ They, and other scientists such as Givargizov and Chernov, then carried out further studies to understand their formation and properties.^{220,221} However, due to limited applicability, research into microwhiskers waned, and limitations of the available characterisation techniques at the time hindered the investigation of these filament crystals down at the nanoscale. Research interest into compound semiconductor nanowires increased again in the late 1990’s and early 2000’s, aided by improved characterisation tools. Early works include that of the Lieber group at Harvard University, demonstrating their suitability for compound semiconductor heterostructures and applications in sensing among other areas.^{161–163,222,223} Other prominent researchers involved in the revitalisation of the field include Samuelsson at Lund University^{224–227}, Yang at University of California, Berkeley^{228–230}, Glas and Harmand at CNRS^{231–234}, Bakkers at Eindhoven University of Technology^{209,235,236} and Jagadish at the Australian National University^{165,237,238} to name a few. Currently there are various groups all over the world investigating nanowire-related topics, ranging from the fundamentals of growth and their functional properties, to their applications in new technologies and new material systems.

2.3.1 Properties

There are two main factors which have propelled the interest in nanowires, namely their elastic strain relaxation and nanophotonic properties. The elastic strain relaxation has been successfully used in the epitaxial growth of nanowires on substrates in which the lattice mismatch is greater than that needed to form misfit dislocations in planar growth, and the growth of both axial and radial heterostructures of material combinations not readily achieved in a planar configuration.^{177,222,224,231,239} The elastic strain relaxation is facilitated by the constant proximity of surfaces, allowing the accommodation of stress, and the restricted interface area.²³¹ Because of the small interface area, the mismatch energy penalty is smaller than that relaxed through plastic relaxation, and the elastic mechanisms dominate.²³¹ This was proven in a seminal paper by Glas in 2006, and has also been shown experimentally since.²³¹ The three types of heterostructures, shown in Figure 2.9, include nanowire/substrate junctions, axial junctions, and radial junctions. The substrate heterojunctions, Figure 2.9a, are conceptually the simplest. They are achieved by growing nanowires of a different material than the substrate. It is actively pursued in e.g. the integration of III-V optoelectronics on silicon.²⁴⁰ Axial heterostructures, Figure 2.9b, are achieved by switching the material during axial growth.^{222,226} However, sharp interfaces are complicated by the reservoir effect, causing intermixing between successive layers due to remnant precursors in the catalyst.²⁴¹ Axial heterostructures have also been achieved by playing with the crystal structure of the materials, as observed in twin superlattice nanowires and wurtzite/zincblende polytypic superlattices in III-V nanowires.^{101,236,242,243} Twin superlattices from zinc phosphide will be the focus of Chapter 5, and are described in more detail later on. The final heterostructure are the radial ones as shown in Figure 2.9c. They are generally achieved in a second growth step after either removing the catalyst, making axial growth impossible, or by changing the growth conditions to favour radial growth over axial, generally achieved by lowering the temperature.²³⁹ Radial heterostructures can also accommodate high levels of elastic strain in the core in lattice-mismatched core-shell systems. They are a promising new platform for the development of direct bandgap group IV semiconductors through core-shell structures, such as germanium-tin alloys or hexagonal germanium and silicon-germanium.^{235,244,245} Furthermore, radial heterostructures of higher order alloys can be used to generate quantum dots through selective segregation, which show promise in single-photon emission for quantum communication.^{246,247} While there are still many material combinations left to explore, this is a possible route to facilitate the application of zinc phosphide. The increased elastic strain relaxation and less stringent requirement on lattice-matched substrates allow for reduced defect density during epitaxial growth and possible accommodation of any thermally related strains.

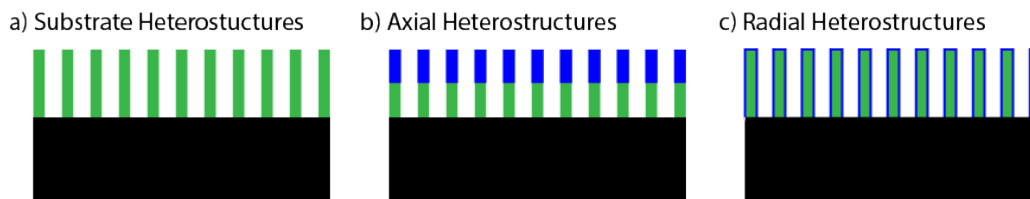


Figure 2.9 Visualisation of (a) substrate heterojunctions, (b) axial heterojunctions, and (c) radial heterostructures. The black material is the substrate, green is material X, and blue is material Y.

The second aspect, nanowire nanophotonics, arise as the nanowire dimensions are in the same order of magnitude as the wavelength of visible light, and in combination with their aspect ratio result in a myriad of interesting phenomena.^{213,248} The first noticeable phenomenon is the enhanced light-absorption cross-section of nanowires.^{249–252} If a photon approaches a nanowire at a normal incidence it is possible for it to couple to a weakly guided (evanescent) electromagnetic resonance mode.²⁴⁹ Due to its weakly guided nature, it may couple even if it is not directly impinging on the nanowire. Therefore, by utilising a correctly spaced array of nanowires, it is possible to absorb as much light as if though a thick film had been used.^{167,251} The anisotropic shape of the nanowires also affects the emission from the nanowire through a property called the directivity.¹⁶⁷ Due to the directivity, photons generated in the nanowires through stimulated or spontaneous emission are more likely to be emitted along the long axis of the nanowire. Furthermore, if the array is ordered properly it may also act as a 2D photonic crystal, further suppressing any in-plane emission.³¹

The combination of these properties has made nanowires a promising platform for photovoltaics.^{166–168,225,251,253–255} First, loosening of lattice matching restrictions faced in 2D systems allows for growth of new materials which previously were limited by substrate availability. Furthermore, it allows for new heterojunction combinations, and even nanowire based tandem cells, which have the possibility to increase the suitable materials in our arsenal and their conversion efficiencies. Secondly, photovoltaic devices based on radial heterostructures have light absorption and charge separation occurring in perpendicular directions. This implies that the charge separating region is always within a few nanometres from where the charges are generated, allowing for a more efficient charge separation by suppressing recombination, and increases the output current.²⁵² While currently the most efficient nanowire photovoltaics are still based on axial nanowires, this is still an active area of research.^{225,253,256} Thirdly, by spacing nanowires appropriately the material quantity needed to absorb all the incoming light can be reduced several orders of magnitude. The reduced quantity makes material combinations based on scarce elements a more viable option. While the coupling with guided modes has a wavelength, radius, and pitch dependence, this can be circumvented by either using tapered nanowires or a combination of wires with different radius and aspect ratio.^{257,258} Very sparse arrays of embedded nanowires have been proposed as a platform transparent photovoltaics working at reduced efficiencies. Fourthly, due to the directivity, the balance in the Schokley-Queisser limit changes as the charge generation and recombination changes, which results in a higher theoretical maximum efficiency in nanowire photovoltaics.¹⁶⁷ This effect is further enhanced in structured arrays of nanowires. Finally, nanowire photovoltaics have also shown promise as a platform for space applications. Nanowire photovoltaics have shown performance retention under irradiation significantly higher than that of planar alternatives.²⁵⁹ Furthermore, cost reduction of sending these panels into space due to the decrease in material and mass needed is desirable. While the maximum conversion efficiencies (15.3%²⁵⁶ for bottom-up and 17.8%²⁵³ for top-down nanowires) is yet to reach that of their planar competitors, it is a thriving area of research with room to reach further heights.

Zinc phosphide is a material which stands to benefit from the advantages of nanowires. Utilising the radial strain relaxation, and the possibility to grow materials epitaxially despite large lattice mismatches provides a route for high-quality growth of zinc phosphide and associated homo/heterostructures, possibly circumventing the limits it has so far experienced in bulk and planar applications. Powders of non-epitaxial nanowire-like bundles have been reported as early as 2006 by Shen *et al.*, and depending on the catalyst it has been shown to result in different morphologies.^{100,102,103} For example, studies by Lombardi *et al.*¹⁴³ and Im *et al.*¹²⁸ grew gold-catalysed zinc phosphide nanowires, which resulted in straight nanowires. However, indium or tin-catalysed nanowires, such as in the studies by Shen *et al.*¹⁰¹, Im *et al.*¹²⁸, Kim *et al.*¹³⁰, and Choi *et al.*²⁶⁰, resulted in zigzag nanowires. These nanowires exhibit a similar morphology as the III-V twin superlattices, and selective area electron diffraction patterns support their similarity. However, as will be demonstrated in Chapter 5, their formation in zinc phosphide is fundamentally different. Other nano-morphologies, such as nanotrumpets and nanoribbons have been demonstrated through bottom-up growth. To date, there have been no photovoltaic devices demonstrated using nanostructured zinc phosphide.

2.3.2 Nanowire Growth

Nanowires have been achieved using a wide range of methods, which as mentioned previously can be widely split up into top-down and bottom-up.^{171–173} Top-down nanowires rely on selective or directional etching of a planar material. These methods are easily

scalable, and to an extent are already applied for different purposes in lithography for semiconductor processing. The processes are mature, and the highest efficiency nanowire photovoltaic was based on top-down nanowires.²⁵³ Some of the drawbacks of top-down nanowires relate to the rough and defective surfaces formed during the etching, and the strain relaxation mechanisms discussed above will not have been active during the initial growth.^{261,262} Hence the interfaces may be riddled with defects in cases where bottom-up would have produced pristine ones, and the same variety of material combinations cannot be achieved. Furthermore, bottom-up approaches allow for the growth of metastable phases, such as wurtzite gallium arsenide and high tin-content germanium-tin alloys.^{243–245,263} However, top-down nanowires can be produced with a high degree of reproducibility and homogeneity across large area devices, which is a challenge for bottom-up nanowires. In short, while top-down nanowire can be readily implemented as they are based on mature technologies, bottom-up nanowires provide a more versatile platform for exploring new material systems, and with further development could provide an excellent platform for various applications.

Bottom-up nanowires can be grown through various means, such as liquid phase synthesis and vapour-based approaches, of which the latter is covered in greater detail in the next sections. Liquid phase synthesis of nanowires has been extensively studied for metallic nanowires and compound semiconductors such as zinc oxide.^{180,264–267} Hydrothermal and polyol reduction growth methods are commonly utilised and rely on surfactants stabilising one set of planes preferentially, forcing the growth to occur in a 1D fashion.^{180,181,266} For example, in the hydrothermal growth of zinc oxide one can use acetate ions to stabilise the non-polar prismatic planes in favour for the polar basal planes of the wurtzite unit cell, resulting in the growth of hexagonal nanowires.²⁶⁷ The aspect ratio of these structures can be further tuned by adding potassium chloride in controlled concentrations.²⁶⁶ These methods show great promise as they can be used to produce large batches in a quick, cheap, and scalable way, and are currently used for industrial production of metallic or semiconductor nanowires. However, if compared to the vapour approaches, the products tend to have more impurities originating from the growth solution, resulting in nanowires with inferior properties. Furthermore, the precise control and hetero-structure formation is not achievable, limiting the possible material combinations.

2.3.2.1 Vapour-Liquid-Solid Growth

The vapour-liquid-solid (VLS) approach is currently the dominant approach to nanowire growth, and has been the go-to technique for the growth of group IV^{219,268}, III-V^{269–272}, II-VI²⁷³, and II-V^{101,130} (compound) semiconductor nanowires, and have also been utilised for metal and oxide nanowires^{274,275}. VLS, as illustrated in Figure 2.10, uses a metal nanoparticle catalyst that selectively absorbs the precursors from a vapour phase, then subsequently precipitates a solid at the interface of the catalyst and the growth substrate. A 1D growth is achieved as the precipitation will preferentially form at the interface with the solid. The important factors in VLS growth are the precursor types, the catalyst, and the epitaxial relationship between the grown material and the substrate.

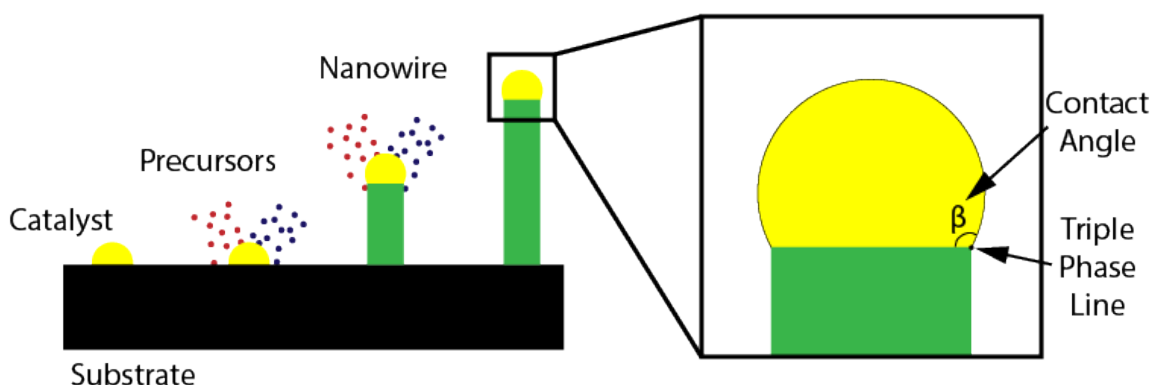


Figure 2.10 Illustration of the VLS process, highlighting the contact angle and triple phase line of the droplet with the nanowire.

The most common growth methods for VLS nanowires are MBE, MOVPE, and CVD, which rely on different ways to provide the precursors to the droplet. In MBE, most of the precursors arrive in either an atomic flux (e.g. gallium and zinc), while some species arrive as bound species (e.g. phosphorus (P_2/P_4) and arsenic (As_2/As_4)), albeit compositionally pure. These are then selectively absorbed in the droplet, which acts as a sink for the precursors to diffuse to before forming the solid product. While the droplet does not chemically catalyse a reaction, the naming has still stuck. To note is that not all species diffuse well on the surface. For example, models describing III-V growth assume arsenic to be immobile on the surface, and only contribute by direct impingement on the droplet.¹⁷⁷ On the other hand, MOVPE and CVD requires the precursors to be broken down before they can contribute to the growth. MOVPE makes use of gaseous metalorganic precursors, such as trimethylgallium (TMA, $Ga(CH_3)_3$), while CVD utilises precursors such as germane (GeH_4) or silicon tetrachloride ($SiCl_4$). The droplet acts as a catalyst and aids in the breaking down of the precursor, and then

subsequently absorbs the precursor species for growth. The non-growth species may contribute both positively and negatively to the growth. There are concerns that the organic part of the precursors may be incorporated in the growing nanowires to the detriment of their functional properties, however, the hydrogen in germane-based growth has been shown to help passivating the surface of the as-grown nanowires.²⁷⁶ Furthermore, the precursors are provided using a carrier gas, and the systems operate at much higher pressures compared to MBE. This allows for higher growth rates and higher throughput. There are also investigations into supplying the precursors through a liquid phase, and a liquid-liquid-solid (LLS) growth mode analogous to the VLS has been demonstrated.²⁷⁷ However, the control and crystal quality are yet to rival that of VLS grown nanowires.

The second aspect, and arguably the most important one, in VLS growth is the catalyst. Initial studies used gold, and it has remained the most popular material due to its catalytic properties, compatibility with various systems, and as it does not readily oxidise, allowing it to be pre-deposited *ex-situ*.^{177,217,219,271,278–281} Some catalyst preparation methods include drop-casting, electron-beam lithography (allowing for controlled nanowire positions), and thin-film deposition and subsequent annealing to break it down into nanoparticles.²⁸¹ The last technique is easily applied in MBE, while the films would need to be pre-deposited for MOVPE or CVD. However, while the gold usually remains in the catalyst, depending on the material it can be incorporated in the wire itself. In the case of silicon, this creates detrimental deep defect states in the bandgap, making it incompatible with CMOS (complimentary metal-oxide-semiconductor) technology.^{282,283} Plenty of other metals have been trialled as potential catalysts for VLS growth, such as copper²⁸⁴, silver²⁸⁵, palladium²⁸⁶, gallium^{269,270}, indium^{128,130}, tin²⁶⁰, and so forth.²¹⁷ One example of particular interest is self-catalysed III-V nanowires, e.g. gallium for gallium arsenide nanowires.^{240,269,270} In this case, one of the main components of the semiconductor is the catalyst, which will have to be replenished continuously as it is being consumed during growth. Self-catalysed growth is advantageous as it inhibits the incorporation of foreign elements, and it is possible to regulate the size of the catalyst through the flux *in situ*, which allows for control over the wire diameter and the contact angle. The initial contact angle of the catalyst with the substrate, and subsequently with the nanowire during growth at the triple phase line, is a parameter found ubiquitously in nanowire literature, as it plays a role in almost all aspects, and is illustrated in Figure 2.10.^{233,240,279,287–289} While there is still plenty to further elucidate regarding the exact workings of the droplets, it is worth noting that the contact angle is thought, or has been proven, to control important aspects such as the crystal phase (polytypism), growth direction, nanowire morphology, nucleation mechanism, and nanowire yield.^{232,240,263} Moreover, there are also other analogous growth methods which utilise a solid catalyst, referred to as vapour-solid-solid (VSS) growth.²⁹⁰ In VSS the catalyst usually acts to decompose the precursors, which are then transported to the growth front through surface diffusion, and generally results in much lower growth rates compared to VLS growth. There are methods through which nanowires grow without the use of a catalyst, such as strain induced methods²⁹¹, template assisted methods (e.g. template-assisted selective epitaxy (TASE)²⁹² and anodised alumina templates²⁹³), and selective area epitaxy, which is covered in greater detail in the next section.

The last factor relates to the substrate and its relationship with the grown material. An epitaxial interface results in the best structural and functional properties. Hence it is advantageous to grow on a substrate with a matching lattice constant. However, as previously mentioned, one of the advantages of nanowire growth is its capability to elastically accommodate strains, allowing for high quality epitaxy even at large lattice mismatch.²³¹ Nanowires have thus been explored in e.g. III-V integration on silicon for CMOS compatible optoelectronics.^{240,294} One factor which can complicate the formation of a good epitaxial interface is the state of the surface. If the oxide is improperly removed or if there are contaminants present it may have detrimental effects on the epitaxial relationship and whether the nanowires grow.^{268,295,296} Furthermore, depending on the surface diffusion of precursor species and thermal properties, one will have to tweak the growth conditions depending on substrate material and doping to find the optimum range. There are methods, such as aerotaxy, which do not use a substrate.²⁹⁷ The nanowires nucleate from catalysts suspended in a gaseous phase in aerotaxy, and will spontaneously grow into nanowires without interacting with a substrate. This allows for high-throughput production of nanowires, which subsequently need to be properly aligned on a substrate for potential device applications. While companies such as SolVoltaic AB have worked out methods to readily align nanowires over a large area with a high yield, it is not commonly achievable. As a result, techniques which result in random bundles of nanowires tend to be less desirable for photovoltaic applications. Thus, some techniques may yield high throughput, but due to the additional requirements are not viable for large-scale photovoltaic production, or they do not take advantage of the enhanced light absorption properties of nanowires. Nanowires grown by VLS on the right substrate allow for devices which fully take advantage of the structural and photonic properties of nanowires.

2.3.2.2 Selective Area Epitaxy

Selective area epitaxy (SAE), sometimes known as selective area growth (SAG), is one of the most prominent catalyst-free growth methods of nanowires.^{175,176,294,298–304} Ideally, SAE is achieved by covering the growth substrate with an amorphous dielectric mask, and then selectively exposing parts to allow for epitaxial growth in these regions. Using for example electron-beam lithography it is thus possible to deterministically choose the location of nanowire growth, and in the case of horizontal nanowires it is possible to

create bottom-up nanowire networks. This technique is being increasingly researched, and this section will cover the mask requirements and fabrication, growth mode, and applications in III-V growth and lateral epitaxial overgrowth (LEO).^{300,305–307}

The ideal properties for a mask are that it is easily deposited, processed, good selectivity during growth, chemically inert, and stability at the temperature range used for growth. The main type of materials suitable for this purpose are oxides, with silicon dioxide being the dominant one as it is a mature material which fulfils all the criteria for an ideal mask. Silicon dioxide has been extensively developed due to its integral part in CMOS and other technologies. It does not readily react or form bond with other materials, and it is stable at elevated temperatures. Other oxides, such as alumina, and materials such as silicon nitride or carbide are also possible mask materials, and depending on their compatibility with the substrate might be the preferred choice.

The mask fabrication for SAE requires multiple cleanroom steps to assure a high-quality surface and well-defined pattern. There are growth substrates, such as silicon, which readily form oxides suitable for SAE masks. However, other substrates such as III-Vs will need to have a mask material deposited. For the most commonly used oxides, such as silicon dioxide, techniques such as plasma-enhanced (PE) CVD can be used for deposition on various types of substrate. There are substrates (e.g. graphene) that are sensitive to the plasma in PECVD. Consequently, atomic layer deposition (ALD) or sol-gel deposition are more suitable in these cases. The oxides are subsequently patterned using lithography and etching. Standard photolithography does not result in feature sizes small enough to produce nanowires. Instead, electron-beam lithography, nanoimprint lithography, or deep-ultraviolet (DUV) stepper-lithography are commonly used. Electron-beam lithography is based on the rastering of an electron beam over the areas which you want to expose, and allows for high accuracy and adaptability of the resist pattern. This technique is commonly found in research facilities as it is easy to tune the pattern between iterations, however, the low throughput makes it less ideal for industrial scale applications. Nanoimprint relies on the mechanical imprint of a nanopatterned mask on the resist, which is high throughput and scalable, but the mask is not readily altered. Similarly, DUV steppers can be used for high-throughput and high-resolution manufacturing. The drawbacks of DUV steppers are that they can be incredibly expensive, and the process of tweaking the pattern is not as simple as in electron-beam lithography as it requires the fabrication of a new mask for each iteration. This is also the case for nanoimprint lithography.

Once the resist is patterned and developed, the substrates are ready to be selectively etched. Common etching methods of silicon dioxide masks include fluorine plasma etching, reactive ion etching, or etching using hydrogen fluoride (HF), either as a liquid or a gas. While all can be used, the fluorine plasma has shown better results and reproducibility when working with III-V substrates. The etch will essentially stop once it reaches the native oxide, and thus result in a high-quality surface in the etched holes. The native oxide is generally desorbed *in situ* or can be removed through a separate etching step if desired. HF-based etches are desired when working with silicon substrates as they will passivate the exposed surface, and if the substrate is promptly introduced into a vacuum environment (such as the growth systems) directly afterwards one can avoid any re-oxidisation. If all the steps have been properly optimised, the surface will at this point be ready for growth. SAE epitaxy is classified as a hybrid top-down/bottom-up due to the top-down nature of the mask fabrication.

While the mask may be used to selectively nucleate droplets for self-catalysed VLS growth *in situ*²⁴⁰, it generally occurs through a vapour-solid (VS) mechanism, as shown in Figure 2.11. The mask material will ideally inhibit the nucleation and growth on it, and the holes will act as low energy sites for these processes instead. As the vapour phase precursors impinge on the surface, there are three possible scenarios: they contribute to the creation of a solid, diffuse, or re-evaporate, as shown in Figure 2.11b. First, if the incident flux hits an exposed area it will directly contribute to the nucleation and growth (except at too high temperatures when it may desorb before contributing). However, if the atoms arrive on the mask, they will either diffuse to the holes, acting as sinks, or if the holes are too far away, they will desorb from the surface. Some species, such as arsenic, are assumed to be immobile on the surface, and will thus only contribute to the growth if they impinge directly on the growth area, or as a secondary flux if by chance they desorb and travel in a direction where it encounters a growing structure.¹⁷⁷ These processes assume that the growth occurs at a suitable growth temperature, the scenarios when this is not the case are detailed at the end of this section.

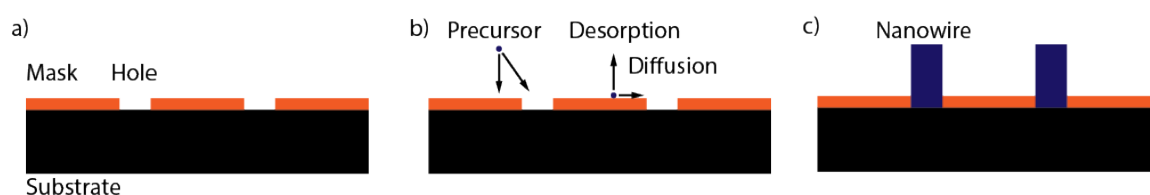


Figure 2.11 Illustration of (a) growth ready substrate, (b) surface processes during growth, and (c) grown sample.

The material starts to grow from the predetermined pattern, and the resulting nanostructure grows to a shape defined by the symmetry of the lowest energy facets, the crystalline relationship with the substrate and kinetic factors. First, crystals grown under thermodynamic equilibrium conditions grow as to maximise its coverage by low surface energy facets to minimise the Gibbs free energy of the system. If the crystal is in free space its shape can be defined by the Wulff construct³⁰⁸, or the Winterbottom³⁰⁹ construct if a substrate is present, as illustrated in Figure 2.12. In the Wulff construct, Figure 2.12a, planes are plotted on a polar plot as a function of their plane normal and surface energy.^{183,308} A lower surface energy results in the plane being further from the centre, and if it is the uttermost facet on the plot it means that it will be the most thermodynamically stable, and thus part of the equilibrium crystal shape. The surface energy is determined by the number of dangling bonds of the facet, which tends to be higher for higher index facets. Consequently, the Wulff construct tends to be made up of low-index facets. However, this scenario is no longer valid in the presence of a substrate, which is taken into account by the Winterbottom construction in Figure 2.12b.^{183,309} The main difference in the plot is the inclusion of the substrate, as the final crystal shape will depend on the angle and distance from the centre at which it lies. In a similar approach to the effect of the substrate, the surface energies (and the resulting equilibrium crystal shape) can be changed by changes in the environment, such as the inclusion of surfactants which selectively stabilise certain planes. Unfortunately, in real systems this is seldom sufficient to predict the final shape of the crystal or nanostructure as kinetics play a significant role. Kinetics tend to be of particular importance in defining the shape during the initial stages of growth and when the growth is carried out at high growth rates, as the atoms do not have the time to fully settle down in the lowest energy position that would result in the thermodynamic shape.^{310,311} The growth rate of different facets can depend on how close-packed a growth direction is (more close-packed required more atoms to grow the same “distance”), how easily atoms are incorporated into the facets, and how much of the incident flux impinges on them, which depends on their relative inclination. The final crystal shape is thus a function of how long the growth has been allowed to proceed and the growth conditions, and can be predicted by modelling methods such as the phase-field approach.³¹¹

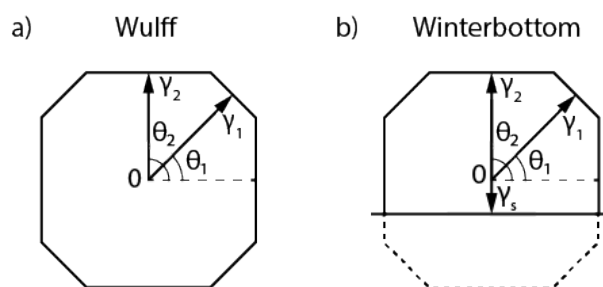


Figure 2.12 (a) Diagram of the Wulff diagram which is symmetric around the Wulff point (0) in free space. (b) shows the inclusion of a substrate in the Winterbottom construct and how it alters the thermodynamic crystal shape.

Different growth modes may also be achieved by the shape of the selectively opened areas. Pinhole shapes have been shown to act as the nucleation point of vertical nanowires³⁰², however, it is similarly possible to make slit like openings, which results in the growth of horizontal nanowires¹⁷⁵. Vertical nanowires growth by SAE is a common approach for gallium nitride, and has also been demonstrated for gallium arsenide and other III-V materials.^{238,302,312,313} While this allows for the creation of nanowires without the use of catalysts, SAE vertical nanowires tend to have a higher density of stacking faults, resulting in inferior properties.¹⁷⁷ The optimisation of SAE nanowires and elucidation of the defect formation is an unresolved topic still under active investigation. Horizontal nanowires grown using the SAE approach have been shown to produce high-quality crystals, and allows for the growth of high-quality heterostructures. Nanowire networks grown based on this approach are currently investigated as a potential platform for Majorana physics in III-V material, with potential as a fault tolerant topological quantum computing platform, and for III-V integration on silicon for optoelectronic applications.^{175,294}

Furthermore, when the material emerges from the confinement of the hole it can grow laterally, overgrowing the mask as illustrated in Figure 2.13. This process was first explored for silicon in the early 1960's.^{314–316} By spacing holes appropriately, it is possible for the overgrown material to join with crystals from other holes to form a thin film. This approach, called either lateral epitaxial overgrowth (LEO) or epitaxial lateral overgrowth (ELO), allows for the growth of thin films with reduced interactions with the substrate, which has been used to improve the quality of the grown film in various lattice-mismatched material combinations.^{300,305–307,317,318} This approach does come with its own challenges and limitations. While the parts which overgrow the oxide tend to be defect free, it is possible for the parts just above the hole to have a high defect density, although this is less likely if nanoscale holes are used. Furthermore, the interface formed by the coalescence of two overgrown crystals can also possess a high density of defects, as it is essentially a grain boundary. A minimum defect density can be achieved if the holes are spaced at an integer multiple of the unit cell apart, or if the lattice mismatch between the two substrates is small.



Figure 2.13 Illustration of LEO, showing cross sections of (a) the initial substrate, (b) the early stages of growth, and (c) the coalescence of the structures into a film.

One complication in the SAE approach is that nucleation on the oxide masks can occur if precautions are not taken, and selectivity is lost. Some examples of scenarios where this can be the case is if either the temperature is too low, the fluxes are too high, if there are nucleation sites due to an improperly prepared surface, or if the growth time is too long.¹⁷⁶ If the temperature is too low during growth, the diffusion distance of the species may be too short to reach the holes, and their thermal energy is too low to desorb. Consequently, nucleation starts to occur on the oxide as the concentration builds up. When the fluxes are too high, the steady-state concentration of atoms on the surface becomes high enough to make nucleation probable outside of the holes. Furthermore, a poorly processed mask may have excessive roughness which facilitates heterogeneous nucleation, or it may have pinholes which can cause selective growth in undesired locations. Finally, as whether nucleation occurs or not is a question of probability, it is still possible to get nucleation simply because the growth time is too long. Higher relative growth temperatures should allow for longer growth times without parasitic growth, however, simply interrupting the growth at regular intervals to desorb material or etch it *in situ* from the oxide has also proven successful.^{319,320} If the temperature is too high, on the other hand, it will instead result in the species desorbing before they can contribute to the growth.

2.4 Summary and Outlook

Nanomaterials present a vibrant area of science and have the possibility to avoid limitations faced in bulk versions, and sometimes even exhibit new properties. Nanoscience and nanotechnology are impacting medicine, electronics, solid-state lighting, energy production, and multiple other areas. There are various ways of fabricating these nanomaterials, be it top-down, bottom-up, vapour-phase or liquid-phase synthesis. Vapour-phase methods, such as MBE and MOVPE, have been behind the production of the highest crystalline quality compound semiconductors, and in combination with techniques such as VLS or SAE they can be used to grow high quality nanowires and other nanostructures. Nanowires are interesting for their stress relaxation mechanisms, facilitating growth on mismatched substrates and heterostructure formation, and their nanophotonic properties, making them suitable for photovoltaic applications, among others.

Zinc phosphide is a material which stands to benefit from some of the advantages of nanomaterials, and the nanowire morphology in particular. The enhanced elastic strain relaxation facilitates the growth on lattice mismatched substrates and allows for higher quality interfaces for potential heterojunction combinations. In addition, it also helps accommodate strain induced from a mismatch in the thermal expansion coefficient. The benefits for photovoltaic applications are further improved by the enhanced light absorption and directivity of nanowire arrays. While nanostructures of zinc phosphide have been grown previously using amongst other the VLS method, it has never been achieved in an epitaxial fashion to produce vertical nanowires, which is ideal for photovoltaic applications. To the best of my knowledge, there are no previous reports of SAE of zinc phosphide. In short, nanostructured zinc phosphide is an area with plenty left to explore, and can lead to the material reaching its full potential for renewable energy applications.

Chapter 3 Introduction – Characterisation

The first way materials were characterised, which still is a very convenient and useful method for qualitative characterisation, is to use our eyes and look at an object. However, we require more specialised tools if an object becomes too small or if we are looking at properties not readily determined simply by sight. We use microscopy to observe and quantify objects smaller than the eye can see, spectroscopy to characterise how it interacts with electromagnetic radiation, mechanical tests to determine its structural properties, as well as observing how charge carriers behave in the material to determine its electrical properties. The most suitable techniques for the experimental circumstances are chosen according to the material and the intended application, as it defines what properties are of greatest interest. Being able to fully understand the properties, and wherefrom they stem, is key to optimising a material and discovering new ones with even greater properties. Materials development is based on an iterative feedback loop, which is heavily reliant on characterisation. It is presented in Figure 3.1 and is currently propelling materials performance to new heights.

In the case of nanotechnology and nanoscience, incredibly high magnification and resolution levels are required to observe features down to the atomic scale to accurately determine their structure, and sensitivity to the minute signals that indicate their functional properties. These types of characterisation have only been made available relatively recently through advances in detectors and experimental setups. Various techniques, such as electron microscopy^{321–327}, scanning probe microscopy^{328,329}, secondary-ion mass spectroscopy (SIMS)³³⁰, micro-photoluminescence spectroscopy (PL)^{55,331}, atom probe tomography (APT)^{332–334}, and nanoindentation³³⁵ to name a few, have helped pave way for significant advances in material science. Furthermore, by contacting nanostructures it is also possible to analyse their electrical properties in various configurations, allowing for the determination of charge carrier type, conductivity, in addition to other electrical characteristics.^{210,224,336,337} In the work carried out in this project, investigating inorganic nanomaterials for photovoltaic applications, the majority of the characterisation has been carried out through electron microscopy-based techniques, which will be the focus of this chapter.

3.1 Electron Microscopy

Before nanomaterials were investigated, the characterisation of the microstructure could readily be achieved using optical microscopes. However, the diffraction limit based on the Rayleigh criterion allows for a maximum resolution in the order of a few hundred nanometres for visible light. An alternative to resolve even smaller features is to use electrons, where standard acceleration voltages (in transmission electron microscopy ~60–300 kV) allow for wavelengths down to 2.3–5 picometres. At this point, any visualisation

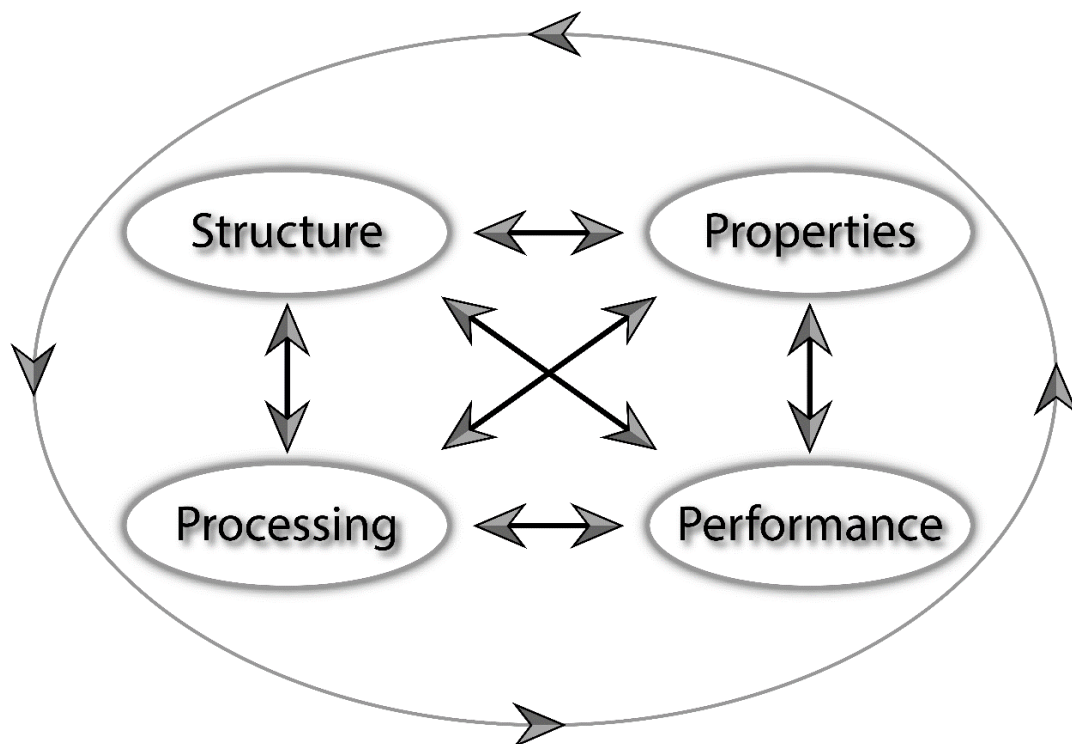


Figure 3.1 Iterative and interdependent feedback loop which is the basis of current material science development.

down to the atomic scale are no longer diffraction limited, however, aberrations in the beam generation and focusing systems will limit the performance, as explained in subsection 3.5. The idea to build electron-based microscopes was first realised by Ernst Ruska in 1931 based on his work in collaboration with Max Knoll, for which he received the 1986 Nobel Prize in physics.^{338–340} Throughout the following decades, the resolution of high-end microscopes has increased following improvements in electron microscopy components, and with the invention of aberration correctors it is now possible to reach down to sub-Ångström resolution levels.^{325,327} This chapter will aim to describe the fundamentals of electron microscopy and how it is useful in materials characterisation.

While this chapter's goal is to highlight the main methods used throughout this thesis, it is far from comprehensive. For more detailed explanations I would recommend the books by Goldstein *et al.* for scanning electron microscopy (SEM)³⁴¹, Egerton³⁴², Williams and Carter³⁴³, and Reimer and Kohl³⁴⁴ for general scanning/conventional transmission electron microscopy (S/C-TEM), Orloff *et al.* and Hawkes and Kasper for electron optics^{345,346}, Brydson *et al.*³⁴⁷ for aberration correction analytical microscopy, Egerton for a comprehensive work on electron energy-loss spectroscopy (EELS)³⁴⁸, and finally Yacobi and Holt for cathodoluminescence (CL)³⁴⁹. If no reference is given in later parts of the chapter it is based on these references.

The world of electron microscopy goes beyond the techniques discussed below, and approaches such as electron beam induced current (EBIC) measurements^{350,351}, photoemission electron microscopy (PEEM)^{352,353}, and Lorentz microscopy^{354,355} can be used to investigate electrical properties, ferroelectric domain structure and magnetic properties, to name a few. However, they are beyond the scope of this chapter, which I will limit to the main techniques used in this thesis.

3.2 Electron-Matter Interactions

When an electron is incident on a material, it can interact in a plethora of different ways, as summarised in Figure 3.2a. The types of interactions can be split into two main categories, namely elastic and inelastic interactions. In elastic interactions the kinetic energy and momentum are conserved, and they generally occur between the incoming electron beam and the atomic nuclei in the material through Coulomb scattering. The most common scattering configurations are incoherent Rutherford scattering or coherent diffraction. On the other hand, inelastic interactions result in a conversion of part of the energy into an atomic or electronic excitation. This can result in the production of photons such as characteristic x-rays through atomic orbital excitation/relaxation processes, and visible light by bandgap relaxation (CL). Electrons can also be emitted through knock-on effects (secondary electrons), or through the Auger effect when excited atoms relax. The emission of characteristic x-rays and Auger electrons occur simultaneously, however, x-ray emission dominates in heavier elements while Auger electrons is observed for lighter elements. The inelastic interactions can also result in Bremsstrahlung, or breaking radiation, which produces a broadband x-ray emission background which generally is not used for any characterisation of the materials. By examining these different signals, it is possible to gain information about the structure, composition, and optoelectronic properties. Furthermore, analysing the energy lost by the primary electron beam is also a powerful technique, known as EELS, which will be discussed later on.

There are two main configurations which are used in electron microscopy, namely SEM and TEM. The first method generally relies on backscattered or secondary electrons to image a sample in a “reflective” geometry. The electrons will act in an area called the interaction volume, as shown in Figure 3.2b. Different forms of signal come from different parts of the interaction volume, and its size is often the resolution limiting factor. As shown in the diagram, secondary electrons have the smallest emission volume, allowing for the highest spatial resolution. Secondary electron emission is mainly sensitive to the topography of the samples, while backscattered electron-based imaging is more sensitive to the composition of the material. As the name implies for the second configuration, TEM, the electrons pass through the sample and the image is formed in “transmission”. The interaction volume in TEM is usually

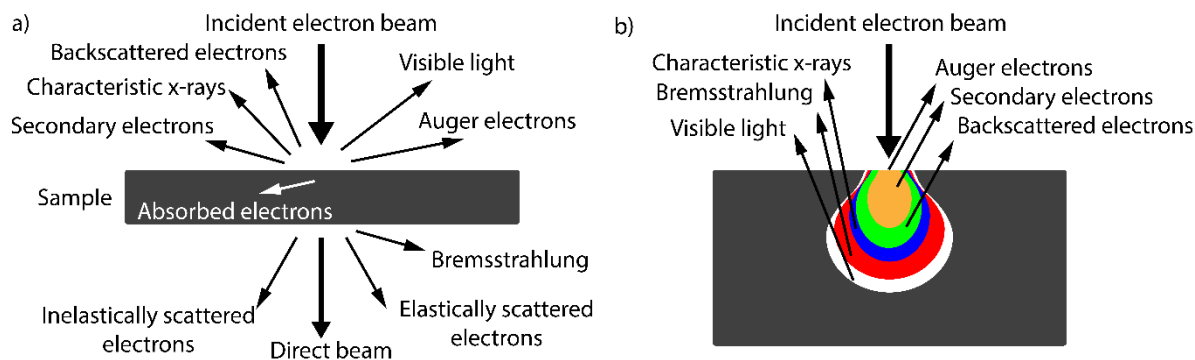


Figure 3.2 (a) Illustration of the electron-matter interactions in a TEM configuration and (b) the interaction volume in a SEM configuration.

greater than the sample thickness as it utilises higher acceleration voltages and thinner samples. Furthermore, the targeted interactions are generally different, and the resolution limitations dictated by the interaction volume does not apply. Although there is some spreading of the electron beam due to electron-matter interactions, for a sufficiently thin sample the limiting factors are generally due to the optics, detectors or the environment.

3.3 Sample Requirements and Preparation

In electron microscopy it is important to avoid charge build-up on the surface, as it prevents any further interactions between the electron beam and the sample. This issue is more prevalent in SEM as larger fraction of the electron beam is absorbed by the sample. The easiest way to avoid charging is to image a conductive sample which is grounded. Unfortunately, many samples in need of characterisation are not good conductors. The techniques most commonly used for such samples are the deposition of a thin surface layer of a conductive material, such as carbon or gold through evaporation or sputtering, an electron flood gun which constantly neutralises the charge on the surface, or by balancing the charge injection by the electron beam and the emission of backscattered and secondary electrons. The final approach is achieved by working at a critical beam energy, which is materials dependent. While tricky, it is possible to achieve critical energy imaging through optimisation. Finally, for the electron beam to propagate, the column has to be under vacuum to assure a high mean free path for the electrons. As such, the samples have to be vacuum compatible, and many biological and liquid-based samples have to be frozen, usually by using liquid nitrogen. Cryo-EM, in both SEM and TEM, is a large field in its own right, and the 2017 Nobel Prize in chemistry was awarded to Dubochet, Frank, and Henderson for its development.^{356–358} Another approach is the use of environmental electron microscopes utilising differential pumping.³⁵⁹

In TEM, on the other hand, most of the electrons transverse the sample and less charge is deposited and accumulated. Consequently, (while still of importance) the conductivity of the sample is less vital. However, for the electrons to transverse the sample it must be electron transparent, which limits the sample thickness. Depending on the characterisation technique and sample material, this limit can vary from ~20 nm to ~500 nm, the general trend being that thinner samples result in higher resolution. Many nanomaterials already have dimensions in this range, and are simply transferred to a TEM grid as is for analysis. For vertical nanowires one simply has to put a TEM grid on the as-grown substrate, and by pressing down with a cotton swab and gently moving it around it is possible to get hundreds, if not thousands of nanowires on the grid. Unfortunately, it is not always this easy. Non-freestanding nanowires need to be cut out into electron transparent lamellae and transferred to the desired grid. This process is most commonly achieved using a focused ion beam (FIB) method. While the processing can induce damage, and potentially amorphise the lamella if not performed correctly, it allows one to specifically choose the region to turn into a lamella and facilitates the analysis in specific regions of interest. This approach also allows for the creation of nanowire cross-section samples. Another approach for cross-sectional sample preparation is ultramicrotomy. By embedding and transferring the nanowires to a resin, it is possible to then use a diamond knife to cut the nanowires into slices which are 50-200 nm thick for cross sectional analysis. This approach, in combination with cryogenic cooling, is commonly used for preparation of biological samples. Other techniques for preparing TEM samples from other sources include wedge polishing, ion milling, and cleaving to obtain parts/corners of the sample which are electron transparent.

3.4 Electron Microscope Components

Electron microscopes rely on four main components: electron guns, apertures, lenses, and detectors. This subsection will focus on the operation and functions of the different parts, and how they are used to produce images. Stigmators and aberration correctors also play an important role in producing the highest quality images, and will be covered in the next section. Examples of standard SEM, TEM, and STEM columns are shown in Figure 3.3, which will be described in more detail below.

The electron guns, often referred to as the cathodes, utilise one of three main electron emission process: thermionic, Schottky, or field effect emission. The ideal properties for high signal-to-noise measurements and high spatial resolution are high current densities, the geometry of the source being as close to a point as possible, and minimal energy spread of the emitted electrons. Thermionic emission occurs through the simple phenomenon where electrons are emitted from a material if it is heated up sufficiently. At these elevated temperatures the kinetic energy of the electrons will be high enough to escape into the vacuum level. This was initially achieved using a tungsten wire which was heated by running a current through it until temperatures in the range 2200-2700 °C were reached. The high melting point, low vapour pressure, high work function to thermal energy ratio at operating conditions, and cheap manufacturing make tungsten a viable cathode material. Another suitable material for thermionic emission is lanthanum hexaboride (LaB_6), usually in the shape of a rod with one end sharpened into a tip. It has a much lower work function (2.7 eV compared to 4.5 eV), allowing for a much lower operating temperature (1100-1700 °C). Furthermore, the electrons are emitted from a much smaller area, which facilitates the focusing of the beam and allows for higher current densities. Drawbacks of lanthanum hexaboride include the increased manufacturing cost, and although lifetimes can be higher if handled correctly, they are more susceptible to poisoning from potential reactions with the environment. Consequently, higher vacuums are needed to operate the gun for sustained periods of time. Applying an electrostatic field to the tip of the gun further facilitates the extraction of electrons, which brings us to Schottky emission guns (also referred to as Schottky field emission guns) that are capable of achieving current densities several orders of magnitude higher than purely thermionic ones.³⁴² These guns are manufactured by coating a sharp tungsten tip with zirconia (ZrO). The electric field will act at a greater extent at the tip, meaning that the effective source size is significantly decreased compared to that of thermionic emitters. Schottky emission guns operate around 1500 °C in combination with an applied electric field. Overall the performance is much better than that of thermionic emitters, however, manufacturing costs and vacuum requirements to maintain

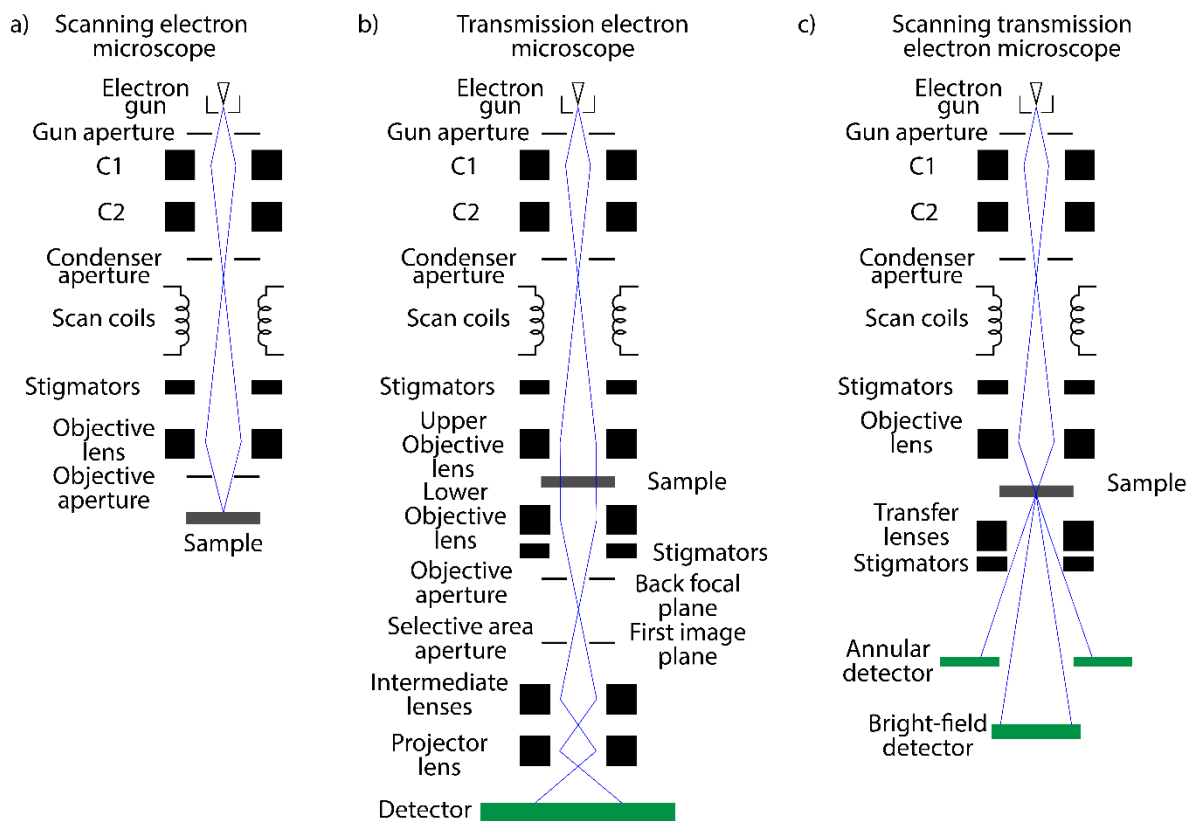


Figure 3.3 Diagrams of the major components of the columns of (a) a SEM, (b) a conventional TEM, and (c) a STEM. Note that in a dedicated STEM setup the gun will be at the base, and the configuration will be flipped.

functionality are more stringent. The last type of electron guns is the field emission guns (FEGs). As for manufacturing, they are very simple and can be achieved by producing sharp tipped tungsten wires through electrocatalytic dissolution, achieving high radius of curvature tips. FEGs can operate at room temperature, and rely on the quantum-mechanical tunnelling of electrons from the cathode into free space under high applied electric fields. FEGs have the highest emission current density, smallest effective source diameter, and lowest energy spread of all electron gun types, making them the most attractive type for high performance equipment. However, they require ultra-high vacuum levels to operate, and any surface contaminations will inhibit the tunnelling and subsequently degrade the performance. To avoid deterioration in the performance, the tips are regularly flashed, i.e. heated to clean them of any surface contamination through degassing. A summary of the different types of electron guns and some of their distinguishing properties are presented in Table 3.1. Once the electrons are extracted, they are accelerated by an electric field to the desired speed, which is roughly 0.1-30 kV in SEMs and 60-300 kV in TEMs, although there are setups capable of working up in the low MV range.³⁶⁰ The gun usually goes on the top of the electron microscope columns, as shown in Figure 3.3, with the exception of dedicated STEM setups, where they are put at the bottom for the improved stability and as they require fewer post specimen lenses.

Table 3.1 Summary of different types of electron guns and their properties. Values based on Egerton, Physical Principles of Electron Microscopy.³⁴²

Type of source	Thermionic		Schottky	FEG
Material	W	LaB ₆	W/ZrO	W
Operating temperature (°C)	2200-2700	1100-1700	~1500	20
Current density (A/m ²)	~10 ⁴	~10 ⁶	~10 ⁷	~10 ⁹
Source diameter (μm)	~40	~10	~0.02	~0.01
Vacuum (Pa)	<10 ⁻²	<10 ⁻⁴	<10 ⁻⁷	~10 ⁻⁸
Lifetime (h)	~10 ²	~10 ³	~10 ⁴	~10 ⁴
Energy spread (eV)	1.5	1.0	0.5	0.3

The next part of the columns is the condenser section, whose purpose is to properly align and focus the beam. The first set of lenses are the magnetic condenser lenses, generally referred to as C1 and C2. The lenses operate by having coils placed in a symmetric pattern around the electron beam, and by running a current through them they generate a magnetic field. The field acts on the electrons through the Lorentz force to focus the beam. C1 produces a strong magnetic field to generate a cross-over and magnification effect, while the C2 lens is weaker, and is used to achieve the correct focus of the beam onto the sample. However, the electron lenses are not perfect, and introduce astigmatism into the beam as different parts may have different focal lengths. Condenser stigmators are used to compensate for this effect and act to minimize the difference in focal length of electrons passing at different azimuthal angles through the lens. The next component in a standard condenser section is the condenser aperture, generally placed just below the C2 lens. The aperture is a metal diaphragm with a small hole in it (10s to 100s μm diameter). First, the size of the aperture dictates how much of the beam passes through. This controls the beam current and the convergence angle of illumination, affecting the final intensity and depth of field. Furthermore, by cutting out the electrons with the highest deviation from the optical axis it reduces spherical aberrations. To help align the electron beam with the optical axis of the microscope, there are also two pairs of coils in this section, the first applying uniform fields to align the beam in the horizontal directions with respect to the beam propagation, and the second one making sure the angle of incidence of the beam, or its tilt from the optical axis, is minimised. At this stage however, the different setups start to vary significantly. SEM and STEM also have scanning coils to raster the focused electron beam across the sample to provide position dependent information, while TEM utilises parallel illumination of the whole area under investigation.

The next part is the objective lens, a strong magnetic lens. In SEM it is placed just before the sample, which is the end of the column. The objective lens is responsible for the final focusing into a nanoprobe of the electron beam onto the sample. Furthermore, to achieve the high resolution even at lower acceleration voltages (which are more sensitive to aberration and the environment) modern SEMs generally operate at higher voltages throughout the column, using so called beam boosters, and the final velocity is adjusted at the end. Some systems also use a combined electrostatic/magnetic lens doublet at the end.

On the other hand, modern transmission-based electron microscopes usually use magnetic immersion lenses, where the sample is situated inside of the lens itself. In this setup, the upper part of the lens, the “pre-field” region, is used to either focus the beam into the final nanoprobe in STEM, or to make the incoming electrons travel in a parallel beam in the case of TEM. The lower part of the lens only acts as a transfer lens in STEM setups, helping align the beam with the detectors. In TEM, however, the post-field of the

objective lens acts as the first imaging lens, producing a cross over at the back-focal plane and a magnification of the image. Both systems have an objective stigmator after the objective lens to correct for any astigmatism it introduces.

After this stage, the only essential components for STEM are the detectors, however, additional transfer lenses which help aligning the signals with the detectors facilitate operation. TEM, on the other hand, has a set of apertures at this stage, namely the objective aperture in the back-focal plane and the selective area aperture in the image plane of the objective lens. These are used to access different imaging modes, as described in more detail below. This is followed by a set of intermediate lenses, which serve two purposes. First, they increase the image magnification by stepwise changing the focal length. Furthermore, they act in combination with the objective/SA apertures to make either the image or diffraction project onto the detectors/screen. The last of these lenses is called the projector lens, as it is the one which projects the final image on the screen or the camera.

There is a multitude of different detectors used in electron microscopy depending on which signal and configuration is used. In SEM, the most common imaging detectors are scintillators and silicon detectors for backscattered electrons, and Everhart-Thornley detectors for secondary electrons.³⁶¹ Scintillators rely on optically active materials, which generate photons when hit by a high-energy electron. The photons are then transported to a photomultiplier, which amplifies the signal and converts it to an electrical signal. Semiconductor detectors, on the other hand, use the excitation of free charge carriers through inelastic scattering by the backscattered electron, and measuring the change in current under an applied bias. These detectors are generally positioned around the end of the electron column. The Everhart-Thornley detectors also utilise scintillators, however, to predominantly attract low-energy secondary electrons they are placed to the side of the chambers and attracts the electrons by an applied bias in the order of a few hundred volts.³⁶¹ The low applied bias does not significantly influence the high-energy backscattered electrons or the primary electron beam. However, this configuration is sensitive to secondary electrons generated in other regions, and backscattered electrons incident on it through randomised scattering. Higher selectivity can be achieved through the in-lens detector configuration, as shown in Figure 3.4. This configuration relies on the magnetic field of the objective lens extending into the region close to the specimen, which then guides the emitted secondary electrons back through the lens, where they are then collected by an Everhart-Thornley detector. This removes the influence of secondary electrons generated at the chamber walls, away from the electron probe, and backscattered electrons randomly hitting the detector.

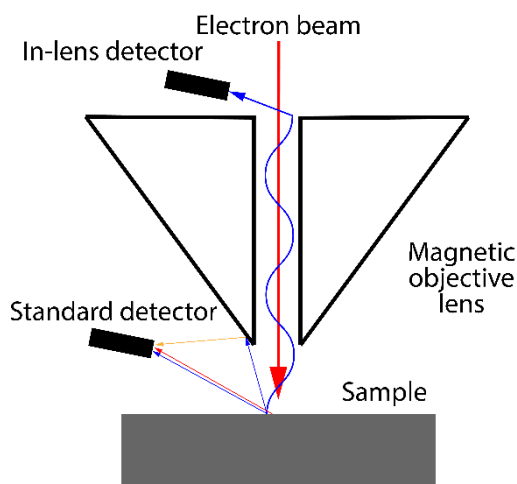


Figure 3.4 Comparison of the in-lens and standard secondary electron detector configuration.

Imaging in TEM is achieved using two main detector types, namely fluorescent screens for viewing, and cameras for recording, which most commonly are either charge-coupled devices (CCD) or an active-pixel sensors. The fluorescent screens usually use zinc sulphide (sometimes combined with cadmium sulphide) powder on a screen, which emit green light when hit by the high-energy electrons. This allows the operator to view the image in real time, however, it is not the most suitable for recording the image. Initially, the recording was done using imaging plates or photographic emulsions, however, modern TEMs rely on cameras. While both systems are based on complimentary metal-oxide-semiconductor (CMOS) components, the active-pixel sensors are generally referred to as “CMOS cameras”. Both cameras have two main components: a thin scintillator and an array of silicon photodiodes. The first part is necessary as the high fluence and energy of the incoming electrons would create defects in the silicon detector, degrading it quickly. By sequentially looking at the signal of each pixel in the array it is possible to construct images, and the manner at which this is achieved is what differs between the cameras. Read-out is achieved in a “column-by-column” fashion in traditional CCDs, while CMOS cameras can do it at an individual pixel level. The advantage of CMOS sensors is their comparably lower cost, higher read-out rates,

higher dynamic ranges, and lower sensitivity to oversaturation and blooming. Their main disadvantage was the rolling-shutter effect, resulting in different parts of the image corresponding to slightly different times due to the pixels read-out sequence. However, with the development of global shutters and increased read-out rate this is becoming less of an obstacle, and they are becoming increasingly more common. To achieve the highest signal-to-noise acquisition, the cameras are cooled using Peltier elements, which decreases the background dark current and allows for longer read-out times. The camera can be used either to image the fluorescent screen itself, or to directly detect the electron beam. Newer microscopes tend to use the camera for both purposes, as it allows for the observation of the fluorescent screen on the same computer screen where the imaging and alignments are carried out.

STEM imaging, on the other hand, relies on similar detector methods, but mainly in annular configuration. One of the advantages of annular detectors is that depending on the collection angle and camera length it is possible to probe different signals, such as Ruthenford scattered electrons at high angles/short camera lengths (used in high-angle annular dark-field (HAADF)), or diffracted electrons (in ADF), and if the angle is sufficiently low (or camera length sufficiently long), it is possible to observe the direct beam (annular/conventional bright-field (BF)). The different imaging modes are explained in more detail in Section 3.6.

In addition to the image detectors described above, analytical detectors are commonly applied to modern microscopes to increase the information they provide. The most common detectors are x-ray detectors for energy dispersive x-ray spectroscopy (SEM/TEM/STEM), optical detectors for CL (SEM/STEM), and finally the detector setup for EELS (TEM/STEM). The standard detector used in modern EDX setups is the silicon drift detector (SDD). Similar to the semiconductor detectors described above, they rely on the generation of charge carriers in silicon by the x-ray. To make it selective to x-rays it is equipped with an x-ray transparent window in front of the detector, typically made from beryllium. The contacts are on the backside of the detector, characterised by a central anode and electrodes surrounding it in a spaced-out circular pattern. The most common artefact in SDDs come from x-ray interactions with the silicon not resulting in the generation of charge carriers, such as silicon x-ray fluorescence resulting in false silicon peaks in the final spectrum. Another common artefact is escape peaks, which are observed as peaks an integer value of the silicon x-ray energy below the initial signal. This occurs when some of the energy is converted to silicon fluorescence and then escapes the detector, resulting in part of the energy being missing when it is read. The EDX detectors are usually placed above the sample at an angle in both SEM and TEM/STEM setups.

CL analysis relies on the detection of photons in the ultraviolet-infrared range. To detect these photons, they are usually coupled out of the vacuum main column using either a set of lenses or an optical fibre (depending on the available space around the sample). The restrictions are more stringent in the case of TEM/STEM setups compared to SEMs as there is less space for the optics around the sample. The photons coming out of the microscope are then dispersed using either a prism or a diffraction grating to be analysed spectroscopically. It is then possible to use a semiconductor detector to analyse the electrons and attribute how many are generated by each wavelength to produce the CL spectra. The semiconductor used in this case depends on the spectral range investigated, which in the Attolight Rosa setup at EPFL are indium gallium arsenide for the infrared region (for wavelengths between 1000-1700 nm) and silicon for the visible to ultraviolet region (for wavelengths between 200 – 1000 nm). A detailed description of the setup is given in ref. [362]. EELS similarly relies on a section which disperses the electrons depending on their energy, namely a magnetic prism. After the prism it is possible to create a spectrum of the relative energies using a CCD by measuring the intensity at each position. The EELS detector setup is generally placed at the end of the column. Furthermore, the incoming electrons have to be incident on the prism at the correct angle (usually calibrated to be the optical axis of the setup) to provide an accurate signal.

In summary, this section has described all the elements required to generate an electron beam, the optics needed to properly manipulate it, and how the signals generated from electron-matter interactions can be detected for imaging and analytical purposes by different detectors.

3.5 Aberrations and their Correction in Electron Microscopes

Aberrations are a consequence of non-perfect electron emission by the gun and focusing by the lenses. With the small wavelengths achievable in STEM/TEM, aberrations are the main factor limiting the achievable resolution instead of diffraction. The ability to overcome them is what has been driving the improvement of electron microscopes in the last few decades. The most common forms of aberrations in electron microscopes are chromatic, spherical, and comatic aberrations, in addition to the previously mentioned astigmatism, which are illustrated in Figure 3.5. In this section I will describe them in brief, and introduce the most common methods applied to deal with them.

The chromatic aberrations (Figure 3.5a) mainly originate in the electron energy dispersion from the electron guns. Electrons with slightly varying energy will experience forces of different magnitude from the lenses, and thus have different focal lengths. This complicates the focusing of the beam into a point, while also broadening the zero-loss peak and lowering the energy resolution in

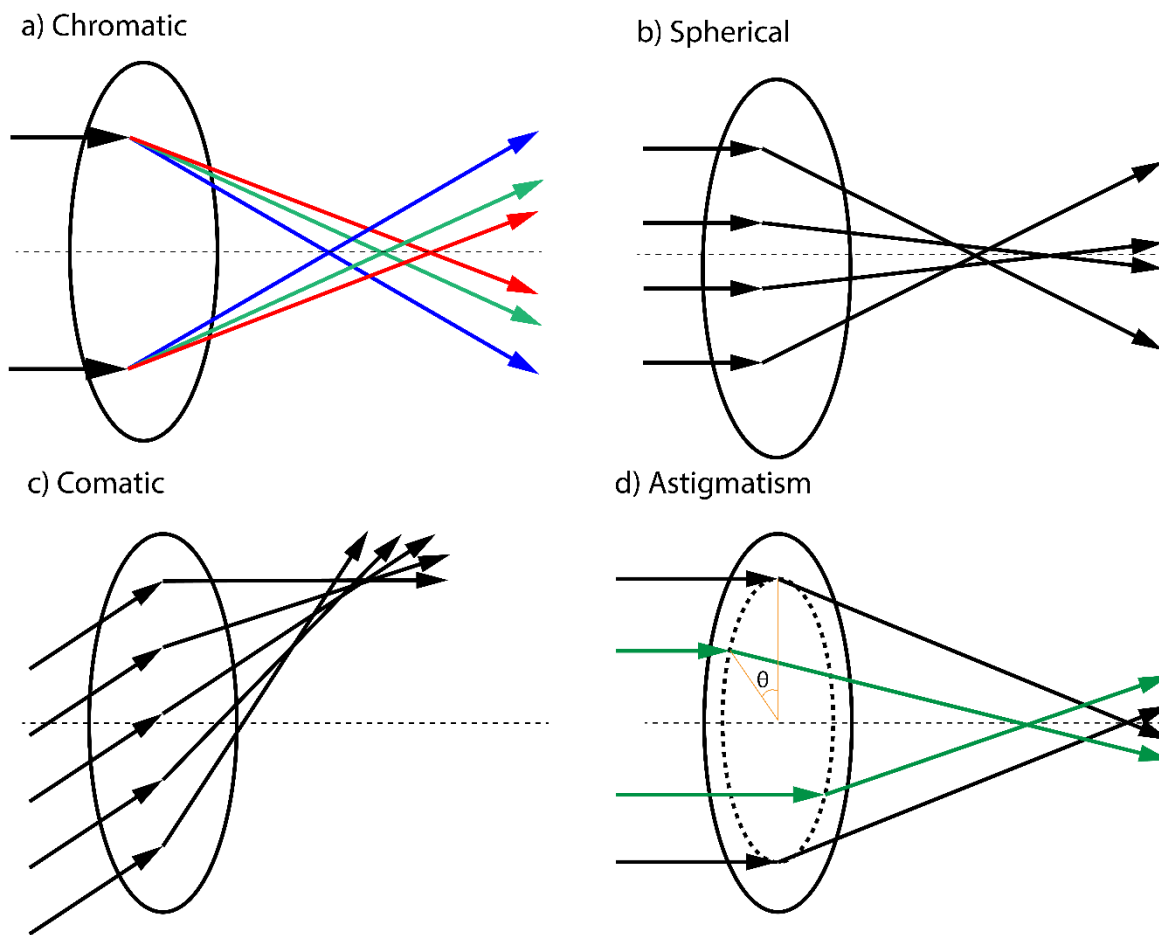


Figure 3.5 Illustrations of (a) chromatic aberrations, (b) spherical aberrations, (c) comatic aberrations, and (d) astigmatism.

EELS. There are two main ways to improve this. The first option is to use FEGs which have the smallest native energy spread. However, to achieve even better energy resolution and further minimise the chromatic aberrations a monochromator is necessary. A common location to monochromate the electron beam is just after the electron gun, and before they have been accelerated to their final voltage. The energy spread is reduced using e.g. Wien filters, which rely on orthogonal electric and magnetic fields. If the velocity/energy of the electron passing through the filter is the correct one it will be deflected and discarded. A potential drawback of monochromators is that they reduce the beam current. With modern FEGs, the final current is still sufficient for high quality imaging and analytical electron microscopy. It is possible for the lenses to introduce chromatic aberrations and correct them. However, this approach for correction is less straight forward to apply and not generally utilised.

Spherical aberrations arise when lenses have different focal lengths for electrons passing through the lens at different distances from the optical axis. The correction of spherical aberrations to a high order took a long time to develop, and is essentially achieved by an extra set of lenses, the aberration corrector, which introduces negative aberrations with respect to the other components to reduce the overall aberrations of the beam. The most commonly applied approach to this extent is to use systems which are not rotationally symmetric. Other potential approaches could rely on either time varying lenses or the absence of charges on the optical axis. The breaking of rotational symmetry is achieved by a combination of multipole lenses, the most common combinations being quadrupole-octupole or multiple hexapole correctors. The location of the corrector varies between TEM and STEM setups. TEMs use image correctors, located after the sample. STEM setups use probe correctors, which are located between the condenser and objective lenses. Some setups are equipped with both image and probe correctors, referred to as double-corrected, and are capable of both aberration corrected TEM and STEM. The operation of these correctors is usually aided by a software in order to achieve the fine level of tuning necessary.

Comatic aberration, also simply referred to as coma, stems from the incident electrons passing through a lens at an angle to the optical axis. In general, it is not the most prevalent of aberrations as most of the electron beam only deviates from the optical axis by small angles, and is simply accounted for by having the beam well aligned with the optical axis. However, coma can be prevalent in aberration correctors which utilise off-axis actions to tune the aberrations, and can be compounded by the different lenses in the

correctors. It is possible to adjust for this in aberration correctors by including an additional dipole lens to control the relative orientation of the lenses in the corrector.³⁴⁷

Astigmatism occurs when a lens is not perfectly radially symmetric. Due to imperfections in the focusing, the focusing power varies with the azimuthal angle (θ) as illustrated in Figure 3.5d. This was the first aberrations commonly corrected, and it is commonly achieved using a so-called stigmator, which is a weak quadrupole lens. These lenses need to be adjusted during operation, which is done by either rotating the quadrupole, or by adjusting the relative strength of the different components.

3.6 Imaging Modes

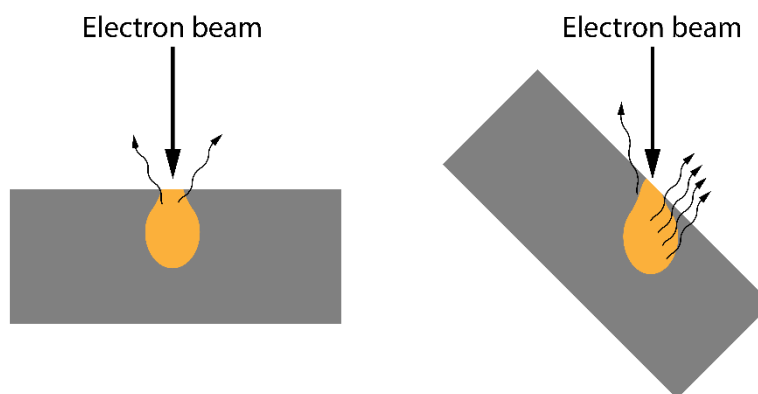


Figure 3.6 Illustration of the relative secondary electron emission on a flat surface (left) and tilted surface (right) due to the proximity to the surface of a larger fraction of the interaction volume being within the escape depth.

Imaging in SEM is achieved through the rastering of the electron beam and reading the signal of the detectors at each step to construct an image. Backscattered electron (BSE) images, relying on e.g. semiconductor detectors, will mainly observe composition contrast as the backscattering probability is mainly dependent on the atomic charge. Comparatively, secondary electron (SE) imaging is less sensitive to the composition, and instead mainly sensitive to the topography. The topography sensitivity is a consequence of the enhanced escape probability of SE if the interaction volume is closer to the surface, as illustrated in Figure 3.6. In a classical placement of the Everhart-Thornley detector, at the side of the chamber, there will still be some BSE incident on the detector, and its location relative to the sample results in a shadowing effect. The in-lens configuration, however, is not susceptible to any stray BSE or other electron sources. Furthermore, it does not introduce any shadowing due to its placement straight above the sample. Finally, as the interaction volume and escape depth of SEs are much smaller than those of BSEs, fundamentally it is possible to achieve higher spatial resolution using SE based imaging (few nm as compared to tens of nm).

Conventional TEM has three main imaging modes, namely bright-field (BF), dark-field (DF), and high-resolution (HR) imaging. BF and DF imaging mainly rely on diffraction contrast. In BF imaging, the areas which strongly diffract appear darker, while non-diffracting regions appear brighter. The opposite is true for DF imaging, where the brighter areas are the ones diffracting in the reflection selected by the objective aperture. Example BF and DF images of zinc phosphide nanopillars are shown in Figure 3.7a-b to illustrate the difference. BF conditions are achieved by introducing the objective aperture into the centre of the optical axis at the back-focal plane. If the aperture is sufficiently small, it will block any scattered electrons from contributing to the formation of the image on the detector. If the objective aperture is not centred on the main beam, but the beam is displaced in the horizontal plane so that it is centred on one of the diffracted beams instead, one achieves DF imaging conditions. In this scenario, the image is formed only by the electrons which were diffracted in the selected condition. Diffraction contrast is convenient to determine relative grain orientations in polycrystalline samples, size of grains, and if the Burger's vector of defects is perpendicular to the incoming electron beam it is also possible to distinguish them. However, care needs to be taken to claim that a sample is defect free, as one would need to sample all zone axes to assure this. In addition to diffractive contrast, attenuation of the electron beam when passing through the sample provides mass-thickness contrast to the final image.

HR-TEM imaging relies on phase contrast, which originates from the interference pattern of the exit wave due to coherent electron-matter interactions with the sample. For example, diffracted and un-diffracted electrons have a phase shift of 90° . Therefore, by either using a large objective aperture that allows for a subset of the diffracted beams to contribute to the image, or by simply not using an objective aperture at all, it is possible to acquire HR-TEM images. A representative image from zinc phosphide-indium phosphide interface is shown in Figure 3.7c. The detectors (e.g. CCD or CMOS cameras) cannot directly detect the phase of the electron.

Thus, the image recorded is that of the amplitude of the interference pattern. The final image is a function of the crystal structure, sample thickness, aberrations present and the defocus used through the contrast transfer function (CTF), an oscillatory function that defines how the spatial frequencies of the exit wave contribute to the image contrast formation. If the sample is sufficiently thin for the weak phase-object approximation to apply one can directly use the intensity transfer function. Ideally, for an interpretable image one wants a wide passband where the oscillatory CTF is relatively constant, as going from e.g. a negative to a positive value shifts the image from a black-atom to white-atom contrast (black-atom is generally preferred). Moreover, when the CTF is equal to 0 it means that there is no contrast, and information at this spatial frequency cannot be collected. The first time the CTF becomes 0 is known as the instrumental information limit as it becomes difficult to interpret the parts with missing spatial frequencies and inversed contrast. If one want to achieve the maximum amount of information in one image (i.e. widest possible passband and the lowest information limit), the ideal defocus, referred to as the Scherzer defocus, is a function of the acceleration voltage (wavelength of the electron used) and the spherical aberration.^{363,364} In the CTEM used in this project, FEI Talos working at 200 kV, the ideal defocus is -62 nm. Aberration-corrected instruments allow for the tuning of the spherical aberration, and can be used to achieve even lower instrumental information limits.

HR-TEM allows for convenient imaging of different grains and interfaces. Unfortunately, patterns are not always straightforward to interpret. If crystals are located on top of each other with respect to the imaging conditions with a slight misorientation, the resulting image will be a Moiré pattern of the superposition of the two separate patterns. Furthermore, the image is not an exact reconstruction of the lattice as it is not a direct imaging mode. To accurately interpret HR-TEM images it is common to compare the data against thickness-defocus plots, which can be modelled in software packages such as JEMS. The thickness cannot be readily controlled *in-operando*, hence the defocus is the variable parameter. An imaging series varying the defocus is known as a through-focus series.

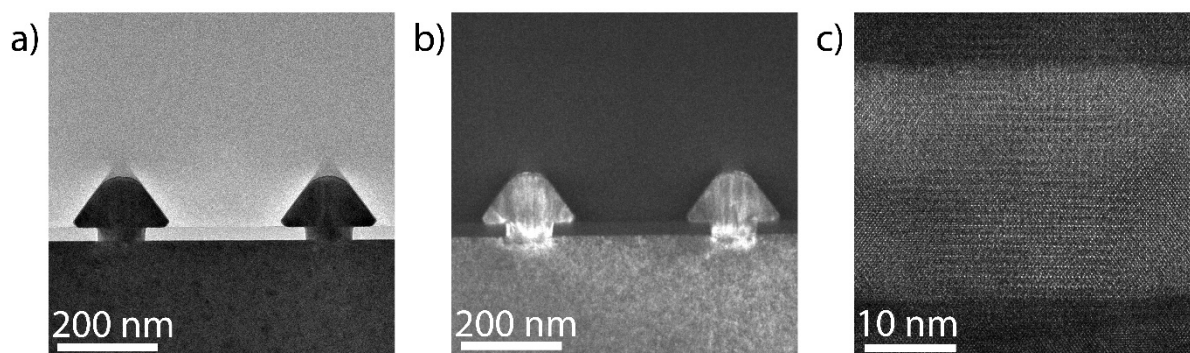


Figure 3.7 (a) BF-TEM image of two zinc phosphide nanopyrramids in cross section and (b) the corresponding DF-TEM image. (c) is a HR-TEM image of the interface between zinc phosphide and the substrate, indium phosphide.

The most common imaging modes in STEM involve annular detectors, such as annular DF (ADF) and annular BF (ABF). Depending on the angle used in ADF it is also split up into high-angle ADF (HAADF), medium-angle ADF (MAADF), and low-angle ADF (LAADF). HAADF is the most commonly used configuration, and images electrons which have been scattered at larger angles (~ 85 -200 mrad) due to Rutherford scattering. The incoherent nature of this scattering, and as annular detectors would average over several fringes, removes any phase sensitivity and the interference pattern observed in HR-TEM. The contrast depends instead on the atomic number, Z , of the imaged atom. A higher Z results in a higher signal on the HAADF detector. This gives excellent composition contrast, and in aberration-corrected microscopes it is even possible to directly image the individual atomic columns with elemental contrast.

A disadvantage of HAADF is that it can be difficult to image very light elements, particularly in the presence of heavier ones. MAADF on, the other hand, relies less on the Rutherford scattered electrons, but instead images using diffracted electrons, similar to normal DF imaging. MAADF gives information about boundaries, phases, and defects. BF-STEM produces an image which is essentially an inverse of the HAADF image, but it also includes phase contrast from the diffracted beams. ABF has also been developed recently.³⁶⁵⁻³⁶⁸ It has the smallest angle collection angle range (11-22 mrad) while excluding the central beam, and was first reported by Okunishi *et al.* as an approach to enhance imaging of light elements alongside heavy elements with a high dynamic range and achieving a non-oscillating transfer function.^{365,366} It gives complementary images to HAADF, albeit heavier elements appear darker instead of brighter, and has successfully been applied to image elements as light as hydrogen in materials.³⁶⁷ This imaging mode was initially achieved by covering the centre of a standard BF detector using a beam stop.³⁶⁵ Nowadays there are dedicated ABF detectors which facilitate simultaneous EELS and ABF imaging. It is also possible to use a HAADF detector for ABF if the camera length is increased sufficiently to change the collection angles to the correct range.

In short, electron microscopy offers a plethora of different imaging modes, allowing for microstructure and atomic scale analysis of materials. The main modes in SEM are SE and BSE imaging, which are more sensitive to topography and composition, respectively. TEM relies on diffraction contrast for BF and DF imaging, and phase contrast for HR-TEM. STEM imaging mainly utilises annular detectors, allowing for imaging of incoherent signals and for the direct visualisation of atomic columns. Furthermore, these setups are capable of acquiring additional analytical information, which will be described in the following section.

3.7 Analytical Electron Microscopy

Analytical electron microscopy allows the user to access information about the crystallography, composition, bonding, and optoelectronic properties of materials. Recent studies using cutting-edge equipment have even managed to perform vibrational spectroscopy in the electron microscope.^{323,369–372} This section will outline the techniques used in this thesis, and explain their origin and how they can be interpreted.

When the electrons interact with a periodic crystal structure it is possible for them to undergo Bragg diffraction under certain conditions. This is the main origin of contrast in BF and DF-TEM, however, it can also provide more detailed information about the crystal structure. Diffraction is the result of constructive interference at certain angles by reflected waves (e.g. electrons or photons) based on the electron energy/wavelength, the interatomic distances and the crystal symmetry. The general conditions for diffraction are summarised by Bragg's law:

$$\text{Equation 3.1} \quad 2d \sin \theta = n\lambda$$

Where d is the lattice spacing, θ is the angle of constructive interference (Bragg angle), λ is the wavelength and n is an integer representing the order of diffraction. However, not all planes will result in constructive interference. This depends on the crystal symmetry, and they are generally referred to as the systematic absences. These absences are determined by the structure factor:

$$\text{Equation 3.2} \quad F_{hkl} = \sum_{j=1}^n f_j \exp 2\pi i \left(\frac{hx}{a} + \frac{ky}{b} + \frac{lz}{c} \right)$$

The structure factor, F_{hkl} , determines the amplitude and phase of the diffracted beams, f_j is the element specific scattering factor of the j -th atom, h , k , and l are the Miller indices of the plane in question, a , b , and c are the lattice vectors, and x , y , and z are the coordinates of the atoms as a multiple of the lattice vectors. Visualisation of these conditions is simpler to achieve using the Ewald's sphere in reciprocal space, illustrated in Figure 3.8. In reciprocal space, the planes are represented by dots for a 3D structure. If the material is confined in one dimension, the dots will instead become lines due to the reciprocity, just as the case of reflective high-energy electron diffraction discussed in Section 2.2.2. The Ewald's sphere has a radius of $1/\lambda$ (where λ is the wavelength of the electron), and is centred on the sample while touching (0 0 0), which is the un-diffracted beam. The points which the sphere crosses are in a diffracting condition, and the corresponding wavevector is indicated through K_D in the figure. For simplicity it has been illustrated as a 2D section, but in reality it is a 3D sphere (as the name would suggest), and depending on the crystal structure it will result in a much more complex pattern.

In a TEM it is possible to observe the electron diffraction pattern by introducing a selective area (SA) aperture in the first image plane, and aligning the intermediate and projector lenses to project the diffraction pattern on the screen/camera. This diffraction pattern is called the selective area electron diffraction (SAED) pattern. There are two main type of patterns observed from crystalline samples, namely spot and ring patterns. The spot pattern indicates that the area determined by the SA aperture is a single crystal, and the symmetry is determined by the zone axis at which the crystal is observed. TEM holders are generally capable of tilting the grid to facilitate the orientation of the sample along a zone axis. Ring patterns are observed when multiple grains are encompassed by the SA aperture, and by measuring the distances from the centre it is possible to get the interplanar spacings, and consequently the lattice parameters. Furthermore, by investigating the systematic absences it is possible to gain more information about the crystal symmetry. To obtain accurate measurements it is preferable to use a calibration standard, which can be either a separate grid with a well-known sample, or it is possible to drop-cast nanoparticles with a well-known lattice structure on the grid with the sample (e.g.

gold nanoparticles). It is also possible to compare the pattern against simulated ones using e.g. JEMS. Other techniques capable of accessing this information include x-ray diffraction³⁷³ and Raman spectroscopy^{374,375}. The first technique is analogous to SAED, however, x-rays are used instead of electrons. Raman spectroscopy measures energy shifts in optical signals due to (anti-)Stokes scattering from phonon modes. The energy and symmetry of these lattice vibrations can also be used to elucidate the lattice structure and symmetry.

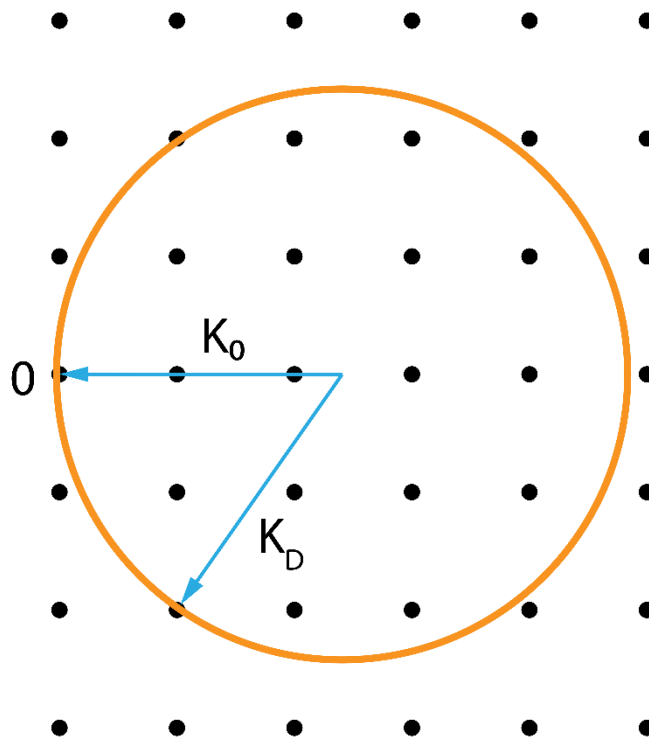


Figure 3.8 Illustration of a 2D slice of the Ewald's sphere, with 0 representing the non-diffracted beam, K_0 the non-diffracted wavevector and K_D the diffracted wavevector. Each dot represents a plane in reciprocal space.

The next analytical technique commonly used in electron microscopy is energy dispersive x-ray spectroscopy (EDX, sometimes (X)EDS). EDX is generally used in scanning modes, such as SEM and STEM, as it is then possible to acquire position dependent spectra. It is technically possible to do it in a standard TEM, however, the signal one would detect is the average of the whole illuminated area and is more susceptible to channelling artefacts if the sample is aligned to a zone axis.³⁷⁶ The EDX signal relies on the inelastic excitation of a core electron in the sample by the incoming electron beam as illustrated in Figure 3.9a. When an electron is excited to the vacuum level, an outer-shell electron will relax into its place. The relaxation transition will emit the change in energy as a photon in the x-ray spectrum. The exact energy of this photon can be used as a fingerprint of an element, as the transition energies are materials dependent. This effect can be used to map the composition of the sample by taking location dependent analysis, such as the EDX maps of an indium-catalysed zinc phosphide nanowire in Figure 3.9b. In SEM, the resolution of EDX maps is limited by the large interaction volume of the x-ray emission, which can be in the μm range. Lower acceleration voltages can reduce this volume, however, it also drastically lowers the x-ray emission and one will not be able to detect elements with characteristic transitions at higher energies. The achievable resolution in STEM however is much higher, and it is even possible to achieve atomic resolution in aberration corrected microscopes under ideal conditions. Generally, as the samples are much thinner than the interaction volume at the higher acceleration voltages typically used (60–300 kV), the limiting factor is the spread of the electron beam when interacting with the sample.

Furthermore, if the acquired spectra are treated correctly it is possible to quantify the composition. The main parameters to account for are the relative emittance of the specific elements, their absorption, and fluorescence in the x-ray region (ZAF correction). For example, lighter elements tend to emit less x-rays in favour of Auger electron emission. Although not common, there are dedicated setups for measuring these as a complementary method to EDX for the quantification of lighter elements. Absorption and fluorescence are generally not a problem in STEM measurements due to the thin nature of the samples, however, have to be corrected for in SEM or if relatively thick samples are measured. Absorption is an issue in thicker samples as the x-rays will travel through a material in which it can excite an electron and subsequently non-radiatively discard the energy, through for example vibrational excitations. Furthermore, the x-rays generated from one of the elements can excite another one, and it then emits x-rays in its characteristic energy (i.e. fluorescence), it will be overrepresented in the signal and needs to be accounted for. The final effect which needs to be

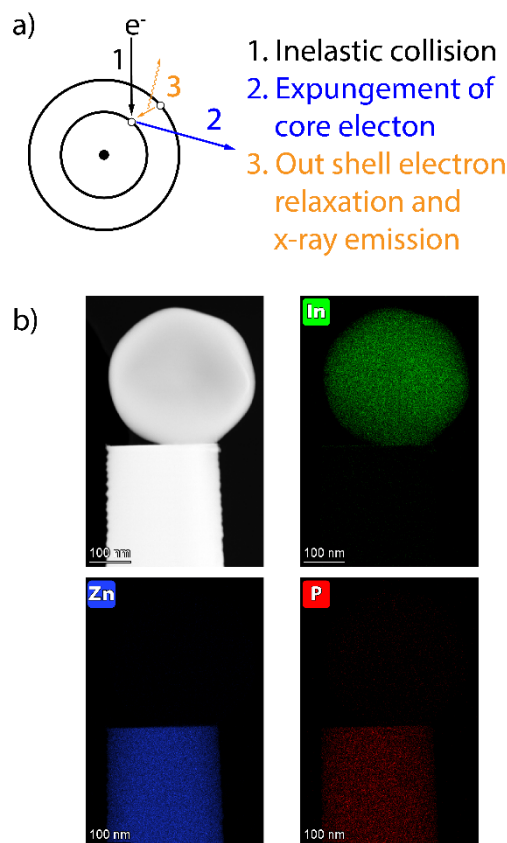


Figure 3.9 (a) Illustration of the characteristic x-ray generation process and (b) HAADF-STEM and EDX maps showing the tip of an indium-catalysed vertical nanowire with the solidified droplet balancing on top.

taken into account is Bremsstrahlung (“breaking radiation”), which is a continuous background of x-rays generated when the primary electrons have inelastic collisions where they change direction, and for the conservation of energy and momentum and x-ray is emitted to make up for the change. The most common approach to use for quantification is the Cliff-Lorimer model, which relies on the comparison of the data with a sample of known composition by a proportionality factor known as the k-factor, calculated from previous experiments or theoretical models. Modern software packages, such as Velox, Digital Micrograph, or INCA, can reference to their databases to facilitate this process. For example, Velox can produce accurate quantifications of the selected elements using the density and thickness of the sample as input. However, the accuracy of EDX is usually in the order of a few percent, and it is not sensitive down to the levels needed to detect dopants in semiconductors. Other techniques, such as secondary-ion mass spectroscopy (SIMS) or APT, can achieve this level of accuracy.^{330,332,333} Unfortunately, SIMS and APT are destructive, as they break apart the sample in order to analyse it.

EELS is a versatile technique which measures inelastic interactions between the electron beam and the sample. EELS can be carried out in both STEM and TEM setups. There are two main regions of an EEL spectrum, namely the core-loss and low-loss regions. Core-loss EELS is very similar to EDX, however, it looks at the energy change of the electrons in the probe as they inelastically excite the core electrons in the elements. Elements have characteristic peaks, called edges in EELS as they have an onset energy and a non-gaussian shape. Fitting of the onset energy allows the peak identification and quantification using e.g. Digital Micrograph. In STEM it is possible to use this effect to map the composition with atomic resolution in aberration corrected microscopes.³²² Furthermore, the tail regions of the edges contain information of the oxidation state and chemical environment of the different species. This part of the signal is not straightforward to interpret, and significant modelling needs to be performed to validate any analysis. An analogous technique using synchrotron x-rays is x-ray absorption near edge structure (XANES) analysis.^{377,378}

Low-loss EELS is a technique which has been increasingly applied with the advent of aberration correctors and monochromators. The precise alignment and small energy spread allow for energy resolutions down to a few to tens of meV in EELS measurements. The first features investigated in the low-loss region, as they were distinguishable before meV resolution, were surface electronic excitations such as plasmons.^{379–382} Plasmon excitations can be used to determine what type of material observed (e.g. metals tend to have much sharper plasmon peaks), and by looking at the excitation energy one can determine the composition by comparing to previously acquired data. However, as plasmons are delocalised it is not possible to achieve the same compositional mapping resolution as core-

loss EELS. Nowadays, high-end setups have small enough zero-loss peaks (ZLP) to resolve the excitation of valence electrons to the conduction band, making it possible to investigate the transition energies of semiconductors with increasingly smaller bandgaps.^{383–389} This analysis is called valence EELS (VEELS), and allows for the direct investigation of local fluctuations in the bandgap down to the nm scale, not achievable by other means. Furthermore, the resolution has now been pushed to the point where spectroscopy of vibrational modes using electron microscopy has become feasible.^{323,369–372} While significant data treatment and analysis are necessary for accurate interpretations, the advances in EELS through the development of monochromators and aberration correctors is opening up new and interesting fields of analytical electron microscopy.

The last analytical electron microscopy technique covered here is cathodoluminescence spectroscopy (CL). CL has the capacity to create spatial maps of the optical bandgap of semiconductors down to the nanoscale.^{349,390} It is possible to determine the nature of the optical recombination observed by altering the excitation power, and plotting the integral of the emitted signal versus excitation power on a log-log plot.^{391,392} If the exponent is larger than one the recombination is related to a direct bandgap, while if it is below one it is either a defect transition or an indirect bandgap.³⁹¹ CL has also been used to determine the defect density, such as threading dislocations in gallium nitride, which act as non-radiative recombination centres.³⁹³ SEM-CL setups tend to have better outcoupling of the emitted light as they have more space around the sample to collect the light from, as compared to STEM-CL which typically has a small optical fibre collecting the signal. CL is often compared to photoluminescence spectroscopy (PL). PL utilises a laser to excite the charge carriers in the sample, and can generally achieve higher energy resolution. The advantage of CL is its high spatial resolution, limited only by the diffusion length of the charge carriers, while the spatial resolution in PL is limited by the focusing capabilities of the setup.

3.8 Summary

Electron microscopy is a versatile tool to image and analyse samples down to the atomic scale. Inorganic semiconductor nanomaterials are readily investigated by electron microscopy, as they either fulfil, or can easily be made to fulfil, all the sample requirements, i.e. electron transparent and conductive. Electron microscopy is ubiquitous in material science, in this work it will be used to gain information about the microstructure, crystallography, composition, optoelectronic properties, chemistry of the zinc phosphide nanostructures through the techniques listed in this chapter. With the invention and development of aberration correctors and monochromators it is now possible to perform this analysis down to the atomic scale, and the possible areas of application of electron microscopy analysis are constantly expanding.

Chapter 4 Vapour-Liquid-Solid Growth of Zinc Phosphide

Zinc phosphide nanowires constitute a promising building block for earth-abundant photovoltaics, however, they are yet to be grown epitaxially. This chapter will focus on the growth and characterisation of various types of zinc phosphide nanowires epitaxially grown on indium phosphide substrates using a vapour-liquid-solid (VLS) approach.

For this publication I performed the growth, scanning electron microscopy, substrate preparation, conventional transmission electron microscopy (TEM), scanning (S)TEM, STEM energy dispersive x-ray spectroscopy (EDX) measurements, and cathodoluminescence spectroscopy. I also performed the data analysis of the data generated from these measurements in addition to the aberration corrected high-angle annular dark-field (HAADF) STEM data. Finally I wrote the manuscript, which was then completed with the input of all co-authors.

The first structures presented in this chapter were grown two years after the start of my PhD after a long and bumpy installation process of the new molecular beam epitaxy system. First we tried gold as the catalyst. We quickly realised that the gold would, depending on the manipulator temperature, either react with the indium phosphide substrate to create micrometre sized droplets, or simply not act as a growth catalyst. However, we did notice the growth of nanowires between the gold particles, and through STEM-EDX we observed that they were indium catalysed. The indium came from the zinc flux reacting with the substrate, forming the nano-droplets necessary for VLS growth. By tuning the surface defects/reaction sites we could in turn tune the nanowire density.

Once we had achieved epitaxial nanowire growth we could start exploring the system in more detail. As an old school explorer we started off by mapping out the area (parameter window for growth) and discovered a plethora of different morphologies of zinc phosphide nanowires. We observed that the morphology is dependent on the growth parameters (temperature and precursor fluxes), and it could even be used to tune the composition of the nanowires. We explored the growth and structure of the different nanowires, and lastly we looked at the effect of composition and morphology on the optoelectronic properties.

To better understand the thermodynamics at play during growth we collaborated with Dr Masoom Ghasemi at Thermo-Calc Software AB to model the Zn-In-P ternary phase diagram using the CALPHAD method. It showed that in our expected regions we did indeed have a liquid phase (catalyst) and a solid zinc phosphide phase (product). With the aid of Dr Thomas LaGrange and Dr Reza R. Zamani, my co-supervisor, at the Interdisciplinary Centre for Electron Microscopy (CIME) at EPFL we also delved deeper into the structural aspects of the material using aberration corrected HAADF-STEM and STEM EDX. We observed how the off-stoichiometric composition could alter the pattern we observe, and that some of the indium catalyst breaks off during growth. The indium would go to the surface of the nanowire where it would form indium phosphide nanoclusters. The removal of indium also explains the tapering we observe on all nanowires, as the catalyst size and nanowire diameter are directly related.

The cryogenic temperature cathodoluminescence spectroscopy of zigzag and vertical nanowires showed two different recombination pathways for the different morphologies. While slightly greater than the previously reported values, the energy difference closest to that observed for the zigzag nanowires is the one previously attributed to phosphorus interstitials, which is feasible due to their phosphorus-rich stoichiometry. The emission from the vertical nanowires varied depending on the composition, but the emission is in the range of those reported in the second column in Table 1.1. However, their exact origin of this peak is yet to be determined.

With this work, we reported the epitaxial growth of zinc phosphide nanowires for the first time. We demonstrate the growth of highly crystalline and tuneable nanowires. While there is room to improve the functional properties, through for example passivation studies, this is a concrete first step towards the application of zinc phosphide nanowires for photovoltaic applications.

The content of this paper, published in *Nanoscale Horizons* (Vol. 5, p. 274-282, 2020) under a Creative Commons Attribution-Non-Commercial 3.0 Unported Licence, has been edited to match the format of this thesis with references combined with those at the end. The content and figures have been reproduced here without modification with the permission of the Royal Society of Chemistry. The supporting information can be found in Appendix A.

4.1 Multiple Morphologies and Functionality of Nanowires made from Earth-Abundant Zinc Phosphide

Simon Escobar Steinvall, Nicolas Tappy, Masoom Ghasemi, Reza R. Zamani, Thomas LaGrange, Elias Z. Stutz, Jean-Baptiste Leran, Mahdi Zamani, Rajrupa Paul, Anna Fontcuberta i Morral

4.1.1 Abstract

Semiconductors made of earth-abundant elements, such as zinc phosphide, have the potential to substitute less abundant, highly functional compound semiconductors such as InAs or InP. Compound semiconductors in the form of nanowires could revolutionise application areas such as energy harvesting and optoelectronics. Here we synthesise Zn_3P_2 nanowires tailored in four different morphologies, namely vertical, straight-titled, zigzag and crawling. The optical properties elucidated by cathodoluminescence spectroscopy indicate a shape and V/II ratio dependence. Band-edge, defects, or surface nanoclusters mediate the luminescence in different degrees. This work opens new avenues for the use of earth-abundant Zn_3P_2 nanowires in photovoltaic applications.

4.1.2 Introduction

Zinc phosphide (Zn_3P_2) is an earth-abundant semiconductor with optoelectronic properties suitable for photovoltaic applications.^{81,394} It exhibits a direct bandgap of roughly 1.5 eV, strong absorption in the visible range of the electromagnetic spectrum, and carrier diffusion lengths in the order of 5-10 μm .^{55,57-61} Despite its promising properties, there has been limited progress in the fabrication of high-quality zinc phosphide devices. The highest photovoltaic conversion efficiency achieved using a Zn_3P_2 absorber was ~6%, which was achieved several decades ago.⁶² There are three main challenges with the processing of this earth-abundant semiconductor, the first being its large tetragonal unit cell ($a=8.089 \text{ \AA}$, $c=11.45 \text{ \AA}$), complicating epitaxial growth.³⁹⁵ The second arises from its high thermal expansion coefficient ($1.4 \times 10^{-5} \text{ K}^{-1}$) which introduces strain and defects upon cooling after growth.^{73,74} The final challenge involves achieving controllable doping. Most growth techniques result in intrinsic p-type doping through phosphorus interstitials. Extrinsic doping, particularly n-type, is not yet fully unravelled.^{71,76,119}

To overcome these challenges, the nanowire morphology shows promising perspectives. First, their small diameter allows for high-quality epitaxial growth on lattice mismatched substrates through radial stress relaxation.^{222,226,231} These factors mitigate the challenges posed by II_3V_2 's large lattice parameter and coefficient of thermal expansion, facilitating virtually defect-free epitaxial growth.^{331,396} Moreover, vertical nanowire arrays exhibit photonic properties enabling increased light absorption with respect to the equivalent thin film.^{167,225,249,252,253,256,397-399} This is a consequence of their enhanced absorption cross-section, and modification of light emission directivity. Altogether, this modifies the Shockley-Queisser limit, resulting in a higher theoretical efficiency for nanowire devices compared to planar ones.^{167,225,249,252,253,256,397-399}

In this work, we demonstrate the growth of Zn_3P_2 nanowires in tailored morphologies using molecular beam epitaxy (MBE). The use of MBE lowers growth temperatures in comparison to other techniques used to obtain Zn_3P_2 , such as chemical vapour transport in a quartz ampule and metal-organic chemical vapour deposition.^{73,89,99,106} The lower growth temperature should significantly reduce the number of grown-in defects induced by strain from differential thermal expansion. Furthermore, by varying the V/II flux ratio in the MBE, the composition of thin films can be adjusted precisely. This is the key to control the density of self-interstitials, which readily form due to the high number of large vacant sites in the zinc sublattice, and thus the degree of intrinsic doping due to deviations from stoichiometry.⁸⁹ In principle, the precise flux control in MBE should also enable the controlled incorporation of extrinsic dopants such as Ag, Mg and In.^{75,76,79,119,144}

Previously, in addition to thin films and bulk crystals, Zn_3P_2 has been obtained in the form of randomly oriented nanowires, nanoribbons, and nanotrumpets.^{100-102,128,130,143,151,400} In most of these studies, nanowires were produced through chemical vapour deposition (CVD) or by a thermochemical method relying on a quartz capsule containing the precursors being heated in a furnace.^{100,101,128,130,143,151} Both of these techniques result in a nanowire powder consisting of randomly aligned nanowires not attached to a substrate. To achieve the 1D nanowire morphology, researchers have mainly relied on the vapour-liquid-solid (VLS) growth mechanism, where a nanoscale liquid catalyst is used to guide 1D growth through enhanced precursor absorption and selective, directional precipitation upon supersaturation.²¹⁹ The catalysts previously reported for zinc phosphide nanowire growth are gold, indium and tin.^{101,128,130,143,260} Whilst gold catalysed nanowires tend to be straight, those grown with indium and tin exhibited a zigzag morphology.^{101,128,143,260} Similar superlattice structures have also been reported for other compound semiconductors. According to Algra *et al.*, twinning minimises the deformation of the droplet on the top facet when the cross-section reaches a truncated triangular geometry, and turns it back to a hexagon.^{236,242,401}

Proper selection of the substrate with suitable crystal structure can promote epitaxial growth. InP (100) has been proposed as a suitable substrate due to the low mismatch between the phosphorus sublattices. It also avoids the formation of an interfacial phosphide, as was observed on GaAs.^{107,129}

Here, we report the epitaxial growth of zinc phosphide nanowires by MBE, in various morphologies. To the best of our knowledge, this is the first report on the growth of tuneable epitaxial Zn₃P₂ nanowires by MBE.

4.1.3 Results and Discussion

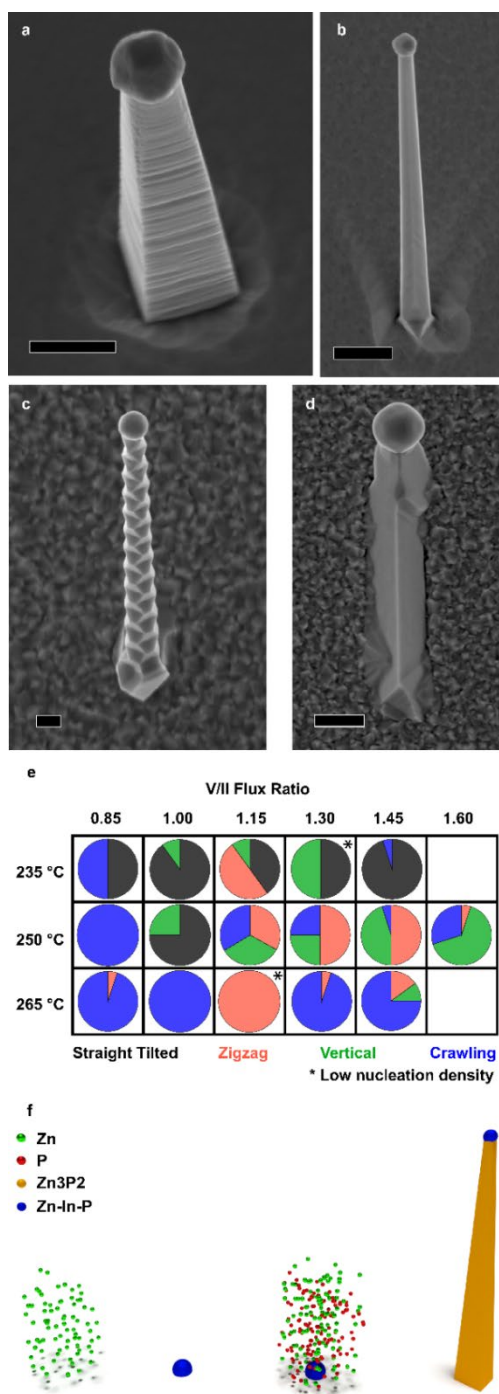


Figure 4.1(a)-(d) are SEM images of vertical, straight-tilted, zigzag and crawling nanowires with scale bars of 500 nm. The first image is at 20 °, whilst the others are normal to the substrate. (e) shows the growth condition and manipulator temperature combination which resulted in what morphologies and (f) is an illustration of the proposed growth mechanism.

$\text{Zn}_{3-x}\text{P}_{2+y}$ nanowires were obtained in 4 different morphologies on InP (100), which we denominate as vertical, straight-tilted, zigzag, and crawling. Scanning electron microscopy (SEM) images of the different morphologies are presented in Figure 4.1a-d, respectively, with lower magnification images included in the supplementary information. The vertical nanowire morphology is ideal for potential photovoltaic applications because of their enhanced light absorption mentioned previously. Figure 4.1e maps the different morphologies yielded as a function of the different growth conditions, i.e. manipulator temperature and V/II ratio. From here on, the reported V/II ratio corresponds to the ratio between the values of Zn and P_2 beam equivalent pressures (BEPs). There is some overlap between the morphologies yielded, but the overall trends are as follows: at lower temperatures, the straight-tilted morphology dominates. At higher temperatures, on the other hand, the dominating morphology is the crawling nanowires, which is also the main type of wires for low V/II ratios. The zigzag nanowires grow mainly at moderate temperatures at intermediate V/II ratios, and the vertical morphology is similarly favoured at moderate temperatures, being the dominant morphology in the higher V/II ratio range. When the V/II ratio exceeds 1.6, a thin film overgrowing the nanoparticles is observed, as shown in the supplementary information.

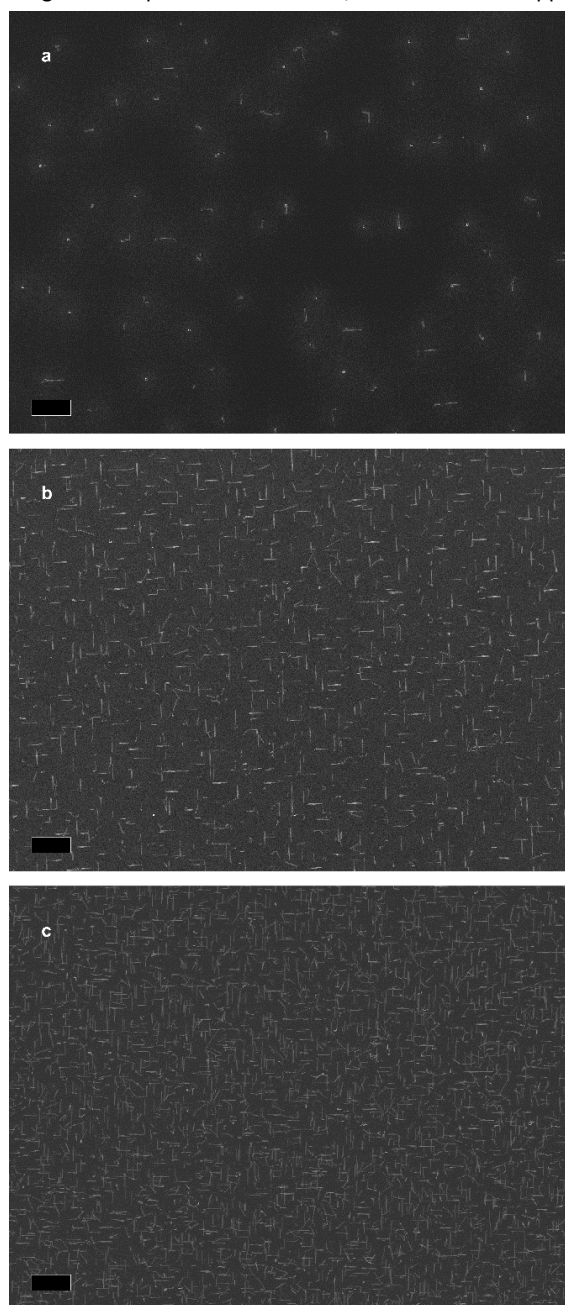


Figure 4.2 (a)-(c) are SEM images of nanowire ensembles obtained after 0 s (a), 5 s (b), and 10 s (c) argon ion beam exposure respectively. We observe an increase in nucleation density of 16x and 82x with respect to (a). All scale bars are 10 μm .

The vertical nanowires exhibit a significant surface roughness, which generally can be attributed to the presence of stacking faults. However, as it will be shown, this is not the case. Im *et al.* investigated Zn_3P_2 nanowires grown by either Au or In catalysed VLS, and they observed the formation of superlattices only in the latter.¹²⁸ Similarly, Shen *et al.* also reported the formation of superlattice nanowires only when growing using an In catalyst.¹⁰¹ However, from this study it is clear that it is possible to achieve different morphologies by simply tuning the growth conditions and not the catalyst.

Figure 4.1f illustrates the proposed growth mechanism of the nanowires. First, during the pre-deposition step, the zinc flux reacts with the indium phosphide substrate, forming a Zn-In-P nanoparticle, shown in the supplementary information. This acts as the liquid-phase catalyst for VLS growth during the subsequent growth step, resulting in the so-called substrate-mediated VLS growth. It is worth mentioning that the nanowire density of most samples remained constant irrespective of the growth condition. We suspected that In droplets would form preferentially at surface irregularities. To test this hypothesis, we exposed the substrates to short Ar ion beam treatments to increase the surface roughness and/or irregularities. Representative SEM micrographs of samples exposed for 0, 5, and 10 s are presented in Figure 4.2a-c. The nanowire density increases by a factor of 16 and 82 times, respectively, reaching a nanowire density of 1 nanowire per $2.4 \mu\text{m}^2$.

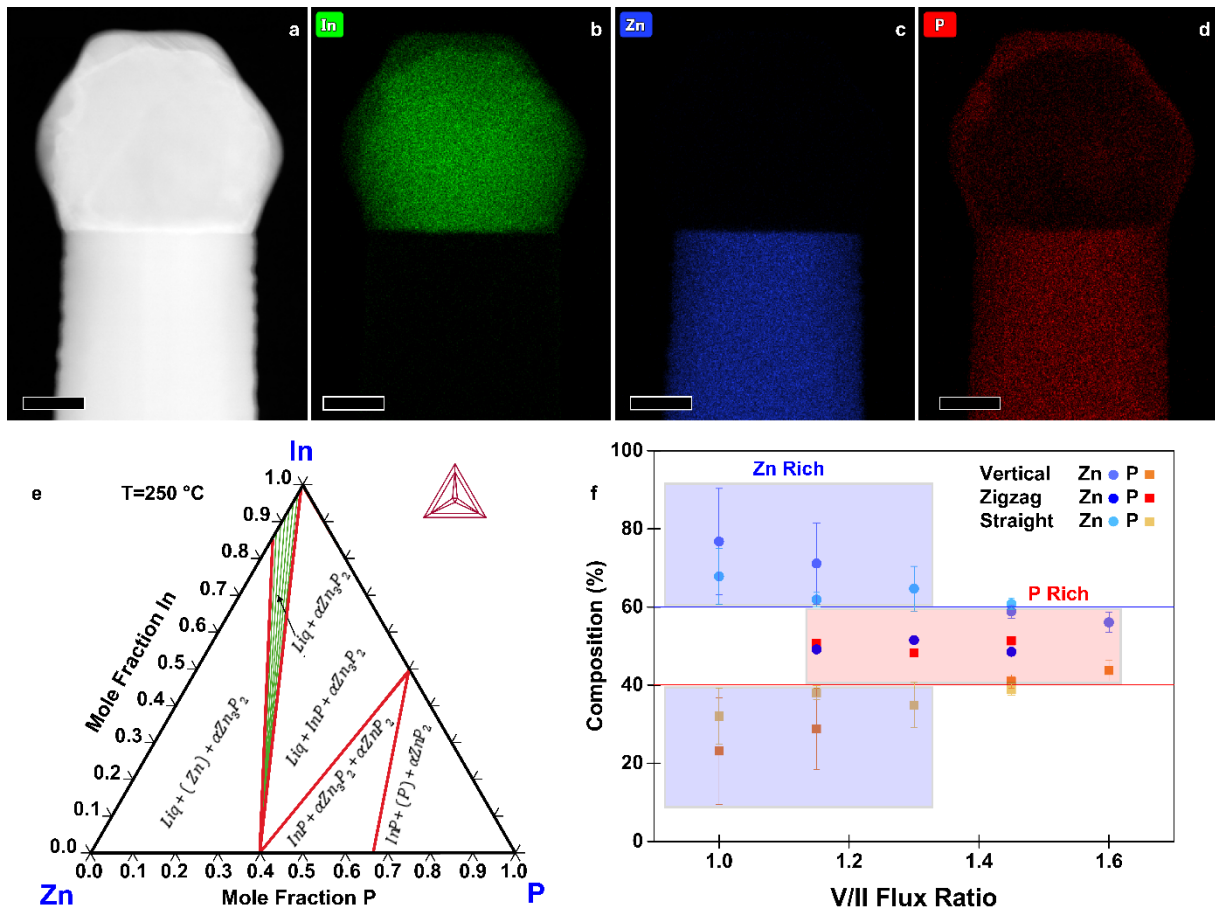


Figure 4.3 (a) HAADF STEM image of the top of a vertical nanowire. (b)-(d) corresponding elemental map of indium, zinc and phosphorus. All scale bars are 50 nm. (e) shows the ternary phase diagram of the Zn-In-P system calculated using the CALPHAD method at 250 °C. (f) shows the deviation from stoichiometry of vertical nanowires grown at different V/II ratios. The straight lines indicate the ideal stoichiometry. The vertical and zigzag nanowires were grown at 250 °C, whilst the straight-titled ones were grown at 235 °C.

To support the proposed growth mechanism, we performed scanning transmission electron microscopy (STEM) energy dispersive x-ray spectroscopy (EDX). Representative measurements of a nanowire tip are shown in Figure 4.3a-d. The main component of the droplet is indeed In. The faceted nature of the catalyst indicates that at room temperature, where the STEM EDX measurements were carried out, the catalyst is solid.

To further elucidate the mechanisms at play we provide an understanding of the thermodynamic Zn-In-P system, obtained by the CALculation of PHase Diagrams (CALPHAD) method.⁴⁰² In the CALPHAD method, the Gibbs energies of the phases are modelled using experimental data as input. The equilibrium phase diagram is then mapped by minimisation of the Gibbs energies of the phases for

all temperatures. One then finds the corresponding compositions of the phases with the lowest Gibbs energy. Although nanowire growth is a non-equilibrium process, thermodynamic diagrams provide information on what equilibrium phases can be obtained. The isothermal section of the Zn-In-P ternary phase diagram at 250 °C is presented in Figure 4.3e. When adding Zn to InP, one moves into a tie triangle with liquid, InP and Zn_3P_2 phases present. The vertical section between Zn and InP, shown in the supplementary information, indicates that a liquid phase is present above 156.3 °C. Below this temperature it undergoes an invariant transition, first forming Zn_3P_2 until the zinc in the droplet is consumed, which would preferentially nucleate at the interface of the already grown nanowire. The remaining In and P will then form an In (core) and InP (shell). These observations allow us to determine that our catalyst is indeed liquid during growth, and to explain the segregation observed in the catalyst at room temperature.

We now turn to the characterisation of the chemical composition of the nanowires as a function of the growth conditions and morphology, as measured by STEM EDX. The average composition of vertical, zigzag, and straight-tilted nanowires grown at different V/II ratios is presented in Figure 4.3f, with the solid lines indicating the stoichiometric composition. The measurements were done for a rectangular section of an area approximately $100 \times 100 \text{ nm}^2$ and corrected for the thickness of the individual nanowires. Moreover, to accurately correct for the varying thickness of the zigzag nanowires, a polygon was used instead of a rectangle to cover an area of approximately constant thickness, and the measurements were taken using aberration corrected (AC) STEM. Low V/II ratios resulted in Zn-rich $\text{Zn}_{3-x}\text{P}_{2+y}$ nanowires. The increase in P_2 flux improves the homogeneity in composition and increase the P content, with the nanowires grown at a V/II ratio of 1.45 being closest to the stoichiometric composition. This sets MBE grown zinc phosphide apart from other growth techniques, which predominantly result in P-rich products.^{71,99} STEM EDX data of straight-tilted nanowires grown at 235 °C showed a similar trend. The zigzag nanowires, on the other hand, exhibit a 1:1 ratio between Zn and P irrespective of the V/II ratio during growth. The composition along the nanowire did not change within the uncertainties of the measurement technique, as shown in the supplementary information.

Growth temperatures below 235 °C result in randomly oriented nanowires, lacking a clear epitaxial relation with the substrate. Furthermore, in this temperature range, we observed nanowires with and without a droplet at the tip, indicating the possible coexistence of the previously mentioned VLS growth mechanism with a vapour-solid (VS) one. These nanowires presented a growth front consisting of exposed facets, similar to what is also found in GaAs.³⁰² SEM images of these nanowires are presented in the supplementary information.

Transmission electron microscopy (TEM) data for zigzag, straight-tilted, and vertical nanowires are presented in Figure 4.4. Selective area electron diffraction (SAED) showed that all nanowires, irrespective of composition and morphology, have the $\text{P4}_2/\text{nmc}$ crystal structure, characteristic of Zn_3P_2 . Due to the thickness of vertical nanowires, they could not be characterised through high resolution (HR) TEM. However, SAED pattern analysis (Figure 4.4m) indicates that the vertical nanowires have a [001] growth direction, whilst both zigzag and straight-tilted nanowires grow along the [101] direction (Figure 4.4d, i). The [101] growth direction was also observed by Shen *et al.*, Brockway *et al.*, and Im *et al.*^{101,128,400} However, Im *et al.* also observed a [201] growth direction for their superlattice nanowires, and other studies have shown zinc phosphide nanowires growing along multiple other directions.^{101,128}

HRTEM images from the zigzag nanowires (Figure 4.4b-c) clearly show the superlattice structure. Structural defects were observed in the zigzag and straight-tilted nanowires (Figure 4.4g-h). All structural defects observed in these nanowires were perpendicular to the [001] direction, and not to the growth direction. There was no preferential ordering observed in the frequency of these structural defects, indicating a more random generation mechanism as compared to the superlattices. A straight-tilted nanowire was also observed along the [111] zone axis, with the images presented in the supplementary information. The defects were not observed along this zone axis as the Burgers vector of the defect and zone axis were not perpendicular.

In the case of the vertical nanowires, we were unable to determine the presence of structural defects through HRTEM investigations. A vertical nanowire obtained with a V/II ratio of 1.00 was investigated using AC high-angle annular dark field (AC-HAADF) STEM. In Figure 4.4e, the bulk atomic arrangement as seen along the [100] zone axis of Zn_3P_2 is shown, with a zoomed out image presented in the supplementary information. By comparing it with simulated HAADF STEM images along the [100] zone axis for different compositions in the Zn-rich range, presented in the supplementary information, we confirm the [001] growth direction, in agreement with the SAED pattern in Figure 4.4m. Furthermore, in low magnification images with the same resolution, we did not observe any stacking faults. The changes in the diameter of the nanowire around non-observed stacking faults may still explain the observed roughness, however, catalyst related effects are more probable.

Another aspect to note is that all nanowires exhibit tapering. There are two main mechanisms that result in tapered growth, either through the morphing of the catalyst or VS growth on the exposed facets. There are multiple pathways for the catalyst to shrink, and as the In catalyst is not replenished, its depletion during growth is an irreversible process. For example, In may evaporate. Given its low vapour pressure at the growth temperatures, we consider this an unlikely scenario. A more probable case is that the In catalyst

is consumed during growth. In could potentially diffuse to the large vacant sites in the Zn_3P_2 lattice or to surface sites, depleting the In in the catalyst, and in turn reducing the nanowire diameter. We have indeed observed the presence of Zn_3P_2 VS growth on the side facets, however, we cannot rule out any catalyst related effects.

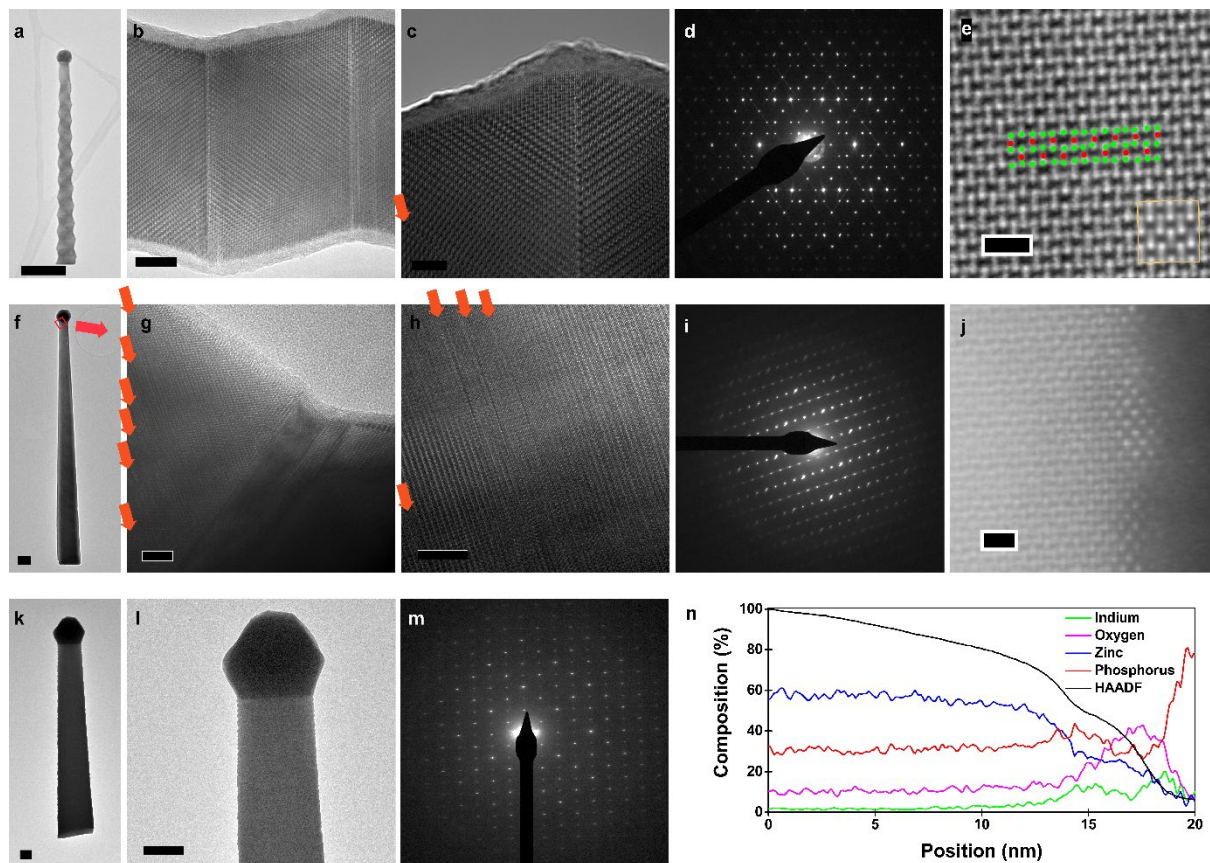


Figure 4.4 (a)-(d) HRTEM images of a zigzag nanowire grown at a V/II ratio of 1.30 at different magnification highlighting the superlattice formation along the growth axis and the superimposed SAED pattern along the $[100]$ zone axis indicating a $[101]$ growth direction. (a) is rotated 90° with respect to the other images. (e) shows a AC-HAADF STEM image inside a vertical nanowire, grown at a V/II ratio of 1.00, nanowire with an overlay of the zinc and phosphorus atoms as matched with the crystal structure as seen down the $[100]$ axis (zinc is green and phosphorus red) alongside with an inset of the simulated structure. (f)-(i) are HRTEM and SAED images of a straight-tilted nanowire grown at a V/II ratio of 1.00 as seen along the $[100]$ zone axis, indicating a growth direction of $[101]$, note, e is rotated 120° in relation to the other images. (j) is an AC-HAADF STEM image of the surface of a vertical nanowire. (k)-(m) TEM images and the SAED pattern of a vertical nanowire along the $[100]$ direction, indicating a growth direction along $[001]$. (n) is the corresponding STEM EDX line scan going from the bulk (0 nm) to the surface and vacuum (20 nm). Scale bars in a, f, k, and l are 200 nm. In b, g and h the scale bars are 10 nm, in c it is 5 nm, and finally in e and j they are 1 nm.

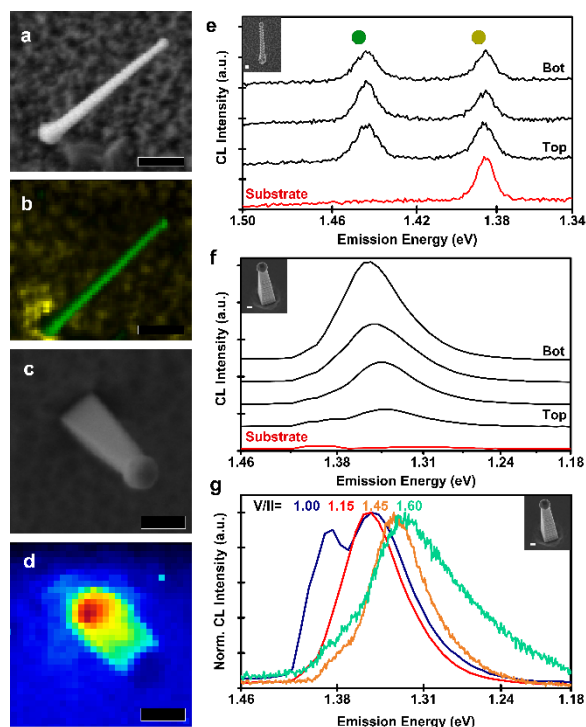


Figure 4.5 (a) is a SEM image of the zigzag nanowire analysed, and (b) shows a colour specific emission map of the zigzag nanowire, where green indicates the Zn_3P_2 emission whilst yellow is the background, InP, emission. (c) is a SEM image of a vertical nanowire grown at a V/II ratio of 1.15. (d) is an intensity map of the emission, showing higher intensity at the base of the nanowire. (e) is the spectra observed at different parts of the zigzag nanowire and also indicates the peak colouring in (b). (f) shows the spectra taken from the different parts of the vertical nanowire in (c), and (g) shows normalised emission spectra from vertical nanowires grown at different V/II ratios. All scale bars are 500 nm.

To ascertain if these processes occurred, we analysed the surface of the vertical nanowire using AC-HAADF STEM and EDX. Small clusters with a different crystal structure were observed scattered along the surface, as shown in Figure 4.4j. Through an EDX line scan perpendicular to the surface in the aberration corrected HAADF STEM, Figure 4.4n, we observed that the surface layer was enriched in indium. There were also significant amounts of phosphorus and oxygen present in these clusters. The symmetry of the AC-HAADF pattern, indicating a [110] zinc-blende zone axis, and their composition suggest that In diffuses from the main catalyst to the surface of the nanowire during growth, reacting with the phosphorus flux, and generated InP nanoclusters. These clusters, and the overall surface of the nanowires, were covered by an amorphous oxide layer created during unloading from the MBE and exposure to air, as confirmed by the EDX line scan data shown in Figure 4.4n. There is a sharp increase in phosphorus at the end of the line scan, but by correlating it to the HAADF intensity, we can deduce that it is an artefact of the quantification as the scan goes into the vacuum. To better understand the structure and distribution of these clusters, we applied fast Fourier transforms (FFT) and filters based on the symmetry to AC-HAADF STEM images, highlighting areas of different crystal symmetry (see supplementary information). By adjusting the focus along the surface, we noted that some clusters were only observed at different focal depths, indicating a random and incomplete coverage of the surface with InP. Thus, we can deduce that the mechanism behind the consumption of In is through the formation of surface InP nanoclusters.

The tapering of the nanowires in itself is not an issue for photovoltaic applications; on the contrary, the range of diameters in a single nanowire allows the interaction between the nanowire optical absorption modes with an increased range of wavelengths.^{251,257,403–405} However, the nanoclusters may still act as a sink for either holes, electrons, or both depending on the alignment of the quantum dot energy level with the $\text{Zn}_{3-x}\text{P}_{2+y}$. Therefore, the nanoclusters may greatly influence the optoelectronic properties of the nanowires by selectively repelling one type of charge carrier whilst acting as a sink for the other, effectively quenching the luminescence. Still, they can potentially be removed by selective chemical etching. The tapering due to droplet reduction could be mitigated through an In flux of roughly $2\text{--}3 \text{ \AA s}^{-1}$, based on direct impingement similar to self-catalysed III-V nanowire growth.^{269,270}

Finally, the optical properties of the nanowires were characterised by cathodoluminescence (CL) spectroscopy. In μ -photoluminescence studies, we did not observe any signal from the zinc phosphide, indicating high levels of non-radiative recombination. The higher excitation density of CL allowed us to observe radiative recombination, however, none indicative of bandgap recombination. The results from zigzag and vertical nanowires are presented in Figure 4.5. In Figure 4.5a-d, we present SEM micrographs and emission maps for zigzag and vertical nanowires. In the case of the zigzag nanowire, we observe emission localised at the nanowire, readily

distinguishable from the background, as seen indicated in the CL map in Figure 4.5b. The panchromatic CL map of the vertical nanowire, Figure 4.5d, shows a different emission behaviour, with its emission mainly originating at the base of the nanowire.

A detailed look into the CL spectra of the different parts of the nanowires is presented in Figure 4.5e-f for a zigzag and vertical nanowire, respectively. For the zigzag nanowire, we observe a sharp emission at 1.43 eV (860 nm), this transition energy is lower than the reported direct bandgap of Zn_3P_2 of 1.50 eV, thus most likely originating from a defect transition.^{55,58–60} For the vertical nanowire, grown with a V/II ratio of 1.15, we observed that the main emission peak shifted from 1.35 eV (918 nm) at the base to 1.33 eV (928 nm) at the top, which could be a function of the tapering. These energies are also below the reported bandgap of Zn_3P_2 , and similarly likely to originate from a defect transition. The InP nanoclusters may also be influencing the radiative recombination. Hence, further studies into the possible passivation of defects or removal of the surface nanoclusters are needed to optimise and clarify the optoelectronic response of the $\text{Zn}_{3-x}\text{P}_{2+y}$ nanowires.

Figure 4.5g depicts the emission of vertical nanowires as a function of V/II ratio. The emission peak redshifts with an increase of the V/II ratio. The main emission peak from the base of the nanowires shifts from 1.35 eV (917 nm) at low V/II ratios to 1.32 eV (940 nm) for higher V/II ratios. The peak shift could originate from different defect transitions in Zn-rich compared to P-rich samples. The emission from the nanowire grown at a V/II ratio of 1.00 also shows an emission peak at 1.38 eV (899 nm), which is attributed to recombination in the InP substrate. This could be a consequence of an enhanced carrier diffusion length of the nanowire, allowing for increased recombination at the substrate. These energies are in a similar range as self-interstitial related defect transitions reported previously, attributed to ionised acceptors.⁷⁸ However, this would not explain the peak observed in Zn-rich samples (1.31 eV) or the shift with composition.

4.1.4 Conclusion

To summarise, we have obtained $\text{Zn}_{3-x}\text{P}_{2+y}$ nanowires in four distinct tailored morphologies, among which the vertical nanowires are of particular interest for future photovoltaic applications. We have outlined the growth conditions yielding different nanowire morphologies and explained the substrate-mediated VLS growth mechanism through which they grow. We demonstrated the engineering of the chemical composition of the nanowires by the growth conditions (V/II ratio), which is crucial for control of the majority carrier type through intrinsic doping. TEM studies showed that the vertical nanowires grow along the [001] growth direction, whilst the straight-tilted and zigzag nanowires both grow along the [101] direction. The straight-tilted and zigzag nanowires also contained structural defects perpendicular to the [001] direction. The tapering of the nanowires was explained by shrinkage of the catalyst via the loss of In, which resulted in the formation of InP nanoclusters on the nanowire surface. Finally, using CL we observed an optical transition at 1.43 eV for zigzag nanowires, whilst the vertical nanowires showed a composition and location dependent emission in the range 1.32–1.35 eV. As the emission is observed at energies lower than the bandgap, their possible origin could be either defect transitions or recombination inside the surface InP nanoclusters. To yield more luminescent nanowires, further studies into passivation of the surface and of the nanoclusters are necessary.

4.1.5 Methodology

$\text{Zn}_{3-x}\text{P}_{2+y}$ nanowires were obtained in a Veeco GENxplor MBE system on InP (001) wafers using separate zinc and phosphorus sources (MBE Komponenten GaP-based P_2 source). Before growth, the substrates were degassed at 580 °C for 10 minutes under a P_2 atmosphere (beam equivalent pressure $> 1 \times 10^{-6}$ Torr) to remove the native oxide, which was verified through reflective high-energy electron diffraction. Indium droplets were generated by a five-minute zinc pre-deposition with a flux of 3.4×10^{-7} Torr and at a manipulator temperature of 250 °C, where it can react and form a liquid phase. The nanowires were then grown for four hours at a manipulator temperature between 220–265 °C using a zinc BEP of 3.4×10^{-7} Torr and the P_2 BEP was varied between $2.8 - 4.9 \times 10^{-7}$ Torr. Ion beam etching of InP (001) wafers was done using a Veeco Nexus IBE350 system using an acceleration voltage of 700V and current of 1100 mA.

The nanowires were characterised using a Zeiss Merlin FE-SEM, FEI Talos for conventional TEM/STEM operating at 200 kV, and FEI Titan Themis for AC STEM operating at 300 kV. The HAADF STEM images were filtered in Velox using a radial Weiner filter. 3D atomic models were generated using the Rhodius software package, and were then used for linear STEM image simulations.⁴⁰⁶ Using STEM_CELL we then performed STEM image simulations, relying on a modified version of the Kirkland “multislice” approach.^{407,408} An Attolight Rosa setup was used for CL measurements, operating at 10 K and using an acceleration voltage of 3 kV. Samples were loaded on a stage with 20° tilt, allowing us to observe the vertical nanowires. The ternary phase diagram of the Zn-In-P system was modelled based on existing thermodynamic descriptions from Lee, Ansara *et al.*, and Ghasemi *et al.*, and through extrapolation of the binary phase diagrams using Thermo-Calc.^{67,409–412} More details of the modelling of the phase diagrams via the CALPHAD method, applied to the Zn-P binary system, can be found in ref. [67] and the supporting information file.

4.1.6 Supplementary Information

The Supplementary Information, which contains additional electron microscopy analysis and the Zn-InP vertical section (isopleth) from the ternary phase diagram, can be found in Appendix A.

4.1.7 Acknowledgements

S Escobar Steinvall, E Stutz, R Paul, M Zamani and A Fontcuberta i Morral were supported by the SNF Consolidator Grant (BSCGI0-157705). R R. Zamani and T LaGrange were supported by the EPFL-CIME. N Tappy and A Fontcuberta i Morral thank SNF funding through grant 20B2-1 176680. The authors also thank Anna Kúkol'ová for the SEM images of the initial catalyst particles.

Chapter 5 Heterotwin Superlattice Nanowires

One of the main morphologies reported in the previous chapter are the zigzag nanowires. These were previously thought to be regular twin superlattice (TSL) nanowires similar to the much more studied III-V analogues. However, using various aberration corrected electron microscopy techniques we elucidated their exact structure in zinc phosphide, which showed this to not be the case. With this knowledge we formulated a new model to describe the formation mechanism of these structures that is more general than previous models based on polar III-V materials. Finally, we investigated the influence of the twins on the optoelectronic properties.

For this publication, I performed the growth, scanning electron microscopy, and cathodoluminescence spectroscopy of the samples, as well as performing the data analysis of these parts. I was also involved in the imaging of the samples using aberration corrected analytical scanning transmission electron microscopy (STEM) at EPFL and SuperSTEM, and contributed to the analysis and treatment of the data generated. I was also involved in the interpretation and refinement of the models created by Lea Ghisalberti. Finally, I contributed to the writing of the manuscript, which was then finished with the input of all co-authors.

Superlattices in materials with remarkable properties can be achieved in various ways, and one of the more elusive ones are the TSLs, where the crystal is rotated between each segment. These were first proposed in 1993, and were achieved experimentally a decade later in metal-catalysed compound semiconductor nanowires. Theoretical predictions based on TSLs show their potential for indirect to direct bandgap conversion in germanium among other interesting electric, phononic, and optic phenomena.

However, while some progress has been made in understanding TSL formation, there are multiple conflicting theories as to the factors influencing their formation, and there is no clear model to predict under what conditions or in which material systems they can form. For example, side-facet polarity has been suggested as one of the most important factors based on results from zincblende III-V nanowires. In this work, however, we show that zinc phosphide zigzag nanowires have non-polar lateral facets. Consequently, we refine the formation model based solely on the catalyst dynamics rather than the side-facet polarity.

Using aberration corrected analytical STEM we noticed another peculiarity about the “twin” in the zigzag nanowires. Instead of a normal twin where the crystal has a mirror plane at the twin, we observed a one monolayer thick discontinuity. By detailed examination through aberration corrected STEM imaging and core-loss electron energy-loss spectroscopy (EELS) mapping we could determine that we form an indium-rich layer at the “twin”, forming a heterotwin. Heterotwins are observed in high stacking fault energy materials, and the higher valency of indium at the interface facilitates the crystal rotation. These measurements were only made possible through the use of cutting-edge research facilities here at EPFL and at our collaborators at SuperSTEM (Dr Fredrik S. Hage and Prof Quentin M. Ramasse).

We were curious of the effect of this indium-rich layer on the optoelectronic properties, so we performed room temperature CL measurements. Our previous studies at cryogenic temperatures had indicated a homogeneous response. However, this could be explained by the enhanced carrier diffusion length, and consequently decreased spatial resolution, at low temperatures. To enhance the spatial resolution we worked at higher magnification and at room temperature (decreasing the carrier diffusion length). Despite our best efforts, we could not discern any influence of the heterotwin on the CL response. Instead we observed some interesting waveguiding influence on the emission profile related to the zigzag and tapered geometry of the nanowire.

The content of this paper, published in *Nanoscale* (Vol 12, p. 22534-22540, 2020) under a Creative Commons Attribution-NonCommercial 3.0 Unported Licence, has been edited to match the format of this thesis with references combined with those at the end. The content and figures have been reproduced here without modification with the permission of the Royal Society of Chemistry. The supporting information can be found in Appendix B.

5.1 Heterotwin Zn_3P_2 Superlattice Nanowires: the Role of Indium Insertion in the Superlattice Formation Mechanism and their Optical Properties

Simon Escobar Steinvall*, Lea Ghisalberti*, Reza R. Zamani*, Nicolas Tappy, Fredrik S. Hage, Elias Z. Stutz, Mahdi Zamani, Rajrupa Paul, Jean-Baptiste Leran, Quentin M. Ramasse, W. Craig Carter, Anna Fontcuberta i Morral

*Equal Contribution

5.1.1 Abstract

Zinc phosphide (Zn_3P_2) nanowires constitute prospective building blocks for next generation solar cells due to the combination of suitable optoelectronic properties and an abundance of the constituting elements in the Earth's crust. The generation of periodic superstructures along the nanowire axis could provide an additional mechanism to tune their functional properties. Here we present the vapour-liquid-solid growth of zinc phosphide superlattices driven by periodic heterotwins. This uncommon planar defect involves the exchange of Zn by In at the twinning boundary. We find that the zigzag superlattice formation is driven by reduction of the total surface energy of the liquid droplet. The chemical variation across the heterotwin does not affect the homogeneity of the optical properties, as measured by cathodoluminescence. The basic understanding provided here brings new perspectives on the use of II-V semiconductors in nanowire technology.

5.1.2 Introduction

Filamentary crystals, also known as nanowires, have provided additional design freedom in the elaboration of materials with desirable properties.^{173,174,227,413} This arises from the possibility of engineering the crystal phase, material composition, and for the possibility of expanding the structure in three dimensions.^{222,227,243} Among the design opportunities, the composition or structure of nanowires can be arranged periodically in the form of superlattices.^{101,236,242,243} The periodicity of the superstructure modulates both the electronic and phonon (vibrational) states, depending on the magnitude of the period.^{374,414–416} Semiconductor superlattices find applications in the optoelectronic and thermoelectric arena.^{164,166,167,214} In thin films, the materials combinations are mostly restrained due to lattice-mismatch and thermal expansion conditions. Superlattice nanowire structures circumvent these limitations, and have been achieved by modulating the composition, crystal phase, and crystal orientation through rotational twins.^{222,236,242,243}

Twin superlattices (TSLs) in semiconductors were predicted by Ikonin *et al.* in 1993.⁴¹⁷ More recently, they were implemented in nanowire form, first in Al_2O_3 and ZnSe , and subsequently in InP .^{273,418,419} These TSLs have been obtained mainly by the vapour-liquid-solid (VLS) method in which a nanoscale liquid droplet preferentially collects the growth precursors.²¹⁹ In addition to a periodic arrangement of twins, these nanowire superlattices adopt a characteristic zigzag morphology with alternating (111)A/B facets in the case of zincblende nanowires.^{236,242} According to Algra *et al.*, twin formation is determined by energy minimisation involving the stability of the droplet and the surface energy of the facets as a function of their polarity $-(111)$ a or B-.²³⁶

Zinc phosphide, Zn_3P_2 , has recently attracted attention as a compound semiconductor made of elements that are abundant in the Earth's crust with optoelectronic properties suitable for photovoltaic applications.^{106,122,124,142,186,420} Zn_3P_2 has been obtained both in the form of bulk crystals^{62,68}, thin films^{89,106,186}, and nanostructures^{101,128,130,260,420}. Zinc phosphide based solar cells with an efficiency of up to 6% have been reported.⁶² This value is still well below the theoretical limit (>30%), illustrating the improvement potential of this material.^{19,421}

The synthesis of Zn_3P_2 nanowires can follow the VLS and the vapour-solid mechanisms, with In, Sn, and Au as catalysts.^{101,128,130,143,147,260,420} Zn_3P_2 nanowires adopt various morphologies depending on the fabrication method and/or growth conditions, including a zigzag superlattice.^{101,128,130,260,420} In contrast with III-V compound semiconductors, Zn_3P_2 exhibits a centrosymmetric tetragonal structure, and thus also non-polar facets and main crystal symmetry directions.⁶⁸ Consequently, all side facets of Zn_3P_2 zigzag nanowires are always Zn-terminated.^{124,130} This means that the mechanism through which Zn_3P_2 obtains a zigzag morphology is inconsistent with the model proposed based on III-Vs.²³⁶

In this paper we reveal the nature of the defects leading to the zigzag structure using aberration-corrected and analytical scanning transmission electron microscopy (STEM). In addition, we explain the formation mechanisms based on simulations of the surface energetics of the droplet as a function of the nanowire cross-section. Finally, we outline the consequences of this periodic structure for the optical functionality through cathodoluminescence spectroscopy (CL).

5.1.3 Experimental

The Zn_3P_2 nanowires were epitaxially grown in a Veeco GENxplor molecular beam epitaxy (MBE) system on InP (100) substrates. They were grown through In catalysed VLS, with the In originating from the substrate.⁴²⁰ The analysed samples were grown at a manipulator temperature of 250°C and a V/II ratio of 1.15 or 1.45 for four hours, with additional details on the growth in [420]. The nanowires were transferred to copper TEM grids with holey carbon by scraping the grid on the growth substrate for TEM studies, and were used as grown for CL studies.

Scanning electron microscopy (SEM) images were acquired using a Zeiss Merlin FE-SEM equipped with a Gemini column. The operating conditions were an acceleration voltage of 3 kV and a beam current of 100 pA. An in-lens secondary electron detector was used for the imaging.

Droplet simulations were performed using the Surface Evolver software⁴²², which computes minimised surface energy by optimising shapes given constraints and wetting angles. We implement the interfacial energy of the liquid-solid interface by means of the Young's equation with a contact angle of 43° when the triple line is unconstrained. The certical axis in Fig 2c is the total energy divided by L^2 , with L being the average length of the sides, and the difference between the solid-liquid and the solid surface tensions. The average length of the side remains constant with a value of 1.57. Regarding the geometrical constraint, the triple line is not pinned to the edge, but is left free to move inside the polygon. To build the polygon, centred at the origin, we define an equation for each side of the hexagon through the lat and shrink parameters, illustrated in the SI. While the lat parameter is fixed at 0.55 and defines the apothem of the reference hexagon, the shrink parameter is variable controlling the shape of the constraint since it represents the normal between the facet centroid and the selected facet. By varying the shrink parameter from -0.25 to 0.25, we can reproduce the evolution of the nanowire cross-section from left oriented triangle to right oriented triangle (HT1 & HT2), passing through the hexagonal geometry at shrink equal to 0. To compare the effect of the volume we performed the simulations for three different droplet volumes: 0.125, 0.225, and 0.325 with dimensions of L^3 .

Aberration-corrected bright-field/high-angle annular dark-field (BF/HAADF) STEM images and electron energy loss spectroscopy (EELS) maps were collected on a STEM-dedicated Nion microscope (US100MC) operating at 60 kV. The Nion UltraSTEM 100MC HERMES is equipped with a C5 Nion probe corrector (full correction up to 6-fold astigmatism C5, 6) and a UHV Gatan Enfinitum ERS spectrometer optimised for high energy resolution with high-stability electronics. The microscope is equipped with a cold-field emission gun (C-FEG), having an energy spread of 0.35 eV. The beam convergence semi-angle was 31.5 mrad and the EEL spectrometer entrance aperture semi-angle was 44 mrad. Image detector angles were 0-14 mrad (BF) and 100-230 mrad (HAADF). To minimise contamination, the specimens were baked prior to insertion at 130 °C in vacuum ($\sim 10^{-6}$ Torr), and the microscope column is maintained at ultrahigh vacuum (UHV). The denoising of STEM-EELS datasets was done using the MSA plugin for Gatan's Digital Micrograph suite, commercially available from HREM research.⁴²³ Example spectra are shown in the SI, and the 443 eV and 1020 eV peaks were used for EEL mapping of In and Zn, respectively. Further imaging was also performed in a FEI Titan Themis 60-300 kV TEM operating at 200 or 300 kV. The machine is equipped with a field emission gun (X-FEG), a monochromators, two aberration correctors (one pre-specimen probe-corrector, and one post-specimen image corrector), and a Fischione HAADF detector. The collection angles are typically 85-200 mrad for HAADF-STEM images. The BF and HAADF images were denoised using radial a Weiner filter. Viewing direction illustrations were created in Mathematica.

An Attolight Rosa setup equipped with an Andor Newton 920 Si-CCD was used for CL measurements. It was operated at room temperature with an acceleration voltage of 3 kV, a beam current of <1 nA, and an exposure time of 50 ms per pixel. The nanowires were mounted on a stage with 20° tilt. Denoising of the hyperspectral maps was done through principal-component analysis (PCA) using the Hyperspy Software.⁴²⁴ Peak fitting was done after data treatment based on the approach described in ref. [425].

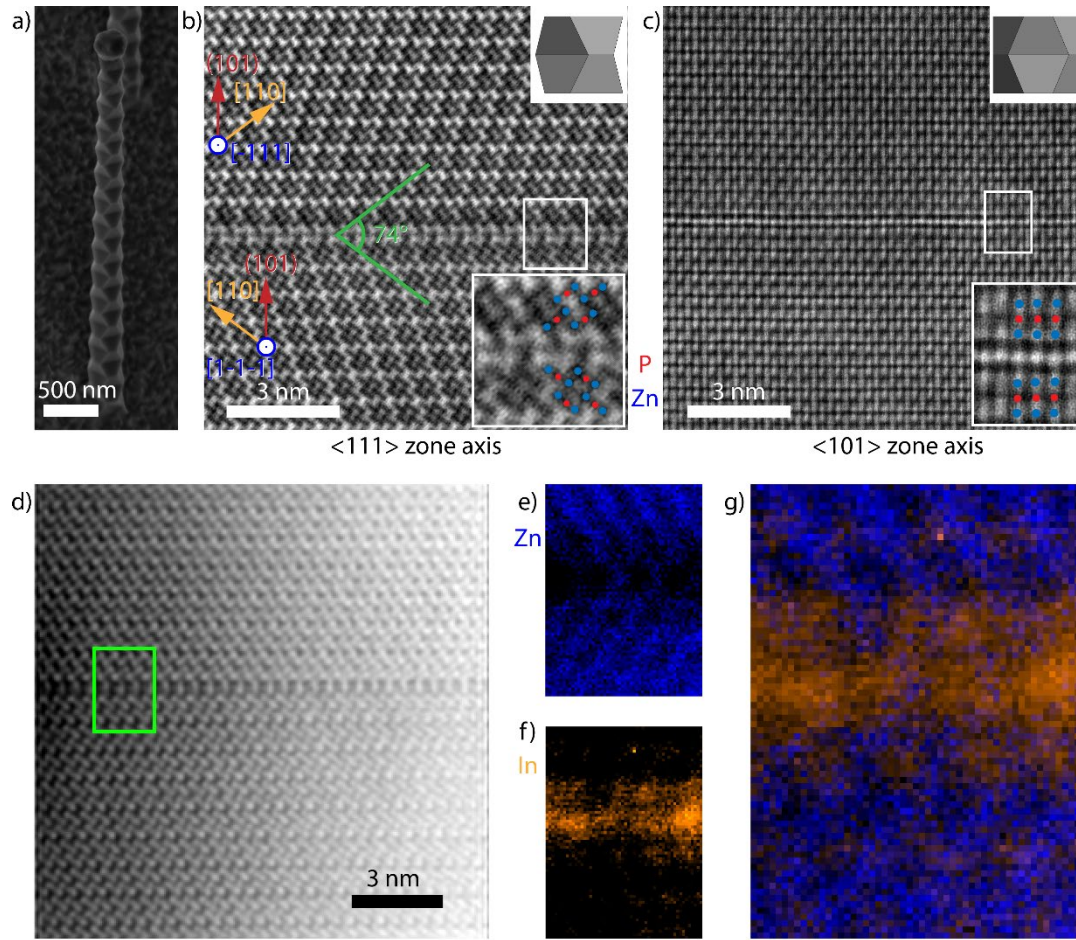


Figure 5.1 a) Secondary electron SEM image of a superlattice nanowire. b) Aberration corrected BF-STEM image taken along a $[111]$ zone axis in the region around the zigzag interface with an inset illustrating the viewing direction. c) Aberration corrected HAADF-STEM image taken along a $[101]$ zone axis in the region around the zigzag interface. The top inset illustrates the viewing direction and the bottom inset displays a “close up” on the interface. d) HAADF-STEM image ($[111]$ zone axis) of the region where the EELS maps were acquired (green). e-g) Core-loss EELS maps of Zn (blue - e), In (orange - f), and the combination (g), showing the localised presence of In in the region around the stacking fault.

5.1.4 Results and Discussion

5.1.4.1 Electron Microscopy

Figure 5.1a shows a representative secondary electron SEM images of a typical zigzag Zn_3P_2 nanowire. These nanowires grow perpendicular to (101) with side facets belonging to $\{101\}$.^{130,420} While the lateral facets in III-V superlattices, $(111)\text{A}$ and $(111)\text{B}$, can exhibit different polarities, this is not the case for Zn_3P_2 (101) facets as they are all Zn-terminated.^{124,236,242} The supposed difference between the lateral facets has been cited as one of the driving forces for the formation of TSL nanowires. This argument cannot be applied to this case as Zn_3P_2 does not display polar facets. Before discussing the mechanism, we disclose the nature of the interface dividing the zigzag regions in the nanowire.

Figure 5.1b shows an aberration-corrected BF-STEM image of a zigzag nanowire ($[111]$ zone axis), revealing a “twin-like” planar defect separating different segments that are mirrored. This structural defect is akin to the twin planes in the III-V TSL nanowires: it interfaces two segments of the nanowire that appear to be rotated 180° around the nanowire growth axis –the (101) plane–, which is the most common twin plane in tetragonal systems.⁴²⁶ Here we observe a (224) planar spacing of $1.97 \pm 0.07 \text{ \AA}$, which is within experimental error of the literature value of 2.024 \AA .⁶⁸

Figure 5.1c shows the HAADF-STEM image of a region equivalent to that shown in Figure 5.1b, viewed along the other major zone axis, $[-101]$. The bottom insets corresponds to “close ups” of the interfaces, identifying sets of trimers (Zn – blue, P – red) at each side of the defect. The topmost insets show a three-dimensional model of the structure, highlighting the viewing direction of the respective zone axes. While the defect is easily discerned by the increase in intensity and break in periodicity in Figure 5.1c, the structure is not perfectly mirrored along this zone axis. Instead, we observe a translation of the top crystal by a (400) plane along the $\langle 100 \rangle$

direction perpendicular to the zone axis. Furthermore, as corroborated below, the interfacial defect extends to more than one monolayer, and is of a different composition than the neighbouring segments. Thus, the two rotated crystals are separated, not sharing any crystal lattice points, and consequently this defect cannot be considered a standard twin.

We now turn to the study of the nature of the interface separating the twinned regions by providing data on the chemical composition. For this, we took the core-loss EELS of the “twin” and the adjacent regions –marked with a green square in Figure 5.1d, resulting in chemical maps with atomic-scale resolution.^{322,427} Figure 5.1e-g display the resulting chemical mapping of Zn (blue – e), In (orange – f), and combined (g). P mapping did not provide the same resolution, and a constant signal was observed throughout. The maps reveal the presence of In at the interface and the neighbouring layers, accompanied by a drop in the Zn content. The presence of In is consistent with the intensity analysis in the HAADF-STEM images, especially from the [-101] direction (Figure 5.1c). The interface there appears slightly brighter than the rest, suggesting the presence of a heavier element, i.e. In. Given the chemical inhomogeneity across the boundary, the defect should rather be identified as a heterotwin.⁴²⁸ The In originates from the droplet that drives the VLS growth⁴²⁰, which was in contact with the twin region during formation.

The utilisation of a chemical heterogeneity at the boundaries or planar defects have been reported in Al/TiN composites and in doped II-VI compounds such as ZnO. In the case of Al, N-terminated TiN lowers the formation energy of twins, and they provide significantly improved mechanical properties.^{428,429} In ZnO, trivalent metals such as Al, Fe, Ga, or In have shown to precipitate at the interface of inversion domain boundaries.³²¹ The presence of trivalent metals in II-VI defects modifies the bonding coordination from four in a tetrahedral fashion to eight in an octahedral one, causing the polarity inversion.^{430–433} However, in the case considered here the defect cannot be classified as an inversion domain boundary as there is no polarity inversion associated with it. In the following section we discuss the mechanism by which Zn_3P_2 forms a zigzag structure via a heterotwin.

5.1.4.2 Zigzag Mechanism

To investigate the driving forces prompting the regular insertion of heterotwins, we analysed the heterotwin periodicity along the nanowire length, x (nm), and as a function of W , an approximation of the cross-sectional apothem. The trend was observed in multiple nanowires, while the equation is based on the high-resolution TEM image shown in Figure B.S3. Similar to III-V TSL nanowires, the heterotwin periodicity in Zn_3P_2 nanowires depends on their diameter.^{242,434} The zigzag morphology results in the width being a periodic function with an amplitude with linear decay:

$$\text{Equation 5.1} \quad W(x) = \left(W_0 - \frac{W_0 - \frac{W_0}{2}}{z} - \frac{x}{\tan \frac{\pi}{2.02}} \right) \left(1 + \frac{1}{3} \cos \frac{2\pi x}{h_0 e^{-2 \times 10^{-5} x}} \right)$$

Where W_0 is the initial width and h_0 is the distance between the initial segment separation. Equation 5.1 shows that the heterotwin interdistance reduces with the reduction of the nanowire diameter, in agreement with studies on non-tapered superlattice ZnSe and GaAs nanowires.^{273,434} In particular, the term $\pi/2.02$ corresponds to 89° , i.e. the measured tapering angle characterising the reduction of the nanowire’s diameter. The origin of the tapering is explored in detail in ref. [420].

Regarding possible explanations for the heterotwin formation mechanism, previous studies argued that twins in a zigzag structure form to minimise the nanowire surface energy.^{236,435} The argument is reasonable for compound semiconductor nanowires exhibiting facets with different polarities and thus different surface energies. However, Zn_3P_2 is not polar. The basic structural unit consists of symmetric Zn-P-Zn trimers, instead of asymmetric cation-anion dumbbells such as In-P in InP, and its centrosymmetric crystal structure.^{68,321,436} Thus, all facets in the zigzag structure are equivalent.¹²⁴ This means we cannot reasonably attribute the instigation of the Zn_3P_2 twinning process to nanowire surface energy minimisation alone. As discussed below, deformation of the liquid droplet during growth provides a more compelling argument.

We studied the droplet stability as a function of the volume and underlying cross-section of the nanowire, which varies during the zigzag formation as depicted in Figure 5.2a-b. To this end, we computed the surface energy of the liquid droplet and the interface with the nanowire using the finite-element based software Surface Evolver.⁴²² We used a Young angle of 43° , which is the experimental value found ex-situ.²⁷⁹ Young’s angles differing from 43° do not change the conclusion regarding alternating stability, the only modify the threshold for heterotwin formation.

Figure 5.2c illustrates the evolution of the surface energy of the droplet plus the liquid-solid interface during one zigzag cycle. We include the curves for three relative values of droplet volumes, which all follow a similar trend. The total surface energy has been normalised by the average length of the sides, constant throughout all simulations, by the surface energy of a floating sphere with an identical volume, and by the surface tension of the liquid-vapour interface. Due to the pinning of the liquid at the edge of the faceted nanowires, an increase in the liquid volume results in the increase of the apparent contact angle.²⁷⁹ The normalised surface

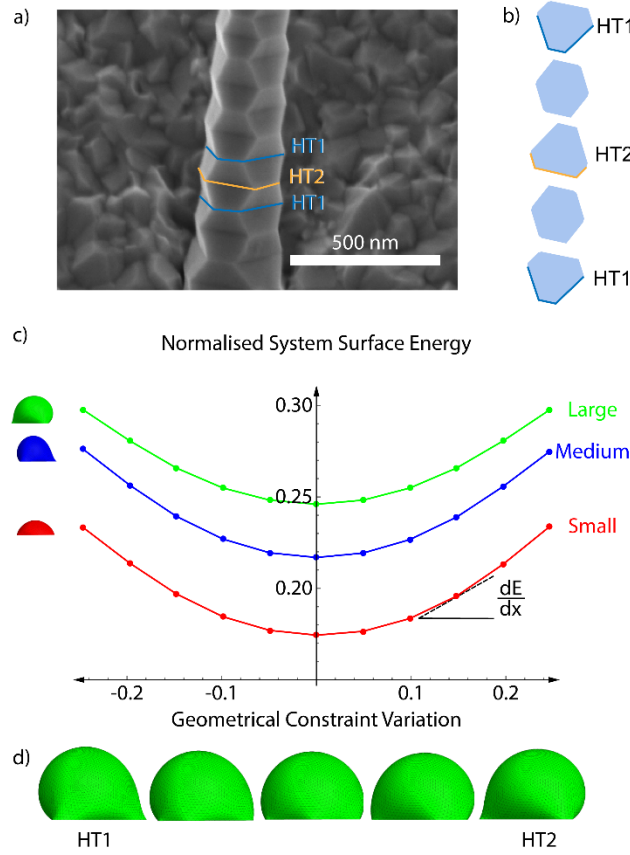


Figure 5.2 a) Secondary electron SEM image of a zigzag Zn_3P_2 nanowire b) schematic of the development of the cross-section of the nanowire as a function of the nanowire's growth axis, c) Results of the computation of the system (droplet and nanowires top facet) normalised surface energy (normalisation explained in the text) as a function of the variation of the geometry of the NW's top facet for three different referential droplet volume: small (red), medium (blue) and large (green); d) 3D sketch of the large droplet morphology upon the zigzag period.

energy increases with the liquid volume due to the expansion and deformation of the liquid surface at the edges. The lowest normalised surface energy corresponds to the configuration with hexagonal nanowire cross-section, where the droplet is the least deformed. The normalised surface energy increases parabolically (to a second order approximation) with the modification of the liquid-solid interface area. The slope of the curve increases with the droplet deformation. A representative display of the predicted droplet shape during the zigzag process is shown in Figure 5.2d. It shows that the deformation is larger at the corners of the cross-section. In addition, the local and overall deformations are the largest when the cross-section is the closest to a triangular shape. This increasing deformation with the deviation from a hexagonal cross-section explains the increase in the normalised surface energy.

The introduction of a heterotwin constitutes a mechanism to stop the increase in surface energy during the nanowire elongation caused by the droplet's deformation.^{434,437} As the energy required to form a heterotwin (E_{HT}) is fixed, there is a critical geometry of the nanowire's cross-section after which it is energetically favourable to insert a heterotwin rather than to continue increasing the total normalised surface energy. The probability of creating a heterotwin along the nanowire axis, $P(x)$, should thus increase with the normalised surface energy of the system, $\gamma(x)$, as:

Equation 5.2
$$P(x) \sim \frac{\gamma(x)}{E_{\text{HT}}A(x)}$$

After formation of a heterotwin, the normalised surface energy decreases with nanowire elongation due to the change in the facet orientation and return towards a hexagonal cross section.

5.1.4.3 Optical Properties

Previous studies on Zn_3P_2 indicate that it exhibits a direct bandgap at ~ 1.5 eV, which is close to the ideal bandgap for the highest efficiency of single junction solar cells.⁵⁵ In our recent work, we demonstrated that zigzag Zn_3P_2 nanowires luminesce at 1.43 eV at cryogenic temperatures, which is relatively close to the expected value of the bandgap.⁴²⁰ We have observed that in Zn_3P_2 nanowires with a square cross-section, luminescence can vary with the relative stoichiometry between the Zn and P.⁴²⁰ Given the composition variation at the heterotwin in the zigzag nanowires, the question arises of whether the optical properties vary at these points. To ascertain their potential influence, we performed CL on zigzag nanowires at room temperature. The experimental conditions were chosen as to decrease the diffusion length and allow for higher spatial resolution measurements compared to previous studies.

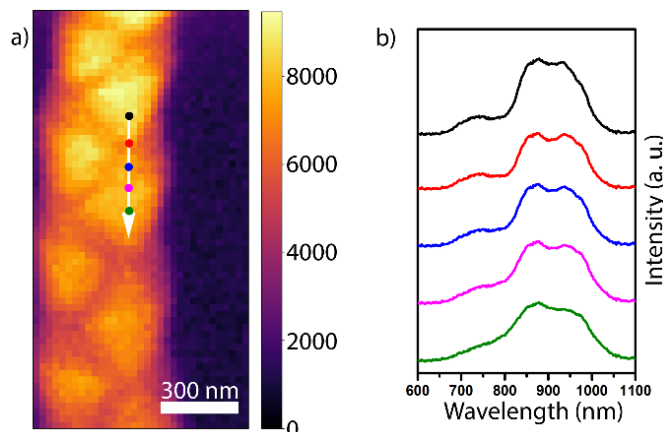


Figure 5.3 (a) High-resolution panchromatic CL intensity map of a zigzag nanowire with the white arrow indicating the linescan of the extracted spectra in (b), of which the second and fourth from the top were extracted from regions on top of the heterotwin.

Figure 5.3a shows a panchromatic map of the CL emission. We observe a $\sim 10\%$ variation in the emission intensity around edges and on the outward facet orientation compared to that of the inward orientation of the zigzag structure. We attribute this fluctuation to the variations in electron-beam excitation as a function of the morphology (see SI for more details). Detailed spectra along one oscillation of the zigzag morphology indicated by the arrow in Figure 5.3a are shown in Figure 5.3b. We observe two main peaks centred around 869 and 950 nm (1.43 eV and 1.30 eV, respectively), which correspond to sub-bandgap emission, potentially caused by the incorporation of indium in the bulk.¹¹⁹ First principle simulations should be performed to confirm this hypothesis. We also distinguish a third weaker peak centred around 748 nm (1.66 eV). This peak could correspond to emission from the Γ^2 transition 260 meV above the bandgap, available due to the high energy excitation of CL.^{55,438} The spectra along and on each side of the heterotwin are qualitatively extremely similar. The similarity of the spectra along the zigzag structure could be due to the carrier diffusion length being larger than the excitation volume.⁵⁵ The spectra's intensity tends to decrease down the nanowire axis. We attribute this to optical wave-guiding effects. The channelling of CL signal between optical modes of a nanowire depends strongly on the exact position.⁴³⁹ In the measurement geometry used here, and with the restricted collection angle of the CL setup, the signal can be collected only when emitted from the top of the wire and for a restricted range of angle. This would explain the peak intensity variation on a $\lambda/2$ spatial scale as observed in Figure 5.3. One would require angle-resolved CL experiments to confirm this.

5.1.5 Conclusion

In conclusion, we have demonstrated that the Zn_3P_2 superlattice nanowires do not form through regular twinning, as observed in their III-V analogue. Instead, an In-rich heterotwin is formed, as shown through EELS mapping and aberration-corrected STEM imaging, which facilitates the rotation of the crystal structure between segments through the inset of a separate material. Furthermore, we developed a model to explain the onset of heterotwin formation. Based on the non-polar nature of Zn_3P_2 we could tie the model solely to the constraints posed by the droplet shape as a function of the nanowire cross-section. Characterisation of the emission through room temperature CL shows no effect of the heterotwins on the functional properties.

5.1.6 Supplementary Information

The Supplementary Information can be found in Appendix B. It contains the definitions of the parameters used in the model, example EEL spectra of In and Zn, additional information on the model describing the effect of tapering on the oscillatory behaviour, and the CASINO simulation explaining the intensity variation at edge features.

5.1.7 Acknowledgements

S. E. S., E. S., M. Z., R. P., J. L., and A. F. i M. were supported by the SNSF Consolidator grant BSCG10-157705. N. T. and A. F. i M. were supported by SNSF grant 20B2-1 17668. L.G., W. C. C., and A. F. i M. were supported by SNSF via project 200021_169908 and SCRO222237. R. R. Z. was supported by EPFL-CIME. F. S. H., Q. M. R., and the SuperSTEM Laboratory, the U. K. National Research Facility for Advanced Electron Microscopy, were supported by the Engineering and Physical Sciences Research Council (EPSRC).

Chapter 6 Selective Area Epitaxy of Zinc Phosphide

The original aim for the last part of the thesis was to investigate the position-controlled growth of zinc phosphide nanowires. However, we quickly realised that the material prefers to grow in the shape of nanopyramids through a vapour-solid (VS) mechanism, which would coalesce into a thin film if grown for long enough. In this part we explore the growth, crystalline structure, and functional properties of the selective area grown zinc phosphide.

For this publication I performed the substrate preparation, growth, scanning electron microscopy, conventional transmission electron microscopy (TEM), scanning (S)TEM, STEM energy dispersive x-ray spectroscopy (EDX) measurements, and atomic modelling. I also performed the analysis of the data generated from these measurements in addition to the aberration corrected HAADF-STEM, and contributed to the analysis of the normal and conductive atomic force microscopy (CAFM) and photoluminescence spectroscopy (PL) data. Finally I wrote the manuscript, which was then completed with the input of all co-authors.

This part of the project started by the exploration of nanowire growth in ordered arrays. While initial nanowire results seemed promising, the pyramids spiked our interest as a promising path towards obtaining thin films and it thus became the focus of continued studies. We mapped out the growth conditions for selective area VS growth to find the optimum conditions producing the highest crystalline and best growth selectivity. We also performed a time series to help better understand the growth sequence. This elucidated the facet growth order and coalescence of the pyramids through lateral epitaxial overgrowth into a thin film. The explanations were also validated through the density functional theory calculations performed by our collaborator, Dr Nelson Y. Dzade at Cardiff University.

With the support of Mahdi Zamani, we then used a focused ion beam to cut cross-sections from these pyramids to investigate them using transmission electron microscopy. With these lamellae we could determine the exact interface structure, growth direction, coalescence and elastic strain relaxation of our structures. There were two results that we did not initially expect. First, we noticed a rotation of around the growth plane when the pyramids start grow laterally, forming a rotational core-shell structure. We also notice through STEM EDX that the composition of the nanopyramids depends on the nominal hole size from which they grow. We could tune it from phosphorus-rich for smaller holes to zinc-rich for larger ones, which in turn will affect the self-interstitial formation and the intrinsic doping.

The functional properties were then assessed using conductive atomic force microscopy (CAFM) and photoluminescence spectroscopy (PL). The CAFM was used to compare zinc phosphide grown on substrates with different doping (n vs p vs intrinsic). The measurements indicated that the grown material is p-type, which is expected for zinc phosphide. However, the change in composition has also been shown to influence the electrical properties, and is currently being investigated as a follow up study. PL showed zinc phosphide bandgap emission close to the expected value (measured = 1.53 eV, literature = 1.50 eV), which shows a high crystalline quality. A hole size and pitch dependence was also observed in the emission, and a more detailed study of this is currently underway.

The content of this paper, published in *Nanoscale Advances* (DOI: 10.1039/d0na00841a, 2020) under a Creative Commons Attribution-NonCommercial 3.0 Unported Licence, has been edited to match the format of this thesis with references combined with those at the end. The content and figures have been reproduced here without modification with the permission of the Royal Society of Chemistry. The supporting information can be found in Appendix C.

6.1 Towards Defect-Free Thin Films of the Earth-Abundant Absorber Zinc Phosphide by Nanopatterning

Simon Escobar Steinvall, Elias Z. Stutz, Rajrupa Paul, Mahdi Zamani, Nelson Y. Dzade, Valerio Piazza, Martin Friedl, Virginie de Mestral, Jean-Baptiste Leran, Reza R. Zamani, Anna Fontcuberta i Morral.

6.1.1 Abstract

Large-scale deployment of thin-film photovoltaics will be facilitated through earth-abundant components. Herein, selective area and lateral overgrowth epitaxy are explored for the growth of zinc phosphide (Zn_3P_2), a promising earth-abundant absorber. The ideal growth conditions are elucidated, and the nucleation of single-crystal nanopillars that subsequently evolve towards coalesced thin-films is demonstrated. The zinc phosphide pillars exhibit room temperature bandgap luminescence at 1.53 eV, indicating a high-quality material. The electrical properties of zinc phosphide and the junction with the substrate are assessed by conductive atomic force microscopy on n-type, p-type and intrinsic substrates. The measurements are consistent with a p-type characteristic of zinc phosphide. Overall, this constitutes a new, and transferrable, approach for the controllable growth of high-quality zinc phosphide, a step forward in the quest for earth-abundant photovoltaics.

6.1.2 Introduction

With current environmental trends there is an increasing need for sustainable energy harvesting, which would be greatly facilitated by the use of earth-abundant components.^{394,440–443} Zinc phosphide (Zn_3P_2) is an earth-abundant semiconductor that could contribute to renewable photovoltaic technology, thanks to its ideal direct bandgap (1.5 eV), long minority carrier diffusion length (7–10 μm), and high optical absorption.^{19,55,56,62,142,444} So far, the promising properties have been limited by the lack of growth substrates with matching lattice parameter and coefficient of thermal expansion (CTE). As a result, it has been challenging to obtain single crystalline layers that fulfil the potential of this material in terms of controlled doping or heterojunction formation, limiting successful charge separation and extraction.^{71,73,87,89,106,186}

Among the growth techniques explored for zinc phosphide, molecular beam epitaxy (MBE) seems extremely promising as it allows for both precise control of the stoichiometry and reduced growth temperature.^{73,89,106} This should limit the formation of self-interstitial defects and cracks, the latter appearing upon substrate cooling.^{89,106,420} MBE also provides a path for precise incorporation of extrinsic dopants, such as magnesium or silver.^{75,76,79,144}

Several substrates have been employed for the epitaxial growth of zinc phosphide thin films.^{87,106,129} For example, we previously showed that single-crystal zinc phosphide flakes can nucleate and grow defect-free on graphene as interactions are restricted to van der Waals.¹⁸⁶ However, the polycrystalline nature of commercial graphene substrates hinders the deployment to large-area single-crystal thin films.¹⁸⁶ Indium phosphide has also shown promise as a growth substrate despite a lattice mismatch of 27% if one were to look at the standard unit cell.⁶⁸ Nonetheless, due to the pseudo-cubic reconstruction of zinc phosphide, where the phosphorus sublattices overlap, it has only $\sim 2.3\%$ mismatch with indium phosphide.^{129,130,395,420} While growing on indium phosphide deviates from the earth-abundant advantages of zinc phosphide it still provides an excellent platform to obtain high crystalline and optical thin film quality and for the understanding of the growth mechanisms.

The stringency of lattice and CTE match with the substrate in epitaxy can be reduced by limiting epitaxy to reduced areas, resulting in nanostructure formation.^{222,226,231} Following this principle, many families of materials have been obtained on a large variety of substrates, including zinc phosphide.⁴²⁰ A particular approach corresponds to selective area epitaxy (SAE).^{174–176,294,298,299,301,310} In SAE, growth is restricted to certain (often nanoscale) regions of the substrate, which can be defined through e.g. electron beam lithography, nanoimprint or stepper photolithography, with the latter one being compatible with high-throughput manufacturing. This is achieved by masking it with e.g. a nanopatterned oxide. At the right temperature, growth precursors preferentially chemisorb or diffuse to the zones free of oxide. In this way, it is possible to limit the nucleation and growth to inside the desired regions, where it proceeds through a vapor-solid (VS) growth mechanism.^{174–176,294,298,299,301,310} This approach has been employed in a variety of materials systems, such as the formation of III-V nanowire networks for next-generation electronics and topological quantum computing schemes.^{174–176,294,298,299,301} Through overgrowth, the structures grow laterally from the holes over the oxide, coalescing into a thin film. The so-called lateral epitaxial overgrowth (LEO) has similarly been explored for the integration of III-Vs on silicon among other systems.^{300,305–307,318,445} For LEO to be successful, growth conditions should lead to faster lateral than vertical overgrowth. To the best of the authors' knowledge, this approach is yet to be applied to earth-abundant photovoltaic materials.

In this report, we present a combination of SAE and LEO to obtain high-quality zinc phosphide on indium phosphide. We elucidate the growth mechanism, the functional properties as well as its suitability as a photovoltaic material. This work opens a new avenue to produce high-quality zinc phosphide films, despite the lack of lattice-matched substrates.

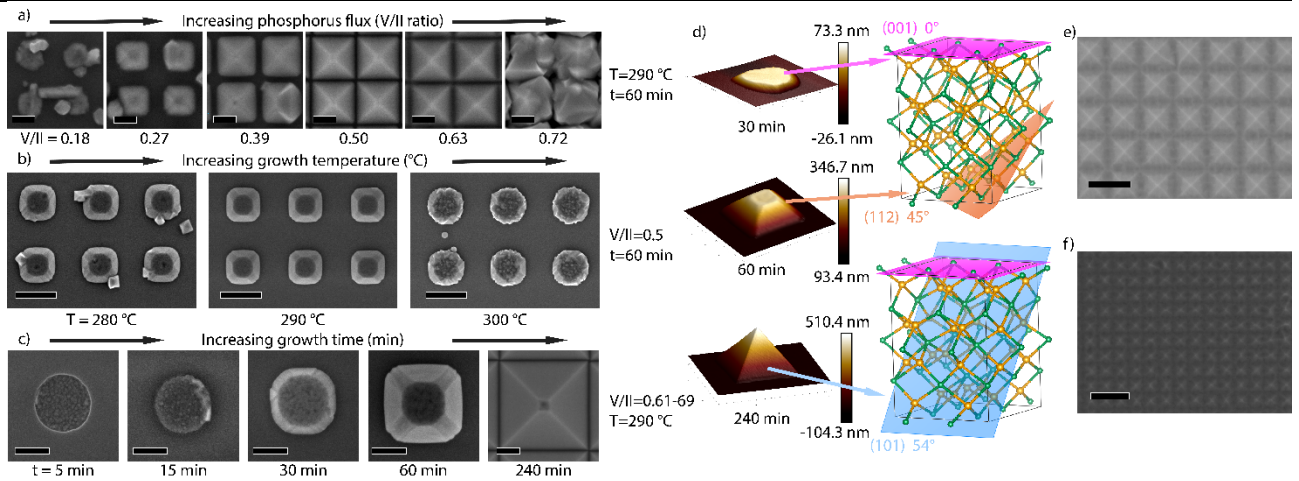


Figure 6.1 (a) SEM images of a flux series, varying the phosphorus to zinc (V/II) ratio at a constant zinc flux of 6.04×10^{-7} Torr from 0.18 to 0.72 for 60 min growth time at 290 °C manipulator temperature (30 nm nominal hole size, 200 nm pitch, 100 nm scale bars). (b) SEM images of a temperature series, varying the manipulator temperature between 280-300 °C at a V/II ratio of 0.5 for a growth time of 60 minutes (150 nm nominal hole size, 800 nm pitch, 500 nm scale bars). (c) SEM images of a time series of a pyramid spanning from 5 minutes to 240 minutes acquired at a V/II ratio of 0.61 (0.69 for the 240 minutes sample) and a manipulator temperature of 290 °C (note: last one taken at lower magnification to fit the full pyramid, 150 nm nominal hole size, 800 nm pitch, 100 nm scale bars). (d) AFM images of pyramids at different growth times and lattice structure models showing the different planes. (e) SEM image of initial stages of coalescence as seen with pyramids with 400 nm pitch and 75 nm nominal hole size (scale bar 500 nm). (f) SEM image of fully overgrown pyramid array with 200 nm pitch and 30 nm nominal hole size, still exhibiting a textured surface (scale bar 500 nm).

6.1.3 Results and Discussion

To fabricate the mask, InP (100) substrates are covered with a 30 nm thick nanopatterned SiO₂ layer. The pattern consisted of nanoscale holes with (nominal) diameters ranging from 30 to 150 nm and pitches from 200 to 2000 nm. Upon introduction to the MBE system, the thin native oxide inside the nanoscale holes is desorbed in the ultra-high vacuum system by high-temperature annealing under a P₂ flux. Prior to growth, the surface is exposed to a zinc pre-deposition as in ref [420]. The exact experimental details are provided in the Methodology section of the Supporting Information.

Following the Zn-P phase diagram, synthesis of Zn₃P₂ requires accurate regulation of the Zn and P₂ fluxes.⁶⁷ On a patterned substrate, the effective fluxes may vary locally as a consequence of the different desorption rates and diffusivity on the SiO₂ mask and openings. We thus vary the Zn and P₂ fluxes to find the parameter space leading to Zn₃P₂. For this we keep the Zn constant at a beam equivalent pressure of 6.04×10^{-7} Torr and vary the P₂ flux, resulting in a V/II (P₂/Zn) series. We also vary the growth time and substrate temperature. Figure 6.1 shows scanning electron micrographs (SEM) of the samples, illustrating the different morphologies obtained under the varied conditions. We observe that the V/II ratio regulates the selectivity and type of growth, similar to III-V materials.¹⁷⁶ At high P₂ flux, the zinc diffusion length is reduced to a degree where it cannot be incorporated into the low-energy sites of a well-defined pyramid. Instead, multiple nucleation occurs in a less ordered manner to produce the irregular shapes observed in Figure 1a for a V/II ratio of 0.72, which was previously shown to be a signature of phosphorus-rich growth conditions.¹⁸⁶ At low P₂ fluxes we observe a significant decrease in the volume of the structures again with poor faceting. The optimum selectivity and crystal shape are observed at V/II ratios of 0.5 to 0.63 at 290 °C. Interestingly, temperature also affects the optimum V/II ratio. Figure 6.1b depicts the shape evolution as a function of temperature at a V/II ratio of 0.5. Lower temperature growth (280 °C) looks similar to slightly zinc-rich growth conditions, while the higher temperature growth (300 °C) is more similar to phosphorus-rich growth. We attribute this to the strong temperature dependence of the sticking and desorption of zinc in vacuum in this temperature range.^{446,447} At 300 °C the faceting can be recovered by lowering the V/II ratio (Supporting Figure C.S2), which shows that it is possible to regain the optimal conditions by readjusting the V/II ratio.

Figure 6.1c illustrates the shape evolution of the structures as a function of time. Growth initiates through multiple small nuclei, which subsequently merge as to fill out the hole. Once the hole is filled, the material continues the faceting while also laterally overgrowing the oxide. Initially, a flat (001) top facet is observed without any clear side facets. After 30 minutes of growth, the (001) facet shrinks, with the development of (112) and (101) facets, with the latter increasingly dominating with time. This is to be expected, as through density functional theory (DFT) calculations we determined the surface energies for the facets to be $E_{(101)} = 0.60 \text{ Jm}^{-2} < E_{(112)} = 0.84 \text{ Jm}^{-2} < E_{(001)} = 1.03 \text{ Jm}^{-2}$.¹²⁴ After a certain time, which depends on the hole size and pitch, a pyramid enclosed only by the

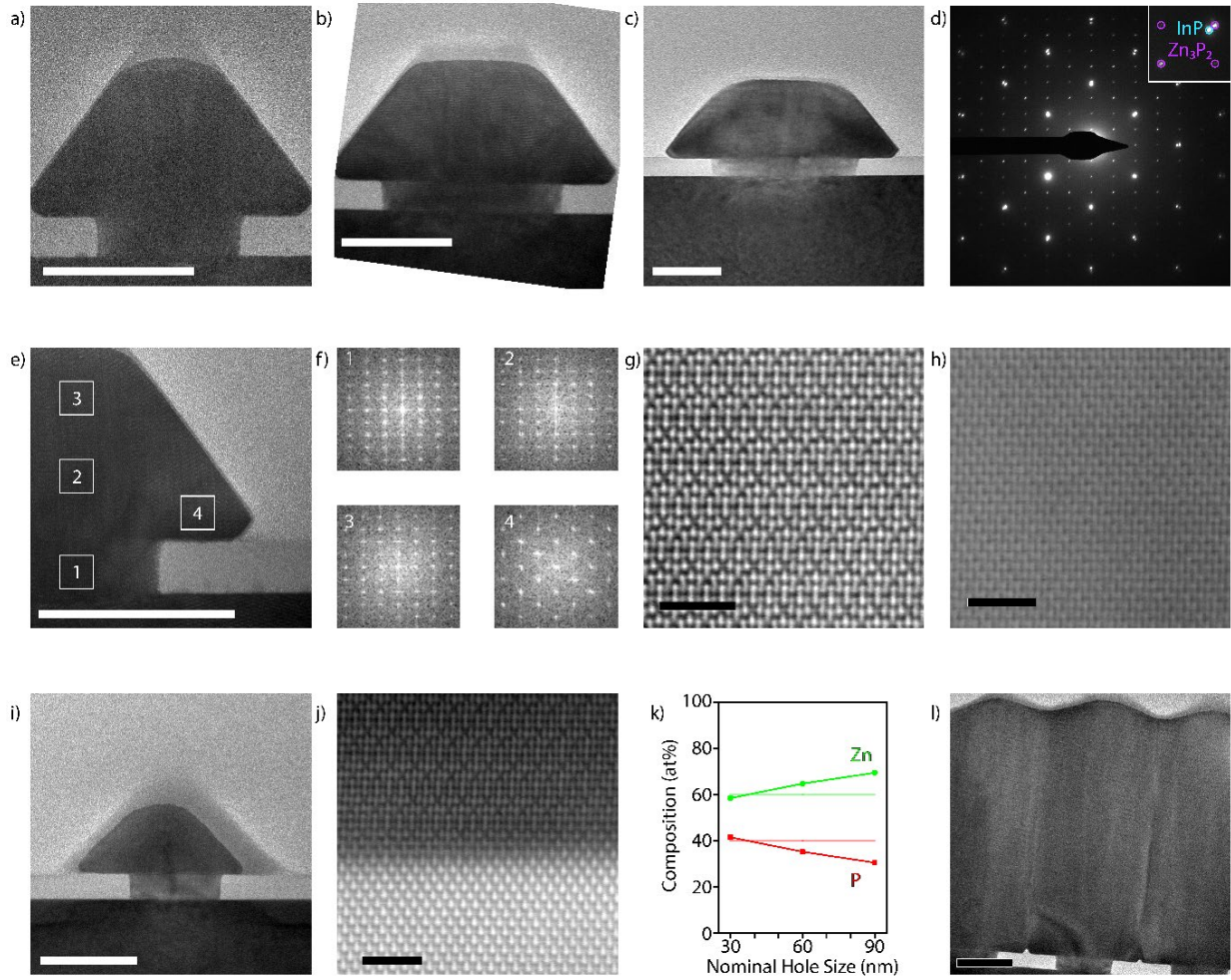


Figure 6.2 (a-c) Low-magnification HR-TEM images along the zinc phosphide [100] zone axis of pyramids grown in 30, 60, and 90 nm nominal holes for 1 hour at a V/II ratio of 0.5 and temperature of 290 °C (100 nm scale bars). (d) A representative SAED pattern showing diffraction from indium phosphide along the [110] zone axis superimposed on the relaxed zinc phosphide pattern along the [100] and [111] zone axes. (e) HR-TEM image of part of a pyramid highlighting areas where the FFT is acquired (100 nm scale bar). (f) FFT patterns from different parts of the pyramid, where 1-3 show a [100] zone axis and 4 shows a [111] zone axis. (g-h) Aberration corrected HAADF-STEM images of the core (g) along a [100] zone axis showing the systematic absences of zinc and the shell (h) along a [111] zone axis where the absences are not observed (2 nm scale bars). (i) Low-magnification HR-TEM image of a 30 nm nominal hole pyramid cut at 45° with respect to (a-c), resulting in a [110] zone axis with respect to zinc phosphide, highlighting the core-shell structure of the pyramids (100 nm scale bar). (j) Aberration corrected HAADF STEM image of the zinc phosphide and indium phosphide interface, showing pseudomorphic growth (2 nm scale bar). (k) Plot of the composition dependence on the nominal hole size as measured by STEM-EDX with the horizontal lines indicating the ideal stoichiometry. (l) Low-magnification HR-TEM image of the cross-section of a coalesced film grown from 30 nm nominal holes and 200 nm pitch with identical conditions as (a-c) but with a 6 hour growth time (100 nm scale bar).

most stable (101) surfaces is formed.^{310,311} The pyramidal shape is desirable due to it aiding in trapping light within the absorber layer.^{26,448,449} Figure 6.1d includes typical atomic force microscopy (AFM) images that are used to determine the facet orientation as a function of time, along with transmission electron microscopy (TEM) as presented below. As the pyramids continue to grow, they coalesce into a thin film in a LEO fashion. Larger hole sizes and smaller pitches were observed to overgrow quicker, with some representative examples of different stages of overgrowth shown in Figure 6.1e-f.

To understand the epitaxial relation in greater detail, a set of focused ion beam (FIB) lamellae of pyramids from different hole sizes, zone axes, and growth times are analysed by TEM. Figure 6.2a-c shows cross-sectional TEM of pyramids observed along a [110] zone axis of indium phosphide ([100] zone axis for zinc phosphide). In the smallest nominal hole size (30 nm) for the same pitch (400 nm) we observe a more complete pyramid compared to that of the larger nominal hole sizes (60 nm and 90 nm), which in turn exhibit a higher degree of lateral overgrowth. All pyramids start with a [001] growth direction, resulting in the epitaxial relationship $[001]_{\text{InP}}/[001]_{\text{Zn}_3\text{P}_2}$ in the interface normal, and $[110]_{\text{InP}}/[100]_{\text{Zn}_3\text{P}_2}$ in the direction perpendicular to the surface (corresponding to $[110]_{\text{InP}}/[110]_{\text{Zn}_3\text{P}_2}$ in the pseudo-cubic configuration of zinc phosphide). Figure 6.2d shows a representative selective area electron diffraction (SAED) pattern. The diffraction spots of zinc phosphide do not overlap with those of the substrate, indicating that the zinc

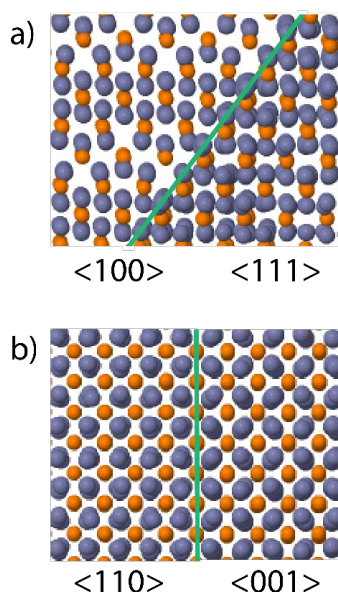


Figure 6.3 (a) Atomic model of the core-shell configuration when observed along the $[100]/[111]$ zone axes and (b) along the $[110]/[001]$ zone axes. Blue represents zinc and orange phosphorus.

phosphide has not taken the lattice parameter of the substrate, and had fully relaxed. The relaxation is further shown through geometric phase analysis (GPA) as presented below.

Figure 6.2e-f illustrate the crystalline orientation of a typical pyramid in different locations by the fast-Fourier transform (FFT) of the high-resolution (HR) TEM images. While the orientation is kept in the vertical direction, we observe that the lateral growth direction rotates 120° around the (101) facet. This also results in a change in the HR-TEM pattern. The different orientation is further confirmed by aberration corrected high-angle annular dark-field scanning (HAADF-S)TEM imaging shown in Figure 6.2g-h. The core-shell structure is also observed when looking at the pyramids through a $[100]$ zone axis with respect to the indium phosphide, shown in Figure 6.2i. A model of this change in orientation is presented further down.

Figure 6.2j illustrates the nature of the interface with the substrate through aberration-corrected HAADF-STEM, where we see the Zn-P-Zn trimers aligning with the In-P dumbbells. The images show the presence of vertical atomic steps at the interface, but no misfit-dislocations are detected. This indicates a pseudomorphic epitaxial relationship between the zinc phosphide and the substrate. Energy-dispersive x-ray spectroscopy (EDX) indicates potential interdiffusion of the indium and zinc at the interface (Supporting Figure C.S3). While slight interdiffusion between the layers is not necessarily detrimental for its properties, it could potentially be reduced by optimising the etching for the desired hole size or by reducing the zinc pre-deposition. We also performed GPA on an aberration-corrected HAADF-STEM image of a full pyramid, shown in Supporting Figure C.S4.^{450,451} This analysis confirms the absence of regular misfit-dislocations along the interface, while the zinc phosphide close to the interface exhibits compressive strain. Zinc phosphide slowly relaxes as it grows, resulting in a fully relaxed structure once outside of the confinement of the hole. The change in strain observed through GPA is $\sim 2.0\%$, in agreement with literature.^{68,130,395}

Next, we performed compositional mapping of the pyramids by EDX. The results as a function of nominal hole size are illustrated in Figure 6.2k. The material evolves from phosphorus-rich to zinc-rich by going from smaller to larger holes. This feature could eventually be used to locally tune the doping nature and density of the material. More detailed investigations are needed to fully characterise this phenomenon, which is outside the scope of this study.

The HR-TEM micrograph in Figure 6.2l shows the coalescence of the pyramids from a 6 hour grown sample. Clear boundaries are observed indicating that the pyramids do not coalesce into a mono-crystalline film. However, the boundaries should not necessarily be detrimental to potential photovoltaic applications. Because the charge separation will occur in a vertical direction, and not in-plane, charges may not interact with the grain boundaries during operation. Furthermore, grain boundaries have been shown to not be a major obstacle for zinc phosphide applications.^{62,452}

An atomic model of the lattice rotation around (101) is shown in Figure 6.3a. This occurs by a change in the ordering of the vacant sites, inherent to the zinc phosphide the crystal structure. The vacant sites are a result of the absence of zinc in 25% of the cubic sublattice of zinc phosphide's pseudo-fluoritic structure. As observed in the aberration-corrected images, we see the ordered absences of zinc atoms in the core of the pyramid, which become filled up towards the edge. This is consistently observed in all pyramids; however, it does not always occur at the same time for all pyramids and may even vary between facets on the same pyramid.

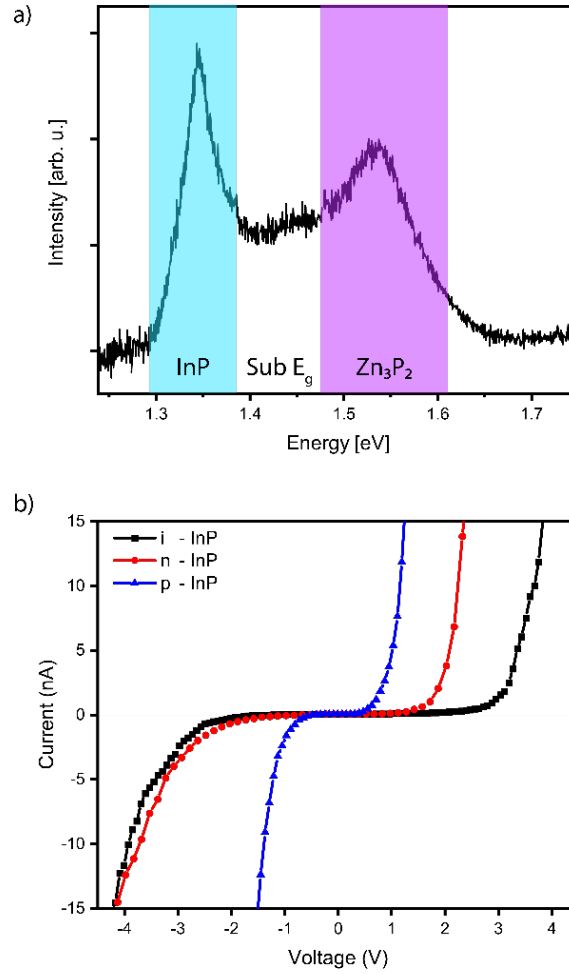


Figure 6.4 (a) PL spectrum acquired from an array with 600 nm pitch and 150 nm nominal hole size, showing the indium phosphide, zinc phosphide, and defect emission. (b) c-AFM I-V curves of zinc phosphide grown on intrinsic, n-type, and p-type indium phosphide.

A potential origin of this shell formation is that the new stacking sequence is energetically favored when the growth surface shifts from (001) to (101). The fact that there is not a clear and consistent trend, and that it does not occur straight away, indicates that the driving force for this process is small, however, first-principle simulations would be needed to clarify the energetics quantitatively. This trend is even clearer when observing the pyramids along the [100] zone axis with regards to the indium phosphide (100) substrate ([110] zone axis for zinc phosphide), where we see a distinct contrast between the core and the shell, which no longer seems to be on zone axis. The atomic model for this interface, shown in Figure 6.3b, indicates that the rotation previously explained will result in both parts still being on zone axis. The disorder observed in the corners could originate from the merging of (101) facets and prevents HR-imaging. However, STEM-EDX maps (shown in Supporting Figure C.S3) show that these regions are still zinc phosphide.

Finally, the functional properties are assessed by photoluminescence spectroscopy (PL) and conductive (C-)AFM, both performed at room temperature. The PL spectrum acquired from pyramids grown from 90 nm holes with a 600 nm pitch is shown in Figure 6.4a. We observed three main emission features: (1) indium phosphide substrate emission (1.34 eV), (2) zinc phosphide bandgap emission (1.53 eV), and (3) sub-bandgap zinc phosphide emission in the region in between.^{55,60,78} The presence of the direct bandgap emission indicates that the material grown through SAE exhibits very high quality. This response was limited to a subset of the larger hole sizes and the lowest pitches. A more detailed study of the optical properties will be reported separately.

C-AFM is carried out on samples grown on intrinsic, p-, and n-doped indium phosphide substrates. Representative I-V curves are shown in Figure 6.4b. The measurements are carried out on pyramids with 30 nm nominal holes and a 200 nm pitch to focus only on the influence of the substrate doping as an example. All the I-V curves exhibit a current rectification behavior under forward bias. The diode threshold voltage is highly dependent on the substrate doping (around 0.5 V, 1.5 V and 2.5 V respectively for p-, n- and intrinsic substrates). The sample grown on p-type indium phosphide shows a significant current under reverse bias. This feature may indicate a poor charge depletion at the substrate interface due to a p-type conductivity for the zinc phosphide pyramids, which is consistent with previous reports of the material.⁷¹ Considering the reverse branch of the n-type substrate I-V curve, we observe a more diode-like characteristic as would be expected for a p-n heterostructure. The I-V curve obtained on intrinsic substrates shows

a wide range with negligible current flow, which could be due to the low conductivity of the substrate. In principle, this could also be consistent with the p-type conduction of zinc phosphide.⁷¹ The influence of hole size and pitch are also of interest due to their influence on composition and interface area, and will be investigated in a separate study.

6.1.4 Conclusion

In summary, we demonstrate how to grow high-quality zinc phosphide nanostructures by SAE and its potential to obtain high-quality thin films through lateral overgrowth. We elucidate the conditions for selective growth and the mechanism by which the material nucleates inside the nanoscale holes and grows into single crystals. As the crystals develop, their surface evolves from a mixture of (001), (112) and (101) facets, into nanopyramids enclosed solely by the most stable (101) facets. The pyramids grow laterally, forming a thin film. Boundaries are observed in the coalescence. The stoichiometry of zinc phosphide depends on the hole size for a given set of conditions, from phosphorus-rich to zinc-rich with increasing hole size. PL measurements reveal a clear transition at 1.53 eV, attributed to bandgap recombination of zinc phosphide. This further illustrates the high-quality nature of the material. C-AFM showed a diode-like behaviour when the zinc phosphide was grown on an n-type substrate, indicating a p-type nature of the material. Due to the small interface area of each pyramid with the substrate, we believe this method is transferable to earth-abundant substrates, such as silicon, which would greatly improve the large-scale prospects of zinc phosphide-based photovoltaics, and the approach itself is a viable route for high-quality epitaxial growth of other earth-abundant materials.

6.1.5 Supporting Information

The supporting information can be found in Appendix C, and includes more in-depth experimental details and figures related to the DFT calculations, high temperature V/I series, STEM-EDX maps and GPA analysis.

6.1.6 Acknowledgements

We acknowledge Didem Dede, Nicholas Morgan and Wonjong Kim for helpful discussions regarding SAE and the substrate patterning procedures. We thank CMi, and in particular Zdenek Benes for support with mask fabrication. Victor Boureau and Lucie Navrátilová at EPFL-CIME are acknowledged for technical support with GPA and FIB, respectively.

S. E. S., E. Z. S., R. P., M. Z., J. -B. L., and A. F. i M were supported by SNSF Consolidator grant BSCGI0-157705 and the Max-Planck-EPFL-Center for Molecular Nanoscience and Nanotechnology. N. Y. D. acknowledges the UK Engineering and Physical Sciences Research Council (EPSRC) for funding (Grant No.EP/S001395/1). V. P. was supported by Piaget. M. F. and A. F. i M. were supported by the NCCR QSIT. R. R. Z. was supported by EPFL-CIME. The DFT calculations were performed using the computational facilities of the Advanced Research Computing @ Cardiff (ARCCA) Division, Cardiff University.

Chapter 7 Summary and Outlook

This thesis has investigated novel ways of growing zinc phosphide in the form of nanostructures to allow it to overcome the challenges which have inhibited its application in photovoltaics. We went about this using two main approaches: vapour-liquid-solid (VLS) nanowire growth and selective area epitaxy (SAE) on indium phosphide substrates by molecular beam epitaxy. I first presented how we could achieve epitaxial zinc phosphide nanowires in Chapter 4. With the help of a brief zinc pre-deposition, we could form indium nano-droplet catalysts through a reaction with the substrate. We mapped out the conditions for nanowire growth, and showed how this could result in various different morphologies (vertical, straight-tilted, zigzag, and horizontal). Furthermore, we showed that through the relative phosphorus to zinc flux (V/II ratio) we could tune the composition of the nanowires as they deviate from the stoichiometric Zn_3P_2 . This was in turn demonstrated to affect the optoelectronic properties.

Next, we delved deeper into the characterisation of the zigzag nanowires and explored their exact formation mechanism in Chapter 5. Using cutting-edge aberration corrected scanning electron microscopy we observed that the twin superlattices were not formed through standard twinning, but rather through heterotwins. Approximately a monolayer of indium from the catalyst would be inserted during the twin formation, consequently forming an indium phosphide-like heterointerface that facilitates the crystal rotation. We looked deeper into whether these heterotwins would affect the functional properties of the nanowires. However, we could not discern any influence on the optoelectronic properties, which was instead dominated through the nanophotonic waveguiding aspects of the tapered zigzag morphology. We also investigated the driving force for the twin superlattice formation in the case of zinc phosphide, which differs from other materials (e.g. III-Vs) as the main crystal facets are non-polar. The polarity has previously been argued to be one of the main aspects controlling the formation process. Taking the case of zinc phosphide into account we then developed a model to explain this which relies only on the geometric constraints of the catalyst deformation as a function of nanowire cross-section during growth. The model is more general than the previous ones with the capability to explain the twin superlattice formation mechanism in any material systems.

Finally, in Chapter 6, we finished off by exploring the growth of zinc phosphide using SAE in nanoscale holes etched in an oxide mask on indium phosphide. Zinc phosphide would initially grow in the form of nanopyramids, which if grown close enough together and for long enough, would coalesce and form a thin film. We observed that when the pyramids start to grow laterally, the growth plane would rotate by 120° to form a rotational core-shell structure. The composition of the nanopyramids was also found to be a function of the hole size which they grew from, with smaller holes being phosphorus-rich and larger ones being zinc-rich. We also presented a brief look into their functional properties, and through electrical characterisation we could determine that the material is p-type which is the standard for zinc phosphide due to the formation of self-interstitials. We could also observe a clear bandgap luminescence, indicative of a high-quality material, which was in the ideal region for photovoltaic applications.

These results demonstrate that the growth of zinc phosphide nanostructures, especially through the latter approach, is a viable method of achieving high-quality material with great control and tunability. Moreover, we have only just started to explore this rich material system and there is still plenty left to elucidate. With regards to VLS growth of zinc phosphide nanowires the areas of interest would be 1. introduction of extrinsic dopants (Mg/Ag), 2. formation of homojunctions by changing the V/II ratio during growth or heterojunctions by finishing the growth by converting the droplet to indium phosphide forming an axial heterostructure, and 3. growth of twin superlattice nanowires on (111) substrates. The first two would be of interest for optimising the material for photovoltaic applications, while the third one is more of a curiosity. We observed on the edge of a sample once that on a microfacet which looked to be (111) oriented we had an extraordinarily high density of these superlattice nanowires, and this could be an approach to further delve into these remarkable structures. As for the functional properties I believe we have only just started to scratch the surface. We are yet to perform any electrical measurements on zinc phosphide nanowires, and the influence of the composition would be of great interest. The initial investigations into the optical properties are very promising, and for example the optical absorptance of the zigzag nanowires have been shown to be greater than that of gallium arsenide nanowires (the material currently used in the bottom-up nanowire solar cells with the highest conversion efficiency). The potential influence of passivation on the functional properties is also still to be investigated.

The results derived from the SAE grown zinc phosphide are also very encouraging. We are observing very promising functional properties with great tuneability, and the nanopyramid geometry is ideal for enhancing light absorption. We are currently exploring the hole size and pitch dependence of the nanopyramids on the functional properties through various means. As for growth, there are two aspects which would be the topic of the next studies: growth on earth-abundant substrates and the growth of arrays large enough for prototype device fabrication. Initial growth on silicon (100) showed good selectivity, albeit the resulting structures exhibited a multifaceted morphology indicative of a phosphorus-rich growth. Due to limited time with the growth setup we could not

explore this further, however, by tuning the V/II ratio (and potentially the temperature) I believe it will still be possible. The difference in lattice constant between silicon and the pseudo-cubic unit cell of zinc phosphide is approximately 5%, which would be towards the limit for defect-free pseudomorphic growth. We are also yet to study the influence of oxide material or thickness, and how it could potentially influence the growth and functional properties. Doping, heterojunction formation, and passivation of these structures are also of great interest to explore for further optimization of the material for devices. SAE consequently provides an excellent platform to investigate the optimisation of zinc phosphide for potential applications.

To conclude, in this work we have successfully explored novel avenues to grow zinc phosphide nanostructures. Through in-depth characterisation we have demonstrated their high-quality and tunability by mapping the ideal growth parameters with molecular beam epitaxy and elucidated the growth mechanisms of the different nanostructures. This project leaves off with a plethora of possible follow-up studies, with the prospect of further optimising zinc phosphide and allowing it to reach its potential as an earth-abundant photovoltaic material. The next step for the utilisation of nanostructured zinc phosphide is to start preparing devices based on them, which will allow for the optimisation of the material with its final purpose in mind. Furthermore, the methods used (particularly SAE and lateral overgrowth into thin films) also stand to facilitate the epitaxial growth of other earth-abundant materials and open up their potential application. The large-scale production of renewable energy sources will be greatly enhanced by the increased viability of high-quality and earth-abundant alternatives, which is imperative to safekeep the environment from the depths of human greed and folly.

References

1. Health, M. of. *Mortality and morbidity during the London fog of December 1952. Reports on public health and medical subjects* (HMSO London, 1954).
2. Arrhenius, S. XXXI. On the influence of carbonic acid in the air upon the temperature of the ground. *Philos. Mag.* **41**, 237–276 (1896).
3. Arrhenius, G., Caldwell, K. & Wold, S. A tribute to the memory of Svante Arrhenius (1859-1927): A scientist ahead of his time. in (IVA, 2008).
4. Edenhofer, O. *et al. Renewable energy sources and climate change mitigation: Special report of the intergovernmental panel on climate change.* (Cambridge University Press, 2011).
5. Williams, A. A., Karoly, D. J. & Tapper, N. The sensitivity of Australian fire danger to climate change. *Clim. Change* **49**, 171–191 (2001).
6. Lin, N., Emanuel, K., Oppenheimer, M. & Vanmarcke, E. Physically based assessment of hurricane surge threat under climate change. *Nat. Clim. Change* **2**, 462–467 (2012).
7. Mann, M. E. & Emanuel, K. A. Atlantic hurricane trends linked to climate change. *Eos Trans. AGU* **87**, 233–241 (2006).
8. Brulle, R. J. Institutionalizing delay: foundation funding and the creation of US climate change counter-movement organizations. *Clim. Change* **122**, 681–694 (2014).
9. Seljom, P. *et al.* Modelling the effects of climate change on the energy system—a case study of Norway. *Energy policy* **39**, 7310–7321 (2011).
10. Schmalensee, R. *et al.* The Future of Solar Energy: An Interdisciplinary MIT Study. (2015).
11. Luque, A. & Hegedus, S. *Handbook of photovoltaic science and engineering.* (John Wiley & Sons, 2011).
12. Walter, M. G. *et al.* Solar water splitting cells. *Chem. Rev.* **110**, 6446–6473 (2010).
13. Yu, J., Low, J., Xiao, W., Zhou, P. & Jaroniec, M. Enhanced photocatalytic CO₂-reduction activity of anatase TiO₂ by coexposed {001} and {101} facets. *J. Am. Chem. Soc.* **136**, 8839–8842 (2014).
14. Gray, H. B. Powering the planet with solar fuel. *Nat. Chem.* **1**, 7–7 (2009).
15. International Energy Agency. World electricity consumption 2017. <https://www.iea.org/data-and-statistics?country=WORLD&fuel=Energy%20consumption&indicator=Electricity%20consumption> (2020).
16. Kurtz, S. Are We Still Overestimating Costs for Wind and Solar? *Joule* **4**, 294–295 (2020).
17. Steffen, B., Beuse, M., Tautorat, P. & Schmidt, T. S. Experience Curves for Operations and Maintenance Costs of Renewable Energy Technologies. *Joule* **4**, 359–375 (2020).
18. Grundmann, M. *The Physics of Semiconductors.* (Springer, 2010).
19. Shockley, W. & Queisser, H. J. Detailed Balance Limit of Efficiency of p-n Junction Solar Cells. *J. Appl. Phys.* **32**, 510–519 (1961).

20. Alta sets flexible solar record with 29.1% GaAs cell. *Optics* <https://optics.org/news/9/12/19> (2018).
21. Yoshikawa, K. *et al.* Silicon heterojunction solar cell with interdigitated back contacts for a photoconversion efficiency over 26%. *Nat. Energy* **2**, 17032 (2017).
22. Green, M. A. *et al.* Solar cell efficiency tables (Version 55). *Prog. Photovolt.* **28**, 3–15 (2020).
23. Todorov, T., Gunawan, O. & Guha, S. A road towards 25% efficiency and beyond: perovskite tandem solar cells. *Mol. Syst. Des. Eng.* **1**, 370–376 (2016).
24. Geisz, J. F. *et al.* Building a six-junction inverted metamorphic concentrator solar cell. *IEEE J. Photovolt.* **8**, 626–632 (2017).
25. Bube, R. H. *Photoelectronic properties of semiconductors*. (Cambridge University Press, 1992).
26. Garnett, E. C., Ehrler, B., Polman, A. & Alarcon-Llado, E. Photonics for Photovoltaics – advances and opportunities. *ACS Photonics* (2020) doi:10.1021/acsp Photonics.0c01045.
27. Atwater, H. A. & Polman, A. Plasmonics for improved photovoltaic devices. *Nat. Mater.* **9**, 205–213 (2010).
28. Chen, X., Peng, D., Ju, Q. & Wang, F. Photon upconversion in core–shell nanoparticles. *Chem. Soc. Rev.* **44**, 1318–1330 (2015).
29. Trupke, T., Green, M. A. & Würfel, P. Improving solar cell efficiencies by down-conversion of high-energy photons. *J. Appl. Phys.* **92**, 1668–1674 (2002).
30. Zhou, D. & Biswas, R. Photonic crystal enhanced light-trapping in thin film solar cells. *J. Appl. Phys.* **103**, 093102 (2008).
31. Yablonovitch, E. Inhibited spontaneous emission in solid-state physics and electronics. *Phys. Rev. Lett.* **58**, 2059 (1987).
32. Jain, A. *et al.* Commentary: The Materials Project: A materials genome approach to accelerating materials innovation. *APL Materials* **1**, 011002 (2013).
33. Liu, J. *et al.* Preparation of Cu (In, Ga) Se₂ thin film by sputtering from Cu (In, Ga) Se₂ quaternary target. *Prog. Nat. Sci.* **23**, 133–138 (2013).
34. Wang, W. *et al.* Device characteristics of CZTSSe thin-film solar cells with 12.6% efficiency. *Adv. Energy Mater.* **4**, 1301465 (2014).
35. Nechache, R. *et al.* Bandgap tuning of multiferroic oxide solar cells. *Nat. Photonics* **9**, 61 (2015).
36. Lim, F. J. *et al.* Addressing the light-soaking issue in inverted organic solar cells using chemical bath deposited fluorinated TiO_x electron transport layer. *J. Mater. Chem. A* **3**, 314–322 (2015).
37. O'Regan, B. & Grätzel, M. A low-cost, high-efficiency solar cell based on dye-sensitized colloidal TiO₂ films. *Nature* **353**, 737–740 (1991).
38. Docampo, P., Ball, J. M., Darwich, M., Eperon, G. E. & Snaith, H. J. Efficient organometal trihalide perovskite planar-heterojunction solar cells on flexible polymer substrates. *Nat. Commun.* **4**, 1–6 (2013).
39. Atesin, T. A., Bashir, S. & Liu, J. L. *Nanostructured Materials for Next-Generation Energy Storage and Conversion*. (Springer, 2017).

40. Lovrić, J. *et al.* Differences in subcellular distribution and toxicity of green and red emitting CdTe quantum dots. *J. Mol. Med.* **83**, 377–385 (2005).
41. Giraldo, S. *et al.* Progress and perspectives of thin film kesterite photovoltaic technology: a critical review. *Adv. Mater.* **31**, 1806692 (2019).
42. Minami, T., Nishi, Y. & Miyata, T. Cu₂O-based solar cells using oxide semiconductors. *J. Semicond.* **37**, 014002 (2016).
43. Minami, T., Nishi, Y. & Miyata, T. Efficiency enhancement using a Zn_{1-x}Ge_xO thin film as an n-type window layer in Cu₂O-based heterojunction solar cells. *Appl. Phys. Exp.* **9**, 052301 (2016).
44. Coll, M. *et al.* Towards oxide electronics: a roadmap. *Appl. Surf. Sci.* **482**, 1–93 (2019).
45. Fridkin, V. M. *Photoferroelectrics*. vol. 9 (Springer Science & Business Media, 2012).
46. Kippelen, B. & Brédas, J.-L. Organic photovoltaics. *Energy Environ. Sci.* **2**, 251–261 (2009).
47. Gong, J., Sumathy, K., Qiao, Q. & Zhou, Z. Review on dye-sensitized solar cells (DSSCs): Advanced techniques and research trends. *Renew. Sust. Energ. Rev.* **68**, 234–246 (2017).
48. Snaith, H. J. Perovskites: the emergence of a new era for low-cost, high-efficiency solar cells. *J. Phys. Chem. Lett.* **4**, 3623–3630 (2013).
49. Kojima, A., Teshima, K., Shirai, Y. & Miyasaka, T. Organometal halide perovskites as visible-light sensitizers for photovoltaic cells. *J. Am. Chem. Soc.* **131**, 6050–6051 (2009).
50. NREL. Best Research-Cell Efficiency Chart. <https://www.nrel.gov/pv/cell-efficiency.html>.
51. Köhnen, E. *et al.* Highly efficient monolithic perovskite silicon tandem solar cells: analyzing the influence of current mismatch on device performance. *Sustain. Energy Fuels* **3**, 1995–2005 (2019).
52. Hasan, S. A. U., Lee, D. S., Im, S. H. & Hong, K.-H. Present Status and Research Prospects of Tin-based Perovskite Solar Cells. *Solar RRL* **4**, 1900310 (2020).
53. Slotcavage, D. J., Karunadasa, H. I. & McGehee, M. D. Light-induced phase segregation in halide-perovskite absorbers. *ACS Energy Lett.* **1**, 1199–1205 (2016).
54. Leijtens, T. *et al.* Stability of metal halide perovskite solar cells. *Adv. Energy Mater.* **5**, 1500963 (2015).
55. Kimball, G. M., Mueller, A. M., Lewis, N. S. & Atwater, H. A. Photoluminescence-based measurements of the energy gap and diffusion length of Zn₃P₂. *Appl. Phys. Lett.* **95**, 112103 (2009).
56. Fagen, E. A. Optical properties of Zn₃P₂. *J. Appl. Phys.* **50**, 6505–6515 (1979).
57. Pawlikowski, J. Absorption-edge of Zn₃P₂. *Phys. Rev. B* **26**, 4711–4713 (1982).
58. Misiewicz, J. Inter-band Transitions in Zn₃P₂. *J. Condens. Matter Phys.* **2**, 2053–2072 (1990).
59. Pawlikowski, J. Band-structure and Properties of Zn₃P₂ - Promising New Infrared Material. *Infrared Phys.* **21**, 181–187 (1981).
60. Briones, F., Wang, F. & Bube, R. Pair Transitions in Zn₃P₂. *Appl. Phys. Lett.* **39**, 805–807 (1981).

-
61. Wyeth, N. & Catalano, A. Spectral Response Measurements of Minority-carrier Diffusion Length in Zn₃P₂. *J. Appl. Phys.* **50**, 1403–1407 (1979).
 62. Bhushan, M. & Catalano, A. Polychrystalline Zn₃P₂ Schottky barrier solar cells. *Appl. Phys. Lett.* **38**, 39–41 (1981).
 63. Bleiwas, D. I. *Byproduct mineral commodities used for the production of photovoltaic cells*. (US Department of the Interior, US Geological Survey, 2010).
 64. Chernoff, C. B. & Orris, G. J. *Data Set of World Phosphate Mines, Deposits, and Occurrences: Part A. Geologic Data*. (US Department of the Interior, US Geological Survey, 2002).
 65. Sittig, M. *Handbook of toxic and hazardous chemicals*. (Noyes Publications, Park Ridge, N.J, USA, 1981).
 66. Stephenson, J. B. P. Zinc phosphide poisoning. *Arch. Environ. Health* **15**, 83–88 (1967).
 67. Ghasemi, M., Stutz, E., Escobar Steinvall, S., Zamani, M. & Fontcuberta i Morral, A. Thermodynamic re-assessment of the Zn-P binary system. *Acta Mater.* **6**, 100301 (2019).
 68. Stackelberg, M. V. & Paulus, R. Investigation on phosphides and arsenides of zinc and cadmium. the Zn₃P₂ lattice. *Z. phys. Chem* **28**, 427–460 (1935).
 69. Lagrenaudie, J. Propriétés semi-conducteurs du phosphure de zinc (P₂ Zn₃). *J. Chim. Phys.* **50**, 545–547 (1953).
 70. Catalano, A. The growth of large Zn₃P₂ crystals by vapor transport. *J. Cryst. Growth* **49**, 681–686 (1980).
 71. Catalano, A. & Hall, R. Defect Dominated Conductivity in Zn₃P₂. *J. Phys. Chem. Solids* **41**, 635–640 (1980).
 72. Wyeth, N. & Catalano, A. Barrier Heights of Evaporated Metal Contacts on Zn₃P₂. *J. Appl. Phys.* **51**, 2286–2288 (1980).
 73. Long, J. The Growth of Zn₃P₂ by Metalorganic Chemical Vapor Deposition. *J. Electrochem.* **130**, 725–728 (1983).
 74. Chu, T., Chu, S., Murthy, K., Stokes, E. & Russell, P. Deposition and Properties of Zinc Phosphide Films. *J. Appl. Phys.* **54**, 2063–2068 (1983).
 75. Kimball, G. M., Lewis, N. S. & Atwater, H. A. Mg doping and alloying in Zn₃P₂ heterojunction solar cells. in *Photovoltaic Specialists Conference (PVSC)* 1039–1043 (2010).
 76. Katsube, R., Kazumi, K., Tadokoro, T. & Nose, Y. Reactive Epitaxial Formation of a Mg-P-Zn Ternary Semiconductor in Mg/Zn₃P₂ Solar Cells. *ACS Appl. Mater. Interfaces* **10**, 36102–36107 (2018).
 77. Demers, S. & van de Walle, A. Intrinsic defects and dopability of zinc phosphide. *Phys. Rev. B* **85**, (2012).
 78. Mirowska, N. & Misiewicz, J. Defect-related transitions in Zn₃P₂ studied by means of photovoltaic effect spectroscopy. *Semi-cond. Sci. Technol.* **7**, 1332–1336 (1992).
 79. Suda, T., Kobayashi, M., Kuroyanagi, A. & Kurita, S. Zn₃P₂/ITO Heterojunction Solar Cells. *Jpn. J. Appl. Phys.* **21**, 63 (1982).
 80. Pawlikowski, J. M., Misiewicz, J. & Mirowska, N. Direct and Indirect Optical Transitions in Zn₃P₂. *J. Phys. Chem. Solids* **40**, 1027–1033 (1979).
 81. Misiewicz, J. *et al.* Zn₃P₂ - A New Material for Optoelectronic Devices. *Microelectron. J.* **25**, R23–R28 (1994).
 82. Bryja, L., Jezierski, K. & Misiewicz, J. Optical Properties of Zn₃P₂ Thin-films. *Thin Solid Films* **229**, 11–13 (1993).

-
83. Sieranski, K., Szatkowski, J. & Misiewicz, J. Semiempirical tight-binding band structure of II3V2 semiconductors: Cd3P2, Zn3P2, Cd3As2, and Zn3As2. *Phys. Rev. B* **50**, 7331 (1994).
 84. Komorowska, M., Sitarek, P. & Misiewicz, J. Electron Paramagnetic Resonance in Zn3P2. *Phys. Status Solidi A* **144**, 189–193 (1994).
 85. Suda, T. Zinc Phosphide Thin-films Grown by Plasma-assisted Vapor-phase Deposition. *J. Cryst. Growth* **99**, 625–629 (1990).
 86. Suda, T. & Bube, R. Deep Levels in Zinc Phosphide. *Appl. Phys. Lett.* **45**, 775–777 (1984).
 87. Suda, T. & Kakishita, K. Epitaxial growth of zinc phosphide. *J. Appl. Phys.* **71**, 3039–3041 (1992).
 88. Suda, T. & Kuroyanagi, A. Effect of Monatomic Hydrogen in Zinc Phosphide. *Jpn. J. Appl. Phys* **25**, L993–L995 (1986).
 89. Suda, T., Kakishita, K., Sato, H. & Sasaki, K. N-type zinc phosphide grown by molecular beam epitaxy. *Appl. Phys. Lett.* **69**, 2426–2428 (1996).
 90. Suda, T., Miyakawa, T. & Kurita, S. Zinc Phosphide Thin-films Grown by RF Sputtering. *J. Cryst. Growth* **86**, 423–429 (1988).
 91. Suda, T., Nishimoto, T. & Kurita, S. Zinc Phosphide Thin-films Grown by Low-pressure Vapor-phase Deposition. *J. Cryst. Growth* **86**, 430–435 (1988).
 92. Suda, T., Murata, Y. & Kurita, S. Anodic oxidation of Zinc Phosphide. *Jpn. J. Appl. Phys* **25**, L162–L164 (1986).
 93. Kakishita, K., Baba, T. & Suda, T. Zn3P2 thin films grown on glass substrates by MOCVD. *Thin Solid Films* **334**, 25–29 (1998).
 94. Kakishita, K., Kondo, S. & Suda, T. Photoresponse of zinc phosphide thin films grown by ionized cluster beam deposition. *Nucl. Instrum. Meth. B* **121**, 175–178 (1997).
 95. Kakishita, K., Aihara, K. & Suda, T. Zn3P2 Photovoltaic Film Growth for Zn3P2/ZnSe Solar Cell. *Sol. Energ. Mat. Sol. C* **35**, 333–340 (1994).
 96. Kakishita, K., Aihara, K. & Suda, T. Zinc Phosphide Epitaxial Growth by Photo-MOCVD. *Appl. Surf. Sci.* **79–80**, 281–286 (1994).
 97. Kakishita, K., Ikeda, S. & Suda, T. Zn3P2 Epitaxial Growth by MOCVD. *J. Cryst. Growth* **115**, 793–797 (1991).
 98. Kato, Y., Kurita, S. & Suda, T. Photoenhanced Chemical Vapor Deposition of Zinc Phosphide. *J. Appl. Phys.* **62**, 3733–3739 (1987).
 99. Kuroyanagi, A. & Suda, T. Single-crystal Growth and Characterization of Zinc Phosphide. *J. Cryst. Growth* **100**, 1–4 (1990).
 100. Shen, G., Bando, Y., Hu, J. & Golberg, D. Single-crystalline trumpetlike zinc phosphide nanostructures. *Appl. Phys. Lett.* **88**, 143105 (2006).
 101. Shen, G., Chen, P.-C., Bando, Y., Golberg, D. & Zhou, C. Single-Crystalline and Twinned Zn3P2 Nanowires: Synthesis, Characterization, and Electronic Properties. *J. Phys. Chem. C* **112**, 16405–16410 (2008).
 102. Shen, G., Chen, P.-C., Bando, Y., Golberg, D. & Zhou, C. Bicrystalline Zn3P2 and Cd3P2 Nanobelts and Their Electronic Transport Properties. *Chem. Mater.* **20**, 7319–7323 (2008).
 103. Shen, G., Ye, C., Golberg, D., Hu, J. & Bando, Y. Structure and cathodoluminescence of hierarchical Zn3P2/ZnS nanotube/nanowire heterostructures. *Appl. Phys. Lett.* **90**, (2007).

-
104. Bosco, J. P., Scanlon, D. O., Watson, G. W., Lewis, N. S. & Atwater, H. A. Energy-band alignment of II-VI/Zn₃P₂ heterojunctions from x-ray photoemission spectroscopy. *J. Appl. Phys.* **113**, (2013).
105. Bosco, J. P., Demers, S. B., Kimball, G. M., Lewis, N. S. & Atwater, H. A. Band alignment of epitaxial ZnS/Zn₃P₂ heterojunctions. *J. Appl. Phys.* **112**, (2012).
106. Bosco, J. P., Kimball, G. M., Lewis, N. S. & Atwater, H. A. Pseudomorphic growth and strain relaxation of alpha-Zn₃P₂ on GaAs(001) by molecular beam epitaxy. *J. Cryst. Growth* **363**, 205–210 (2013).
107. Jeon, S. *et al.* Growth Mechanism and Electronic Structure of Zn₃P₂ on the Ga-Rich GaAs(001) Surface. *J. Phys. Chem. C* **118**, 12717–12726 (2014).
108. Kimball, G. M., Lewis, N. S. & Atwater, H. A. Synthesis and Surface Chemistry of Zn₃P₂. in *PVSC: 2008 33rd IEEE Photovoltaic Specialists Conference, Vols 1-4* 150–155 (IEEE, 2008).
109. Kimball, G. M., Lewis, N. S. & Atwater, H. A. Direct evidence of Mg-Zn-P alloy formation in Mg/Zn₃P₂ solar cells. *Photovoltaic Specialists Conference (PVSC) 37th IEEE*, 3381 (2011).
110. Vazquez-Mena, O. *et al.* Performance Enhancement of a Graphene-Zinc Phosphide Solar Cell Using the Electric Field-Effect. *Nano Lett.* **14**, 4280–4285 (2014).
111. Green, M. & O'Brien, P. A Novel Metalorganic Route to Nanocrystallites of Zinc Phosphide. *Chem. Mater.* **13**, 4500–4505 (2001).
112. Lubber, E. J., Mobarok, M. H. & Buriak, J. M. Solution-Processed Zinc Phosphide (α -Zn₃P₂) Colloidal Semiconducting Nanocrystals for Thin Film Photovoltaic Applications. *ACS Nano* **7**, 8136–8146 (2013).
113. Mobarok, M. H. & Buriak, J. M. Elucidating the Surface Chemistry of Zinc Phosphide Nanoparticles Through Ligand Exchange. *Chem. Mater.* **26**, 4653–4661 (2014).
114. Mobarok, M. H. *et al.* Phase-Pure Crystalline Zinc Phosphide Nanoparticles: Synthetic Approaches and Characterization. *Chem. Mater.* **26**, 1925–1935 (2014).
115. Lee, K., Huang, Y. & Corrigan, J. F. Facile synthesis of a hexanuclear zinc-acetato-trimethylsilylphosphinidene cluster: a single-source precursor to Zn₃P₂ nanoparticles. *Chem. Commun.* **55**, 11466–11469 (2019).
116. Glassy, B. A. & Cossairt, B. M. Ternary synthesis of colloidal Zn₃P₂ quantum dots. *Chem. Commun.* **51**, 5283–5286 (2015).
117. Glassy, B. A. & Cossairt, B. M. Resolving the Chemistry of Zn₃P₂ Nanocrystal Growth. *Chem. Mater.* **28**, 6374–6380 (2016).
118. Glassy, B. A. & Cossairt, B. M. II₃V₂ (II: Zn, Cd; V: P, As) Semiconductors: From Bulk Solids to Colloidal Nanocrystals. *Small* **13**, 1702038 (2017).
119. Katsube, R. *et al.* Growth and characterization of indium-doped Zn₃P₂ bulk crystals. *Jpn. J. Appl. Phys.* **55**, 041201 (2016).
120. Katsube, R. & Nose, Y. Orientation of Zn₃P₂ films via phosphidation of Zn precursors. *J. Cryst. Growth* **459**, 95–99 (2017).
121. Katsube, R. & Nose, Y. Thermodynamic considerations on interfacial reactivity concerning carrier transport characteristics in metal/p-Zn₃P₂ junctions. *J. Mater. Chem. C* **5**, 5538–5543 (2017).

-
122. Katsube, R. & Nose, Y. Experimental investigation of phase equilibria around a ternary compound semiconductor $\text{Mg}(\text{Mg}_x\text{Zn}_{1-x})\text{P}_2$ in the Mg-P-Zn system at 300 °C using Sn flux. *J. Solid State Chem.* **280**, 120983 (2019).
123. Dzade, N. Y. First-Principles Insights into the Interface Chemistry between 4-Aminothiophenol and Zinc Phosphide (Zn_3P_2) Nanoparticles. *ACS Omega* **5**, 1025–1032 (2020).
124. Dzade, N. Y. Unravelling the early oxidation mechanism of zinc phosphide (Zn_3P_2) surfaces by adsorbed oxygen and water: a first-principles DFT-D3 investigation. *Phys. Chem. Chem. Phys.* **22**, 1444–1456 (2020).
125. Li, W. *et al.* Self-supported Zn_3P_2 nanowire arrays grafted on carbon fabrics as an advanced integrated anode for flexible lithium ion batteries. *Nanoscale* **8**, 8666–8672 (2016).
126. Bichat, M.-P., Pascal, J.-L., Gillot, F. & Favier, F. Electrochemical Lithium Insertion in Zn_3P_2 Zinc Phosphide. *Chem. Mater.* **17**, 6761–6771 (2005).
127. Nam, K.-H., Hwa, Y. & Park, C.-M. Zinc Phosphides as Outstanding Sodium-Ion Battery Anodes. *ACS Appl. Mater. Interfaces* **12**, 15053–15062 (2020).
128. Im, H. S. *et al.* Zn_3P_2 - Zn_3As_2 Solid Solution Nanowires. *Nano Lett.* **15**, 990–997 (2015).
129. Sudhakar, S. & Baskar, K. Influence of cooling rate on the liquid-phase epitaxial growth of Zn_3P_2 . *J. Cryst. Growth* **310**, 2707–2711 (2008).
130. Kim, H. S. *et al.* Three-Dimensional Structure of Twinned and Zigzagged One-Dimensional Nanostructures Using Electron Tomography. *Nano Lett.* **10**, 1682–1691 (2010).
131. Lagrenaudie, J. Propriétés du phosphore de zinc P_2Zn_3 en cristaux. *J. Phys. Radium* **16**, 234–235 (1955).
132. Muñoz, V., Decroix, D., Chevy, A. & Besson, J. M. Optical properties of zinc phosphide. *J. Appl. Phys.* **60**, 3282–3288 (1986).
133. Misiewicz, J. Optical and electrical investigations of imperfection levels in Zn_3P_2 . *J. Phys. Chem. Solids* **50**, 1013–1022 (1989).
134. Misiewicz, J., Sujak-Cyrul, B. & Bartczak, A. Optical transitions in Zn_3P_2 within the 0.06–1.4 eV energy range. *Solid State Commun.* **58**, 677–679 (1986).
135. Zdanowicz, W. & Henkie, Z. Some Electric Properties of Zn_3P_2 . *B. Acad. Pol. Sci.-Chim.* **7**, 729–734 (1964).
136. Kurbatov, L. N. *et al.* Luminescence of cadmium and zinc phosphides. *Sov. J. Quantum Electron.* **6**, 166–168 (1976).
137. Möller, A. *et al.* Growth, electronic and device properties of Zn_3P_2 single crystals. *Inst. Phys. Conf. Ser.* **43**, 825–828 (1979).
138. Wang, F.-C., Fahrenbruch, A. L. & Bube, R. H. Electrical properties of Zn_3P_2 single crystals. *J. Electron. Mater.* **11**, 75–88 (1982).
139. Sierański, K. & Szatkowski, J. Electrical conductivity of Zn_3P_2 . *Phys. Status Solidi A* **94**, K133–K135 (1986).
140. Szatkowski, J. & Sieranski, K. Electrical conductivity of Zn_3P_2 . *Acta Phys. Pol.* **A71**, 297–299 (1987).
141. Muñoz, V., Gonzalez, J. & Chevy, A. Effect of surface damage on the photoconductivity response of zinc phosphide. *Phys. Status Solidi A* **97**, 587–591 (1986).
142. Swinkels, M. Y. *et al.* Measuring the Optical Absorption of Single Nanowires. *Phys. Rev. Applied* **14**, 024045 (2020).

143. Lombardi, G., de Oliveira, F., Teodoro, M. & Chiquito, A. Investigation of trapping levels in p-type Zn₃P₂ nanowires using transport and optical properties. *Appl. Phys. Lett.* **112**, 193103 (2018).
144. Bhushan, M. Mg diffused zinc phosphide n/p junctions. *J. Appl. Phys.* **53**, 514–519 (1982).
145. Catalano, A. & Bhushan, M. Evidence of p-n Homojunction Formation in Zn₃P₂. *Appl. Phys. Lett.* **37**, 567–569 (1980).
146. Mirowska, N., Szatkowski, J. & Gumieny, Z. Photoelectric properties of undoped and Cd-doped Zn₃P₂-Mg junctions. *Infrared Phys.* **28**, 97–99 (1988).
147. Yang, R. *et al.* Single-crystalline branched zinc phosphide nanostructures: Synthesis, properties, and optoelectronic devices. *Nano Lett.* **7**, 269–275 (2007).
148. Bhushan, M. & Meakin, J. D. *Zn₃P₂ as an Improved Semiconductor for Photovoltaic Solar Cells: Final Report, April 1983-March 1984.* (1985).
149. Pawlikowski, J. M. Preparation and characterization of close-spaced vapour transport thin films of ZnSe for heterojunction solar cells. *Thin Solid Films* **127**, 9–28 (1985).
150. Sun, T. *et al.* Synthesis and characterization of Zn₃P₂/ZnS core/shell nanowires. *Phys. Lett. A* **375**, 2118–2121 (2011).
151. Wu, P. *et al.* Novel Type-II Zn₃P₂/ZnO Core/Shell Nanowires: Synthesis, Characteristic, and Photoluminescence Properties. *Cryst. Growth Des.* **11**, 1417–1421 (2011).
152. Nayar, P. & Catalano, A. Zinc Phosphide Zinc Oxide Heterojunction Solar Cells. *Appl. Phys. Lett.* **39**, 105–107 (1981).
153. Nayar, P. Properties of Zinc Phosphide Zinc Oxide Heterojunctions. *J. Appl. Phys.* **53**, 1069–1075 (1982).
154. Kuroyanagi, A. & Suda, T. Photovoltaic properties in CdS/Zn₃P₂ heterojunctions prepared by ionized evaporation of CdS. *Electr. Eng. Jpn.* **109**, 48–56 (1989).
155. Feynman, R. P. There's plenty of room at the bottom. *California Institute of Technology, Engineering Science Magazine* (1960).
156. Huang, X., Jain, P. K., El-Sayed, I. H. & El-Sayed, M. A. Plasmonic photothermal therapy (PPTT) using gold nanoparticles. *Lasers Med. Sci.* **23**, 217 (2007).
157. Wagner, V., Dullaart, A., Bock, A.-K. & Zweck, A. The emerging nanomedicine landscape. *Nat. Biotechnol.* **24**, 1211–1217 (2006).
158. Iyer, A. K., Khaled, G., Fang, J. & Maeda, H. Exploiting the enhanced permeability and retention effect for tumor targeting. *Drug Discov. Today* **11**, 812–818 (2006).
159. Prabhakar, U. *et al.* Challenges and Key Considerations of the Enhanced Permeability and Retention Effect for Nanomedicine Drug Delivery in Oncology. *Cancer Res.* **73**, 2412 (2013).
160. Brannon-Peppas, L. & Blanchette, J. O. Nanoparticle and targeted systems for cancer therapy. *Adv. Drug Deliv. Rev.* **56**, 1649–1659 (2004).
161. Cui, Y. & Lieber, C. M. Functional Nanoscale Electronic Devices Assembled Using Silicon Nanowire Building Blocks. *Science* **291**, 851 (2001).

-
162. Duan, X., Huang, Y., Cui, Y., Wang, J. & Lieber, C. M. Indium phosphide nanowires as building blocks for nanoscale electronic and optoelectronic devices. *Nature* **409**, 66–69 (2001).
163. Huang, Y. *et al.* Logic Gates and Computation from Assembled Nanowire Building Blocks. *Science* **294**, 1313 (2001).
164. Guan, N., Dai, X., Babichev, A. V., Julien, F. H. & Tchernycheva, M. Flexible inorganic light emitting diodes based on semiconductor nanowires. *Chem. Sci.* **8**, 7904–7911 (2017).
165. Saxena, D. *et al.* Optically pumped room-temperature GaAs nanowire lasers. *Nat. Photonics* **7**, 963–968 (2013).
166. Krogstrup, P. *et al.* Single-nanowire solar cells beyond the Shockley–Queisser limit. *Nat. Photonics* **7**, 306–310 (2013).
167. Mann, S. A., Grote, R. R., Osgood, R. M., Jr., Alu, A. & Garneet, E. C. Opportunities and Limitations for Nanophotonic Structures To Exceed the Shockley–Queisser Limit. *ACS Nano* **10**, 8620–8631 (2016).
168. Garnett, E. C., Brongersma, M. L., Cui, Y. & McGehee, M. D. Nanowire Solar Cells. in *Annual Review of Materials Research, Vol 41* (ed. Clarke, DR and Fratzl, P) vol. 41 269–295 (2011).
169. Chan, C. K. *et al.* High-performance lithium battery anodes using silicon nanowires. *Nat. Nanotechnol.* **3**, 31–35 (2008).
170. Wang, Q. H., Kalantar-Zadeh, K., Kis, A., Coleman, J. N. & Strano, M. S. Electronics and optoelectronics of two-dimensional transition metal dichalcogenides. *Nat. Nanotechnol.* **7**, 699–712 (2012).
171. Hobbs, R. G., Petkov, N. & Holmes, J. D. Semiconductor Nanowire Fabrication by Bottom-Up and Top-Down Paradigms. *Chem. Mater.* **24**, 1975–1991 (2012).
172. Lu, W. & Lieber, C. M. Nanoelectronics from the bottom up. *Nat. Mater.* **6**, 841–850 (2007).
173. McIntyre, P. C. & Fontcuberta i Morral, A. Semiconductor nanowires: to grow or not to grow? *Mater. Today Nano* **9**, 100058 (2020).
174. Güniat, L., Caroff, P. & Fontcuberta i Morral, A. Vapor Phase Growth of Semiconductor Nanowires: Key Developments and Open Questions. *Chem. Rev.* **119**, 8958–8971 (2019).
175. Friedl, M. *et al.* Template-Assisted Scalable Nanowire Networks. *Nano Lett.* **18**, 2666–2671 (2018).
176. Aseev, P. *et al.* Selectivity Map for Molecular Beam Epitaxy of Advanced III–V Quantum Nanowire Networks. *Nano Lett.* **19**, 218–227 (2019).
177. Dubrovskii, V. G. *Nucleation Theory and Growth of Nanostructures*. (Springer, 2014).
178. Mueller, B. O. *et al.* Review of Spark Discharge Generators for Production of Nanoparticle Aerosols. *Aerosol Sci. Technol.* **46**, 1256–1270 (2012).
179. Svanberg-Larsson, J. *et al.* A Comparison of Explicitly-terminated Diamond Electrodes Decorated with Gold Nanoparticles. *Electroanalysis* **28**, 88–95 (2016).
180. Tao, A. R., Habas, S. & Yang, P. Shape Control of Colloidal Metal Nanocrystals. *Small* **4**, 310–325 (2008).
181. Xia, Y., Xiong, Y., Lim, B. & Skrabalak, S. E. Shape-Controlled Synthesis of Metal Nanocrystals: Simple Chemistry Meets Complex Physics? *Angew. Chem. Int.* **48**, 60–103 (2009).

-
182. Loiudice, A. *et al.* Tailoring copper nanocrystals towards C2 products in electrochemical CO2 reduction. *Angew. Chem. Int.* **55**, 5789–5792 (2016).
183. Markov, I. V. *Crystal growth for beginners: fundamentals of nucleation, crystal growth and epitaxy*. (World scientific, 2003).
184. Lester, S. D., Ponce, F. A., Craford, M. G. & Steigerwald, D. A. High dislocation densities in high efficiency GaN-based light-emitting diodes. *Appl. Phys. Lett.* **66**, 1249–1251 (1995).
185. Kang, M. S., Lee, C.-H., Park, J. B., Yoo, H. & Yi, G.-C. Gallium nitride nanostructures for light-emitting diode applications. *Nano Energy* **1**, 391–400 (2012).
186. Paul, R. *et al.* van der Waals Epitaxy of Earth-Abundant Zn3P2 on Graphene for Photovoltaics. *Cryst. Growth Des.* **20**, 3816–3825 (2020).
187. Frank, F. C. & van der Merwe, J. H. One-dimensional dislocations. I. Static theory. *Proc. R. Soc. A* **198**, 205–216 (1949).
188. Frank, F. C. & Van der Merwe, J. One-dimensional dislocations. II. Misfitting monolayers and oriented overgrowth. *Proc. R. Soc. A* **198**, 216–225 (1949).
189. Frank, F. C. & Van der Merwe, J. One-dimensional dislocations-III. Influence of the second harmonic term in the potential representation, on the properties of the model. *Proc. R. Soc. A* **200**, 125–134 (1949).
190. Frank, F. C. & Van der Merwe, J. One-dimensional dislocations IV. Dynamics. *Proc. R. Soc. A* **201**, 261–268 (1950).
191. Volmer, M. & Weber, A. Keimbildung in übersättigten Gebilden. *Z. Phys. Chem.* **119**, 277–301 (1926).
192. Stranski, I. N. & Krastanow, L. Zur Theorie der orientierten Ausscheidung von Ionenkristallen aufeinander. *Monatsh. Chem. Verw. Tl.* **71**, 351–364 (1937).
193. Toda, Y., Moriwaki, O., Nishioka, M. & Arakawa, Y. Efficient Carrier Relaxation Mechanism in InGaAs/GaAs Self-Assembled Quantum Dots Based on the Existence of Continuum States. *Phys. Rev. Lett.* **82**, 4114–4117 (1999).
194. Yamaguchi, K., Yujobo, K. & Kaizu, T. Stranski-Krastanov Growth of InAs Quantum Dots with Narrow Size Distribution. *Jpn. J. Appl. Phys* **39**, L1245–L1248 (2000).
195. Cho, A. Y. & Arthur, J. R. Molecular beam epitaxy. *Prog. Solid. State Ch.* **10**, 157–191 (1975).
196. Tsao, J. *Materials Fundamentals of Molecular Beam Epitaxy*. (Academic Press, INC., 1993).
197. Orton, J. W. & Foxon, T. *Molecular beam epitaxy: a short history*. (Oxford University Press, USA, 2015).
198. Farrow, R. F. *Molecular beam epitaxy: applications to key materials*. (Elsevier, 1995).
199. Henini, M. *Molecular beam epitaxy: from research to mass production*. (Newnes, 2012).
200. Kasper, E., Herzog, H. J. & Kibbel, H. A one-dimensional SiGe superlattice grown by UHV epitaxy. *Appl. Phys.* **8**, 199–205 (1975).
201. Kwo, J. *et al.* Structural and superconducting properties of orientation-ordered YBa2Cu3O7-x films prepared by molecular-beam epitaxy. *Phys. Rev. B* **36**, 4039–4042 (1987).
202. Webb, C. *et al.* Growth of high Tc superconducting thin films using molecular beam epitaxy techniques. *Appl. Phys. Lett.* **51**, 1191–1193 (1987).

203. He, L., Kou, X. & Wang, K. L. Review of 3D topological insulator thin-film growth by molecular beam epitaxy and potential applications. *Phys. Status Solidi RRL* **7**, 50–63 (2013).
204. Biefeld, R. M., Koleske, D. D. & Cederberg, J. G. The Science and Practice of Metal-Organic Vapor Phase Epitaxy (MOVPE). in *Handbook of Crystal Growth* 95–160 (Elsevier, 2015).
205. Rähmer, B., Pristovsek, M., Breusing, M., Kremzow, R. & Richter, W. In situ scanning tunneling microscopy during metal-organic vapor phase epitaxy. *Appl. Phys. Lett.* **89**, 063108 (2006).
206. Eason, R. *Pulsed laser deposition of thin films: applications-led growth of functional materials*. (John Wiley & Sons, 2007).
207. Christen, H. M. & Eres, G. Recent advances in pulsed-laser deposition of complex oxides. *J. Phys. Condens. Matter* **20**, 264005 (2008).
208. Greer, J. A. & Tabat, M. D. Large-area pulsed laser deposition: Techniques and applications. *J. Vac. Sci. Technol. A* **13**, 1175–1181 (1995).
209. Mourik, V. *et al.* Signatures of Majorana Fermions in Hybrid Superconductor-Semiconductor Nanowire Devices. *Science* **336**, 1003–1007 (2012).
210. Potts, H. *et al.* Electrical control of spins and giant g-factors in ring-like coupled quantum dots. *Nat. Commun.* **10**, 5740 (2019).
211. Jia, C., Lin, Z., Huang, Y. & Duan, X. Nanowire Electronics: From Nanoscale to Macroscale. *Chem. Rev.* **119**, 9074–9135 (2019).
212. Tian, B. & Lieber, C. M. Nanowired Bioelectric Interfaces. *Chem. Rev.* **119**, 9136–9152 (2019).
213. Quan, L. N., Kang, J., Ning, C.-Z. & Yang, P. Nanowires for Photonics. *Chem. Rev.* **119**, 9153–9169 (2019).
214. Swinkels, M. Y. & Zardo, I. Nanowires for heat conversion. *J. Phys. D* **51**, 353001 (2018).
215. Chen, R., Lee, J., Lee, W. & Li, D. Thermoelectrics of Nanowires. *Chem. Rev.* **119**, 9260–9302 (2019).
216. Higgins, S. G. *et al.* High-Aspect-Ratio Nanostructured Surfaces as Biological Metamaterials. *Adv. Mater.* **32**, 1903862 (2020).
217. Dick, K. A. & Caroff, P. Metal-seeded growth of III–V semiconductor nanowires: towards gold-free synthesis. *Nanoscale* **6**, 3006–3021 (2014).
218. Zhang, A., Zheng, G. & Lieber, C. M. *Nanowires: Building blocks for nanoscience and nanotechnology*. (Springer, 2016).
219. Wagner, R. & Ellis, W. Vapor-liquid-solid mechanism of single crystal growth. *Appl. Phys. Lett.* **4**, 89–90 (1964).
220. Givargizov, E. Fundamental aspects of VLS growth. in *Vapour Growth and Epitaxy* 20–30 (Elsevier, 1975).
221. Givargizov, E. & Chernov, A. Rate of whisker growth by the vapor-liquid-crystal mechanism and the role of surface energy. *Sov. Phys. Cryst.* **18**, 89–92 (1973).
222. Gudiksen, M. S., Lauhon, L. J., Wang, J., Smith, D. C. & Lieber, C. M. Growth of nanowire superlattice structures for nanoscale photonics and electronics. *Nature* **415**, 617–620 (2002).
223. Wu Y, C. Y., Huynh L, Barrelet C. J, Bell D. C. and Lieber C. M. Controlled growth and structures of molecular-scale silicon nanowires. *Nano Lett.* **4**, 433 (2004).
224. Björk, M. T. *et al.* One-dimensional Steeplechase for Electrons Realized. *Nano Lett.* **2**, 87–89 (2002).

225. Wallentin, J. *et al.* InP Nanowire Array Solar Cells Achieving 13.8% Efficiency by Exceeding the Ray Optics Limit. *Science* **339**, 1057 (2013).
226. Björk, M. T. *et al.* One-dimensional heterostructures in semiconductor nanowhiskers. *Appl. Phys. Lett.* **80**, 1058–1060 (2002).
227. Dick, K. A. *et al.* Synthesis of branched ‘nanotrees’ by controlled seeding of multiple branching events. *Nat. Mater.* **3**, 380–384 (2004).
228. Huang, M. H. *et al.* Catalytic Growth of Zinc Oxide Nanowires by Vapor Transport. *Adv. Mater.* **13**, 113–116 (2001).
229. Kind, H., Yan, H., Messer, B., Law, M. & Yang, P. Nanowire Ultraviolet Photodetectors and Optical Switches. *Adv. Mater.* **14**, 158–160 (2002).
230. Huang, M. H. *et al.* Room-Temperature Ultraviolet Nanowire Nanolasers. *Science* **292**, 1897 (2001).
231. Glas, F. Critical dimensions for the plastic relaxation of strained axial heterostructures in free-standing nanowires. *Phys. Rev. B* **74**, 121302 (2006).
232. Harmand, J.-C. *et al.* Atomic Step Flow on a Nanofacet. *Phys. Rev. Lett.* **121**, 166101 (2018).
233. Harmand, J. *et al.* Analysis of vapor-liquid-solid mechanism in Au-assisted GaAs nanowire growth. *Appl. Phys. Lett.* **87**, 203101 (2005).
234. Cirlin, G. E. *et al.* Critical diameters and temperature domains for MBE growth of III-V nanowires on lattice mismatched substrates. *Phys. Status Solidi RRL* **3**, 112–114 (2009).
235. Fadaly, E. M. T. *et al.* Direct-bandgap emission from hexagonal Ge and SiGe alloys. *Nature* **580**, 205–209 (2020).
236. Algra, R. E. *et al.* Twinning superlattices in indium phosphide nanowires. *Nature* **456**, 369–372 (2008).
237. Joyce, H. J., Wong-Leung, J., Gao, Q., Tan, H. H. & Jagadish, C. Phase Perfection in Zinc Blende and Wurtzite III-V Nanowires Using Basic Growth Parameters. *Nano Lett.* **10**, 908–915 (2010).
238. Gao, Q. *et al.* Selective-Area Epitaxy of Pure Wurtzite InP Nanowires: High Quantum Efficiency and Room-Temperature Lasing. *Nano Lett.* **14**, 5206–5211 (2014).
239. Goldthorpe, I. A., Marshall, A. F. & McIntyre, P. C. Synthesis and Strain Relaxation of Ge-Core/Si-Shell Nanowire Arrays. *Nano Lett.* **8**, 4081–4086 (2008).
240. Vukajlovic-Plestina, J. *et al.* Fundamental aspects to localize self-catalyzed III-V nanowires on silicon. *Nat. Commun.* **10**, 869 (2019).
241. Dick, K. A., Bolinsson, J., Borg, B. M. & Johansson, J. Controlling the Abruptness of Axial Heterojunctions in III-V Nanowires: Beyond the Reservoir Effect. *Nano Lett.* **12**, 3200–3206 (2012).
242. Caroff, P. *et al.* Controlled polytypic and twin-plane superlattices in III-V nanowires. *Nat. Nanotechnol.* **4**, 50–55 (2009).
243. Dick, K. A., Thelander, C., Samuelson, L. & Caroff, P. Crystal Phase Engineering in Single InAs Nanowires. *Nano Lett.* **10**, 3494–3499 (2010).

-
244. Meng, A. C. *et al.* Core-Shell Germanium/Germanium–Tin Nanowires Exhibiting Room-Temperature Direct- and Indirect-Gap Photoluminescence. *Nano Lett.* **16**, 7521–7529 (2016).
245. Assali, S. *et al.* Growth and Optical Properties of Direct Band Gap Ge/Ge_{0.87}Sn_{0.13} Core/Shell Nanowire Arrays. *Nano Lett.* **17**, 1538–1544 (2017).
246. Francaviglia, L. *et al.* Segregation scheme of indium in AlGaInAs nanowire shells. *Phys. Rev. Mater.* **3**, 023001 (2019).
247. Heiss, M. *et al.* Self-assembled quantum dots in a nanowire system for quantum photonics. *Nat. Mater.* **12**, 439–444 (2013).
248. Kim, S. & Cahoon, J. F. Geometric Nanophotonics: Light Management in Single Nanowires through Morphology. *Acc. Chem. Res.* **52**, 3511–3520 (2019).
249. Frederiksen, R. *et al.* Visual Understanding of Light Absorption and Waveguiding in Standing Nanowires with 3D Fluorescence Confocal Microscopy. *ACS Photonics* **4**, 2235–2241 (2017).
250. Mann, S. A. *et al.* Quantifying losses and thermodynamic limits in nanophotonic solar cells. *Nat. Nanotechnol.* **11**, 1071 (2016).
251. Heiss, M. *et al.* III–V nanowire arrays: growth and light interaction. *Nanotechnology* **25**, 014015 (2013).
252. Kayes, B., Atwater, H. & Lewis, N. Comparison of the device physics principles of planar and radial p-n junction nanorod solar cells. *J. Appl. Phys.* **97**, 114302 (2005).
253. van Dam, D. *et al.* High-Efficiency Nanowire Solar Cells with Omnidirectionally Enhanced Absorption Due to Self-Aligned Indium–Tin–Oxide Mie Scatterers. *ACS Nano* **10**, 11414–11419 (2016).
254. Kelzenberg, M. D. *et al.* Photovoltaic measurements in single-nanowire silicon solar cells. *Nano Lett.* **8**, 710–714 (2008).
255. Kelzenberg, M. D. *et al.* Enhanced absorption and carrier collection in Si wire arrays for photovoltaic applications. *Nat. Mater.* **9**, 239–244 (2010).
256. Aberg, I. *et al.* A GaAs Nanowire Array Solar Cell With 15.3% Efficiency at 1 Sun. *IEEE J. Photovolt.* **6**, 185–190 (2016).
257. Fountaine, K. T., Kendall, C. G. & Atwater, H. A. Near-unity broadband absorption designs for semiconducting nanowire arrays via localized radial mode excitation. *Opt. Express* **22**, A930–A940 (2014).
258. Mann, S. A. & Garnett, E. C. Resonant Nanophotonic Spectrum Splitting for Ultrathin Multijunction Solar Cells. *ACS Photonics* **2**, 816–821 (2015).
259. Espinet-Gonzalez, P. *et al.* Radiation Tolerant Nanowire Array Solar Cells. *ACS Nano* **13**, 12860–12869 (2019).
260. Choi, S. B., Song, M. S. & Kim, Y. Zn₃P₂ Twinning Superlattice Nanowires Grown on Fluorine-Doped Tin Oxide Glass Substrates. *J. Phys. Chem. C* **123**, 4597–4604 (2019).
261. Lim, J., Hippalgaonkar, K., Andrews, S. C., Majumdar, A. & Yang, P. Quantifying Surface Roughness Effects on Phonon Transport in Silicon Nanowires. *Nano Lett.* **12**, 2475–2482 (2012).
262. Martin, P., Aksamija, Z., Pop, E. & Ravaioli, U. Impact of Phonon-Surface Roughness Scattering on Thermal Conductivity of Thin Si Nanowires. *Phys. Rev. Lett.* **102**, 125503 (2009).
263. Jacobsson, D. *et al.* Interface dynamics and crystal phase switching in GaAs nanowires. *Nature* **531**, 317–322 (2016).

-
264. Caswell, K., Bender, C. M. & Murphy, C. J. Seedless, surfactantless wet chemical synthesis of silver nanowires. *Nano Lett.* **3**, 667–669 (2003).
265. Sun, Y., Gates, B., Mayers, B. & Xia, Y. Crystalline silver nanowires by soft solution processing. *Nano Lett.* **2**, 165–168 (2002).
266. Downing, J. M., Ryan, M. P. & McLachlan, M. A. Hydrothermal growth of ZnO nanorods: The role of KCl in controlling rod morphology. *Thin Solid Films* **539**, 18–22 (2013).
267. Vayssieres, L. Growth of Arrayed Nanorods and Nanowires of ZnO from Aqueous Solutions. *Adv. Mater.* **15**, 464–466 (2003).
268. Adhikari H, M. A. F., Chidsey C. E. D. and McIntyre P. C. Germanium nanowire epitaxy: shape and orientation control. *Nano Lett.* **6**, 318 (2006).
269. Fontcuberta i Morral, A., Colombo, C., Abstreiter, G., Arbiol, J. & Morante, J. R. Nucleation mechanism of gallium-assisted molecular beam epitaxy growth of gallium arsenide nanowires. *Appl. Phys. Lett.* **92**, 063112 (2008).
270. Colombo, C., Spirkoska, D., Frimmer, M., Abstreiter, G. & Fontcuberta i Morral, A. Ga-assisted catalyst-free growth mechanism of GaAs nanowires by molecular beam epitaxy. *Phys. Rev. B* **77**, 155326 (2008).
271. Dick, K. A. A review of nanowire growth promoted by alloys and non-alloying elements with emphasis on Au-assisted III-V nanowires. *Prog. Cryst. Growth Ch.* **54**, 138–173 (2008).
272. Seifert, W. *et al.* Growth of one-dimensional nanostructures in MOVPE. *J. Cryst. Growth* **272**, 211–220 (2004).
273. Li, Q. *et al.* Size-Dependent Periodically Twinned ZnSe Nanowires. *Adv. Mater.* **16**, 1436–1440 (2004).
274. Yanagida, T. *et al.* Enhancement of oxide VLS growth by carbon on substrate surface. *J. Phys. Chem. C* **112**, 18923–18926 (2008).
275. Wang, S. *et al.* Synthesis of single-crystalline tungsten nanowires by nickel-catalyzed vapor-phase method at 850°C. *J. Cryst. Growth* **306**, 433–436 (2007).
276. Adhikari, H., McIntyre, P. C., Sun, S., Pianetta, P. & Chidsey, C. E. D. Photoemission studies of passivation of germanium nanowires. *Appl. Phys. Lett.* **87**, 263109 (2005).
277. Trentler, T. J. *et al.* Solution-Liquid-Solid Growth of Crystalline III-V Semiconductors: An Analogy to Vapor-Liquid-Solid Growth. *Science* **270**, 1791 (1995).
278. Dick, K. A. *et al.* Failure of the Vapor–Liquid–Solid Mechanism in Au-Assisted MOVPE Growth of InAs Nanowires. *Nano Lett.* **5**, 761–764 (2005).
279. Ghisalberti, L. *et al.* Questioning liquid droplet stability on nanowire tips: from theory to experiment. *Nanotechnology* **30**, 285604 (2019).
280. Dick, K. A. *et al.* Control of III–V nanowire crystal structure by growth parameter tuning. *Semicond. Sci. Technol.* **25**, 024009 (2010).
281. Messing, M. E. *et al.* A comparative study of the effect of gold seed particle preparation method on nanowire growth. *Nano Res.* **3**, 506–519 (2010).

282. Bullis, W. M. Properties of gold in silicon. *Solid State Electron.* **9**, 143–168 (1966).
283. Schmidt, V., Wittemann, J. V., Senz, S. & Gösele, U. Silicon Nanowires: A Review on Aspects of their Growth and their Electrical Properties. *Adv. Mater.* **21**, 2681–2702 (2009).
284. Hillerich, K., Messing, M. E., Reine Wallenberg, L., Deppert, K. & Dick, K. A. Epitaxial InP nanowire growth from Cu seed particles. *J. Cryst. Growth* **315**, 134–137 (2011).
285. Vogel, A. T. *et al.* Ag-assisted CBE growth of ordered InSb nanowire arrays. *Nanotechnology* **22**, 015605 (2010).
286. Heun, S. *et al.* Coexistence of Vapor–Liquid–Solid and Vapor–Solid–Solid Growth Modes in Pd-Assisted InAs Nanowires. *Small* **6**, 1935–1941 (2010).
287. Mårtensson, E. K., Lehmann, S., Dick, K. A. & Johansson, J. Simulation of GaAs Nanowire Growth and Crystal Structure. *Nano Lett.* **19**, 1197–1203 (2019).
288. Breuer, S., Feiner, L.-F. & Geelhaar, L. Droplet Bulge Effect on the Formation of Nanowire Side Facets. *Cryst. Growth Des.* **13**, 2749–2755 (2013).
289. Dubrovskii, V. G. Refinement of Nucleation Theory for Vapor-Liquid-Solid Nanowires. *Cryst. Growth Des.* **17**, 2589–2593 (2017).
290. Kodambaka, S., Tersoff, J., Reuter, M. C. & Ross, F. M. Germanium Nanowire Growth Below the Eutectic Temperature. *Science* **316**, 729 (2007).
291. Dubrovskii, V. G. *et al.* Growth kinetics of GaAs nanoneedles on silicon and sapphire substrates. *Appl. Phys. Lett.* **98**, 153113 (2011).
292. Schmid, H. *et al.* Template-assisted selective epitaxy of III–V nanoscale devices for co-planar heterogeneous integration with Si. *Appl. Phys. Lett.* **106**, 233101 (2015).
293. Routkevitch, D., Bigioni, T., Moskovits, M. & Xu, J. M. Electrochemical fabrication of CdS nanowire arrays in porous anodic aluminum oxide templates. *J. Phys. Chem.* **100**, 14037–14047 (1996).
294. Raya, A. M. *et al.* GaAs nanoscale membranes: prospects for seamless integration of III–Vs on silicon. *Nanoscale* **12**, 815–824 (2020).
295. Matteini, F., Tütüncüoğlu, G., Rüffer, D., Alarcón-Lladó, E. & Fontcuberta i Morral, A. Ga-assisted growth of GaAs nanowires on silicon, comparison of surface SiO_x of different nature. *J. Cryst. Growth* **404**, 246–255 (2014).
296. Matteini, F., Tütüncüoğlu, G., Potts, H., Jabeen, F. & Fontcuberta i Morral, A. Wetting of Ga on SiO_x and Its Impact on GaAs Nanowire Growth. *Cryst. Growth Des.* **15**, 3105–3109 (2015).
297. Metaferia, W. *et al.* GaAsP Nanowires Grown by Aerotaxy. *Nano Lett.* **16**, 5701–5707 (2016).
298. Chi, C.-Y. *et al.* Twin-Free GaAs Nanosheets by Selective Area Growth: Implications for Defect-Free Nanostructures. *Nano Lett.* **13**, 2506–2515 (2013).
299. Li, R. R. *et al.* Dense arrays of ordered GaAs nanostructures by selective area growth on substrates patterned by block copolymer lithography. *Appl. Phys. Lett.* **76**, 1689–1691 (2000).

-
300. Ren, D., Zhou, W. & Dapkus, P. D. Low-dislocation-density, nonplanar GaN templates for buried heterostructure lasers grown by lateral epitaxial overgrowth. *Appl. Phys. Lett.* **86**, 111901 (2005).
301. Desplanque, L., Bucamp, A., Troadec, D., Patriarche, G. & Wallart, X. Selective area molecular beam epitaxy of InSb nanostructures on mismatched substrates. *J. Cryst. Growth* **512**, 6–10 (2019).
302. Ikejiri, K. *et al.* Growth characteristics of GaAs nanowires obtained by selective area metal-organic vapour-phase epitaxy. *Nanotechnology* **19**, 265604 (2008).
303. Tutuncuoglu, G. *et al.* Towards defect-free 1-D GaAs/AlGaAs heterostructures based on GaAs nanomembranes. *Nanoscale* **7**, 19453–19460 (2015).
304. Wang, N. *et al.* Shape Engineering of InP Nanostructures by Selective Area Epitaxy. *ACS Nano* **13**, 7261–7269 (2019).
305. Nishinaga, T., Nakano, T. & Zhang, S. Epitaxial Lateral Overgrowth of GaAs by LPE. *Jpn. J. Appl. Phys* **27**, L964–L967 (1988).
306. Kobayashi, N. P., Kobayashi, J. T., Zhang, X., Dapkus, P. D. & Rich, D. H. Epitaxial lateral overgrowth of GaN over AlO_x surface formed on Si substrate. *Appl. Phys. Lett.* **74**, 2836–2838 (1999).
307. Bushroa, A. R., Jacob, C., Saijo, H. & Nishino, S. Lateral epitaxial overgrowth and reduction in defect density of 3C-SiC on patterned Si substrates. *J. Cryst. Growth* **271**, 200–206 (2004).
308. Wulff, G. XXV. Zur Frage der Geschwindigkeit des Wachstums und der Auflösung der Krystallflächen. *Z. Kristallogr. Cryst. Mater.* **34**, 449–530 (1901).
309. Winterbottom, W. L. Equilibrium shape of a small particle in contact with a foreign substrate. *Acta Metall. Mater.* **15**, 303–310 (1967).
310. Albani, M. *et al.* Growth kinetics and morphological analysis of homoepitaxial GaAs fins by theory and experiment. *Phys. Rev. Mater.* **2**, 093404 (2018).
311. Albani, M. *et al.* Competition Between Kinetics and Thermodynamics During the Growth of Faceted Crystal by Phase Field Modeling. *Phys. Status Solidi B* **256**, 1800518 (2019).
312. Guo, W., Zhang, M., Banerjee, A. & Bhattacharya, P. Catalyst-Free InGaN/GaN Nanowire Light Emitting Diodes Grown on (001) Silicon by Molecular Beam Epitaxy. *Nano Lett.* **10**, 3355–3359 (2010).
313. Tomioka, K., Motohisa, J., Hara, S. & Fukui, T. Control of InAs Nanowire Growth Directions on Si. *Nano Lett.* **8**, 3475–3480 (2008).
314. Mark, A. Growth of Single Crystal Silicon Overgrowths on Silicon Substrates. *J. Electrochem. Soc.* **107**, 568 (1960).
315. Theuerer, H. C. Epitaxial Silicon Films by the Hydrogen Reduction of SiCl₄. *J. Electrochem. Soc.* **108**, 649 (1961).
316. Joyce, B. D. & Baldrey, J. A. Selective Epitaxial Deposition of Silicon. *Nature* **195**, 485–486 (1962).
317. McClelland, R. W., Bozler, C. O. & Fan, J. C. C. A technique for producing epitaxial films on reusable substrates. *Appl. Phys. Lett.* **37**, 560–562 (1980).

-
318. Hiramatsu, K. *et al.* Fabrication and characterization of low defect density GaN using facet-controlled epitaxial lateral overgrowth (FACELO). *J. Cryst. Growth* **221**, 316–326 (2000).
319. Jastrzebski, L. SOI by CVD: Epitaxial Lateral Overgrowth (ELO) process—Review. *J. Cryst. Growth* **63**, 493–526 (1983).
320. Jastrzebski, L., Corboy, J. F. & Pagliaro, R. Growth of Electronic Quality Silicon Over SiO₂ by Epitaxial Lateral Overgrowth Technique. *J. Electrochem. Soc.* **129**, 2645–2648 (1982).
321. Zamani, R. R. & Arbiol, J. Understanding semiconductor nanostructures via advanced electron microscopy and spectroscopy. *Nanotechnology* **30**, 262001 (2019).
322. Zamani, R. R., Hage, F. S., Lehmann, S., Ramasse, Q. M. & Dick, K. A. Atomic-Resolution Spectrum Imaging of Semiconductor Nanowires. *Nano Lett.* **18**, 1557–1563 (2018).
323. Krivanek, O. L. *et al.* Vibrational spectroscopy in the electron microscope. *Nature* **514**, 209–212 (2014).
324. Browning, N. D., Chisholm, M. F. & Pennycook, S. J. Atomic-resolution chemical analysis using a scanning transmission electron microscope. *Nature* **366**, 143–146 (1993).
325. Krivanek, O. L., Dellby, N. & Lupini, A. R. Towards sub-Å electron beams. *Ultramicroscopy* **78**, 1–11 (1999).
326. Krivanek, O. L. *et al.* Atom-by-atom structural and chemical analysis by annular dark-field electron microscopy. *Nature* **464**, 571–574 (2010).
327. Batson, P. E., Dellby, N. & Krivanek, O. L. Sub-ångstrom resolution using aberration corrected electron optics. *Nature* **418**, 617–620 (2002).
328. Tersoff, J. & Hamann, D. R. Theory and Application for the Scanning Tunneling Microscope. *Phys. Rev. Lett.* **50**, 1998–2001 (1983).
329. Tersoff, J. & Hamann, D. R. Theory of the scanning tunneling microscope. *Phys. Rev. B* **31**, 805–813 (1985).
330. Chia, A. C. E., Boulanger, J. P. & LaPierre, R. R. Unlocking doping and compositional profiles of nanowire ensembles using SIMS. *Nanotechnology* **24**, 045701 (2013).
331. Stutz, E. Z. *et al.* Nanosails Showcasing Zn₃As₂ as an Optoelectronic-Grade Earth Abundant Semiconductor. *Phys. Status Solidi RRL* **13**, 1900084 (2019).
332. Koelling, S. *et al.* Atom-by-Atom Analysis of Semiconductor Nanowires with Parts Per Million Sensitivity. *Nano Lett.* **17**, 599–605 (2017).
333. Chang, A. S. & Lauhon, L. J. Atom probe tomography of nanoscale architectures in functional materials for electronic and photonic applications. *Curr. Opin. Solid State Mater. Sci.* **22**, 171–187 (2018).
334. Xu, T. *et al.* Growth of Si nanowires on micropillars for the study of their dopant distribution by atom probe tomography. *J. Vac. Sci. Technol. B* **26**, 1960–1963 (2008).
335. Fischer-Cripps, A. Nanoindentation - Mechanical Engineering Series. *Appl. Mech. Rev.* **57**, B12 (2004).

-
336. Storm, K. *et al.* Spatially resolved Hall effect measurement in a single semiconductor nanowire. *Nat. Nanotechnol.* **7**, 718–722 (2012).
337. Hultin, O. *et al.* Comparing Hall Effect and Field Effect Measurements on the Same Single Nanowire. *Nano Lett.* **16**, 205–211 (2016).
338. Ruska, E. The development of the electron microscope and of electron microscopy. *Biosci. Rep.* **7**, 607–629 (1987).
339. Ruska, E. Über Fortschritte im Bau und in der Leistung des magnetischen Elektronenmikroskops. *Z. Phys.* **87**, 580–602 (1934).
340. Knoll, M. & Ruska, E. Das elektronenmikroskop. *Z. Phys.* **78**, 318–339 (1932).
341. Goldstein, J. I. *et al.* *Scanning electron microscopy and X-ray microanalysis*. (Springer, 2017).
342. Egerton, R. F. *Physical principles of electron microscopy*. (Springer, 2005).
343. Williams, D. B. & Carter, C. B. The transmission electron microscope. in *Transmission electron microscopy* 3–17 (Springer, 1996).
344. Reimer, L. & Kohl, H. *Transmission Electron Microscopy: Physics of Image Formation*. (Springer, 2008).
345. Orloff, J. Charged Particle Optics. *Encyclopedia of Imaging Science and Technology* (2002).
346. Hawkes, P. W. & Kasper, E. *Principles of electron optics*. vol. 3 (Academic press, 1996).
347. Brydson, R. *Aberration-corrected analytical transmission electron microscopy*. vol. 3 (John Wiley & Sons, 2011).
348. Egerton, R. F. *Electron energy-loss spectroscopy in the electron microscope*. (Springer Science & Business Media, 2011).
349. Yacobi, B. G. & Holt, D. B. Cathodoluminescence. in *Cathodoluminescence Microscopy of Inorganic Solids* 55–88 (Springer, 1990).
350. Piazza, V. *et al.* Investigation of GaN nanowires containing AlN/GaN multiple quantum discs by EBIC and CL techniques. *Nanotechnology* **30**, 214006 (2019).
351. Akamatsu, B., Henoc, J. & Henoc, P. Electron beam-induced current in direct band-gap semiconductors. *J. Appl. Phys.* **52**, 7245–7250 (1981).
352. Cinchetti, M. *et al.* Photoemission Electron Microscopy as a Tool for the Investigation of Optical Near Fields. *Phys. Rev. Lett.* **95**, 047601 (2005).
353. Zhao, T. *et al.* Electrical control of antiferromagnetic domains in multiferroic BiFeO₃ films at room temperature. *Nat. Mater.* **5**, 823–829 (2006).
354. Berruto, G. *et al.* Laser-Induced Skyrmion Writing and Erasing in an Ultrafast Cryo-Lorentz Transmission Electron Microscope. *Phys. Rev. Lett.* **120**, 117201 (2018).
355. Pollard, S. D. *et al.* Observation of stable Néel skyrmions in cobalt/palladium multilayers with Lorentz transmission electron microscopy. *Nat. Commun.* **8**, 14761 (2017).
356. Dubochet, J., Adrian, M., Chang, J.-J., Lepault, J. & McDowell, A. W. Cryoelectron microscopy of vitrified specimens. in *Cryotechniques in Biological Electron Microscopy* 114–131 (Springer, 1987).

-
357. van Heel, M. & Frank, J. Use of multivariate statistics in analysing the images of biological macromolecules. *Ultramicroscopy* **6**, 187–194 (1981).
358. Henderson, R. & Unwin, P. N. T. Three-dimensional model of purple membrane obtained by electron microscopy. *Nature* **257**, 28–32 (1975).
359. Hetherington, C., Jacobsson, D., Dick, K. A. & Wallenberg, L. R. In situ metal-organic chemical vapour deposition growth of III–V semiconductor nanowires in the Lund environmental transmission electron microscope. *Semicond. Sci. Technol.* **35**, 034004 (2020).
360. Kawasaki, T. *et al.* Development of a 1 MV field-emission transmission electron microscope. *Microscopy* **49**, 711–718 (2000).
361. Everhart, T. E. & Thornley, R. F. M. Wide-band detector for micro-microampere low-energy electron currents. *J. Sci. Instrum.* **37**, 246–248 (1960).
362. Francaviglia, L. Mechanisms shifting the emission energy of self-assembled quantum dots in nanowires. (EPFL, 2019). doi:10.5075/epfl-thesis-9058.
363. Scherzer, O. Sphärische und chromatische korrektur von elektronen-linsen. *Optik* **2**, 114–132 (1947).
364. Haider, M. *et al.* Electron microscopy image enhanced. *Nature* **392**, 768–769 (1998).
365. Okunishi, E. *et al.* Visualization of Light Elements at Ultrahigh Resolution by STEM Annular Bright Field Microscopy. *Microsc. Microanal.* **15**, 164–165 (2009).
366. Findlay, S. D. *et al.* Dynamics of annular bright field imaging in scanning transmission electron microscopy. *Ultramicroscopy* **110**, 903–923 (2010).
367. Ishikawa, R. *et al.* Direct imaging of hydrogen-atom columns in a crystal by annular bright-field electron microscopy. *Nat. Mater.* **10**, 278–281 (2011).
368. Kim, Y.-M., Pennycook, S. J. & Borisevich, A. Y. Quantitative comparison of bright field and annular bright field imaging modes for characterization of oxygen octahedral tilts. *Ultramicroscopy* **181**, 1–7 (2017).
369. Hage, F. S. *et al.* Nanoscale momentum-resolved vibrational spectroscopy. *Sci. Adv.* **4**, eaar7495 (2018).
370. Hage, F. S., Kepaptsoglou, D. M., Ramasse, Q. M. & Allen, L. J. Phonon Spectroscopy at Atomic Resolution. *Phys. Rev. Lett.* **122**, 016103 (2019).
371. Jokisaari, J. R. *et al.* Vibrational Spectroscopy of Water with High Spatial Resolution. *Adv. Mater.* **30**, 1802702 (2018).
372. Hachtel, J. A. *et al.* Identification of site-specific isotopic labels by vibrational spectroscopy in the electron microscope. *Science* **363**, 525 (2019).
373. Cullity, B. D. *Elements of X-ray Diffraction*. (Addison-Wesley Publishing, 1956).
374. Spirkoska, D. *et al.* Structural and optical properties of high quality zinc-blende/wurtzite GaAs nanowire heterostructures. *Phys. Rev. B* **80**, 245325 (2009).

-
375. Nakashima, S. Raman imaging of semiconductor materials: characterization of static and dynamic properties. *J. Phys. Condens. Matter* **16**, S25–S37 (2003).
376. Ek, M., Lehmann, S. & Wallenberg, R. Electron channelling: challenges and opportunities for compositional analysis of nanowires by TEM. *Nanotechnology* **31**, 364005 (2020).
377. Gencarelli, F. *et al.* Extended X-ray absorption fine structure investigation of Sn local environment in strained and relaxed epitaxial Ge_{1-x}Sn_x films. *J. Appl. Phys.* **117**, 095702 (2015).
378. Koningsberger, D. C. *X-ray absorption: principles, applications, techniques of EXAFS, SEXAFS, and XANES*. (John Wiley and Sons, 1988).
379. Rocca, M. Low-energy EELS investigation of surface electronic excitations on metals. *Surf. Sci. Rep.* **22**, 1–71 (1995).
380. Layet, J. M., Contini, R., Derrien, J. & Lüth, H. Coupled interface plasmons of the Ag-Si(111) system as investigated with high-resolution electron energy-loss spectroscopy. *Surf. Sci.* **168**, 142–148 (1986).
381. Froitzheim, H. & Ibach, H. Interband transitions in ZnO observed in low energy electron spectroscopy. *Z. Phys.* **269**, 17–22 (1974).
382. Powell, C. J. & Swan, J. B. Origin of the Characteristic Electron Energy Losses in Aluminum. *Phys. Rev.* **115**, 869–875 (1959).
383. Keller, D. *et al.* Local Band Gap Measurements by VEELS of Thin Film Solar Cells. *Microsc. Microanal.* **20**, 1246–1253 (2014).
384. Keller, D. *et al.* Band gap widening at random CIGS grain boundary detected by valence electron energy loss spectroscopy. *Appl. Phys. Lett.* **109**, 153103 (2016).
385. Erni, R. & Browning, N. D. Valence electron energy-loss spectroscopy in monochromated scanning transmission electron microscopy. *Ultramicroscopy* **104**, 176–192 (2005).
386. Erni, R. & Browning, N. D. The impact of surface and retardation losses on valence electron energy-loss spectroscopy. *Ultramicroscopy* **108**, 84–99 (2008).
387. Erni, R. & Browning, N. D. Quantification of the size-dependent energy gap of individual CdSe quantum dots by valence electron energy-loss spectroscopy. *Ultramicroscopy* **107**, 267–273 (2007).
388. Erni, R., Lazar, S. & Browning, N. D. Prospects for analyzing the electronic properties in nanoscale systems by VEELS. *Ultramicroscopy* **108**, 270–276 (2008).
389. Stöger-Pollach, M. & Schattschneider, P. The influence of relativistic energy losses on bandgap determination using valence EELS. *Ultramicroscopy* **107**, 1178–1185 (2007).
390. Coenen, T. & Haegel, N. M. Cathodoluminescence for the 21st century: Learning more from light. *Appl. Phys. Rev.* **4**, 031103 (2017).
391. Schmidt, T., Daniel, G. & Lischka, K. The excitation power dependence of the near band edge photoluminescence of II-VI semiconductors. *J. Cryst. Growth* **117**, 748–752 (1992).

-
392. Schmidt, T., Lischka, K. & Zulehner, W. Excitation-power dependence of the near-band-edge photoluminescence of semiconductors. *Phys. Rev. B* **45**, 8989–8994 (1992).
393. Rosner, S. J. *et al.* Cathodoluminescence mapping of epitaxial lateral overgrowth in gallium nitride. *Appl. Phys. Lett.* **74**, 2035–2037 (1999).
394. Wadia, C., Alivisatos, A. P. & Kammen, D. M. Materials Availability Expands the Opportunity for Large-Scale Photovoltaics Deployment. *Environ. Sci. Technol.* **43**, 2072–2077 (2009).
395. Pistorius, C., Clark, G., Ceotzer, J., Kruger, G. & Kunze, O. High pressure phase relations and crystal structure determination for Zn₃P₂ & Cd₃P₂. *High Press. High Temp.* **9**, 471–482 (1977).
396. Burgess, T. *et al.* Zn₃As₂ Nanowires and Nanoplatelets: Highly Efficient Infrared Emission and Photodetection by an Earth Abundant Material. *Nano Lett.* **15**, 378–385 (2015).
397. Dorodnyy, A. *et al.* Efficient Multiterminal Spectrum Splitting via a Nanowire Array Solar Cell. *ACS Photonics* **2**, 1284–1288 (2015).
398. Hu, L. & Chen, G. Analysis of Optical Absorption in Silicon Nanowire Arrays for Photovoltaic Applications. *Nano Lett.* **7**, 3249–3252 (2007).
399. Muskens, O. L., Rivas, J. G., Algra, R. E., Bakkers, E. P. A. M. & Lagendijk, A. Design of Light Scattering in Nanowire Materials for Photovoltaic Applications. *Nano Lett.* **8**, 2638–2642 (2008).
400. Brockway, L., Van Laer, M., Kang, Y. & Vaddiraju, S. Large-scale synthesis and in situ functionalization of Zn₃P₂ and Zn₄Sb₃ nanowire powders. *Phys. Chem. Chem. Phys.* **15**, 6260–6267 (2013).
401. Karlsson, L. S. *et al.* Understanding the 3D structure of GaAs < 111 > B nanowires. *Nanotechnology* **18**, 485717 (2007).
402. Kaufman, L. & Bernstein, H. *Computer Calculation of Phase Diagrams*. (New York: Academic, 1970).
403. Diedenhofen, S. L., Janssen, O. T. A., Grzela, G., Bakkers, E. P. A. M. & Gómez Rivas, J. Strong Geometrical Dependence of the Absorption of Light in Arrays of Semiconductor Nanowires. *ACS Nano* **5**, 2316–2323 (2011).
404. Fountaine, K. T., Cheng, W.-H., Bukowsky, C. R. & Atwater, H. A. Near-Unity Unselective Absorption in Sparse InP Nanowire Arrays. *ACS Photonics* **3**, 1826–1832 (2016).
405. Yalamanchili, S. *et al.* Enhanced Absorption and <1% Spectrum-and-Angle-Averaged Reflection in Tapered Microwire Arrays. *ACS Photonics* **3**, 1854–1861 (2016).
406. Bernal, S. *et al.* The interpretation of HREM images of supported metal catalysts using image simulation: profile view images. *Ultramicroscopy* **72**, 135–164 (1998).
407. Grillo, V. & Rotunno, E. STEM_CELL: A software tool for electron microscopy: Part I—simulations. *Ultramicroscopy* **125**, 97–111 (2013).
408. Grillo, V. & Rossi, F. STEM_CELL: A software tool for electron microscopy. Part 2 analysis of crystalline materials. *Ultramicroscopy* **125**, 112–129 (2013).

-
409. Lee, B.-J. Thermodynamic assessments of the Sn-Zn and In-Zn binary systems. *Calphad* **20**, 471–480 (1996).
410. Ansara, I. *et al.* A binary database for III–V compound semiconductor systems. *Calphad* **18**, 177–222 (1994).
411. Sundman, B., Jansson, B. & Andersson, J.-O. The Thermo-Calc databank system. *Calphad* **9**, 153–190 (1985).
412. Andersson, J.-O., Helander, T., Höglund, L., Shi, P. & Sundman, B. Thermo-Calc & DICTRA, computational tools for materials science. *Calphad* **26**, 273–312 (2002).
413. Arbiol, J., de la Mata, M., Eickhoff, M. & Morral, A. F. i. Bandgap engineering in a nanowire: self-assembled 0, 1 and 2D quantum structures. *Mater. Today* **16**, 213–219 (2013).
414. De Luca, M. *et al.* Phonon Engineering in Twinning Superlattice Nanowires. *Nano Lett.* **19**, 4702–4711 (2019).
415. Ikonc, Z., Srivastava, G. P. & Inkson, J. C. Optical properties of twinning superlattices in diamond-type and zinc-blende-type semiconductors. *Phys. Rev. B* **52**, 14078–14085 (1995).
416. Ikonc, Z., Srivastava, G. P. & Inkson, J. C. Electronic properties of twin boundaries and twinning superlattices in diamond-type and zinc-blende-type semiconductors. *Phys. Rev. B* **48**, 17181–17193 (1993).
417. Ikonc, Z., Srivastava, G. P. & Inkson, J. C. Twinning superlattices. *Solid State Commun.* **86**, 799–802 (1993).
418. Fang, X.-S., Ye, C.-H., Zhang, L.-D. & Xie, T. Twinning-Mediated Growth of Al₂O₃ Nanobelts and Their Enhanced Dielectric Responses. *Adv. Mater.* **17**, 1661–1665 (2005).
419. Shen, G., Bando, Y., Liu, B., Tang, C. & Golberg, D. Unconventional Zigzag Indium Phosphide Single-Crystalline and Twinned Nanowires. *J. Phys. Chem. B* **110**, 20129–20132 (2006).
420. Escobar Steinvall, S. *et al.* Multiple morphologies and functionality of nanowires made from earth-abundant zinc phosphide. *Nanoscale Horiz.* **5**, 274–282 (2020).
421. Rühle, S. Tabulated values of the Shockley–Queisser limit for single junction solar cells. *Sol. Energy* **130**, 139–147 (2016).
422. Brakke, K. A. The Surface Evolver. *Exp. Math.* **1**, 141–165 (1992).
423. *MSA for Digital Micrograph*. (HREM Research, <https://www.hremresearch.com/Eng/plugin/MSAEng.html>).
424. de la Pena, F. *et al.* Electron Microscopy (Big and Small) Data Analysis With the Open Source Software Package HyperSpy. *Microsc. Microanal.* **23**, 214–215 (2017).
425. Mooney, J. & Kambhampati, P. Correction to “Get the Basics Right: Jacobian Conversion of Wavelength and Energy Scales for Quantitative Analysis of Emission Spectra”. *J. Phys. Chem. Lett.* **5**, 3497–3497 (2014).
426. Klein, C., Dutrow, B., Dana, J. D. & Klein, C. *Manual of mineral science*. (Wiley New York, 2002).
427. Mundy, J. A., Mao, Q., Brooks, C. M., Schlom, D. G. & Muller, D. A. Atomic-resolution chemical imaging of oxygen local bonding environments by electron energy loss spectroscopy. *Appl. Phys. Lett.* **101**, 042907 (2012).
428. Bhattacharyya, D. *et al.* Heterotwin formation during growth of nanolayered Al-TiN composites. *Appl. Phys. Lett.* **96**, 093113 (2010).

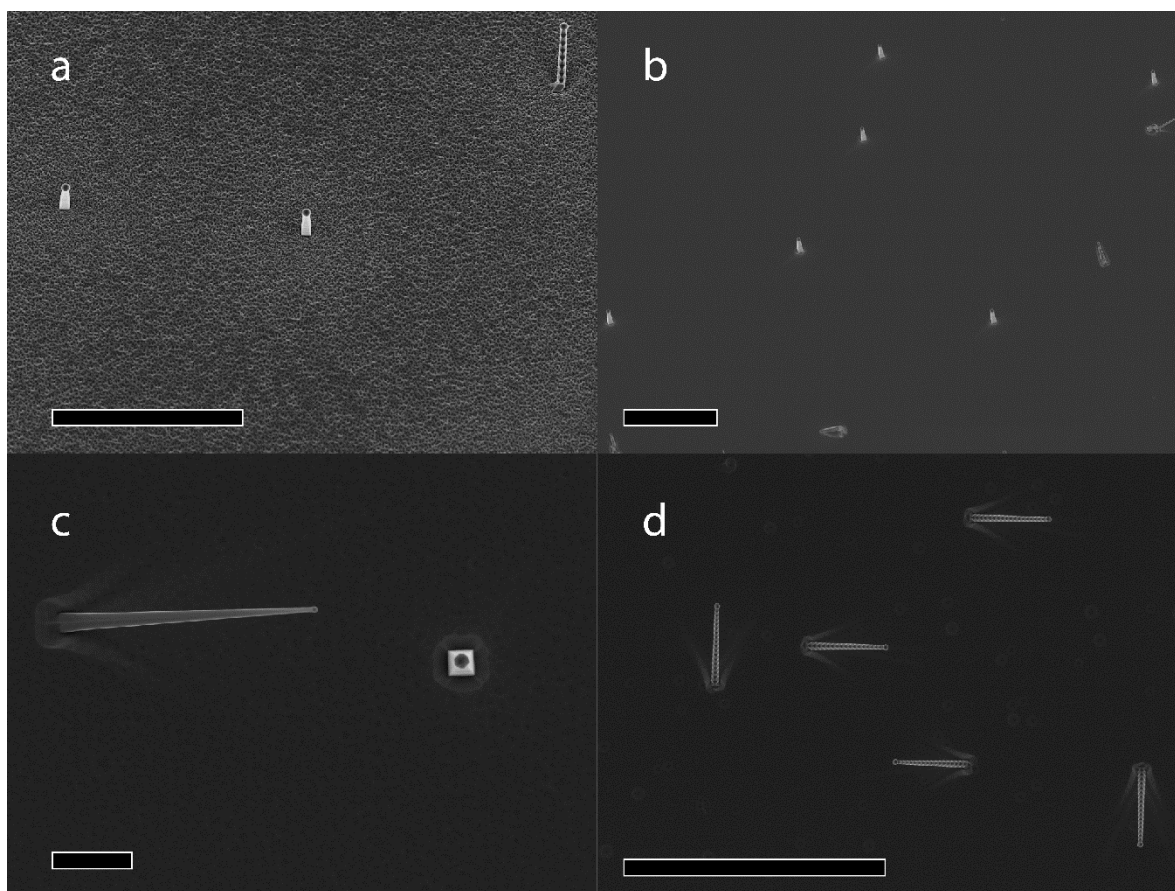
-
429. Bhattacharyya, D., Mara, N. A., Dickerson, P., Hoagland, R. G. & Misra, A. Compressive flow behavior of Al–TiN multilayers at nanometer scale layer thickness. *Acta Mater.* **59**, 3804–3816 (2011).
430. Goldstein, A. P. *et al.* Zigzag Inversion Domain Boundaries in Indium Zinc Oxide-Based Nanowires: Structure and Formation. *ACS Nano* **7**, 10747–10751 (2013).
431. Hoemke, J. *et al.* Inversion domain network stabilization and spinel phase suppression in ZnO. *J. Am. Ceram. Soc* **101**, 2616–2626 (2018).
432. Hoemke, J. *et al.* Inversion domain boundaries in Mn and Al dual-doped ZnO: Atomic structure and electronic properties. *J. Am. Ceram. Soc* **100**, 4252–4262 (2017).
433. Schmid, H., Okunishi, E., Oikawa, T. & Mader, W. Structural and elemental analysis of iron and indium doped zinc oxide by spectroscopic imaging in Cs-corrected STEM. *Micron* **43**, 49–56 (2012).
434. Burgess, T. *et al.* Twinning Superlattice Formation in GaAs Nanowires. *ACS Nano* **7**, 8105–8114 (2013).
435. Isik Goktas, N., Sokolovskii, A., Dubrovskii, V. G. & LaPierre, R. R. Formation Mechanism of Twinning Superlattices in Doped GaAs Nanowires. *Nano Lett.* **20**, 3344–3351 (2020).
436. de la Mata, M. *et al.* The Role of Polarity in Nonplanar Semiconductor Nanostructures. *Nano Lett.* **19**, 3396–3408 (2019).
437. Ross, F. M., Tersoff, J. & Reuter, M. C. Sawtooth Faceting in Silicon Nanowires. *Phys. Rev. Lett.* **95**, 146104 (2005).
438. Andrzejewski, J. & Misiewicz, J. Energy Band Structure of Zn₃P₂-Type Semiconductors: Analysis of the Crystal Structure Simplifications and Energy Band Calculations. *Phys. Status Solidi B* **227**, 515–540 (2001).
439. Brenny, B. J. M. *et al.* Directional Emission from Leaky and Guided Modes in GaAs Nanowires Measured by Cathodoluminescence. *ACS Photonics* **3**, 677–684 (2016).
440. Shin, D., Saparov, B. & Mitzi, D. B. Defect Engineering in Multinary Earth-Abundant Chalcogenide Photovoltaic Materials. *Adv. Energy Mater.* **7**, 1602366 (2017).
441. Wong, L. H. *et al.* Emergin inorganic solar cell efficiency tables (Version 1). *J. Phys. Energy* **1**, 032001 (2019).
442. Ki, W. & Hillhouse, H. W. Earth-Abundant Element Photovoltaics Directly from Soluble Precursors with High Yield Using a Non-Toxic Solvent. *Adv. Energy Mater.* **1**, 732–735 (2011).
443. Lewis, N. S. Research opportunities to advance solar energy utilization. *Science* **351**, aad1920 (2016).
444. Sun, M., Liu, H., Qu, J. & Li, J. Earth-Rich Transition Metal Phosphide for Energy Conversion and Storage. *Adv. Energy Mater.* **6**, 1600087 (2016).
445. Ohshita, Y. & Ishitani, A. Low-temperature and selective growth of β -SiC using the SiH₂Cl₂/C₃H₈/H₂/HCl gas system. *J. Appl. Phys.* **66**, 4535–4537 (1989).
446. McKinley, J. D. & Vance, J. E. The Vapor Pressure of Zinc between 150° and 350°C. *J. Chem. Phys.* **22**, 1120–1124 (1954).
447. Melville, H. & Gray, S. The vapour pressure of red phosphorus. *J. Chem. Soc. Faraday Trans.* **32**, 1026–1030 (1936).

-
448. Liang, D. *et al.* Optical Absorption Enhancement in Freestanding GaAs Thin Film Nanopyramid Arrays. *Adv. Energy Mater.* **2**, 1254–1260 (2012).
449. Battaglia, C. *et al.* Light Trapping in Solar Cells: Can Periodic Beat Random? *ACS Nano* **6**, 2790–2797 (2012).
450. Zhu, Y., Ophus, C., Ciston, J. & Wang, H. Interface lattice displacement measurement to 1pm by geometric phase analysis on aberration-corrected HAADF STEM images. *Acta Materialia* **61**, 5646–5663 (2013).
451. Hÿtch, M. J., Snoeck, E. & Kilaas, R. Quantitative measurement of displacement and strain fields from HREM micrographs. *Ultramicroscopy* **74**, 131–146 (1998).
452. Bhushan, M. Schottky solar cells on thin polycrystalline Zn3P2 films. *Appl. Phys. Lett.* **40**, 51–53 (1982).
453. Kresse, G. & Hafner, J. Ab initio molecular dynamics for liquid metals. *Phys. Rev. B* **47**, 558–561 (1993).
454. Kresse, G. & Hafner, J. Ab initio molecular-dynamics simulation of the liquid-metal–amorphous-semiconductor transition in germanium. *Phys. Rev. B* **49**, 14251–14269 (1994).
455. Kresse, G. & Furthmüller, J. Efficient iterative schemes for ab initio total-energy calculations using a plane-wave basis set. *Phys. Rev. B* **54**, 11169–11186 (1996).
456. Blöchl, P. E. Projector augmented-wave method. *Phys. Rev. B* **50**, 17953–17979 (1994).
457. Kresse, G. & Joubert, D. From ultrasoft pseudopotentials to the projector augmented-wave method. *Phys. Rev. B* **59**, 1758–1775 (1999).
458. Perdew, J. P., Burke, K. & Ernzerhof, M. Generalized Gradient Approximation Made Simple. *Phys. Rev. Lett.* **77**, 3865–3868 (1996).
459. Perdew, J. P., Burke, K. & Ernzerhof, M. Generalized Gradient Approximation Made Simple [Phys. Rev. Lett. 77, 3865 (1996)]. *Phys. Rev. Lett.* **78**, 1396–1396 (1997).
460. Grimme, S., Antony, J., Ehrlich, S. & Krieg, H. A consistent and accurate ab initio parametrization of density functional dispersion correction (DFT-D) for the 94 elements H–Pu. *J. Chem. Phys.* **132**, 154104 (2010).
461. Monkhorst, H. J. & Pack, J. D. Special points for Brillouin-zone integrations. *Phys. Rev. B* **13**, 5188–5192 (1976).
462. Watson, G. W., Kelsey, E. T., de Leeuw, N. H., Harris, D. J. & Parker, S. C. Atomistic simulation of dislocations, surfaces and interfaces in MgO. *J. Chem. Soc., Faraday Trans.* **92**, 433–438 (1996).

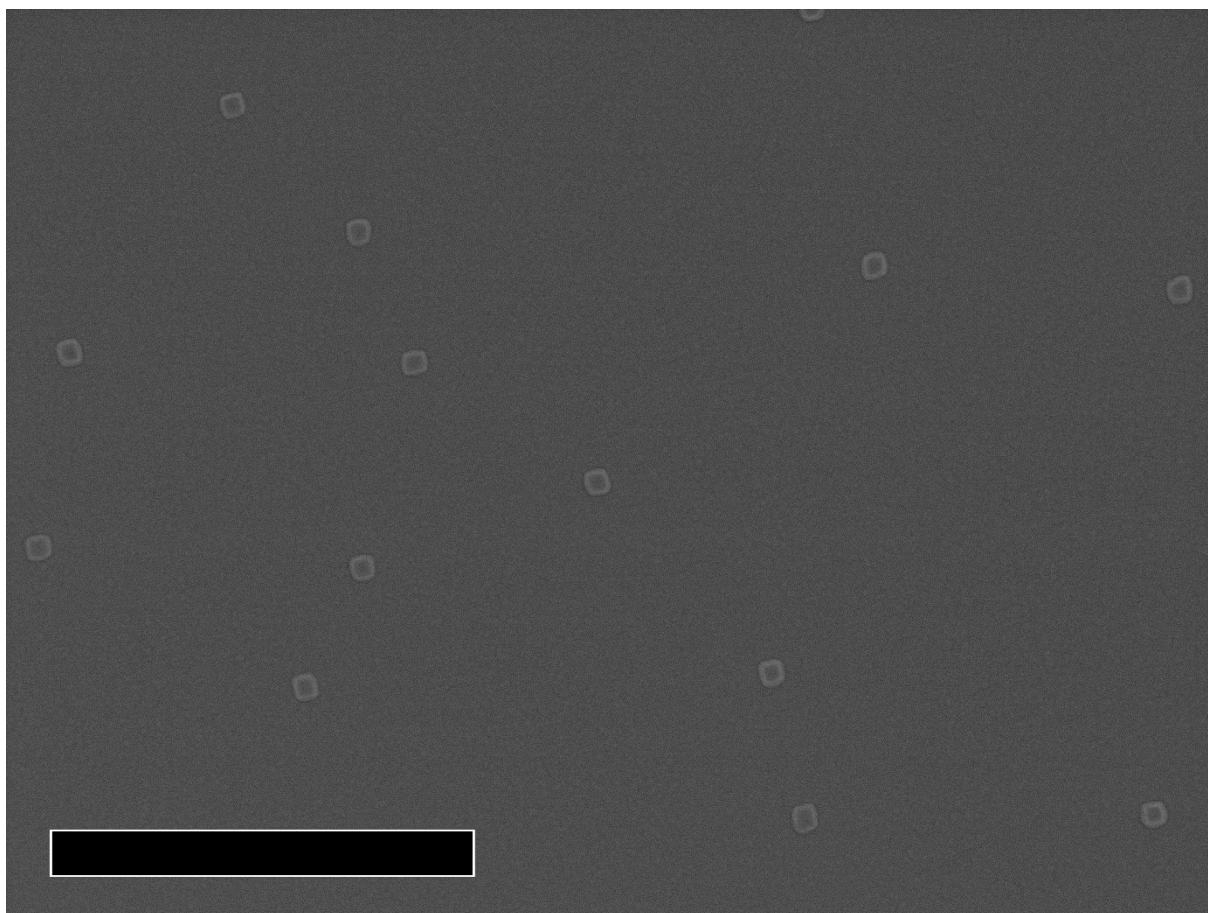
Appendix A – Supplementary Information for “Multiple Morphologies and Functionality of Earth-Abundant Zinc Phosphide Nanowires”

Simon Escobar Steinvall, Nicolas Tappy, Masoomah Ghasemi, Reza R. Zamani, Thomas LaGrange, Elias Z. Stutz, Jean-Baptiste Leran, Mahdi Zamani, Rajrupa Paul, Anna Kúkol'ová, Anna Fontcuberta i Morral

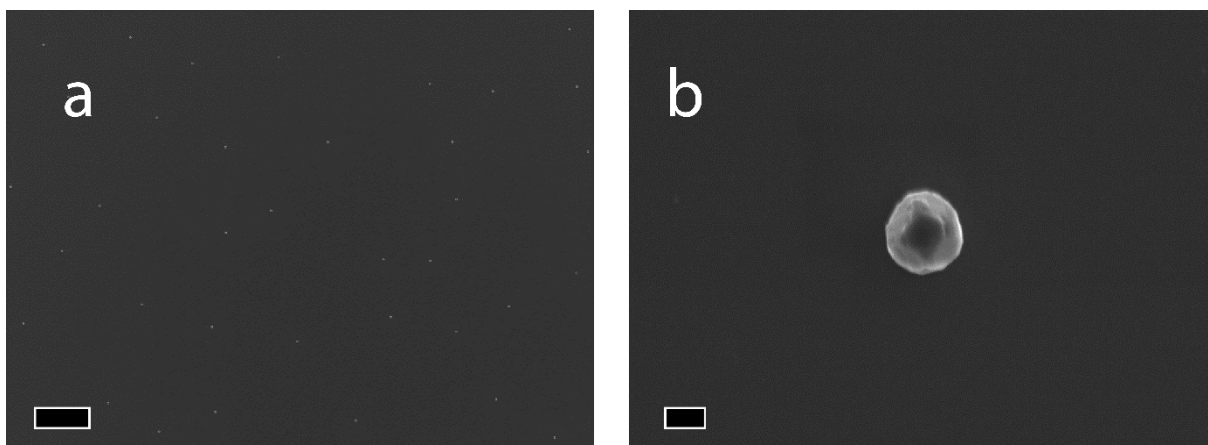
Supplementary Figures



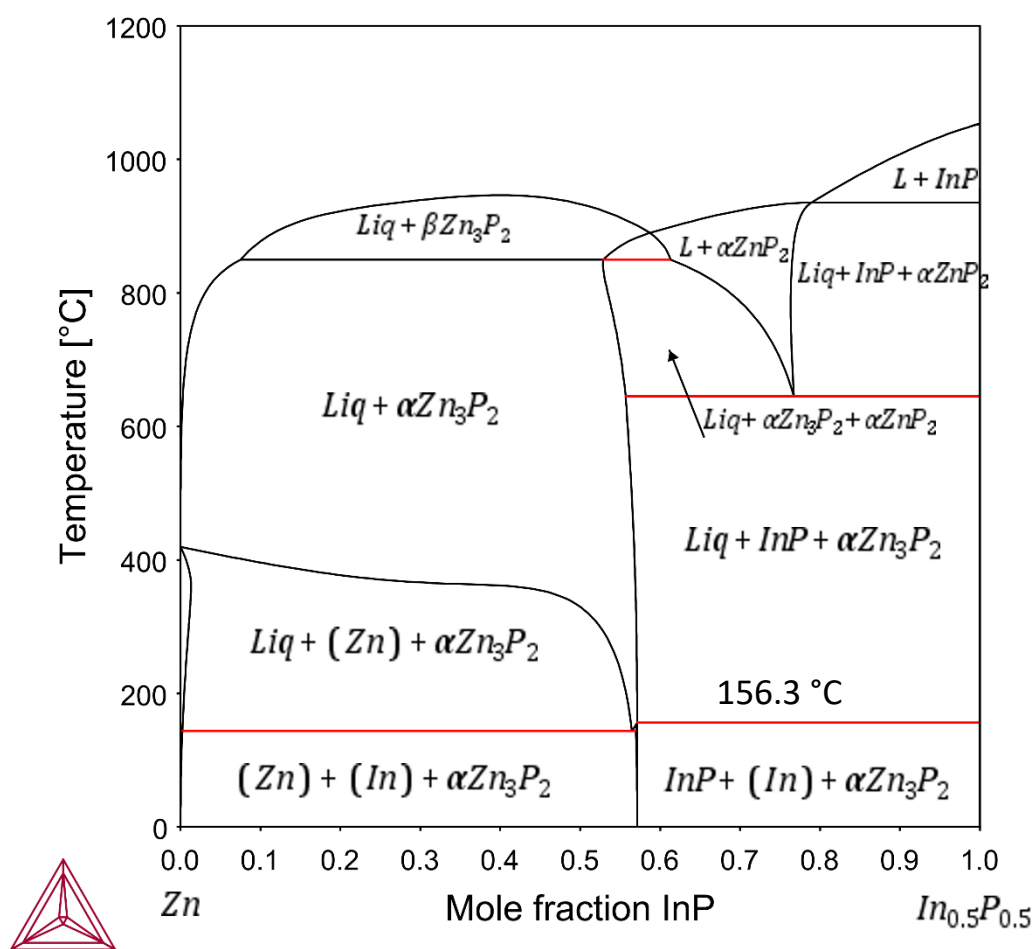
Supplementary Figure A.S 1. SEM of nanowires at different magnifications. (a) and (b) are of vertical nanowires observed at 20° tilt (V/II ratio = 1.15 and 1.30, respectively). (c) shows a straight-tilted and vertical nanowire in close proximity (V/II ratio = 1.00) (d) is a top view image of zigzag nanowires (V/II ratio = 1.45). a, b and d have 10 µm scalebars, c has a 1 µm scale bar.



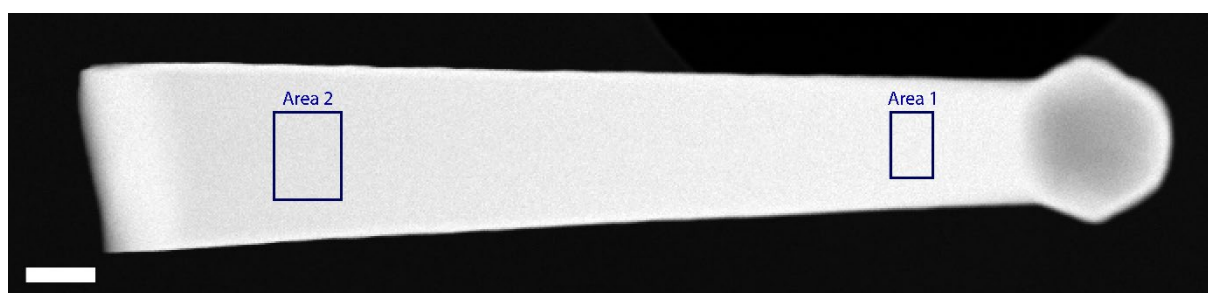
Supplementary Figure A.S 2. SEM of thin film overgrowing the catalyst particles. 10 μm scalebar.



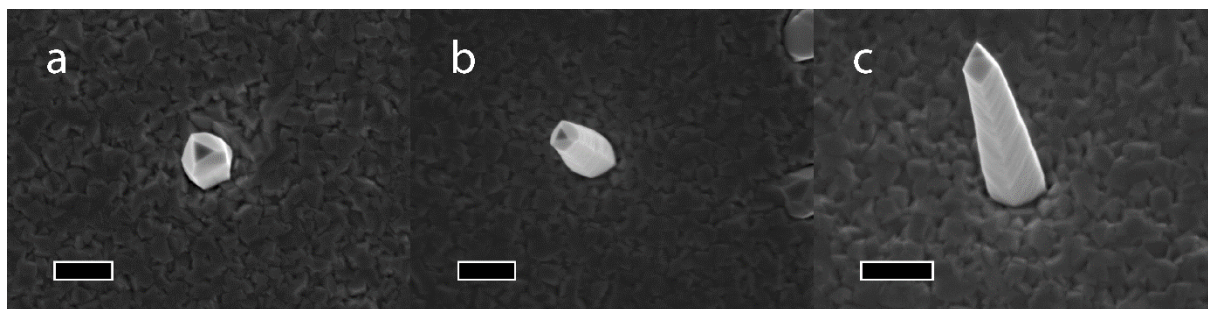
Supplementary Figure A.S 3. SEM images of the initial catalyst particles at room temperature at different magnifications. The particles were generated using a 5 minutes zinc predeposition at 200 $^{\circ}\text{C}$ at a flux of 3.4×10^{-7} Torr. The average size was 365 nm with a standard deviation of 8 nm, and a density of one particle per 323 μm^2 . Scale bars are 10 μm and 200 nm respectively.



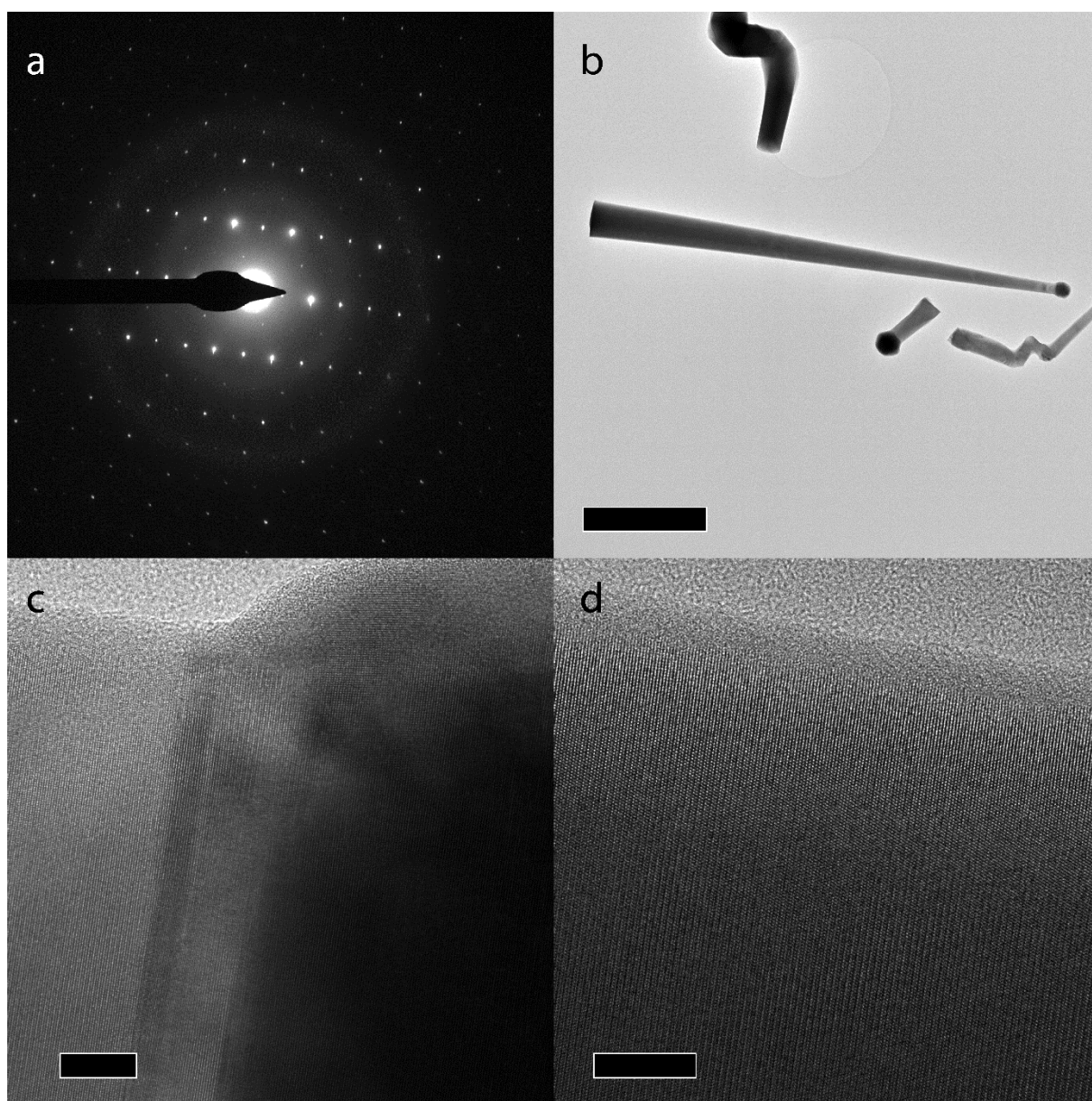
Supplementary Figure A.S 4. Vertical section between Zn and InP, showing the transition at 156.3 °C from the liquid phase to the room temperature phases.



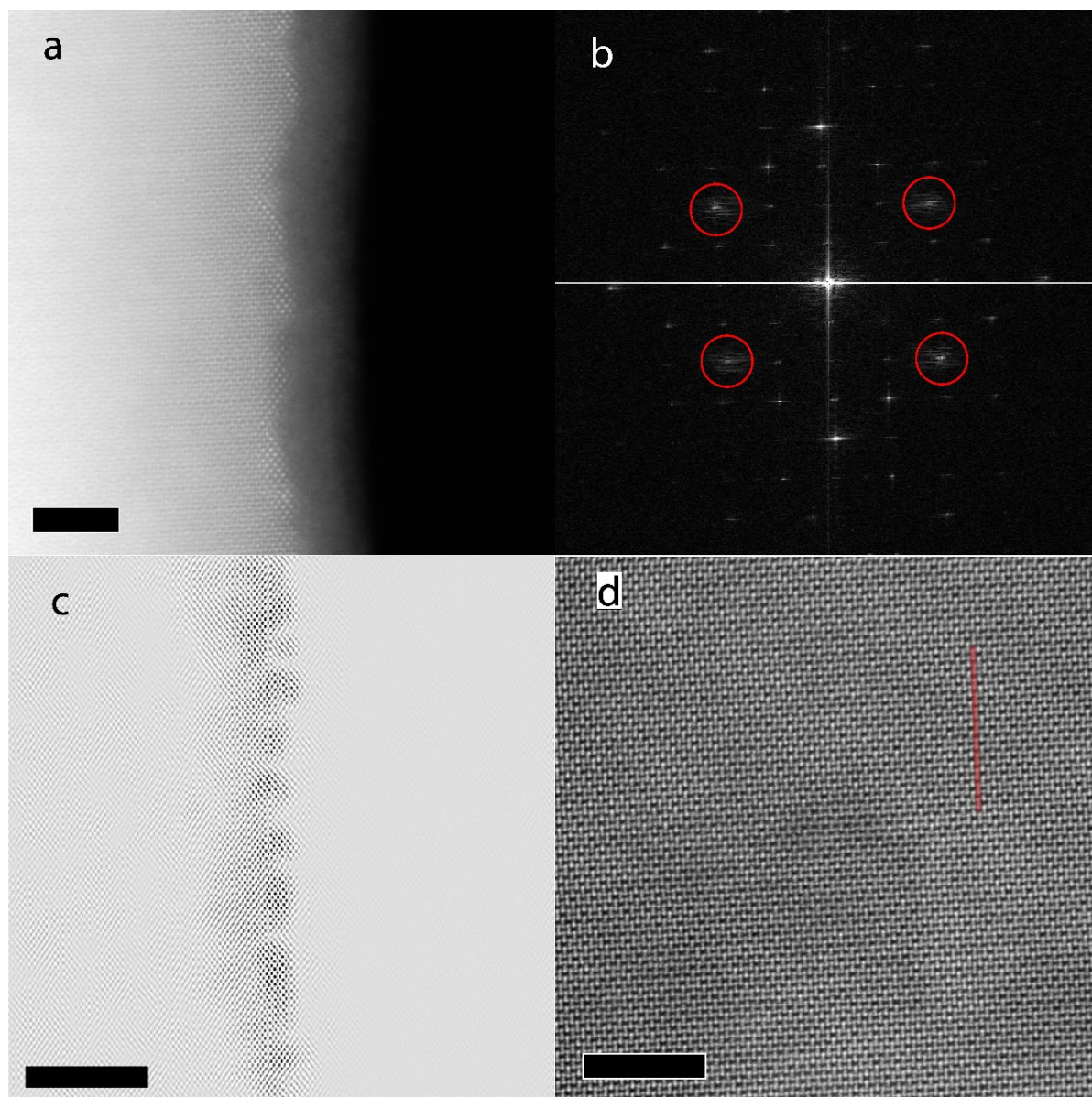
Supplementary Figure A.S 5. HAADF-STEM image of a vertical nanowire grown at a V/II ratio of 1.45 used for full wire EDX analysis. The composition of Area 1 (top) is 60.34% Zn and 39.66% P. The composition of Area 2 (bottom) is 60.71% Zn and 39.29% P. The scale bar is 250 nm.



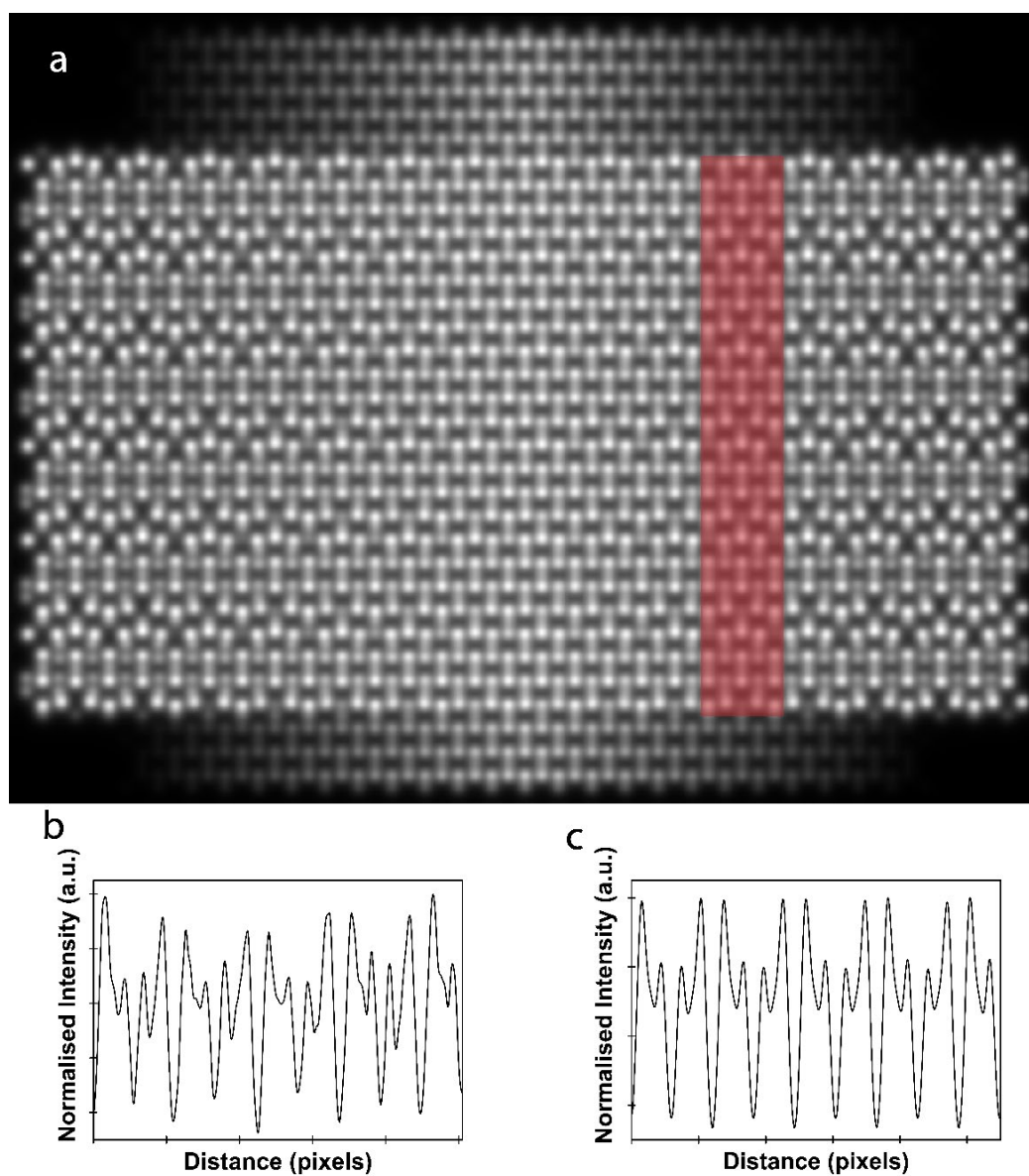
Supplementary Figure A.S 6 SEM of VS grown Zn_3P_2 nanowires. (a) and (b) are top view images, whilst (c) is acquired at 20° tilt. Scale bars are 500 nm.



Supplementary Figure A.S 7. (a) shows the SAED pattern along the $[111]$ zone axis. (b) is a low magnification image of the whole nanowire. (c) and (d) are HRTEM images of the nanowire in regions close to the droplet and towards the centre of the nanowire, respectively. Note that no stacking faults are observed along this zone axis. Scale bar in b is $1\ \mu\text{m}$, scale bars in c and d are 10 nm.



Supplementary Figure A.S 8. (a) is a low magnification AC-HAADF STEM image of the surface of a vertical nanowire. (b) shows the FFT, and the red circles show the areas where we applied a mask to do an inverse FFT (c). (c) highlights the areas with a different crystal structure based on the applied mask. (d) shows a low magnification AC-HAADF STEM image of the bulk of the nanowire. The red line indicates where the line profile, presented below, was taken to compare with models to match the pattern and composition. Scale bar in c is 10 nm, in a and d they are 5 nm.

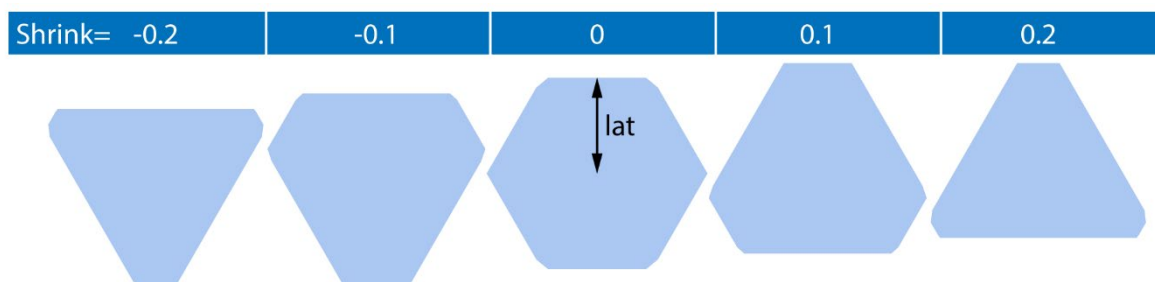


Supplementary Figure A.S 9. (a) Simulated STEM image of the zinc rich Zn_3P_2 along the $[100]$ zone axis. The edges shows the expected pattern for stoichiometric Zn_3P_2 whilst the centre shows Zn_2P , where all vacant sites are filled with Zn atoms, assuming no change in crystal symmetry. The pattern observed in Figure 4I and Supplementary Figure S5d corresponds to a very Zn rich material, close to the highlighted region, as supported by the line intensity profiles of the measured (b) and modelled (c) intensities.

Appendix B – Supplementary Information to “Heterotwin Zn₃P₂ Superlattice Nanowires: the Role of Indium Insertion in the Superlattice Formation Mechanism and their Optical Properties”

Simon Escobar Steinvall*, Lea Ghisalberti*, Reza R. Zamani*, Nicolas Tappy, Fredrik S. Hage, Elias Stutz, Mahdi Zamani, Rajrupa Paul, Jean-Baptiste Leran, Quentin M. Ramasse, W. Craig Carter, Anna Fontcuberta i Morral

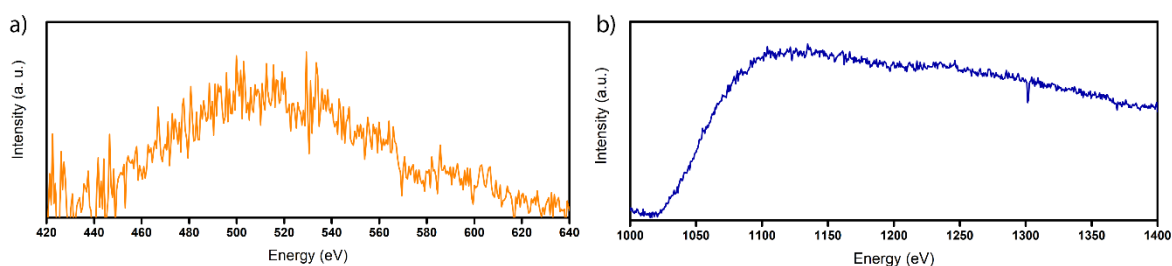
Parameter definition



Supplementary Figure B.S 1. Illustration of the parameters used to model the droplet behaviour.

Core-loss electron energy-loss spectra

Fitting of the EEL maps are done using the peak at 443 eV for In and 1020 eV for Zn. EEL spectra after denoising are shown in Figure B.S2, showing the In (a) and Zn signal (b). The fitting is done using the software Gatan Digital Micrograph v2.32.

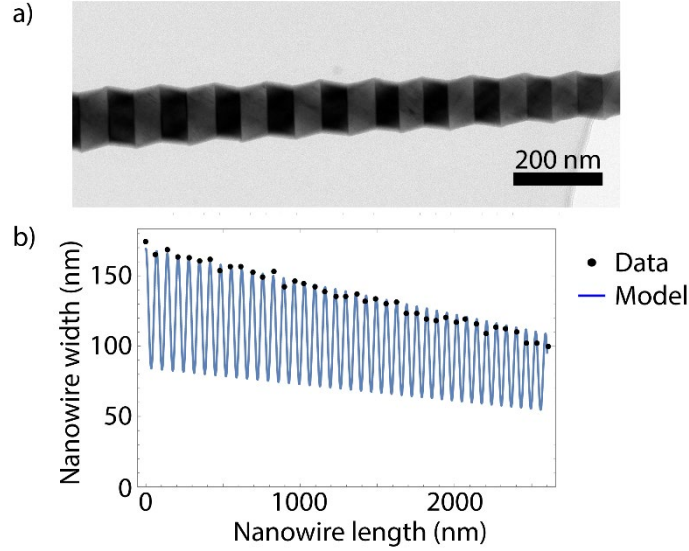


Supplementary Figure B.S 2. (a) EEL spectrum showing the In peak and (b) EEL spectrum showing the Zn peak used for mapping.

Oscillation Modelling

In Figure B.S3a we show a HR-TEM image of a zigzag Zn₃P₂ nanowire. We can clearly observe the presence of a sharp interface between regions having different crystal orientation (having different contrast as well). This interface occurs where the heterotwin forms and produces the change the crystal orientation. To investigate the driving forces at the origin of this growth process, we looked for a periodicity rule in the insertion of these heterotwins as a function of the

length of the nanowire. Due to the tapering effect influencing the width of the nanowire along its growth axis, we decided to measure the position and the nanowire’s width at which the heterotwin is inserted through the software ImageJ. In Figure B.S3b we show the data points collected and the periodic function fitting the data.



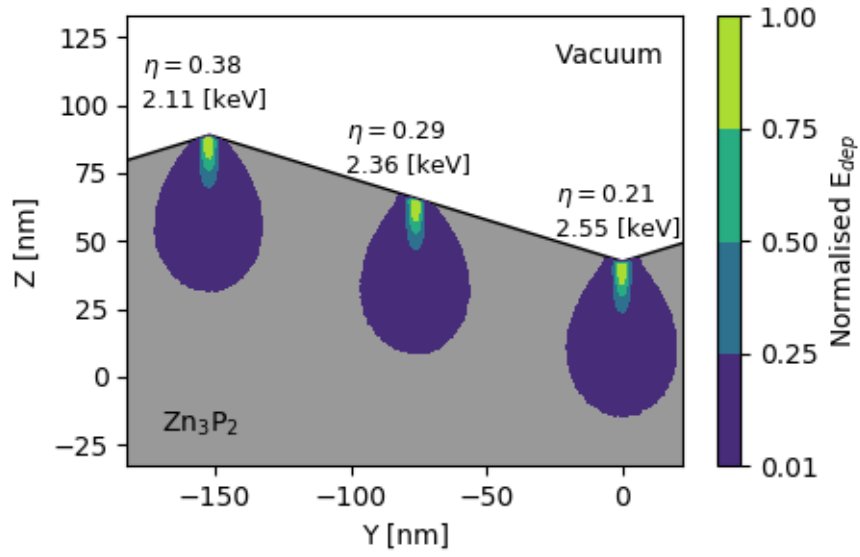
Supplementary Figure B.S 3. a) TEM image of zigzag Zn₃P₂ nanowire grown by MBE and b) plot of the development of an approximation of the nanowire’s width as a function of the nanowire’s growth axis: the dots represent the measurements taken on the sample shown in a) with fitting function reported in Equation 5.1.

The selected periodic function (eq. 5.1) has a linear decay in the amplitude and an exponential decay in the frequency of insertion of the heterotwin. W_0 and h_0 are the initial width of the nanowire and the initial separation between the first two consecutive heterotwins observed in the nanowire. The fitting to the data produces $\pi/2.02$ (89°) for the tapering factor, which corresponds to the tapering angle measured in zigzag nanowires through SEM analysis (i.e., the amplitude linear decay); and 2×10^{-5} for the continuous decay rate of the separation, characterizing the exponential decay in the heterotwin insertion periodicity. We believe that the tapering factor and the continuous decay rate coefficient depends on the MBE growth conditions, i.e. temperature and II-V ratio.

$$W(x) = \left(W_0 - \frac{W_0 - \frac{W_0}{2}}{2} - \frac{x}{\tan \frac{\pi}{2.02}} \right) \left(1 + \frac{1}{3} \cos \frac{2\pi x}{h_0 e^{-2 \times 10^{-5} x}} \right) \quad (5.1)$$

Casino simulations of energy deposition in a superlattice nanowire

The simulations performed using CASINO software (V3.3) are presented in Figure B.S4. It can be observed that the extent of the beam interaction volume in Zn₃P₂ does not exceed 50 nm in depth and laterally at an acceleration voltage of 3kV. The assumption that no energy reaches through the sample at this acceleration voltage is thus well verified for most probed points on the CL map. Additionally, the total amount of energy deposited in the sample varies by 17% between outwards and inwards facing apices. This is explained by the variation in backscattering coefficient (η), which is largely influenced by the local geometry. We make the argument that the CL emission should follow the energy deposited by the beam. Accordingly, the superlattice nanowire local geometry is sufficient to explain the dark edge-contrast observed in the panchromatic CL map (Figure 5.3).



Supplementary Figure B.S 4. CASINO Simulation of energy deposited in the sample for different edge configuration. Coloured surfaces show the decrease in energy density deposited in the sample, normalised to the maximum. Annotations show the fraction of backscattered electrons (η) and the total amount of energy (in keV) deposited in the sample per electron, for each edge configuration. It is observed that outwards facing apices (left) show enhanced backscattering compared to inwards facing apices (right) or facets (middle). Simulations were performed using a collimated electron beam of 10 nm diameter at 3 kV and a density of 4.55 g cm^{-3} for Zn₃P₂. Due to the limited possibilities of simulating complex geometries in CASINO 3, we model the sample with truncated pyramids. This approximation reproduces well local edge configuration, but would not be valid in experiment conditions where a significant part of the beam energy is transmitted through the sample, e.g. at high beam energies.

Appendix C – Supporting Information to “Towards Defect-Free Thin Films of the Earth-Abundant Absorber Zinc Phosphide by Nanpatterning”

Simon Escobar Steinvall, Elias Z. Stutz, Rajrupa Paul, Mahdi Zamani, Nelson Y. Dzade, Valerio Piazza, Martin Friedl, Virginie de Mestral, Jean-Baptiste Leran, Reza R. Zamani, Anna Fontcuberta i Morral

Methodology

Substrate Fabrication. Indium phosphide (100) substrates were prepared by depositing 30 nm of silicon dioxide (SiO_2) using plasma-enhanced chemical vapour deposition (PECVD) in an Oxford Plasmalab System 100. The samples were then spin-coated with 40 nm ZEP resist before they were exposed using a Raith EBPG5000+ electron beam lithography system operating at 100 kV. The samples were then cold developed using n-amylacetate which was kept at -18°C for one minute followed by one minute in isopropanol. The resist was then descummed for 10 seconds at low power in a Tepla GiGAbatch oxygen plasma system, and subsequently the oxide was etched using SPTS APS Dielectric etcher for 30 seconds. The resist was then stripped using the previously mentioned oxygen plasma system for 10 minutes at a high power. Finally, a 10 second dip in a 1:39 BHF and deionised water solution was performed, and after a rinse the substrates were ready for introduction into the MBE system.

Growth. The growth was carried out in a Veeco GENxplor MBE system. First, the substrate was degassed for one and a half hours at 150°C in the load lock, and then for 2 hours at 300°C in the buffer module. The samples were then introduced to the growth module (base pressure $\sim 1.5 \times 10^{-10}$ Torr), where the native oxide was removed by degassing at a manipulator temperature of 580°C for 10 minutes under a phosphorus atmosphere (phosphorus flux $> 1 \times 10^{-6}$ Torr), supplied by a MBE Komponenten GaP sublimation source. Fluxes are defined by the beam flux monitor (BFM) reading. The manipulator is then ramped to the growth temperature (280 – 300°C for intrinsic substrates, 280°C for doped substrates), and a five-minute zinc pre-deposition was performed (zinc flux of 3.4×10^{-7} Torr). Growth was then carried out for a time ranging from five minutes to six hours depending on the sample, using a zinc base pressure of 6.04×10^{-7} Torr whilst varying the phosphorus flux between 1.09×10^{-7} Torr and 4.35×10^{-7} Torr.

Electron Microscopy. SEM images were acquired in a Zeiss Merlin operating at 3 kV and 100 pA using an InLens detector. TEM lamellae were prepared by focused ion beam in a Zeiss NVision 40 CrossBeam FIB and SEM setup on a sample grown for 4 hours at 280°C at a V/II ratio of 0.39 on a p-type indium phosphide substrate and a sample grown for 6 hours on intrinsic indium phosphide with a V/II ratio of 0.5 to observe coalescence. Conventional TEM and STEM analysis were performed in a FEI Talos TEM operating at 200 kV, while aberration-corrected STEM imaging was performed in a FEI Titan Themis operating at 200 kV, equipped with a cold field-emission gun, monochromator, and a CEOS aberration correctors (probe and image). GPA was done using the Gatan Digital Micrograph plugin GEM-GPA v10.1. The AC-HAADF-STEM images were treated using a radial Wiener filter.

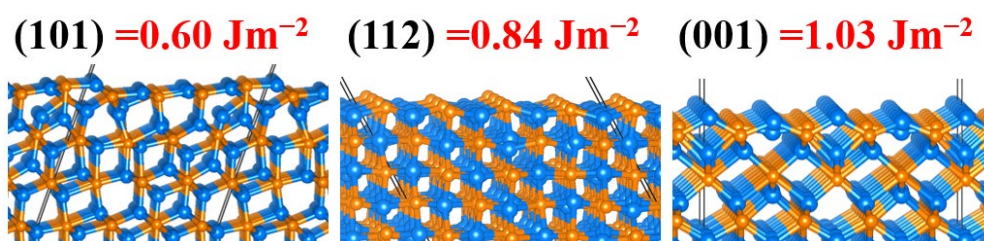
Optical Characterisation. Room temperature PL was carried out on a sample grown for 4 hours at a V/II ratio of 0.5 and at 290°C using a 488 nm Ar^+ laser (25 μW) and Andor iDus DV420A-OE detector using 3s integration with 20 accumulations.

Atomic Force Microscopy. Normal AFM was done using a Bruker FastScan AFM equipped with an Si tip operating in contact mode. Conductive AFM was performed in an Asylum Research Cypher VRS AFM with a platinum–silicide (PtSi-FM) tip. Contact mode was used to acquire the I-V curves. The cantilever is grounded while a bias is applied across the sample. The tip is employed as the top contact and the bottom contact is made using silver paste to join the backside of the InP chip to the stage.

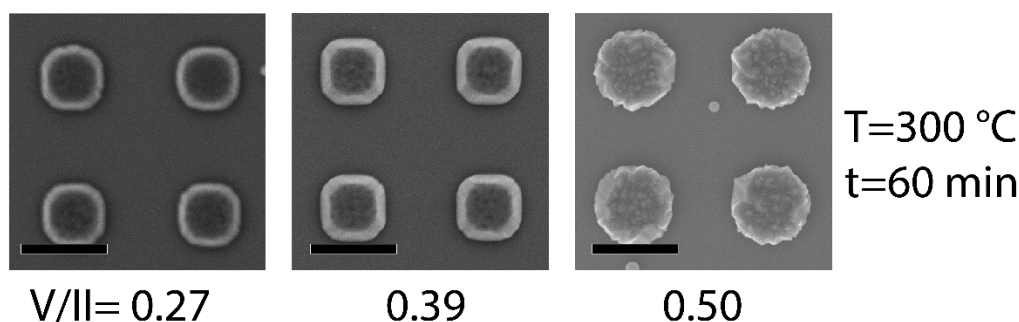
Atomic Models. The unit cell model was illustrated using VESTA using data from the Crystallography Open Database based on the report by Stackelberg and Paulus.⁶⁸ The 3D core-shell models were created using the Rhodius software package.⁴⁰⁶

Density Functional Theory. The electronic structure was calculated through density functional theory (DFT), using Vienna Ab initio Simulation Package (VASP) to implement the periodic boundary conditions.^{453–455} Valence and core electron interactions were de-

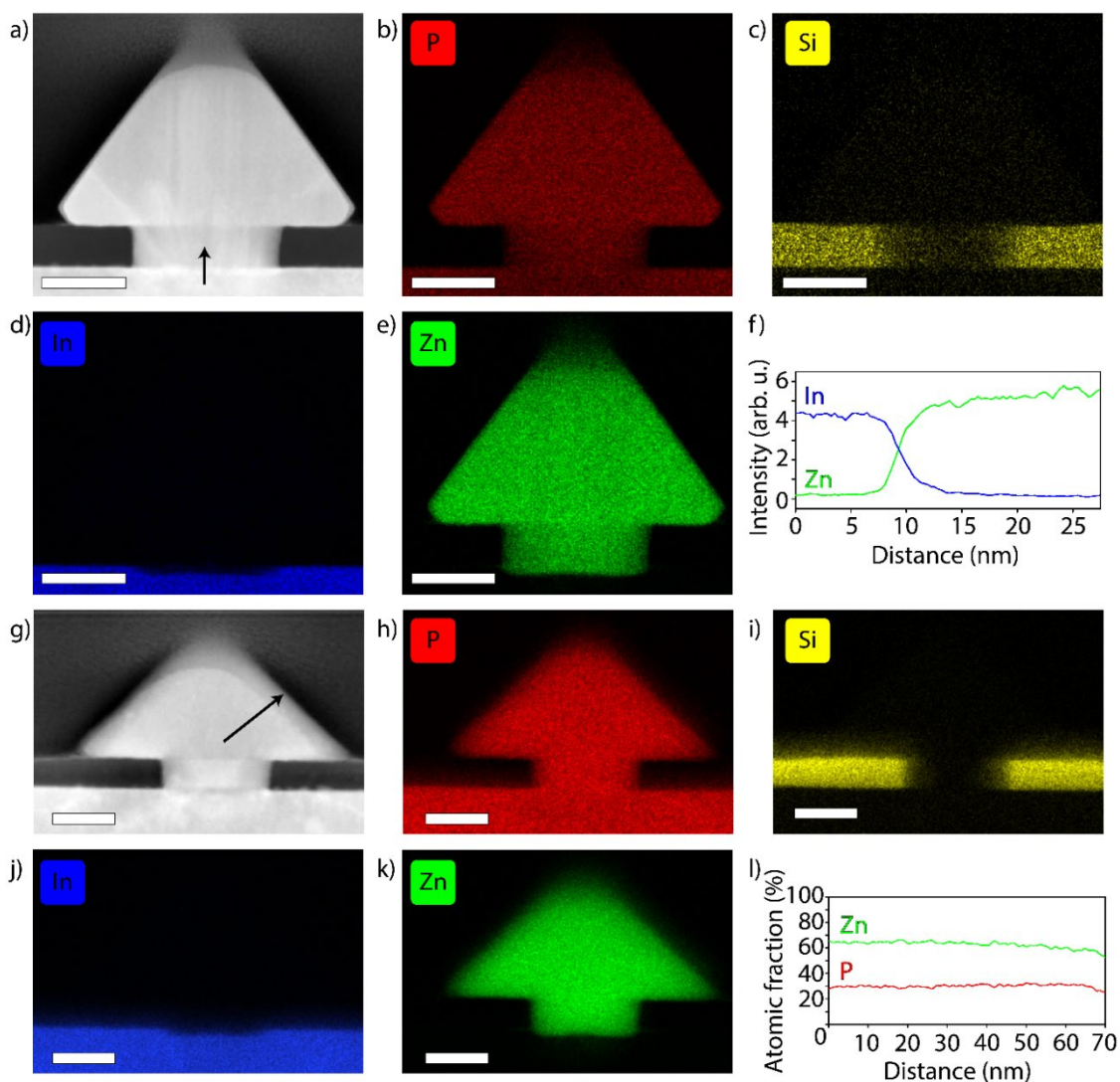
scribed with the projected augmented wave (PAW) method.^{456,457} The GGA-PBE functional was used to calculate the electronic exchange-correlation potential, and the Grimme DFT-D3 method was used to account for the long-range dispersion forces.^{458–460} To converge the total energy of the system a plane-wave basis with a kinetic energy cut-off of 600 eV was used. This allowed it to converge to within 10^{-6} eV and for the residual Hellmann-Feynman forces to reach 10^{-3} eV \AA^{-1} for the relaxed atoms. A $5 \times 5 \times 3$ Monkhorst–Pack K -points mesh was used to sample the Brillouin zone of the bulk Zn_3P_2 .⁴⁶¹ For the (001), (101), and (112) surfaces, K -points meshes of $5 \times 3 \times 1$, $5 \times 3 \times 1$, and $3 \times 3 \times 1$ were used, respectively, to ensure electronic and ionic convergence. The $P4_2/nmc$ space group was used in the META-DISE code to generate the (001), (101), and (112) surfaces, ensuring zero dipole moment perpendicular to the surface plane.^{68,462} The surface energies calculated and visualisations of the different surfaces are shown in Figure C.S1.



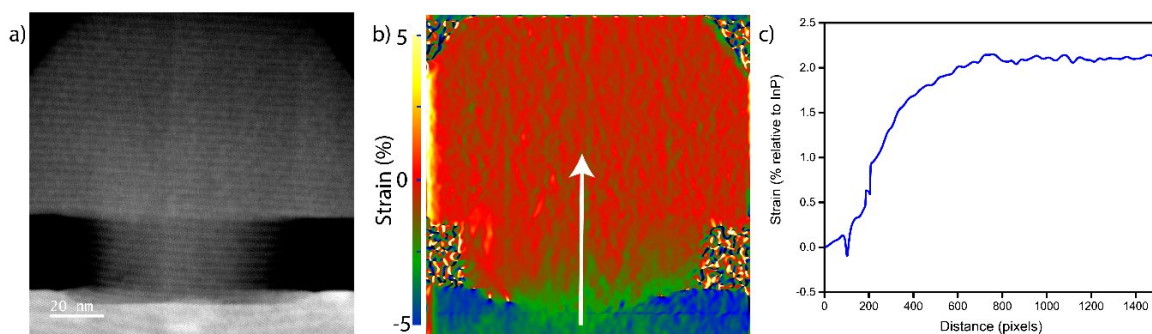
Supplementary Figure C.S 0-1. Surface energies for the different planes considered and an illustration of the structures used for the DFT calculations.



Supplementary Figure C.S 0-2. SEM images of a V/II series grown at a manipulator temperature of 300 °C, showing how the ideal growth conditions shift from a V/II ratio of 0.5-0.63 to 0.27-0.39 (500 nm scale bars).



Supplementary Figure C.S 0-3. (a) HAADF image of pyramid grown in a 30 nm nominal hole along [100]. (b-e) EDX maps of P, Si, In, Zn of the pyramid. (f) Line-scan of the interface between the base and the pyramid showing a diffuse boundary between In and Zn in the area as indicated by the arrow in (a). (g) HAADF image of a pyramid grown in a 30 nm nominal hole along [110]. (h-k) EDX maps of P, Si, In, Zn of the pyramid. (l) Line-scan showing a homogeneous composition along the pyramid along the area indicated by the arrow in (g). (50 nm scale bars.)



Supplementary Figure C.S 0-4. (a) AC-HAADF-STEM of a pyramid grown from a 30 nm nominal hole. (b) Strain map acquired through GPA in the in-plane (xx) direction, perpendicular to the surface normal. (c) Line-scan along the arrow in (b) showing the strain relaxation of the zinc phosphide (right) in relationship to the indium phosphide (0) as it grows out from the hole.

Curriculum Vitae – Simon Escobar Steinvall

Date of birth: 7th May 1992
 Address: Rue du Jura 4
 ZIP/City: 1023 Crissier
 Country: Switzerland

Nationality: Swedish (SE)
 Phone: 0041 (0)78 672 06 81
[Google Scholar](#)
[ORCID-iD](#)

Research Interests

My research interest lies in the growth and characterisation of functional inorganic nanomaterials. To this end, I have investigated the growth of nanowires through chemical and physical synthesis routes and specialised in characterisation through electron microscopy, optical spectroscopy, and electrical measurements. To aid these endeavours I am also well versed in cleanroom nano/microfabrication.

Education

Sep 2016 – **École Polytechnique Fédérale de Lausanne**, PhD (Material Science and Engineering)
 Topic: Growth of earth-abundant semiconductor nanostructures for solar energy harvesting
 Supervisors: A. Fontcuberta i Morral, R. R. Zamani
 Date of thesis defence: 3rd November 2020

Sep 2012 – **Imperial College London**, MEng (Material Science and Engineering)
 Jun 2016 Thesis topic: Fluorescence Enhancing Zinc Oxide Nanoflowers for Biosensing Applications
 Supervisor: F. Xie
 Specialisation: Nanomaterials and functional materials

2010 – 2012 **Katedralskolan Uppsala**, International Baccalaureate Diploma

Professional Experience

2015
 Jul - Sep **Paul Scherrer Institut**, Summer Research Student (3 months)
 Topic: *In situ* x-ray tomography of polymer electrolyte fuel cells at the Swiss Light Source Synchrotron.
 Supervisors: J. Eller, F. Büchi

2014
 Jul - Sep **Westinghouse Electric Sweden AB**, Summer Research Student (3 months)
 Topic: Computational research related to in-pile nuclear fuel.
 Supervisor: P. Blair

2013
 Jul - Sep **Imperial College London & Oxford University**, Summer Research Student (3 months)
 Topic: Deposition and characterisation of gold nanoparticles on B-doped diamond substrates.
 Supervisors: G. Nelson, J. S. Foord, D. Payne

Institutional Responsibilities

- Co-responsible for installation, maintenance and upkeep of a Veeco GENxplor molecular beam epitaxy system (~1.5 Mio CHF) at the Laboratory of Semiconductor Materials, EPFL, as well as training and assisting users, and writing user manuals.
- In charge of the labs supply of electron microscopy related consumables, as well as helping to teach and assist less experienced users.
- Organising outreach and collaborator visits and presentations, e.g.:
 - Bassett Green Primary School, 11th March 2019. [Link](#)
 - Yearly University of Tokyo Student Visit, EPFL, Early March 2017-2020
- Teaching assistant for undergraduate courses and supervision of bachelor and master projects.
- Collaborations with the groups of Prof. Zardo (Basel), Prof. Nose (Kyoto), Prof. Grundler (EPFL), Prof. Ramasse (SuperSTEM/Leeds), Dr. Martelli (CNR Rome).

Language & IT Skills

Languages	Swedish (native)	Japanese (advanced)
	Spanish (fluent)	French (intermediate)
	English (fluent)	
Programming:	Matlab, Mathematica	

Prizes & Funding

2019	Successful proposal for beamtime at the SuperSTEM electron microscopy facilities.
2018	EPFL EDMX Research Day Poster Award.
2016	Institute of Materials Award: Overall academic performance and contributions to the Materials Department at Imperial College London.
2015	Engineering Dean's list at Imperial College London. Student Activities Award from the Old Centralians' Trust.
2014	Ronald Jock McGregor Prize for highest rated case study in my year group.
2013	Scholarship from the Engineering and Physical Sciences Research Council (EPSRC) to cover living expenses and consumables during my summer research internship.
2012	Graduated from Katedralskolan with a scholarship from Axel Johanssons Donationsfond. Ranked 7th in the Swedish National Chemistry Olympiad.

Peer-reviewed Publications

Total Citations (Google Scholar):30

11. Towards Defect-Free Thin Films of the Earth-Abundant Absorber Zinc Phosphide by Nanopatterning
S. Escobar Steinvall, E. Z. Stutz, R. Paul, M. Zamani, N. Y. Dzade, V. Piazza, M. Friedl, V. de Mestral, J. B. Leran, R. R. Zamani, A. Fontcuberta i Morral
Nanoscale Advances, 2020. (DOI: 10.1039/d0na00841a) [Link](#)

10. Raman Spectra and Lattice Dynamic Calculations of Tetragonally-Structured Zinc Phosphide (Zn_3P_2)
E. Z. Stutz, S. Escobar Steinvall, A. P. Litvinchuk, J. B. Leran, M. Zamani, R. Paul, A. Fontcuberta i Morral, M. Dimitrievska
Nanotechnology, 2020. (DOI: 10.1088/1361-6528/abc91b) [Link](#)

9. Optical Properties and Carrier Dynamics in Co-doped ZnO Nanorods
A. K. Sivan, A. Galan-Gonzalez, L. Di Mario, N. Tappy, J. Hernandez-Ferrer, D. Catone, S. Turchini, A. M. Benito, W. K. Maser, S. Escobar Steinvall, A. Fontcuberta i Morral, A. Gallant, D. A. Zeze, D. Atkinson, F. Martelli
Nanoscale Advances, 2020. (DOI:10.1039/d0na00693a) [Link](#)

8. Heterotwin Zn_3P_2 Superlattice Nanowires: the Role of Indium Insertion in the Superlattice Formation Mechanism and their Optical Properties
S. Escobar Steinvall, L. Ghisalberti, R. R. Zamani, N. Tappy, F. Hage, M. Zamani, R. Paul, E. Z. Stutz, J. B. Leran, Q. M. Ramasse, W. C. Carter, A. Fontcuberta i Morral
Nanoscale, **12**, 22534-22540, 2020. [Link](#) (Back cover)

7. Plasma-Enhanced Atomic Layer Deposition of Nickel Nanotubes with low Resistivity and Coherent Magnetization Dynamics for 3D Spintronics
M. C. Giordano, K. Baumgaertl, S. Escobar Steinvall, A. Fontcuberta i Morral, D. Grundler
ACS Applied Materials & Interfaces, **12**(36), 40443-40452, 2020. [Link](#)

6. Measuring the Optical Absorption of Single Nanowire
M. Y. Swinkels, A. Campo, D. Vakulov, W. Kim, L. Gagliano, S. Escobar Steinvall, H. Detz, M. De Luca, A. Lugstein, E. P. A. M. Bakkers, A. Fontcuberta i Morral, I. Zardo
Physical Review Applied, **14**, 024045, 2020. [Link](#)

5. Van der Waals Epitaxy of Earth-Abundant Zn_3P_2 on Graphene for Photovoltaics

R. Paul, N. Humbolt, **S. Escobar Steinvall**, E. Z. Stutz, S. S. Joglekar, J. B. Leran, M. Zamani, C. Cayron, R. Logé, A. Granados del Aguila, Q. Xiong, A. Fontcuberta i Morral
 Crystal Growth & Design, **20**(6), 3816-3825, 2020. [Link](#)

4. Multiple Morphologies and Functionality of Nanowires made from Earth-Abundant Zinc Phosphide

S. Escobar Steinvall, N. Tappy, M. Ghasemi, R. R. Zamani, T. LaGrange, E. Z. Stutz, J. Leran, M. Zamani, R. Paul, A. Fontcuberta i Morral
 Nanoscale Horizons, **5**, 274-282, 2020. [Link](#)

3. Segregation Scheme of Indium in AlGaInAs Nanowire Shells

L. Francaviglia, G. Tütüncüoğlu, S. Martí-Sánchez, E. Di Russo, **S. Escobar Steinvall**, J. Segura Ruiz, H. Potts, M. Friedl, L. Rigutti, J. Arbiol, A. Fontcuberta i Morral
 Physical Review Materials, **3**, 023001, 2019. [Link](#)

2. Thermodynamic Re-Assessment of Zn-P Binary System

M. Ghasemi, E. Z. Stutz, M. Zamani, **S. Escobar Steinvall**, A. Fontcuberta i Morral
 Acta Materialia, **6**, 100301, 2019. [Link](#)

1. A Comparison of Explicitly-Terminated Diamond Electrodes Decorated with Gold Nanoparticles

J. Svanberg-Larsson, G. W. Nelson, **S. Escobar Steinvall**, B. Leo, E. Brooke, D. J. Payne, J. S. Foord
 Electroanalysis, **28**(1), 88-95, 2016. [Link](#)

Conferences & Workshops

- CIME Day, EPFL, Switzerland, 6th March 2020. [Link](#)
 - Talk titled “Growth and characterisation of zinc phosphide nanostructures”
- Nanowire Week, Pisa, Italy, 23rd – 27th September 2019. [Link](#)
 - Poster titled “Zinc phosphide nanowire growth by molecular beam epitaxy and their functional properties”
- European Materials Research Society Spring Meeting, Nice, France, 27th – 31st May 2019. [Link](#)
 - Talk titled “Growth and Functional Properties of Zn_3P_2 Nanowires for Energy Harvesting”
- Winterschool on “Quantum effects and miniaturization in Mechanics, Fluidics, Optics and Electronics”, Tegernsee, Germany, 7th – 11th January 2019. [Link](#)
 - Poster titled “Earth-abundant semiconductor nanowires for energy harvesting”
- EDMX Research Day, 12th December 2018. [Link](#)
 - Poster titled “Earth-abundant semiconductors for energy harvesting”
- Material Research Society Fall Meeting, Boston, USA, 26th – 30th November 2018. [Link](#)
 - Talk titled “Earth-abundant semiconductor nanowires for energy harvesting”
- EPFL-Max Planck Day 11th – 12th October 2018. [Link](#)
 - Talk titled “Growth of Zinc Phosphide nanowires using molecular beam epitaxy: a novel photovoltaic material”.
- University of Antioquia, Medellin, Colombia, 15th May 2018
 - Talk titled “Laboratoire des Matériaux Semiconducteurs”.
- NRG 2018 Winter School, Crans-Montana, Switzerland, 5th – 9th March 2018. [Link](#)
 - Poster titled “Investigation of Zinc Phosphide as a novel earth-abundant material for photovoltaics”.
- Summer school on “Nanotechnology meets Quantum Information”, Sab Sebastian, Spain, 23rd – 28th July 2017. [Link](#)
- Nanowire Week, Lund, Sweden, 29th May – 2nd June 2017. [Link](#)
 - Poster titled “Characterisation of earth abundant semiconductor nanostructures based on zinc phosphide and zinc arsenide”.
- Conference on Molecular Nanostructures, Ascona, Switzerland, 5th – 10th March 2017. [Link](#)

Teaching & Supervision

École Polytechnique Fédérale de Lausanne

- Teaching Assistant
 - Functional Properties of Materials (3rd Year Bachelor Course) 2016-2018
 - Linear Algebra I (1st Year Bachelor Course) 2016, 2019
- Semester Student Supervisor
 - 1 Bachelor Student Semester Project (7h/week) 2018
 - 3 Master Student Semester Projects (10h/week) 2017-2020

Imperial College London

- Organised and chaired a weekly lecture series where academics at the Materials Department presented overviews of their research to undergraduate and postgraduate students. 2015-2016
- Organised and helped with biweekly student help sessions for undergraduate students in the Materials Department 2014-2016

Publications under Peer-review

12. Van der Waals Epitaxy of $\text{Co}_{10-x}\text{Zn}_{10-y}\text{Mn}_{x+y}$ Thin Films: Chemical Composition Engineering and Magnetic Properties

A. Kúkol'ova, **S. Escobar Steinvall**, R. Paul, J. B. Lerañ, P. Che, M. Hamdi, A. Mucchietto, D. Grundler, A. Fontcuberta i Morral